

---

**Mobility of Charge Carriers, Particle Charging and  
Electro-Hydrodynamic Processes in Dielectric Liquids and  
Nanofluids**

Thesis presented for the degree of

**Doctor of Philosophy**

In the

Department of Electronic & Electrical Engineering

University of Strathclyde

2021

By

**Qingjiang Xue**

B.Sc., Beihang University (2014)

M.Res., University of Strathclyde (2017)

Department of Electronic & Electrical Engineering

University of Strathclyde

Glasgow, U.K.

## DECLARATION OF AUTHENTICITY AND AUTHOR'S RIGHTS

This thesis is the result of the author's original research. It has been composed by the author and has not been previously submitted for examination which has led to the award of a degree.

The copyright of this thesis belongs to the author under the terms of the United Kingdom Copyright Acts as qualified by University of Strathclyde Regulation 3.50. Due acknowledgement must always be made of the use of any material contained in, or derived from, this thesis.

Signed:  薛清江.

Date: 30<sup>th</sup> May 2021

## ACKNOWLEDGEMENT

---

I would like to give my warmest felt thanks to my supervisor, Dr. Igor Timoshkin, for his invaluable help, careful guidance, and continues support during my PhD study. Thank you for giving me a comprehensive training on my research. I quite believe that I will benefit from this in my future study.

Moreover, I would like to express my thanks to my second supervisor Dr Mark Wilson for his kind assistance and kindly guidance over the years.

Thanks to Dr. Wei Guoke, who influenced me so much on both my personal development and career plan over the decades. Thanks also to members of the HVT Group in Strathclyde: Song Bolin, Liu Ting, Dr Burhan Tariq and also, Dr Hong Qiteng and Mrs Xie Liping, Dr Li Chunpeng, and Dr Duan Xvhui, without you I would not have such an enjoyable life in Strathclyde.

Thanks to Mr. Andy Carlin and Mr Sean Doak of the HVT Workshop, who helped me so much on the experiment supply.

Others I wish to acknowledge my lovely friends: Mr Tu Hejun (ToTo), you helped me a lot and wish you could complete your mission perfectly as soon as possible. Mr Min Yongxin and Mrs Cui Yaqin, who gave me such a lot of help to both my life and study.

Thanks to Dr Qin Jian, Mrs Wang Bin and lovely Qin Xiao.

Finally, I would like to thank my parents for the support they gave to my life and my studies, especially their love for all the years.

## ABSTRACT

---

For over a century, different dielectric liquids are used as insulators and coolants in high voltage systems. Currently, with stricter environmental regulations and developments of more compact and elevated voltage apparatuses, the power and pulsed power industries require environmentally friendly dielectric liquids with better insulation and cooling ability, and higher adaptability. Among these liquids, ester liquids, including synthetic and natural esters, are introduced in the past decades: first synthetic ester liquids were introduced in the 1970s and now are utilised in high voltage power systems as liquid insulators. Apart from the pure dielectric liquids, nanofluids, which are developed by adding nanoparticles into dielectric liquids, started to generate significant interest among researchers and practitioners in high voltage technology. This is because the nanofluids may have greater dielectric strength and better heat conduction properties than pure dielectric liquids. However, physical mechanisms which result in this potential increase in breakdown strength of nanofluids are not fully understood and require further investigation.

In the present work field, both the dielectric liquids and the nanofluids hosted by these dielectric liquids were studied experimentally.

Three types of dielectric liquids were studied in this thesis: mineral oil, synthetic ester, and natural ester. The investigation is focused on the mobility of charge carriers in these dielectric liquids stressed with an external electric field with different magnitudes. The obtained results show that the mobility of charge carriers in all tested dielectric liquids has the same order of magnitude under the same electric field. Thus, it is concluded that the space charge density in the ester liquids, which have greater electrical conductivity than the conductivity of the mineral oils, is significantly higher than that in the mineral oil.

Nanofluids have been developed using these three types of dielectric liquids and two types of nanoparticles:  $\text{TiO}_2$  and BN nanoparticles. This study included developing an analytical model of field charging processes in nanofluids stressed with the external electric field and experimental investigation of the mobility of charge carriers and electrohydrodynamic (EHD) behaviours in nanofluids.

The analytical modelling is based on the Maxwell-Wagner relaxation theory. The surface charge distribution across the surface on a nanoparticle placed in an insulating liquid stressed with a step external electric field has been analytically obtained. The obtained results show that the surface charge density is governed by the electric conductivity and the dielectric permittivity of the dispersed particles and the hosting liquid. Furthermore, the Coulomb force between two particles immersed in a liquid was obtained analytically, enabling the analysis of the force acting between particles suspended in the host liquid, laying the foundation for further investigation of the EHD effects based on the experiment results.

The experimental investigation of the EHD effects in the nanofluids demonstrated that both the TiO<sub>2</sub> and BN nanoparticles acquired a net negative charge in both ester liquids when stressed with the external electric field. However, in the case of mineral-oil-based nanofluid, TiO<sub>2</sub> the BN particles become only polarised under the action of the external electric field, leading to the formation of ‘particle chains’ in the host liquid. The appearance of the ‘particle chains’ observed in the experiments was explained by the mathematical model developed in this work.

The results obtained in this work will be of interest to researchers and practitioners working in the field of insulation liquids and their practical applications in high voltage power and pulsed power systems.

## LIST OF ACRONYMS

AC	Alternative Current
ASTM	American Society of Testing Materials
BN	Boron Nitride
CCD	Coupled Charge
DAQ	Data Acquisition
DC	Direct Current
DID	Dipole-Induced-Dipole
EHD	Electrohydrodynamic
HV	High Voltage
IEC	International Electrotechnical Commission
LED	Light-Emitting Diode
MO	Mineral Oil
NE	Natural Ester
OHP	Outer Helmholtz Plane
PMMA	Polymethyl Methacrylate
SCLC	Space Charge Limited Current
SE	Synthetic Ester
TiO <sub>2</sub>	Titanium Dioxide
ToF	Time of Flight

# TABLE OF CONTENTS

<b>CHAPTER 1 INTRODUCTION .....</b>	<b>- 1 -</b>
1.1 INTRODUCTION TO THE RESEARCH PROJECT.....	- 1 -
1.2 RESEARCH OBJECTIVES .....	- 2 -
1.3 THESIS STRUCTURE .....	- 4 -
<b>CHAPTER 2 BACKGROUND AND LITERATURE REVIEW .....</b>	<b>- 7 -</b>
2.1 DIELECTRIC LIQUIDS .....	- 8 -
2.1.1 Dielectric Liquids for Electrical Insulation .....	- 8 -
2.1.2 Traditional Liquid Insulators: Mineral Insulating Oils.....	- 12 -
2.1.3 Recent Developments: Ester-Based Dielectric Fluids.....	- 14 -
2.2 ELECTRICAL CONDUCTION IN DIELECTRIC LIQUIDS.....	- 18 -
2.2.1 Charge Carriers and Their Origin .....	- 19 -
2.2.2 Electric Conduction in Dielectric Liquids .....	- 25 -
2.2.3 Charge injection Mechanisms at the Electrode-Liquid Interface .....	- 33 -
2.3 CHARGE CARRIERS AND THEIR MOBILITY.....	- 39 -
2.3.1 Mobility Measurement: Time of Flight Method.....	- 39 -
2.3.2 Mobility Measurement: Space Charge Limited Current Method .....	- 43 -
2.3.3 The Electrohydrodynamic Effect.....	- 46 -
2.4 NANOFUIDS AND THEIR USE IN ELECTRICAL SYSTEMS.....	- 50 -
2.4.1 Nanofluids: History and Applications .....	- 50 -
2.4.2 Polarisation and Charging of Particles .....	- 53 -
2.5 SUMMARY.....	- 57 -

**CHAPTER 3 MATHEMATICAL MODEL OF PARTICLE CHARGING IN DIELECTRIC LIQUIDS..... - 60 -**

3.1 *PARTICLES IN DIELECTRIC LIQUID: DEVELOPMENT OF MATHEMATICAL MODEL* - 61 -

3.1.1 Electric Response of Single Particle ..... - 61 -

3.1.2 Forces Acting on Particles in Liquids ..... - 65 -

3.1.3 Coulomb Force Acting between Two Particles ..... - 67 -

3.2 *SIMULATION RESULTS AND DISCUSSIONS* ..... - 73 -

3.2.1 Maxwell-Wagner Relaxation Time ..... - 73 -

3.2.2 Surface Charge Distribution ..... - 75 -

3.3 *SUMMARY*..... - 92 -

**CHAPTER 4 EXPERIMENTAL AND DATA ANALYSIS METHODOLOGIES ..... - 93 -**

4.1 *NANOFUIDS: DEVELOPMENT AND PARTICLE SIZE EXAMINATION* ..... - 94 -

4.1.1 Properties of the Raw Materials ..... - 94 -

4.1.2 Development of Nanofluids ..... - 96 -

4.1.3 Particle Size Distribution in Nanofluids ..... - 97 -

4.2 *DESIGN OF EXPERIMENTAL SYSTEM: INSTRUMENTS* ..... - 104 -

4.2.1 Power Supplies and Control System..... - 104 -

4.2.2 Experimental Design: Electric Current Measurements ..... - 106 -

4.2.3 Experimental Design: Optical Instruments ..... - 108 -

4.3 *TEST CELLS* ..... - 109 -

4.3.1 Test Cell with a Guard-Ring Electrode ..... - 109 -

4.3.2 Transparent Test Cell with Parallel Disk Electrodes ..... - 112 -

4.3.3 Coaxial Test Cell ..... - 115 -

4.3.4 Test Cell with Needle-Plane Electrodes ..... - 117 -

4.4 *SUMMARY*..... - 119 -

**CHAPTER 5 MOBILITY OF CHARGE CARRIERS: UNIFORM ELECTRIC FIELD..... - 122 -**

5.1 *EXPERIMENTAL PROCEDURE*.....- 123 -

5.1.1 Reverse-Polarity Method..... - 123 -

5.1.2 Single-Polarity Method..... - 124 -

5.2 *REVERSE-POLARITY METHOD*.....- 125 -

5.2.1 Mobility of Charge Carriers in Synthetic Ester ..... - 125 -

5.2.2 Mobility of Charge Carriers in Natural Ester ..... - 131 -

5.2.3 Mobility of Charge Carriers in Mineral Oil..... - 134 -

5.3 *SINGLE-POLARITY METHOD* .....- 137 -

5.3.1 Mobility of Charge Carriers in Synthetic Ester ..... - 138 -

5.3.2 Mobility of Charge Carriers in Natural Ester ..... - 142 -

5.3.3 Mobility of Charge Carriers in Mineral Oil..... - 145 -

5.4 *DISCUSSION AND SUMMARY* .....- 149 -

**CHAPTER 6 MOBILITY OF CHARGE CARRIERS: NON-UNIFORM ELECTRIC FIELD..... - 155 -**

6.1 *EXPERIMENTAL PROCEDURE*.....- 156 -

6.2 *SPACE CHARGE SATURATION REGIME OF CONDUCTION AND MOBILITY OF CHARGE CARRIERS*.....- 159 -

6.2.1 Mobility of Charge Carriers in Synthetic Ester ..... - 159 -

6.2.2 Mobility of Charge Carriers in Natural Ester ..... - 164 -

6.2.3 Mobility of Charge Carriers in Mineral Oil..... - 168 -

6.3 *SPACE CHARGE GOVERNED ELECTRIC FIELD* .....- 173 -

6.3.1 The Field Strength of the Needle Tip ..... - 173 -

6.3.2 Field Distribution in the Point-Plane Topology..... - 175 -

6.4	<i>DISCUSSION AND SUMMARY</i> .....	- 179 -
-----	-------------------------------------	---------

**CHAPTER 7 ELECTROHYDRODYNAMIC PROCESSES IN NANOFUIDS**

.....		<b>- 186 -</b>
-------	--	----------------

7.1	<i>EXPERIMENTAL PROCEDURE</i> .....	- 187 -
7.1.1	Test Cell with a Guard-Ring Electrode .....	- 187 -
7.1.2	Transparent Test Cell with Parallel Disk Electrodes .....	- 188 -
7.2	<i>PARTICLE DYNAMICS IN SYNTHETIC-ESTER-BASED NANOFUIDS</i> .....	- 188 -
7.2.1	Direct Observation .....	- 189 -
7.2.2	Micro-scale observation .....	- 194 -
7.3	<i>PARTICLE DYNAMICS IN NATURAL-ESTER-BASED NANOFUIDS</i> .....	- 200 -
7.3.1	Direct Observation .....	- 200 -
7.3.2	Micro-scale Observation .....	- 205 -
7.4	<i>PARTICLE DYNAMICS IN MINERAL-OIL-BASED NANOFUIDS</i> .....	- 207 -
7.4.1	Direct Observation .....	- 208 -
7.4.2	Micro-scale Observation .....	- 214 -
7.5	<i>DISCUSSION AND SUMMARY</i> .....	- 218 -

**CHAPTER 8 CONDUCTION CURRENT AND MOBILITY OF CHARGE**

<b>CARRIERS IN NANOFUIDS</b> .....		<b>- 225 -</b>
------------------------------------	--	----------------

8.1	<i>EXPERIMENTAL PROCEDURE</i> .....	- 226 -
8.1.1	Tests Conducted in the Guard-Ring Test Cell .....	- 226 -
8.2	<i>EXPERIMENTAL RESULTS: NANOFUIDS WITH TiO<sub>2</sub> PARTICLES</i> .....	- 227 -
8.2.1	Electric Current and Mobility of Charge Carriers in Synthetic-ester-based Nanofluids .....	- 227 -
8.2.2	Electric Current and Mobility of Charge Carriers in Natural-ester-based Nanofluids .....	- 236 -

8.2.3	Electric Current in Mineral-oil-based Nanofluids .....	- 242 -
8.3	<i>EXPERIMENTAL RESULTS: NANOFUIDS WITH BN PARTICLES</i> .....	- 251 -
8.3.1	Electric Current and Mobility of Charge Carriers in Synthetic-ester-based Nanofluids .....	- 251 -
8.3.2	Electric Current and Mobility of Charge Carriers in Natural-ester-based Nanofluids .....	- 258 -
8.3.3	Electric Current in Mineral-oil-based Nanofluids .....	- 264 -
8.4	<i>DISCUSSION AND SUMMARY</i> .....	- 270 -
<b>CHAPTER 9 CONCLUSIONS AND FURTHER WORK.....</b>		<b>- 273 -</b>
9.1	<i>MAIN CONCLUSIONS</i> .....	- 273 -
9.1.1	Liquids in Uniform Electric Field.....	- 273 -
9.1.2	Dielectric Liquids in Non-uniform Electric Field .....	- 274 -
9.1.3	Nanofluids in Uniform Electric Field .....	- 275 -
9.2	<i>SUMMARY OF CONTRIBUTIONS</i> .....	- 275 -
9.3	<i>FUTURE WORK</i> .....	- 276 -
<b>REFERENCES .....</b>		<b>- 278 -</b>
<b>APPENDIX I MATHEMATICAL DERIVATION .....</b>		<b>- 287 -</b>
<b>APPENDIX II PARAMETERS FOR QUICKFIELD MODELLING.....</b>		<b>- 291 -</b>
<b>APPENDIX III DATA ANALYSIS METHODS.....</b>		<b>- 294 -</b>
	<i>ERRORS AND UNCERTAINTY</i> .....	- 294 -
	<i>DATA FILTERING</i> .....	- 296 -
<b>APPENDIX IV PUBLISHED WORK.....</b>		<b>- 302 -</b>



## Chapter 1 INTRODUCTION

---

### 1.1 Introduction to the Research Project

Electric power provides the foundation for the economic and social needs of modern society. The development of modern society, in turn, imposes new stricter requirements on the power systems, such as reduction of the emission of greenhouse gases, new safety restrictions and wider use of environmentally friendly (biodegradable) materials. The dielectric liquids play a crucial role in the electric insulation of different high voltage power systems. These liquids are widely used in the power and pulsed power industries. As a result, there is a strong demand for safer and more environmentally friendly materials for industrial high voltage applications.

New types of dielectric liquids are introduced to meet these requirements: ester liquids and nanofluids developed by dispersing sub- $\mu\text{m}$  dielectric particles in pure host liquids.

Synthetic and natural dielectric fluids have been developed by different manufacturers, these insulating liquids include MIDELE 7131 [1] and MIDELE eN1204 [2], produced by M&I Materials Ltd; Envirottemp 360 [3] and Envirottemp FR3 [4], produced by Cargill Ltd; and BIOTEMP [5], produced by ABB Ltd. The ester liquids have several advantages over the mineral oil, which is the most commonly used insulating liquid, including their non-toxic nature, bio-degradability and higher flash point. However, wider application of the ester liquids in high voltage systems and facilities still requires further understanding of the breakdown and conduction mechanisms when they are stressed with external electric fields.

Generally, these mechanisms include electrical conductivity, AC and lightning impulsive breakdown strength, dissipation factor, and relative permittivity. The mobility of charge carriers and their concentration define the electrical conductivity of insulating liquids. Several breakdown theories also include the mobility of charge carriers in the liquids: the development of the space charge is influenced by the mobility of charge carriers. The localised Joule heating in the bubble theory is also based on the electrical conductivity of the liquid, which is governed by the mobility of charge carriers. Thus, investigation of the

mobility in the ester liquids can provide further information which will help to increase their practical applications as liquid insulators in different high voltage power and pulsed power systems.

Recently, nanofluids have been introduced as novel insulating liquids with improved dielectric and thermal properties. The nanofluids are manufactured by adding nanoparticles into pure dielectric liquids: Eastman (1999) used  $\text{Al}_2\text{O}_3$  and  $\text{CuO}$  nanoparticles to improve the thermal conductivity of the oil-based nanofluids [6], Segal (1998) described the enhancement of the breakdown strength of nanofluids consisting of mineral oil and  $\text{Fe}_3\text{O}_4$  nanoparticles [7]. Different particles were used to develop oil-based and ester-based nanofluid described in the literature, like  $\text{SiO}_2$  [8][9],  $\text{BN}$  [10][11],  $\text{ZnO}$  [12], and  $\text{AlN}$  [13]. The theories explaining a potential increase in the dielectric strength of nanofluids were also introduced and discussed: it is proposed that the enhancement of the dielectric strength is caused by trapping free electrons and ions by the nanoparticles dispersed in nanofluids. An increase in the thermal conductivity of the nanofluids can be attributed to the motion of nanoparticles and the nanoparticles with a greater thermal conductivity.

However, the mechanisms which result in the improvement in the dielectric and thermal properties of the nanofluids are complex and still not fully understood. Thus, new analytical approaches and experimental results that can help design new types of nanofluids with further improvement in their dielectric strength and thermal properties are urgently required. To address this issue, the investigation of the nanofluids, including the EHD behaviour of nanoparticles and the mobility of charge carriers in the nanofluids, has been carried out in the present study.

## **1.2 Research objectives**

This thesis is focused on the systematic study of the conduction mechanisms and the EHD movement in pure dielectric liquids (synthetic ester, natural ester, and mineral oil) and nanofluids prepared by suspending  $\text{TiO}_2$  and  $\text{BN}$  nanoparticles in these liquids. To explain the EHD behaviour of the particles in the nanofluids stressed with the external electric field, a comprehensive analytical model which describes the polarisation and charging of a poorly conductive particle in liquid stressed with an external electric field has been developed. Using

this model, the charging and polarisation processes have been investigated. Moreover, the surface charge distribution on particles with different relative permittivities and electrical conductivities suspended in the dielectric liquids has been obtained.

The experimental part of this work is aimed on the investigation of the conduction current in pure dielectric liquids and nanofluids prepared based on these liquids, obtaining, and analysing the mobility of charge carriers in these liquids.

The mobility of charge carriers in the dielectric liquids was obtained using three ranges of the external field: from 40 kV/m to 80 kV/m, from  $4 \cdot 10^2$  kV/m to  $1.2 \cdot 10^3$  kV/m, and from  $\sim 1.6 \cdot 10^9$  kV/m to  $\sim 4 \cdot 10^9$  kV/m. Using this wide range of electric fields, the functional dependency of the mobility of the charge carriers on the field magnitude was established and discussed.

The EHD movement of suspended particles in the nanofluids was also studied using the direct and micro-scale observation methods. The functional behaviour of the suspended nanoparticles in the external electric field was established.

The main research objectives of this study are summarised as follows:

- Investigation of the mobility of charge carriers in ester liquids and mineral oils in the quasi-uniform field using the reverse-polarity and single-polarity methods.
- Investigation of the mobility of charge carriers in ester liquids and mineral oils in the strongly divergent field governed by the space charge limited current.
- Investigation of the electric field redistribution in the point-plane electrode topologies filled with dielectric liquids.
- Investigation of the conduction processes and mechanisms in nanofluids stressed with the external electric field.
- Investigation of the EHD behaviour of nanoparticles suspended in the dielectric liquids (nanofluids) stressed with the external electric field.
- Investigation of the mobility of charge carriers in ester-based nanofluids.
- Development of the mathematical model of charging and polarisation of poorly conductive particles in dielectric liquids stressed with an external electric field.

## 1.3 Thesis Structure

The present thesis consists of 8 Chapters. Analytical Chapters provide a comprehensive literature review of existing theories and experimental results on conduction in different insulating fluids. Moreover, the model developed and used in the present work investigated field charging and polarisation of solid particles immersed in insulating liquids. The experimental Chapters of this thesis describe the methods and methodologies used in the present thesis to study the conduction and electrohydrodynamic processes in dielectric liquids. These chapters present and discuss the obtained experimental results as follows.

Chapter 2 provides a comprehensive literature review on electrical conduction mechanisms in the dielectric liquids, electrohydrodynamic effects and conduction characteristics of pure insulating liquids and nanofluids. This chapter discusses different types of dielectric liquids used in high voltage engineering. It also provides a review and analysis of different nanofluids, which potentially can be used as insulating liquids. The literature review in this chapter helps to identify gaps in the knowledge which restrict the development and practical applications of novel dielectric liquids, including natural esters, synthetic esters, and nanofluids in high voltage power and pulsed power applications. Chapter 2 presents a critical analysis of the previously obtained results and fundamental theories on the conduction processes in dielectric liquids, particle charging, and movement of particles in liquids stressed with an external electric field. The mechanism(s) of electric conduction in the dielectric liquids are presented and discussed. The mobility of charge carriers and relative measurement methods in dielectric liquids are presented and analysed. Different factors which may affect the mobility measurements are also discussed to explain the experimental results obtained in the present study.

Chapter 3 focuses on the development of the analytical model, which describes the field charging of dielectric and poor conductive particles in liquid dielectrics. Maxwell-Wagner polarisation theory is introduced at the beginning of this chapter. The field charging of a single particle in the hosting liquid stressed with a step DC voltage (suddenly applied electric field) was investigated. A complete analytical solution to this problem which considers both conductivities and dielectric permittivities of the particle and the hosting liquid, has been obtained. Then, based on this analytical solution, the dipole moment of a single particle was obtained, which enabled an analytical analysis of the Coulomb forces acting between two

particles located in the host fluid. The obtained analytical solution allows for the analysis of electrodynamic interaction between two particles in the fluid. Different combinations of these parameters were used in the modelling presented in this chapter allowing for analysis of the electrohydrodynamic behaviour of different particles used in the present study.

Chapters 4 to 8 present the experimental results obtained in this thesis.

Chapter 4 describes the experiment setup, including tests cells and diagnostic instruments. The experimental test system includes

- different power supplies
- custom built and commercially available tests cells
- LabVIEW controlling system
- optical diagnostic system for visualisation of the particle motion in nanofluids
- electrical diagnostic systems for measurements of voltage and conduction current

The experimental methodology and the analysis methodology of obtained experimental data are presented and discussed in Chapter 4. Chapter 4 also discusses insulating liquids and fluids used in this study and nanoparticles used to develop nanofluids.

Chapters 5 and 6 are focused on the study of the mobility of charge carriers in dielectric liquids. Chapter 5 presents the experimental system and methodology based on the Time of Flight method. This method was implemented in two different test cells: the coaxial test cell, which enables the reverse-polarity method, and the guard-ring structured test cell, which enables the single-polarity method. The mobility of charge carriers in three different dielectric liquids was obtained: mineral oil, synthetic and natural ester liquids. The mobility of charge carriers was obtained under different field strengths, which allows for characterisation of the functional behaviour of the mobility of charge carriers. Based on the obtained values of the mobility, the space charge density in the three dielectric liquids was compared and discussed.

Chapter 6 is also focused on the study of the mobility of charge carriers in dielectric fluids. However, in this chapter, another method ‘the Space Charge Limited Current method, that provides significantly higher electric field magnitude, was used. The test cell with a needle-

plane topology of electrodes was used in Chapter 6. The field strength in this test cell is significantly higher than the field strength used in the test cells used in the Time of Flight method in Chapter 5. Such a design enabled the platform to compare the mobility of charge carriers in the three dielectric liquids under the electric field ranging from  $10^{-3}$  kV/m to  $10^3$  kV/m. The critical analysis of the obtained results and their comparison with the published literature data is provided at the end of this chapter.

Chapter 7 presents and discusses the electrohydrodynamic motion of nanoparticles in nanofluids stressed with DC high voltage. Two types of particles: TiO<sub>2</sub> and BN, were selected for the synthesis of the nanofluids. Two observation methods were used to monitor the movement of the nanoparticles in nanofluids: direct and micro-scale observations. The behaviour of nanoparticles was explained with the supports from the experimental results and the analytical model developed in Chapter 3. Based on the obtained results, the field charging mechanisms of nanoparticles have been explained, and this discussion is presented in the conclusion part of Chapter 7.

The results of the study on the mobility of charge carriers and conduction characteristics of nanofluids are presented and discussed in Chapter 8. The current in the nanofluids as a function of time was obtained and the current-time characteristics are presented and discussed. The mobility of charge carriers in the ester-based nanofluids is also presented in this chapter. The potential reason for the difference between the mobilities of charge carriers in nanofluids and pure dielectric liquids is proposed and presented in this chapter.

The thesis is completed with Chapter 9, which presents, summarises, and critically discusses the original results and conclusions obtained in this study. The mechanisms responsible for the electric conduction in both pure dielectric liquids and nanofluids are presented and critically analysed. Recommendations for future work, including further development of the analytical model(s) and potential experiment tests, which will provide further information on the conduction mechanisms and electrohydrodynamic effects in the liquid dielectrics and nanofluids, are presented in Chapter 9.

## Chapter 2 BACKGROUND AND LITERATURE REVIEW

---

To meet the development of the electric system, various insulating liquids are developed over the past century, including mineral oils and ester liquids. Apart from the pure liquids, nanofluids, which are synthesised by dispersing nanoparticles in dielectric liquids, have also been proposed for electric facilities as insulating liquids with advanced characteristics.

The main functions of these liquids in electric systems are insulating and cooling. Both of these two functions are closely linked with the underlying mechanisms that happened in these liquids when they are stressed with external electric fields. Thus, further knowledge and information on these physical mechanisms are needed to select suitable liquids for different practical applications.

This chapter starts with a brief review of the history of the practical use of dielectric liquids for electrical insulation purposes. Detailed introduction of the mineral oils, synthetic esters, and natural esters is presented.

The conduction mechanisms in the dielectric liquids are presented and discussed based on the behaviour of the charge carriers in these liquids. Attention is paid to the different mechanisms of production and injection of the charge carriers into the dielectric liquid stressed with an external electric field.

Two methods of obtaining the mobility of charge carriers in dielectric liquids are presented, including the factors affecting the accuracy of experimental measurements, i.e., the electrohydrodynamic in the liquids due to the external electric fields.

This chapter also provides an overview of nanofluids manufactured by dispersing nanoparticles into the dielectric liquid. The electrical and dielectric properties of different nanofluids are discussed in the chapter, together with the current conduction and particle charging theories in nanofluids under external electric fields.

## **2.1 Dielectric Liquids**

In this section, the history, classification, and basic aspects of production of dielectric liquids have been reviewed. This section also provides an overview of the physical and electrical properties of dielectric liquids and fluids used in the present study.

### **2.1.1 Dielectric Liquids for Electrical Insulation**

Significant contributions have been made by the progress of the modern electric system in pushing our society forward. At the same time, as society moves forward, new requirements for the electric system are emerging: higher dielectric strength, compactness and minimum footprint, higher thermal conductivity, and environmental safety. Insulation systems, as a key component in the electric system, therefore, will face new challenges.

In general, electrical insulation materials can be classified based on their state, i.e., solid insulation, gaseous insulation, and liquid insulation.

The commonly employed solid insulating materials include polymers like PVC (polyvinyl chloride), PTFE (polytetrafluoroethylene), rubber, etc., which are used for wire insulation in low voltage power apparatuses. Ceramic is a common insulation material used in high voltage systems, while paper/pressboard insulators are used in power transformers (liquid-filled transformers). These materials are economical and reliable. However, there are limitations in the use of solid insulators: one of them is permanent damage caused by electrical breakdown. Since solid insulators are non-self-restoring, once the solid insulator is damaged by the breakdown event, it then must be replaced to ensure the proper protection of the power/HV equipment, which may result in a high cost in term of time and finances under some circumstances.

Different from solid insulators, the insulating gases are “self-healing”, which means that their insulation properties can be re-established after each breakdown in the gaseous medium (although specific time is required for complete recovery of the breakdown strength of gases after each breakdown/discharge). Examples of dielectric gases, i.e., gases which can be used as insulators in high voltage systems, include air, nitrogen, sulphur hexafluoride (SF<sub>6</sub>), and

other gases. Air is the most common gas which is being used in power systems such as dry transformers and open space substations as an insulator due to its availability and low cost. SF<sub>6</sub> is a popular gaseous insulator as its breakdown strength 2.7 times greater than that of air at atmospheric pressure [14]. Moreover, SF<sub>6</sub> is a non-toxic and non-flammable fluid, which makes it an ideal gaseous insulator for compact systems such as Gas Insulated Systems/Lines (GIS/GIL). However, the emission of SF<sub>6</sub> into the atmosphere is now limited by governmental regulations as SF<sub>6</sub> is a highly potent green gas, which “has a global warming potential (GWP) 23,900 times greater than that of CO<sub>2</sub> and an atmospheric life of 3200 years[15]”. Thus, the power industry now aims to minimise the use of this gas in power equipment and substitute SF<sub>6</sub> with environmentally friendly fluids.

Liquid insulators have the advantages of both the solid insulators and the gaseous insulators: compared with the solid insulators, liquid insulators have the ability to conform into complex configurations and the ability of self-restoring; compared with gaseous insulators, liquid insulators have the greater dielectric strength, and higher thermal conductivity [16][17].

Due to these characteristics, insulating liquids have been widely used in high voltage power and pulsed power systems such as transformers, regulators, reactors, high voltage switches, circuit breakers, and other equipment. Liquid insulators are also utilised to prevent the oxidation of metallic components and parts immersed in these liquids. Compared with the other two types of insulation materials, liquids can also act as an ageing indicator of the equipment, i.e., the dissolved gas analysis (DGA), moisture content analysis and acidity analysis on the transformer oil can provide a quantitatively indication of the internal condition of a transformer, assisting in evaluating and predicting the risks on the protected system.

The main research objective of this thesis is to investigate the conduction mechanisms and charge carrier properties of different dielectric insulation liquids, specifically the dielectric liquids used in high voltage power systems such as power transformers. The main purpose of employing insulating (transformer) oils in power transformers is to suppress internal arcing, corona discharges and to dissipate heat generated inside the transformers. These oils age during their service, and thus their state should be monitored to prevent a catastrophic electrical failure of the power system insulated with these liquids.

The dielectric liquids can be classified based on their chemical composition as mineral-based, silicone-based, and ester-based liquids. Among these, the insulating liquids called mineral oil are produced by the refining of the crude oil stock. Mineral oils have the longest history of employment for insulation purposes. The silicone-based liquids, which appeared as insulation liquids in the 1970s, are more used in the environment with higher requirements for fire safety. The ester-based fluids, including both synthetic esters and natural esters, are attracting the attention of commercial users and researchers due to their non-toxic nature and environmentally friendly aspects (biodegradability). Natural ester liquids are based on vegetable oils, and these types of liquid dielectrics have been used as insulators at the very beginning of the development of electric systems (at the dawn of the power industry as we know it). However, their use was abandoned shortly after that due to their higher viscosity and poorer oxidation stability compared with the mineral oils, i.e., the earliest simple natural ester dielectrics were subsequently found to be incompatible with free breathing equipment, and were gradually replaced by mineral oils [18]. Figure 2-1 illustrates the brief timeline of these dielectric liquids for high-voltage applications.

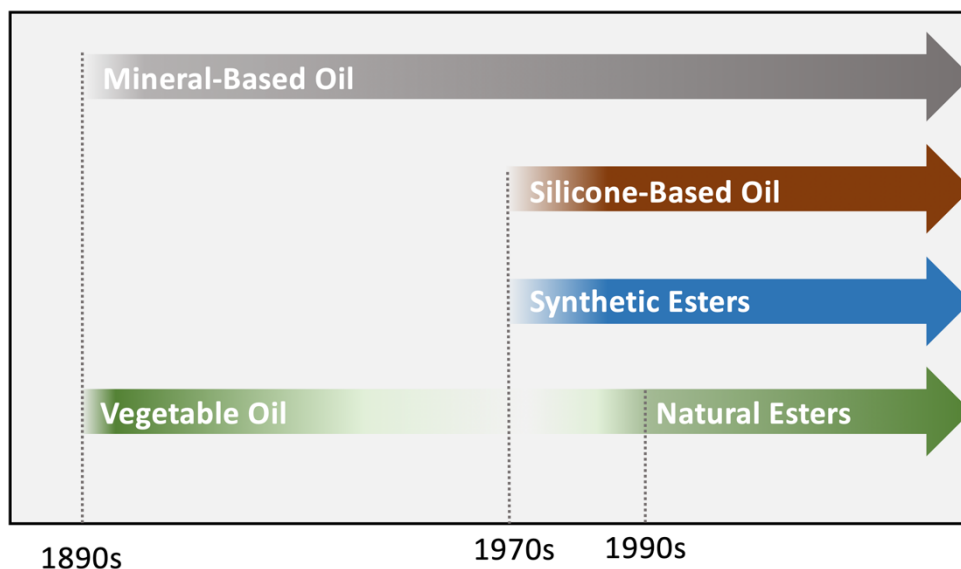


Figure 2-1 Timeline of dielectric liquids' application in high voltage applications (data source: [19])

The critical parameters to evaluate the dielectric liquids are their dielectric strength, and thermal conductivity, both of which are studied by researchers. There are other parameters and specific properties of the dielectric liquids which are important for characterisation of insulating liquids, the main of which are introduced below:

- Dissipation factor, which is also known as loss factor or tan delta of transformer oil. It is the tangent of the angle between the alternating field vector and the dielectric liquids' loss component. The higher the value of the tan delta, the significant the dielectric loss should be. The dissipation factor can be measured according to the IEC 60247 and the ASTM D1531-06.
- Viscosity, which is directly linked with the cooling effect of the dielectric liquids. A low viscosity leads to the high heat transfer ability of the dielectric liquids, indicating their high cooling performance.
- Flash point, and fire point, both of which are descriptions of the fire resistance performance of the dielectric liquids. The flash point is the minimum temperature at which the vapour pressure is sufficient to form a flammable mixture with air near the surface of the liquid, while the fire point is the minimum temperature at which the mixture can continue to burn for more than 5 s. Generally, the fire point can be assumed to be 10°C higher than the flash point.
- Pour point, is the minimum temperature that the liquid can still flow, which is critical to the dielectric liquids used in colder areas.
- Oxidation stability is the assessment of the oxidation resistance of the dielectric liquids by determining the amount of acid or sludge products formed, which is directly linked with the liquids' reliability in applications.
- Water and moisture tolerance, which influences the dielectric strength, and the lifetime of the dielectric liquids, respectively.
- Environmental safety, which can be divided as biodegradability and non-toxicity, whose importance has increased over recent decades due to the wider application circumstances of the electrical utilities. This is because the leakages of the dielectric liquids in some of these circumstances can cause a direct negative impact on the soil and waters, resulting in serious environment accidents.

In this research project, the mineral oil and two different ester liquids have been used and studied. A more detailed, specific introduction to these liquids is required before commencing the experimental investigation.

### 2.1.2 Traditional Liquid Insulators: Mineral Insulating Oils

The mineral insulating oils are made from crude oil, and their industrial application history is dated back to the 1890s when Brown, Boveri & Cie (now known as ABB) first used it in Europe [20]. There are four main chemical components of mineral oil: paraffins, naphthenes, aromatic compounds, and olefins, molecule structures of which are illustrated in Figure 2-2.

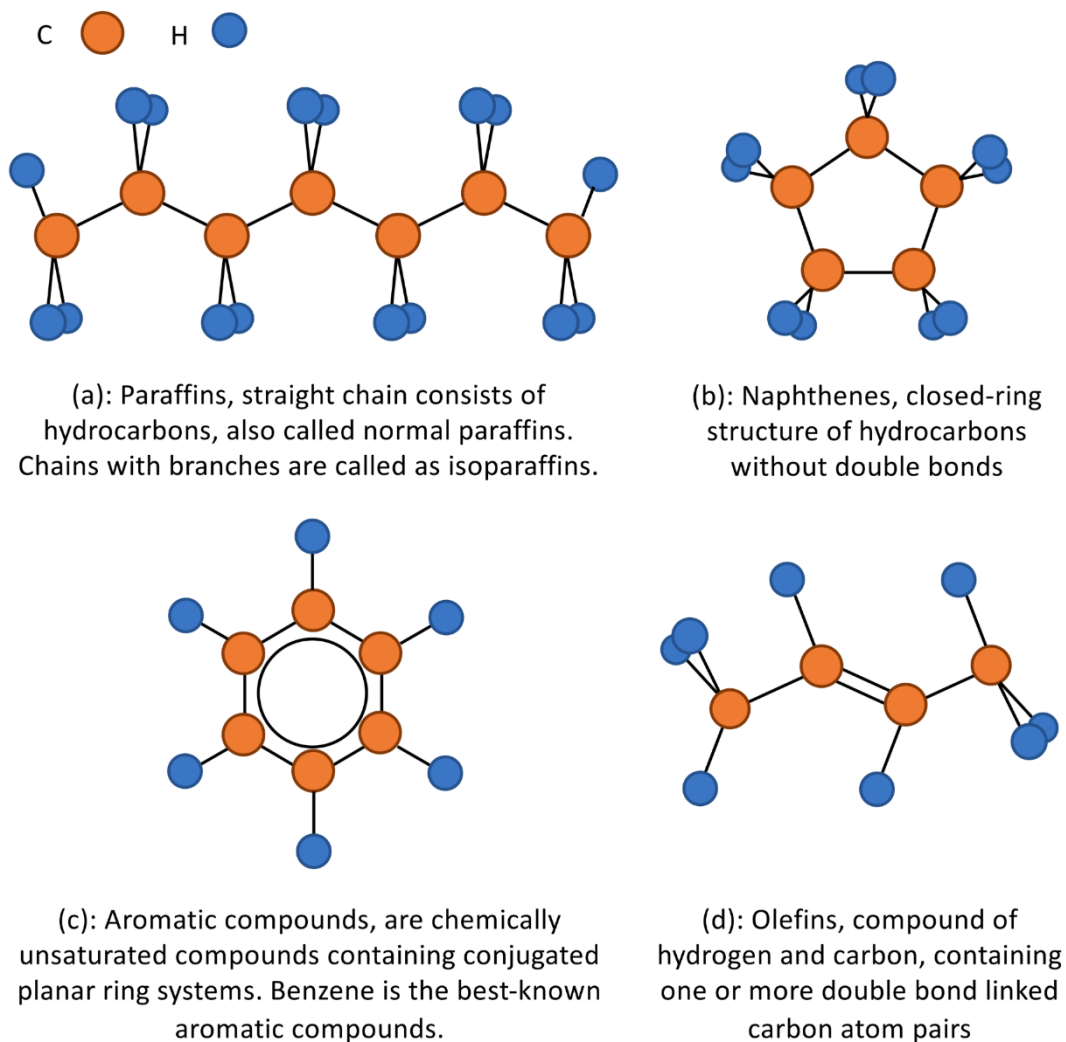


Figure 2-2 Molecule Structures of Paraffins, Naphthenes, Aromatic Compounds, and Olefins (Figure based on [21]).

With a long history of serving in electric power systems, mineral oils are the most commonly used insulating liquids in the power industry nowadays. On one hand, mineral oil can offer an excellent electrical insulating property at the lowest cost compared with other insulation liquids. On the other hand, traditional mineral oil has disadvantages related to safety and environmental aspects due to its low fire point (flammability) and weak biodegradability.

The major industry standards for the mineral insulation oil used in electrical apparatus are the ASTM D3487 and the IEC 60296, both of which describe test methods and specifications of the unused mineral oil.

For the classifications of mineral oils, both of these two standards classify mineral oils in accordance with their deoxidation aspects, such as oxidation stability, as the oxidation stability of dielectric liquids is directly linked with their lifetime. According to the ASTM D3487 standard, two types of mineral transformer oils can be defined in accordance with their practical use in high voltage systems: Type I is used in the equipment that does not require much oxidation resistance, and Type II is used to offer greater deoxidation to immersed equipment [22]. The IEC 60296 specification divides mineral oils into three types according to their additive (inhibitor) content: the uninhibited oils are marked with 'U', i.e., oils with 0% antioxidant content, the liquids with antioxidant content is less than 0.08% (are marked with 'T', and the liquids with antioxidant content is less than 0.4%, are marked with 'I' [23].

Apart from these two standards, all mineral oils can also be divided into two main categories in accordance with their chemical composition: paraffin based and naphthene based oils. Mineral oils which consist of carbon atoms by more than 50% in their paraffinic structures are classified as paraffin based oils. If mineral oil has less than 50% of carbon atoms in its paraffinic structures, such oil will be classified as naphthenes based oil [24].

The early industrial-grade mineral oils were paraffinic oils, but later they were replaced with naphthenic oils due to their higher pour points [25]. During recent years, naphthenic oils became a dominant insulating liquid used in the power industry, and nowadays, they account for the largest market share of 55% in the global market, followed by paraffinic oils [26]. But it is difficult to state which of these two types of oils is a better choice as the factors influencing the selection of insulating liquids for specific high voltage applications are complex: for example, the long chain of the paraffin can obstruct the flow of the paraffinic

oil especially at low temperatures, leading to that the paraffin based oils are vicious in comparison to the naphthene based oils in cool circumstances [27]. Besides, the viscosity decreases with an increase in temperature of the paraffins based oil is also lower than that of the naphthenic oil [24]. These two aspects result in the lower cooling effect of the paraffinic oils than the naphthenic oils. On the other hand, in terms of lifetime, the paraffinic oils can be produced as sulphur-free fluids to increase their oxidative stability, while the naphthenic oils can only be manufactured with low sulphur content but not totally free from it [28].

Although mineral oils were widely used for over one century in the power industry, the limitations for practical applications of mineral-based insulation oils still exist. First, mineral oils are flammable, and they provide an increased risk of incidents. In addition, the toxicity of mineral oils (as they contain, for example, benzene) limits their indoor applications. In recent years, the increasing requirements to use environmentally friendly materials raise new challenges for manufactures of insulation oils, power industry practitioners, and manufacturers of power equipment. These new requirements encourage oil manufactures and manufacturers of high voltage equipment to find safer and environmentally friendly replacements for the mineral insulation oils. In this case, the ester-based fluids are introduced in the high voltage system, of which the details are presented in the following section.

### **2.1.3 Recent Developments: Ester-Based Dielectric Fluids**

The potential of natural-ester-based dielectric fluids, such as vegetable oils, to serve as insulation liquids started to be explored about one century ago, but their poor oxidation stability, higher pour point, and elevated relative permittivity restricted their industry applications [29]. Since then, not too much effort was contributed to this area until the severe oil crisis of the 1970s, which forces the industry to find potential replacements to the mineral oils [30]. Over the recent decades, *Sustainable Development* becomes a dominant trend in many industries, including the power industry, requiring the insulation liquid to be non-toxic and biodegradable, encouraging the commercial development of ester-based insulation liquids [31].

To date, the ester-based insulation liquids can be divided into two main groups: natural esters and synthetic esters. The standards on the applications of the natural esters in transformers and similar oil-impregnated electrical equipment are IEC 62770 and ASTM D 6871, both of

which include the descriptions and test methods of the natural esters. Similar standards on the synthetic esters are IEC 61099 and ASTM WK46195 (draft under development by ASTM Committee D27).

From the chemical composition point of view, an ester is an organic compound formed from an alcohol and an acid. The molecule structure of an ester linkage (-COOR, R represents the organic groups) is illustrated in Figure 2-3 (a). In the power industry, in relation to electrical insulation, esters typically mean the insulation liquids, which are either natural esters or synthetic esters.

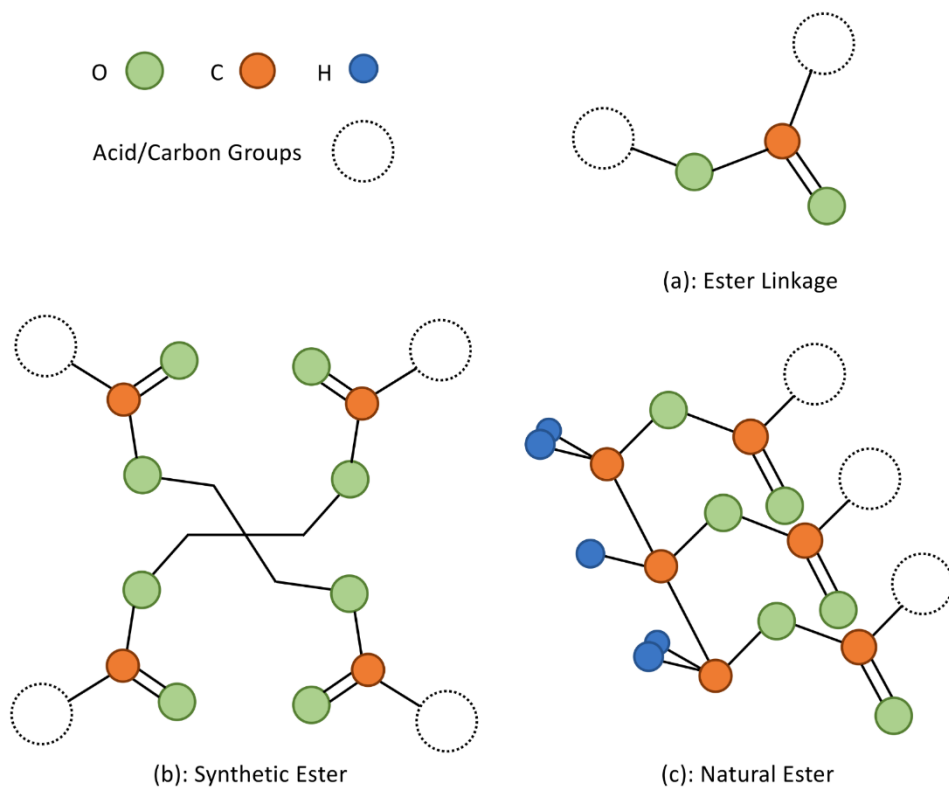


Figure 2-3 Molecule Structures of Ester Linkage, Synthetic Ester, and Natural Ester  
 (figures based on [21])

The synthetic esters, whose molecule structure is shown in Figure 2-3 (b), are manufactured from selected raw materials via chemical reactions. The four groups connected to the central polyol backbone are usually designed as saturated fatty acid groups to improve the oxidation ability of the synthetic esters [32].

The natural esters, whose molecule structure is illustrated in Figure 2-3 (c), are typically extracted from oil plant seeds like sunflower, rapeseed, soybean, and canola. Compared with synthetic esters, natural esters are chain structures with different lengths [33]. Such differences typically come from the differences among the raw materials and lead to the different properties of these natural esters. For example, the proportion of the saturated acids and the unsaturated acids are varying from different seed oils, some of which are listed in Table 2-1:

Table 2-1 Acid Compositions of Some Typical Seed Oils (Data from [34])

Seed oil	Saturated fatty acid (%)	Unsaturated fatty acid (%)		
		Mono-	Di-	Tri-
Canola	7.9	55.9	22.1	11.1
Soybean	14.2	22.5	51	6.8
Sunflower	10.5	19.6	65.7	-
Sunflower, high oleic	9.2	80.8	8.4	0.2
Cottonseed	25.8	17.8	51.8	0.2

The saturated fatty acids can improve the resistance of the esters to the oxidation but induce a higher pour point and higher viscosity; the triple unsaturated fatty acids have a low viscosity but poor oxidation stability [34].

Compared with mineral oils, the main advantage of ester liquids is their environmental friendliness (biodegradability). They are non-toxic fluids and have significantly higher fire point, which makes them preferable insulating liquids from the safety point of view. The details of these aspects are presented as follows.

‘Biodegradability’ describes the ability of a liquid to be broken down into simple inorganic molecules by naturally occurring microbes in soil or water. The importance of dielectric liquids’ biodegradability increases significantly during recent years with the development of electricity: electricity is introduced to wider and more complex circumstances, i.e., the location deep inside the natural environment, like high altitudes, where requires the liquids to become biodegradable to avoid the risk regarding soil disposal.

‘Non-toxicity’ is another requirement for becoming an environmentally friendly substance. With the wider involvement of electrical power in people’s daily life, the need for non-toxic insulation liquids also rises. As a non-toxic liquid, esters can be safely used in the living spaces, like the distributor transformers locating closely to people’s life.

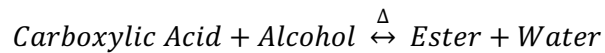
‘Higher flash/fire point’, esters also have a much higher flash point, and fire point than mineral oils, all of whose fire properties are listed in Table 2-2:

Table 2-2 Fire Properties of Dielectric Liquids (Data Source: [35])

<b>Dielectric liquids</b>	<b>Flash Point °C</b>	<b>Fire Point °C</b>
<b>Mineral Based</b>	160 - 170	170 – 180
<b>Natural Esters</b>	>300	>350
<b>Synthetic Esters</b>	>250	>300

The higher flash and fire point of the esters means the lower risks of fire incident for the esters compared with mineral oils, which extends esters' applications in an indoor environment.

In addition, esters also have a better water tolerance than mineral oils, which can be attributed to their chemical structure and ability to react with water:



The chemical reactions above is reversible, leading to the much higher water tolerance of the esters compared with mineral oils [36], and enabling the esters to become more suitable than the mineral oils in some environmental conditions, for example in high voltage facilities for offshore electric generators which operate in the environment with an elevated humidity/moisture content.

However, there are also some disadvantages associated with the esters. Generally, the esters, especially the natural esters, have a higher viscosity than the mineral oil, which potentially decreases the cooling ability of esters.

Apart from the general descriptions of both the mineral-based liquids and the ester-based liquids presented above, the intrinsic properties of the three liquids, particularly the underlying mechanisms in these liquids when they are stressed under external electric fields, are the focus of this study. As these are closely linked with the development of the main usages of the dielectric liquids in high voltage systems: insulating and cooling. Besides, the property related to the inner electric mechanisms in these liquids also differs from each other, which is one of the targets studied in this research. Therefore, it is necessary to conduct a review of electric mechanisms in dielectric liquids under an external electric field, this review and critical analysis of the conduction processes are introduced in the following section.

## **2.2 Electrical Conduction in Dielectric Liquids**

As discussed in the previous sections, the dielectric liquids used in practical applications in the power industry have complex chemical compositions. Their molecules consist of many

different hydrocarbons, leading to a complex molecular structure. Besides, even freshly manufactured, “as received” liquids, still contain different molecular species and various impurities. These characteristics bring challenges to the analysis of the electrical conduction mechanisms in dielectric liquids. To overcome these challenges, the ‘charge carrier’ concept is introduced as it can be measured practically and reflect the conduction aspects quantitatively, forming a solid foundation of the conduction processes analysis in the dielectric liquids.

### **2.2.1 Charge Carriers and Their Origin**

When a dielectric liquid is stressed with an external electric field, a low but noticeable electric current flows through this liquid, which is a manifestation of the movement of charge carriers in this liquid. The charge carriers in the dielectric liquids may be different: typically, these carriers are ions, which appear in the liquid due to disassociation of its molecules. Also, quasi-free electrons may be present in the liquid due to field emission at the metal (electrode)-liquid interface, details of these field emission mechanisms will be presented in Section 2.2.3.

These different types of charge carriers are the result of the following aspects: the complex nature of the dielectric liquids and unavoidable impurities in the dielectric liquids. The effect of their concentration and their nature on the electric conduction in dielectric liquids is difficult to quantify, which leads to difficulties in the accurate analysis and prediction of the electric conduction current in dielectric liquids [37].

Considering the complex sources of the charge carriers and mechanisms of the electric conduction in dielectric liquids, in the present work, the term “charge carriers” is used to describe all different types of charge carriers instead of specific species (unless specifically indicated). The discussion on the development of the charge carriers in the dielectric liquid is divided into two parts: the charge carrier development at the electrode-liquid interface and their presence in the bulk of the liquid [38].

The charge carriers created at the electrode-liquid interface can be produced by the emission of electrons from the cathode into the liquid. These electrons can attach to the liquid molecules forming negative ions. Typically, the electron transfer process at the metal-dielectric interface mostly depends on the energy that electrons can gain. Thus, the factors and parameters

influencing the electron emission process are field-dependent parameters. These processes are also affected by the temperature and exposure to ionising radiation such as X-rays [39].

Given all other conditions are the same, i.e., same environmental temperature, same radiation state, the electron emission mechanism is mainly controlled by electron tunnelling for the electric field strength above  $(1 - 2) \cdot 10^5 \text{ kV/m}$  [37]. For the electric field strength lower than  $10^5 \text{ kV/m}$ , the Schottky effect is the dominant mechanism in the electronic emission process. To simplify the analysis of the electron emission process, the following introduction is conducted based on the metal-vacuum condition rather than metal-liquid condition. The effect of the external electric field on the electron emission is presented in Figure 2-4: for the metal-vacuum interface, the application of an external electric field can reduce the energy barrier height, leading to a higher electron transfer rate. With an increase in the electric field strength, the energy barrier becomes lower and narrower, as shown in Figure 2-4 (c). Alternatively, the electron tunnelling mechanism, which is also called the Fowler-Nordheim tunnelling, starts to contribute significantly to the emission current under this stronger field.

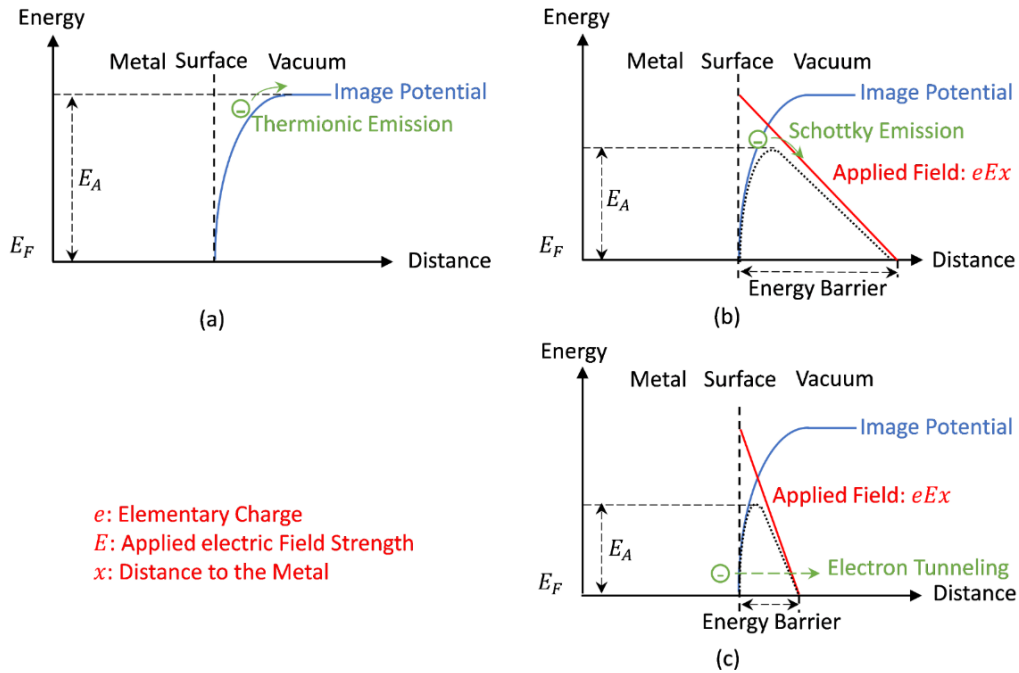


Figure 2-4 Electron Transfer Illustration (a) without external electric field: thermionic emission; (b) with external electric field: Schottky emission; (c) with external electric field: electron tunnelling. The images are based on the description provided in [40].

The ‘field emission’ process refers to the electron transfer from the energised metallic electrode to the liquid, while the ‘molecular ionisation’ refers to the electron transfer from the liquid to the electrode or other molecules. The result of the emission and charge generation processes is the chemical oxidation or reduction of neutral species: molecules of the liquid, impurities in the liquid, or even the metallic electrode [41]. Due to the high resistivity of dielectric liquids, this chemical degradation is quite weak, especially when the electric field strength is below  $\sim 10^7 \text{ V/m}$ , where the electric conduction in the dielectric liquids is mainly due to the charge carriers created in the bulk liquid through the self-dissociation process [37]. The details of this process are presented in the next paragraph.

The charge carriers in the bulk of the liquid can be generated through the self-dissociation process with or without an externally applied electric field. This process is part of the dissociation equilibrium (without electric field) and molecule ionisation (with external electric field), which is illustrated in Figure 2-5:

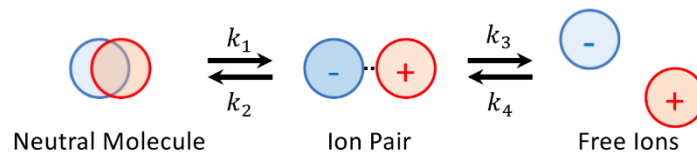


Figure 2-5 Molecule Dissociation and Recombination,  $k_1$ , and  $k_3$  are the dissociation rate while  $k_2$ , and  $k_4$  are the recombination rate. The '+' and '-' represent the positive and negative polarity of the ions.

As presented in Figure 2-5, the generation of ions in the bulk of the liquid involves two steps: formation and dissociation of ionic pairs. Furthermore, the kinetic rates of the transition between any two states are defined as  $k_1$ ,  $k_2$ ,  $k_3$ , and  $k_4$ . The first two rates,  $k_1$ , and  $k_2$  are generally unknown, while the kinetic rate constants of dissociation  $k_3$ , and recombination  $k_4$  are studied and developed with expressions by researchers for years [42][43].

To calculate the constant rates of dissociation and recombination, the criteria which defines the 'free ions' is introduced using the Bjerrum distance [44], and the Onsager distance [45].

Under the definition of the Bjerrum distance  $l_B$ , the paired ions separated over the  $l_B$  can be defined as free ions, with the expression of the  $l_B$  is presented as:

$$l_B = \frac{e^2}{4\pi\epsilon_r\epsilon_0k_B T} \quad 2-1$$

Where,  $e$  is the elementary charge,  $\epsilon_r$  is the relative permittivity,  $\epsilon_0$  is the vacuum permittivity,  $k_B$  is the Boltzmann constant and  $T$  is the Kelvin temperature. The Bjerrum distance originates from the assumption that the Coulombic attraction between the two opposite charged ions is balanced by their thermal motion. According to Equation 2-1, the Bjerrum distance for water ( $\epsilon_r = 80$ ) and dielectric liquids ( $\epsilon_r = 5$ ) at room temperature ( $T = 300\text{ K}$ ) is about  $7\text{ \AA}$ , and  $112\text{ \AA}$ , respectively. The significantly large distance that the dielectric liquids molecule should overcome to become free indicates the low free ions concentration in the dielectric liquids compared with water under the zero-field state.

Once the liquid is stressed with the external electric field, this field can stimulate the dissociation process. Dissociation intensifies in a stronger electric field. This enhancement in the dissociation process can be evaluated by the electric field dependent dissociation constant rate  $k_D(E)$  introduced by Onsager, which is a further development of the Bjerrum theory [45]:

$$k_D(E) = k_D \frac{I_1(4\beta)}{2\beta} \quad 2-2$$

where

$$\beta = \frac{e}{4k_B T} \sqrt{\frac{eE}{\pi\epsilon_r\epsilon_0}} \quad 2-3$$

Here,  $E$  is the strength of the electric field,  $k_D$  and  $I_1$  in Equation 2-2 is the dissociation rate without the field, and the modified Bessel function of the first kind with the first order, respectively.

Combining Equation 2-2, and 2-3, it can be found that: On one hand, the stronger electric field strength can lead to a higher dissociation degree; on the other hand, the increase in the dissociation rate is not a strong function of the field strength, i.e., given an external electric field  $E = 10 \text{ kV/m}$ , and room temperature  $T = 300 \text{ K}$ , the dissociation rate of a typical dielectric liquid with  $\epsilon_r = 2$ , only increases by 5.48 % of the zero-field dissociation rate while the dissociation rate of a dielectric liquid with  $\epsilon_r = 5$ , only increases by 2.17 % of the zero-field dissociation rate [37][45].

Debye provided the basic equations for the recombination constant rate in [42]:

$$k_R = \frac{2e\mu}{\epsilon_r \epsilon_0 \left[ 1 - \exp\left(-\frac{l_B}{a}\right) \right]} \quad 2-4$$

The equation above is the modified formula of Debye's result obtained in the assumption that the positive and negative ions have not only the same radius  $a$ , but also the same mobility  $\mu$ . As the Bjerrum distance  $l_B$  of the dielectric liquids is much longer than the radius of the ions:  $a$ , Equation 2-4 can be rewritten as:

$$k_R = \frac{2e\mu}{\epsilon_r \epsilon_0} \quad 2-5$$

which is the rate of the Langevin recombination. Based on these results, it can be concluded that the recombination rate can be affected by both the mobility of charge carriers and the dielectric constant but remains constant when the liquid is stressed with the external electric field.

The charge carriers are injected into the liquid at the electrode-liquid interface and generated in the bulk of the liquid, therefore it can be found that the higher field strength leads to a higher concentration of the charge carriers in the liquid. This conclusion agrees with the fact that the higher field strength typically leads to higher electric conduction in the dielectric liquids until the breakdown event. Taking into account the process of generation of the charge

carriers, it is important to discuss the role of the charge carriers in electrical conduction, which will lead to a better understanding of the conduction mechanisms in the dielectric liquids and be discussed in the following section.

## **2.2.2 Electric Conduction in Dielectric Liquids**

The conduction current in dielectric liquids is the result of the motion of charge carriers in the external electric field. Although it must be stated that the liquid itself cannot stay static when stressed with sufficiently high electric field and hence affects the motion of charge carriers, the analysis presented in this section assumes that the motion of the charge carrier is only caused by the electric force acting on the ions and electrons presented in this liquid. More detailed discussion of the effect of liquid EHD motion on the conduction current is provided in Section 2.3.3.

To simplify the analysis of the motion of charge carriers, a rectangular cell filled with a dielectric liquid is used to analyse the conduction process(es) in the liquid. Two plane parallel electrodes are located at both ends of the cell. The external electric field across this test cell is produced by energising one of the electrodes with a DC voltage, and another electrode is grounded. The 3D view of the test cell is presented in Figure 2-6:

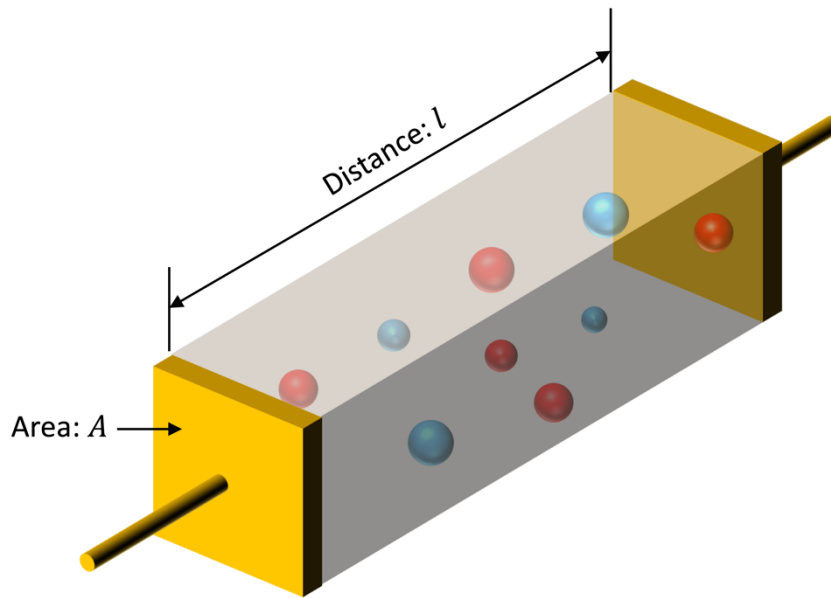


Figure 2-6 3D view of the rectangular cell filled with the liquid. Spherical particles represent the charge carriers in the liquids: red particles represent the positive charge carriers and blue particles represent the negative charge carriers. The distance between the two electrodes is  $l$ , and the area of each electrode is  $A$ .

Once the DC voltage is applied, the charge carriers in the liquids start to move towards the electrodes due to the electric force. These charge carriers are produced by different mechanisms, as discussed in Section 2.2.1, which has stated that the electric conductivity and the concentration of charge carriers can be affected by different factors, like temperature and external ionising radiation. As this investigation is focused on the effect of the electric field on conduction in dielectric liquids, it is assumed that all environmental factors remain the same except the externally applied electric field strength.

The conduction processes in the liquids can be discriminated into three main phases based on the electric field strength [46]:

Phase 1: Low Field Ohmic conduction. In this Phase, the current density is directly proportional to the electric field. In this case, the electric conductivity due to intrinsic charges plays the dominant role. The field in the liquid is not significantly disturbed by the space charge effects and can be described by the Laplace equation.

Phase 2: Medium Field. In this Phase, the field emission due to the Fowler-Nordheim mechanism makes substantial contributes to the space charge density in the liquid, which is responsible for the total current through the liquid.

Phase 3: High Field. In this Phase, the electric field is close to the breakdown field, the field distribution is significantly affected by the space charge and governed by the Poisson equation, the current through the liquid is the SCLC.

In phase 1, when the dielectric liquid is stressed with a low electric field, the electric conduction is mainly due to the motion of the charge carriers, including the ions formed by the dissociation processes and the impurities which are present in the bulk of the liquid. As a result of Equation 2-2 and 2-3, which demonstrates that the enhancement of the dissociation rate due to the external electric field is low, the conduction in this phase follows the Ohmic law, which can be explained with the ion drift model:

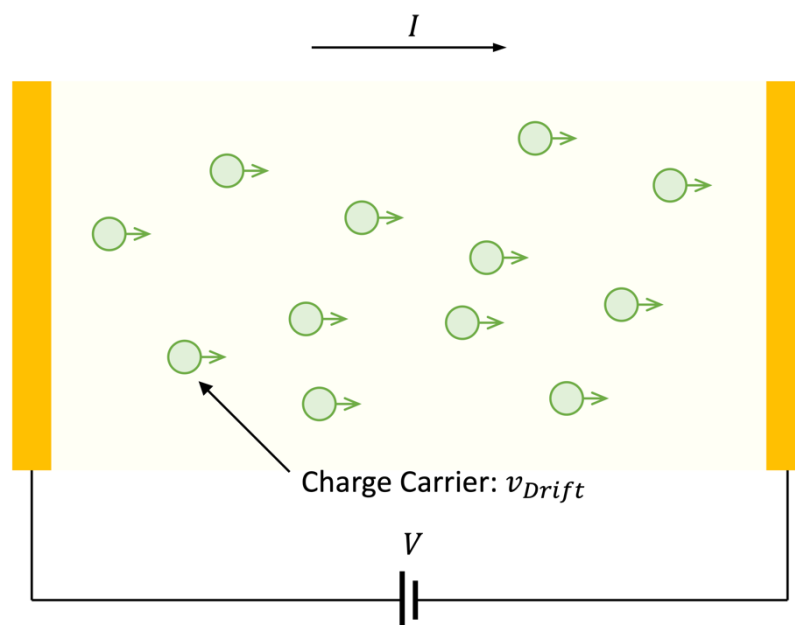


Figure 2-7 Ion drift model for phase 1, single polarity charge carriers move in the low electric field with a constant, drift velocity.

In the ion drift model, it assumes that only single polarity charge carriers exist in the dielectric liquids. Once DC voltage,  $V$ , is applied to the electrodes, a uniform electric field is established between the electrodes, and the electric force acts upon the charge carriers pushing them towards an oppositely charged electrode. The charge carriers move with a constant velocity  $v_{drift}$ , which is called the drift velocity. For a given liquid and at the fixed temperature, the drift velocity is directly proportional to the external electric field strength, and the coefficient proportionality is called the mobility of charge carriers,  $\mu$ :

$$v_{drift} = \mu E \quad 2-6$$

where,  $\mu$  is the mobility of charge carriers in liquids,  $E$  is the electric field. Equation 2-6 is written for the 1D model shown in Figure 2-7. Thus, both parameters, the drift velocity, and the electric field, are scalars. In the general case, both parameters should be used in their vector form.

In the 1D model in Figure 2-7, the current density  $J$  is also a scalar, which can be presented as:

$$J = nv_{drift}q \quad 2-7$$

where,  $n$  is the number density of the charge carrier in the liquid (expressed in  $1/m^3$ ),  $q$  is the charge of the individual charge carrier (expressed in C), and  $v_{drift}$  is the drift velocity expressed in m/s. In the general case, the current density  $J$  (which is expressed in  $A/m^2$ ) should be used in its vector form.

The resistance  $R$  of the liquid in the topology shown in Figure 2-7 can be obtained as:

$$R = \frac{V}{I} = \frac{V}{JA} \quad 2-8$$

where,  $A$  is the cross-sectional area of the electrodes, as can be seen in Figure 2-6.

The electric conductivity  $\sigma$  of the dielectric liquids in the model can be expressed as:

$$\sigma = \frac{l}{RA} \quad 2-9$$

where,  $l$  is the length of the test cell shown in Figure 2-6.

Combination of Equations 2-6 and 2-9, gives the following expression for the resistance:

$$R = \frac{l}{\mu n q A} \quad 2-10$$

In Equation 2-10, the resistance  $R$  of the dielectric liquid under the low field is dictated by the parameters of the rectangular reservoir with the liquid, i.e., its length  $l$  and electrode's cross-section  $A$  and the characters of the liquid:  $\mu$ ,  $n$ .

Following the discussion of the effect of the electric field strength on the dissociation and recombination rates provided in Section 2.2.1, it can be stated that the charge carrier density  $n$  remains almost the same in the low electric field in the test cell filled with the liquid, resulting in the constant resistance  $R$  of the dielectric liquids in the low electric field, and the ohmic behaviour of the electric conduction of the dielectric liquids.

In phase 2, which is determined by higher electric fields, the electric conduction process in the liquids is dominated by the charge carriers created at the electrode-liquid interface due to electron tunnelling. The mechanisms of generation of charge carriers in phase 2 include the

field emission and the field ionisation. Since the conduction current due to these two mechanisms has the same functional dependence on the applied voltage, a single mathematical model could be used to establish the quantitative relationship between the current and the electric field strength.

Latham (1982) proposed a model based on a metal cathode covered by materials with good dielectric properties [47][48]. In his model, the emission current is assumed to be provided by the electrons obeying the Maxwell-Boltzmann statistics. This electron current  $J$  can be expressed by the analogy with the Richardson-Dashman relationship:

$$J = AT_e^2 \exp\left(-\frac{e\chi}{k_B T_e}\right) \quad 2-11$$

where,  $A$  is Richardson's constant treated as an empirical constant,  $T_e$  is the enhanced electron temperature,  $\chi$  is the height of the potential barrier at the metal-dielectric interface,  $e$  is the elementary charge, and  $k_B$  is the Boltzmann constant.

For the Maxwell Boltzmann distribution with three-degrees of freedom, the energy equals to  $\frac{3}{2}k_B T$ . Thus, for the electronic current, the electron temperature is given by [47][48]:

$$T_e = -\frac{2e\Delta V}{3k_B} \quad 2-12$$

For the dielectric material, there is a relation [47][48]:

$$\frac{\Delta V}{V} \cong \frac{\Delta d}{\epsilon d} \quad 2-13$$

where  $\varepsilon$  is the dielectric constant of the material:  $\varepsilon = \varepsilon_0 \varepsilon_r$ , and  $d$  is the thickness of the dielectric material,  $\Delta V$  is the potential of the position located at  $\Delta d$  from the surface of the metal cathode. Equation 2-11 can then be presented as:

$$J = A \left( \frac{2e\Delta d}{3k_B\varepsilon d} \right)^2 V^2 \exp\left(-\frac{3\chi\varepsilon d}{2\Delta d} \frac{1}{V}\right) \quad 2-14$$

From Equation 2-14, it can be found that in phase 2, the current-voltage relationship is given by a straight line in coordinates  $\ln(I/V^2)$  vs  $1/V$ . This aspect is important as it can quantitatively distinguish phase 2 from two other phases.

In Phase 3, the applied field is strong (reaching the values which can be close to the breakdown field of the dielectric liquid) and the space charge in the dielectric liquids is assumed to be saturated. Correspondingly, the electric field in the liquid is controlled by the SCLC, which is reflected by the  $I-V^2$  dependency of the electric current on the applied voltage. The  $I-V^2$  plot for this conduction stage is a (virtually) straight line, its slope is defined by the liquids' dielectric constant and the mobility of charge carriers. Mathematic description of the  $I(V)$  functional dependency in the case of strong electric fields is presented and discussed in Sections 2.3.2 and 6.4.

Since the equations which describe the current-voltage characteristics in phase 3 include the mobility of charge carriers, the mobility can then be derived from the  $I-V^2$  experimental curves. However, the precondition for this derivation is that the voltage ranges of all three phases are known. These ranges can be identified by the Fowler-Nordheim plot.

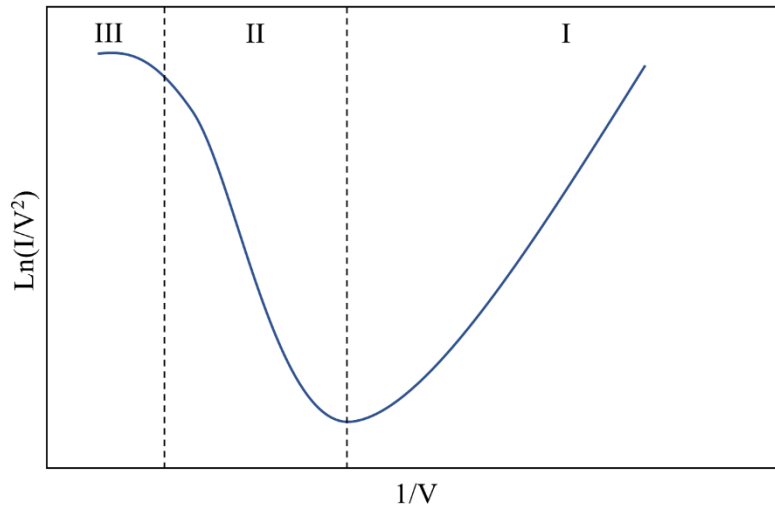


Figure 2-8 A schematic Fowler-Nordheim plot for conduction current in dielectric liquid (based on [49]).

Figure 2-8 provides a schematic Fowler-Nordheim plot for a conduction current in a dielectric liquid, i.e., the current and voltage in  $\ln(I/V^2)$  vs  $1/V$  coordinates. There is an inflexion point between phase 1, and phase 2, which can be attributed to the different current behaviours in these two phases: the current in phase 1 follows the ohmic behaviour, leading to a quasi-constant  $I/V$ , while the current in phase 2 is presented by Equation 2-11, indicating the straight line aspect in phase 2.

In the case of phase 3, since the  $I-V^2$  plot within this phase is a quasi-straight line, the plot of phase 3 in the Fowler-Nordheim plot is a horizontal line, which differs the phase 3 from phase 2, enabling the further analysis on the mobility of charge carriers in dielectric liquids.

The mechanisms of generation and injection of charges into the liquid introduced in the previous section provide a basic understanding of the conduction processes in the liquids, enabling further investigation of dielectric liquids and nanofluids (will be introduced in Section 2.4).

The conduction processes in the dielectric liquids are governed by a number of parameters. Among them, the mobility of charge carriers has attracted an attention as it is the parameter which describes the ability of charge carries to move in the electric field. Thus, the mobility of charge carriers in dielectric liquids was selected as the main subject of this research. In Section 2.3.1 and 2.3.2, two methodologies of measurement of the mobility of charge carriers are presented. Also, the electrohydrodynamic process is introduced as this process affects the mobility measurements in practical conditions.

### **2.2.3 Charge injection Mechanisms at the Electrode-Liquid Interface**

Sections 2.2.1 and 2.2.2 are focused on the charge carrier generation and motion in the external electric field. In this section, this behaviour and the mechanisms are considered from the viewpoint of the charge carrier distribution, especially their distribution at the electrode-liquid interface. The understanding of the charge carrier injection from the electrode relies on the understanding of the charge carrier distribution at the electrode-liquid interface. Also, since this research involves not only the dielectric liquids but also nanofluids based on these liquids (detailed description of these nanofluids is given in Section 2.4), the discussion and analysis of the charge carrier distribution at the electrode-liquid interface are required: in this research it was found that this distribution is closely related to the nanoparticles' behaviour.

To obtain an accurate distribution of the charge carriers at the electrode-liquid interface, several models were introduced. The Electric Double Layer (EDL) model, which was first proposed up by Hermann von Helmholtz in 1853 [50], was then further developed by Louis Georges Gouy in the 1900s [51], and Herr Otto Stern in the 1920s [52]. This model is commonly used in analysis of the electric mechanisms at the electrode-liquid interface.

In the Helmholtz model, the liquid at the electrode-liquid interface consists of two layers that have opposite polarity. Both sections are created by the electron tunnelling between the metallic electrode and the charges generated in the liquid, (the tunnelling mechanisms have been introduced in Section 2.2.1).

In the Helmholtz model, the proposed structure of the double layer at the electrode-liquid interface allows consideration of this double layer as a capacitor: two layers with the opposite

charges are distributed in the electrode and liquid phase, respectively, as illustrated in Figure 2-9 (a).

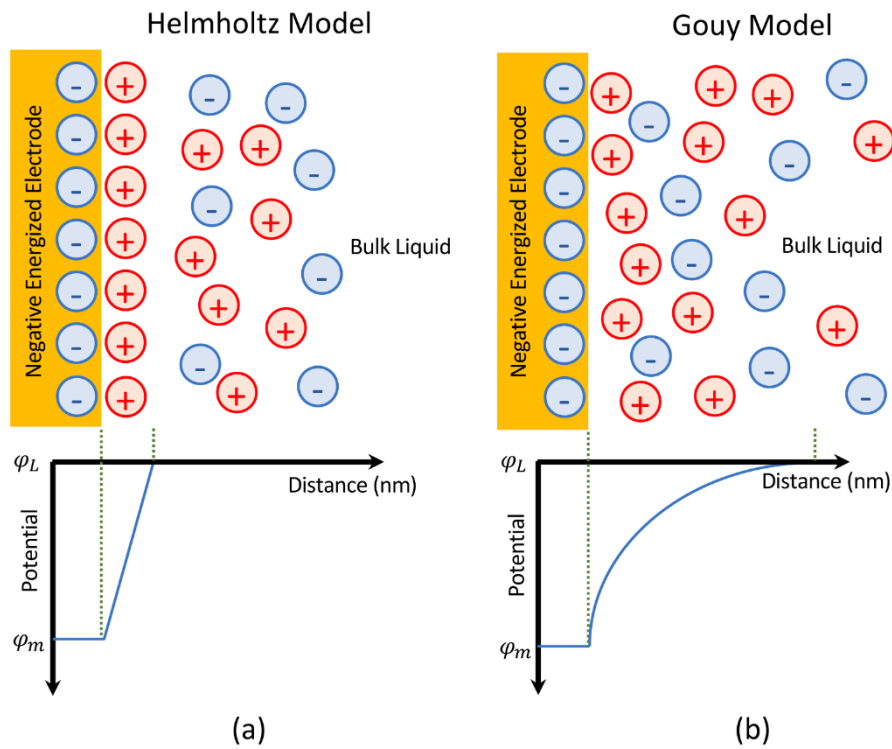


Figure 2-9 Schematic Representation of Helmholtz Model and Gouy Model based on [53]

The distance between two layers is assumed as the radius of the attached charges. In this model, the potential drop across the electrode-liquid interface  $\varphi_m$  and the bulk solution  $\varphi_L$  is linear as illustrated in the bottom part of Figure 2-9 (a). Following this, the differential capacitance of the double layer becomes constant and depends on the dielectric constant of the liquid and the thickness of the double layer.

The foundation of this hypothesis is the rigid boundary of the layer; however, this assumption does not exist in practical interfaces. The experiments show that the differential capacity

varies with the potential between the electrode-liquid interface and the bulk liquid [54]. Thus, a more accurate model is required.

Gouy found that the capacitance of the EDL depends on the applied potential and the concentration of charge carriers within the diffusion region. In the Gouy model, though the charge within the electrode is confined to the electrode surface, the charge carriers with opposite polarity are distributed as the function of distance from the electrode-liquid interface in the liquid, which is illustrated at the bottom in Figure 2-9 (b). In the Gouy model, the charges are considered as point charges at the electrode-liquids interface. The electric potential decays exponentially between the liquid-electrode interface and the bulk liquid. The Poisson-Boltzmann equation derived from the combination of the Gauss Law and the Boltzmann distribution gives the following expression for the concentration of charges: [55][56]

$$C = C_L \exp\left(-\frac{w}{k_B T}\right) \quad 2-15$$

where  $C$  is the local charge concentration,  $C_L$  is the charge concentration in the bulk of the liquid,  $k_B$  is the Boltzmann's constant, and  $T$  is the thermodynamic temperature.  $w$  denotes the work done by moving the charge from the bulk of the liquid to the local position.

The work,  $w$ , done in the external electric field is:

$$w = ze\varphi \quad 2-16$$

where,  $z$  is the valence of the positive charges,  $e$  denotes the elementary electric charge,  $\varphi$  is the potential difference between the local position and the bulk of the liquid.

The potential of the electric field can be determined by the Poisson equation expressed as Equation 2-17:

$$\nabla^2 \varphi = -\frac{\rho}{\varepsilon} \quad 2-17$$

where,  $\varphi$  is the electric potential,  $\rho$  is the volumetric space charge density, and  $\varepsilon$  is the dielectric constant of the medium,  $\varepsilon = \varepsilon_0 \varepsilon_r$ .

Combining Equation 2-15, 2-16, and 2-17 the Poisson-Boltzmann equation is obtained: :

$$\nabla^2 \varphi = -\frac{C_L z e}{\varepsilon} \exp\left(-\frac{z e \varphi}{k_B T}\right) \quad 2-18$$

This equation is the key equation for understanding of the diffusion layer, i.e., the Debye length can be defined by solving Equation 2-18. However, there are some discrepancies between the Gouy model and the experimental results: the experimentally obtained thickness of the double layer is typically greater than the calculated thickness. Moreover, the potential difference predicted via the Gouy model goes to infinity as it approaches the electrode-liquid surface, which is a result of the point charge assumption. To avoid such discrepancies, a modified model was developed by Stern via the combination of the Helmholtz model and the Gouy model, as illustrated in Figure 2-10.

In Stern's model, the point charge assumption is partly replaced: a stationary layer of finite-sized charges (ions) was placed between the electrode-liquid interface and the Outer Helmholtz Plane (OHP). Therefore, due to the finite size of the charges, the potential drop between the electrode-liquid interface and the OHP is linear, as presented in the bottom part of Figure 2-10.

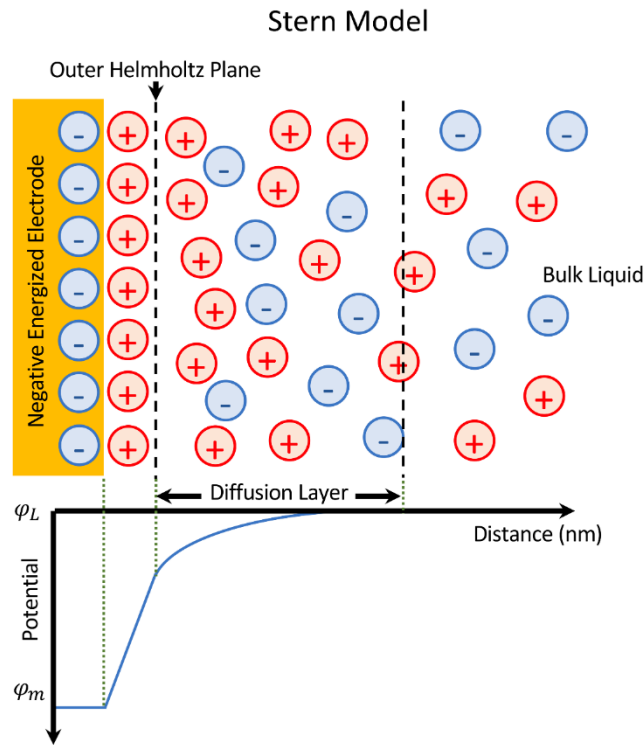


Figure 2-10 Schematic illustration of Stern Model based on [53]

Attached to the OHP is the diffusion layer defined in the Gouy model, which can be described by Equation 2-18 with the following condition:  $|ze\phi| < k_B T$ , which means that the electrical energy is smaller than the thermal energy. Therefore, the exponential part of Equation 2-18 can be expanded, yielding the first two terms as:

$$\nabla^2 \phi = -\frac{1}{\epsilon} \left[ C_L z e - \frac{z^2 e^2 C_L \phi}{k_B T} \right] \quad 2-19$$

Since the model requires the electroneutrality of the bulk of the liquid, then the first summation term must be zero, and it gives:

$$\nabla^2 \varphi = \frac{z^2 e^2 C_L}{\epsilon k_B T} \varphi \quad 2-20$$

As this simplification is based on the lower electrical energy, potential  $\varphi$  should be small. This simplification is called the *Debye-Hückel approximation*, and an important parameter: the *Debye-Hückel length*, can be obtained by dimensional analysis:

$$\nabla^2 \varphi = \kappa^2 \varphi \quad 2-21$$

where,

$$\kappa = \sqrt{\frac{z^2 e^2 C_L}{\epsilon k_B T}} \quad 2-22$$

The quantity  $\kappa^{-1}$  is commonly referred as the *Debye-Hückel length*. The Debye length is a quantitative description of the effective range of the potential due to the double layer.

In the Stern model, the thickness of the attached diffusion layer is of the order of  $3/\kappa$  to  $4/\kappa$ . In addition, it can be seen from Equation 2-22 that the Debye length depends only on the temperature and charge carrier concentration in the bulk of the liquid. In practice, for most colloids, the Debye length ranges from sub-nm to  $\sim 100$  nm, which will be taken into account in the analysis of the experimental results in this research [56].

This section described different mechanisms of electric conduction in the dielectric liquids. This discussion illustrates the importance the mobility of charge carriers in description of the conduction processes.

Therefore, the following section will present two methods of obtaining the mobility of charge carriers in dielectric liquids.

## **2.3 Charge Carriers and Their Mobility**

The measurements on the mobility of charge carriers in dielectric liquids have been developed over the years. In this thesis, two commonly used methodologies of obtaining the mobility were used: the ToF method and the SCLC method. The combination of these two methods enables the mobility of charge carriers to be obtained under a wide range of electric field magnitudes. The fundamental link between the mobility of charge carriers and the electrohydrodynamic motion of the liquid is also discussed in this section.

### **2.3.1 Mobility Measurement: Time of Flight Method**

Since its introduction in the 60s of the last century, the ToF method of obtaining the mobility of charge carrier has been successfully used in the case of both solid and liquid dielectrics [57][58]. The mobility measurements using the ToF method are based on the detection of the current peak and measuring the time interval from application of voltage to the appearance of the current peak. In a dielectric liquid under no external electric field, the charge carriers, including both the ions from purities and the ions produced by the dissociation process, are randomly distributed in the bulk of the liquid. Once stressed with an external electric field, the equilibrium of the charge carriers in the liquids is broken, and it takes time which is called the relaxation time to restore this equilibrium. During the relaxation process, the motion of the existing charge carriers towards the electrodes can be detected as by measuring the current through the liquid. If the charge carriers are similar to each other in their nature, or there is a single dominant type of the charge carriers, a single current peak occurs when the majority of charge carriers arrived at the electrode.

Based on this model, an equation describing the charge carriers' motion during the relaxation process can be obtained as:

$$v = \frac{d}{ToF} \quad 2-23$$

where,  $v$  is the drift velocity of the charge carriers,  $d$  is the travelling distance of the charge carriers, and  $ToF$  is the time interval between the application of the external electric field and the occurrence of the current peak.

Based on Equation 2-6, the mobility of charge carriers can be presented as:

$$\mu = \frac{d^2}{ToF \cdot U} \quad 2-24$$

where  $U$  is the potential difference along with the distance  $d$ .

In practical tests, the ToF can be obtained by two methods: the reverse-polarity method and the single-polarity method.

In the reverse-polarity method, a step DC voltage is applied to the tested liquids for a specific time interval, and after this time, the voltage suddenly changes its polarity, and this voltage stress with the opposite polarity is applied to the liquid for a longer time interval during which the current through the liquid is measured. A schematic illustration of the reverse-polarity method is shown in Figure 2-11.

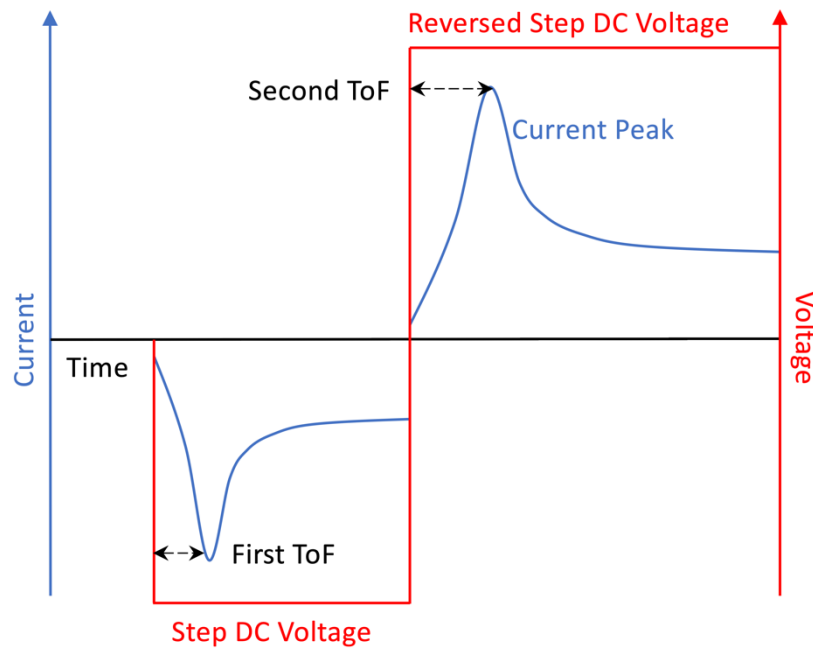


Figure 2-11 Schematic illustration of the Reverse-polarity method. The blue line in the graph indicates the current through the tested material, while the red line indicates the applied voltage.

During this process, two ToFs can be obtained, and the second ToF, which is obtained after the change of the voltage polarity, can be taken as the time during which the charge carriers travel across the whole gap between two electrodes, leading to the distance  $d$  in Equation 2-23 equals to the electrode separation (length of the gap).

However, due to experimental limitations of the present work, the ToF method can only be implemented using the single polarity energisation in some tests. A schematic illustration of the single-polarity method is shown in Figure 2-12.

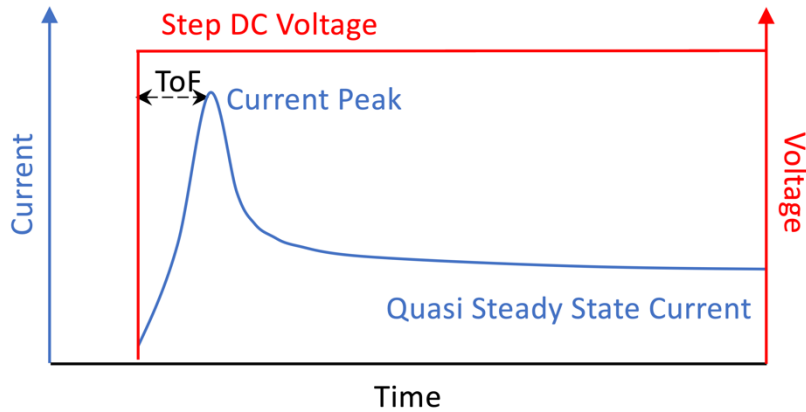


Figure 2-12 Schematic illustration of the Single-polarity method. The blue line in the graph indicates the current through the tested material, while the red line indicates the applied voltage.

In the case of the single-polarity method, the charge carriers responsible for the current peak does not cross the complete inter-electrode gap,  $d$ . And the distance required to calculate the mobility in Equation 2-24 is defined using a correction factor which is introduced in the present work.

In the reverse-polarity method, two ToFs can be obtained in each individual test: the first one,  $ToF_1$ , equals to the time interval between the application of voltage, and the occurrence of the current peak. The second one,  $ToF_2$ , equal to the time interval between the moment of reversing polarity and the corresponding current peak, as shown in Figure 2-11.

Following this, an equation for the correction coefficient  $\beta$  can be obtained as:

$$\beta = \frac{l}{d} = \frac{ToF_1}{ToF_2} \quad 2-25$$

where, the  $ToF_1$ , and  $ToF_2$  is the first and second ToF, respectively.  $d$  is the electrode separation, and  $l$  is the distance the charge carriers traveling during the  $ToF_1$ . Alternatively, the equation for calculation of the mobility of charge carriers in the single-polarity method can be obtained as:

$$\mu = \frac{\beta^2 d^2}{ToF \cdot U} \quad 2-26$$

In this section, two practical implementations of the ToF method are introduced; compared with the reverse-polarity method, the calculation of mobility based on the single-polarity method is straightforward and accurate. However, the single-polarity method put higher requirements on the instrumentation as compared with the reverse-polarity method. The introduction of the correction coefficient in this research has improved the accuracy of the reverse-polarity method, which has extended the voltage range of the ToF measurements. However, to conduct the mobility measurements in a wider voltage range (at higher voltages), and to improve the confidence of the measurement results, another methodology, the SCLC method, was also implemented in this work. This method is presented in the next section.

### **2.3.2 Mobility Measurement: Space Charge Limited Current Method**

The ToF method provides a base for obtaining the mobility of charge carriers in a relatively low uniform electric field. The mobility of charge carriers can also be obtained in highly divergent electric fields based on the space charge saturated assumption.

Section 2.2.2 provides the discussion of the electric conduction mechanisms and phases in dielectric liquids. The third Phase is based on the assumption that the space charge is saturated and the current in this region is the SCLC. Using the SCLC assumption, equations for obtaining the mobility of the charge carriers via the I-V<sup>2</sup> characters for different materials and configurations have been developed. The mobility of charge carriers in solids can be obtained based on the Mott-Gurney law [59]. The analytical approach for obtaining the mobility of charge carriers in gas in the coaxial and point-plane configurations were developed in [60].

Halpern (1969) developed the I-V equations for the point-plane configuration for dielectric liquids [61]. Using this model and relevant boundary conditions, the equation for the mobility is:

$$I = \frac{3\alpha}{8} \left( \frac{\mu\varepsilon}{d} \right) V_{app}^2 \quad 2-27$$

where,  $\varepsilon$  is the dielectric constant of the liquid,  $d$  is the separation of the electrodes,  $V_{app}$  is the applied voltage. The factor  $\alpha$  equals to  $0.6\pi$  is the emission cone angle.

The Halpern's model is based on the Laplacian field distribution: the assumption which not always holds. In [61], Coelho (1971) introduced his model based on the Poisson equation, in which the field is distorted due to the space charge formed by the charge carriers in the liquid. The Poisson electric field in this model is obtained along the central line in the point-plane electrode configuration. This field distortion is especially pronounced at the electrode tip and is dictated by the topology and by the injection of the charge carriers. In [62], an analytical expression for the electric field strength along the line of symmetry in the tip-plane electrode configuration was obtained in the hyperboloid coordinates for two scenarios: no space charge, i.e. the Laplacian field, and full space charge saturation, in which the field is governed by the Poisson equation.

For the Laplacian electric field, it is assumed that the space between the needle tip and the plane is free of charge. The electric field strength  $E(x)$  at the point away from the tip apex with the axial distance  $x$  can be described by Equation 2-28:

$$E(x) = \frac{2aV_0}{\ln \frac{4a}{r} [x(2a - x) + r(a - x)]} \quad 2-28$$

where,  $a$  denotes distance between the point of the tip to the plane spacing,  $r$  is the radius of the tip, and  $V_0$  is the potential difference between the tip and the plane.

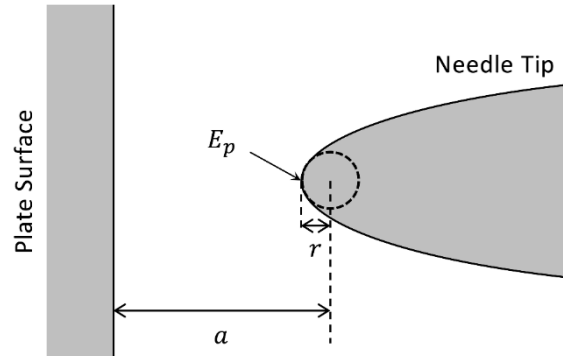


Figure 2-13 Schematic Illustration of the needle -plane electrode configuration

Equation 2-28 was used to obtain the electric field to support the analysis of the electric forces which govern the EHD effects in the dielectric liquids [63][64]. However, in the analysis of the mobility of charge carriers, the re-distribution of the Poisson electric field due to the space charge should be considered. In this case, a new assumption should be introduced: there are free charges in the space between the tip and the plane, and the current through the liquid between electrodes is a steady-state current. The mobility of the charge carriers is assumed to be independent from the field strength and the diffusion current is assumed to be negligible with respect to the conduction current. Then, the magnitude of the Poisson field along the central axis in the point plane configuration is given by [62]:

$$E(v) = \frac{\sqrt{\rho^2(2 - \rho)^2 E_p^2 + Av \left[ \rho(2 - \rho) + v(1 - \rho) - \frac{v^2}{3} \right]}}{(v + \rho)(2 - v - \rho)} \quad 2-29$$

where,  $v = x/a$ , and  $\rho = r/2a$ . The factor  $A$  can be calculated with the current  $I$ , the dielectric constant of the liquids  $\epsilon_r$ , and the mobility  $\mu$  of the charge carrier in the liquids as:

$$A = \frac{2I}{\pi a \epsilon_r \epsilon_0 \mu} \quad 2-30$$

Using Equation 2-29 and 2-30, the equation describing the relationship between the electric field strength, and the applied voltage can be obtained as:

$$\int_0^{1-\rho} E(v) dv = \frac{-V}{a} \quad 2-31$$

By integrating Equation 2-29 within different domains both analytically and numerically, [62], the equation which describes the I-V<sup>2</sup> relationship can be obtained as:

$$I = \frac{\pi \mu \epsilon}{0.78 a} V^2 \quad 2-32$$

This equation can be used to obtain the mobility of charge carriers with the consideration of the field distortion effect. Alternatively, the corresponding electric field strength can also be calculated using Equation 2-29, which supports further analysis of the relationship between the charge carrier and the electric field strength.

### **2.3.3 The Electrohydrodynamic Effect**

The Mobility of charge carriers, as indicated by its definition, reflects the charge carrier's moving ability due to the electric field. The measurement principles introduced in the previous two sections also rely on this definition, i.e., the mobility is defined by the motion of the charge carriers in the external electric field.

However, this assumption is not valid in all cases as the EHD fluid motion can also contribute to the motion of the charge carriers. In this case, the obtained mobility (by both the ToF and

the SCLC methods) is affected by the EHD movement of the liquid in the field. Thus, such mobility obtained by the ToF, and SCLC methods is referred as the ‘apparent mobility’, and its value can be higher than the mobility of charge carries obtained purely based on the movement of charged particles in the external field in a stationary fluid.

Therefore, it is necessary to discuss this important factor that influences the mobility of charge carriers in dielectric liquids via the fluid motion: the EHD effect.

The EHD effect is the field of study of the dynamics of electrically charged but less conductive fluids, like air, water. The fundamental equation which describes the force acting upon a charged object (an element of fluid which may contain charge  $q$ ) is given by Landau [65]:

$$\mathbf{F} = q\mathbf{E} - \frac{1}{2}E^2\nabla\varepsilon + \nabla\left[\rho\frac{E^2}{2}\left(\frac{\partial\varepsilon}{\partial\rho}\right)_T\right] \quad 2-33$$

where,  $F$  is the electrostatic force acting on the object in the external electric field  $\mathbf{E}$ . The first term of Equation 2-33,  $q\mathbf{E}$ , describes the Coulomb force acting on an element of fluid with charge density  $q$ . The second term, which includes the dielectric constant  $\varepsilon$  of the fluid, is the dielectric force. The third term, which includes the mass density of the fluid  $\rho$ , and the factor  $\left(\frac{\partial\varepsilon}{\partial\rho}\right)_T$ , is the electrostriction force. In this research, the dielectric liquids are assumed to be isothermal, resulting in the dielectric constant and mass density of the fluid being invariant. Therefore, the second term and third term in Equation 2-33 in this assumption, and the force acting on an element of fluid is only the Coulomb force,  $\mathbf{F} = q\mathbf{E}$ .

The dynamics of the fluid can be analysed in the framework of two following aspects.:

First, the dielectric liquid is incompressible, which gives:

$$\nabla \cdot \mathbf{v} = 0 \quad 2-34$$

where,  $\mathbf{v}$  is the velocity of the dielectric liquids.

The second assumption is: the momentum of the fluids is conserved yielding:

$$\rho \frac{d\mathbf{v}}{dt} = -\nabla p + \eta \nabla^2 \mathbf{v} + \mathbf{F} \quad 2-35$$

where,  $\rho$ ,  $p$  and  $\eta$  is the mass density, pressure, and dynamic viscosity, respectively.  $\mathbf{F}$  represents the external force including gravity and electric force here. As the electric force described by Equation 2-33 is reduced into to the Coulomb force only, Equation 2-35 can be rewritten as:

$$\rho \frac{d\mathbf{v}}{dt} = -\nabla p + \eta \nabla^2 \mathbf{v} + q\mathbf{E} + \rho g \quad 2-36$$

Equation 2-35 and 2-36 are the Navire-Stokes equations for incompressible liquids.

Equations 2-34, and 2-35, 2-36 have laid out the theoretical foundation for the EHD analysis. However, it is impossible to obtain a general solution describing the effect of the electric field on velocity. This is because the factors influencing the velocity are complex, difficult to measure, and sensitive to any changes in the system. For example, in asymmetrical electrode assemblies like the point-plane electrodes, the charge creation source in dielectric liquids under an external electric field is largely depending on the radius of the curvature of the needle electrode: most charges are generated by injection from the point electrode and the molecule ionisation near the tip. However, for topologies with sufficiently large radius of curvature of the needle electrode, this dominant mechanism of charge generation is the development of the heterocharge layer around this point electrode rather than the charge injection from the point electrode [66].

Therefore, the typical method used to obtain the solution of specific problems is setting up the boundary conditions according to the factors involved, like the geometry of the space

studied. Then, numerical solution can be obtained using the computational methods rather than analytic solution.

Further discussion on the relationship between the EHD and the electric field requires deeper mathematical analysis, which is out of the scope of the present research. Thus, the following discussion is focused on the effect of the EHD motion on the charge carriers and their mobility, which can be simply segmented as two types: direct influence and indirect influence.

The direct influence of the EHD motion is an increase of the charge carrier velocity by the fluid motion. As discussed, the straightforward use of Equation 2-36 could be problematic due to insufficient knowledge of the required parameters. However, analysis of the EHD effect(s) could be conducted from the energy viewpoint. Since the fluid motion is caused by the electric field, the kinetic energy of the fluid can be linked to the electric energy, yielding the relation:

$$\frac{1}{2}\varepsilon E^2 \propto \frac{1}{2}\rho v^2 \quad 2-37$$

where,  $\varepsilon$  and  $E$  is the dielectric permittivity of the liquid, and the electric field strength, respectively.  $\rho$  and  $v$  is the density, and the motion velocity of the liquid, respectively. According to this equation, the velocity of the fluid is proportional to the electric field strength:  $v \propto E\sqrt{\varepsilon/\rho}$ .

Therefore, it can be concluded that the velocity of the charge carriers obtained in the ToF tests is enhanced by the fluid motion, and this enhancement increases in a higher electric field.

Similar to the ToF method, the SCLC method is also affected by the EHD effect, as the hydrodynamic turbulence near the needle tip can be enhanced with the fluid velocity [67].

Apart from the direct influence, there is also an indirect influence on the mobility of charge carriers as the field may change the charge carrier concentration.

Due to the incompressible aspect of the dielectric liquids, the liquids moving toward the electrode by the EHD effect rebounded from the electrode surface. The charge carriers near the electrode are then also be removed by this rebound, resulting in a lower concentration of the injected charge carriers and promoting the injection of new charge carriers [49].

Although the EHD effect on the mobility of charge carriers is unavoidable, the results which include this EHD effect (EHD motion of the liquid) are important as they provide further understanding of the behaviour of both, pure liquids and nanofluids, in the external electric fields.

## **2.4 Nanofluids and their use in Electrical Systems**

The term ‘nanofluid’ was firstly coined by Choi in 1995 [68]. Since then, a significant number of studies focused on the synthesis of nanofluids, and measurement of their dielectric and thermal characteristics have been conducted. However, the conduction mechanisms in nanofluids, especially in ester-based nanofluids, are not fully understood. Thus, to address this lack of information on conduction and the EHD motion in ester and oil-based nanofluids, the present study includes a comprehensive investigation of the EHD movement of particles in the nanofluids stressed with DC electric field and analysis of the mobility of charge carriers in the nanofluids. The literature review in this section provides an analysis of the literature data on conduction processes in the nanofluids, which underpins the experimental study presented in Chapter 7 and 8.

### **2.4.1 Nanofluids: History and Applications**

Generally, a nanofluid is a colloid system containing nanometre-size solid particles and a liquid hosting medium. For convenience, the term ‘nanofluids’ in this thesis refers to the nanofluids developed to serve as an insulation liquid in electrical industries.

The chemical composition of dielectric liquids plays an important role in defining and improvement of their parameters such as dielectric strength, thermal conductivity, pour-point, antioxidation, etc.

Nano-sized particles can also be added to insulating liquids to improve and modify their specific properties, such as their breakdown strength, their permittivity and thermal conductivity. These potential improvements make the nanofluids attractive for practical applications in high voltage power and pulsed power systems. The nano-sized particles have dramatically increased the ratio between the particle surface area and its volume, which brings several benefits for their applications: better dispersing stability in the host liquids, less pronounced effect on the final product's density, and others.

Choi (1995) developed nanofluids with a higher thermal conductivity compared with the pure host liquid(s) [68]. Later on, Segal (1998) developed nanofluid(s) with an improved dielectric strength [7], which introduced another main direction for the development and practical application of nanofluids.

Although nanofluids also can provide an improvement in the flash and fire point compared with the pure liquids [69], or may help to prolong the serving lifetime of the transformer oil [70], the main aspects which make nanofluids attractive as insulating liquids are their higher dielectric strength and thermal conductivity. To improve these two parameters, a number of particles were selected and tested by different research groups. It was found that SiO<sub>2</sub> [8][9] and Fe<sub>3</sub>O<sub>4</sub> [10][71] can enhance both the dielectric strength and thermal conductivity of the nanofluids; Al<sub>2</sub>O<sub>3</sub> [12][72], ZnO [12], AlN [13], and TiO<sub>2</sub> [73][74] can enhance the dielectric strength of the nanofluids; and BN [10][11] and CuO [75] can enhance the thermal conductivity of the nanofluids.

The methods of synthesis of the nanofluids have also been developed over the decades. Two types of the synthesis methods can be defined according to the processes involved: the one-step and two-step methods [76].

The one-step method of production of the nanofluids involves synthesis and dispersion of nanoparticles in the hosting fluids simultaneously. Thus, the agglomeration of nanoparticles is minimised. Besides, the one-step process can also be used to produce nanoparticles with a high uniform dimension. The dispersion stability of the nanoparticles is also improved in the one-step process. However, there are also some drawbacks in the one-step process: its cost is high, and it is not suitable for large-scale production. In addition, the residuals of the reaction remain in the nanofluid(s), which increases their degree of impurity.

The two-step process is a more commonly used process. The two-step process involves preparation of nanoparticles independently from the dispersing process, which typically yields the particles in the form of powder with their surface modified by a surfactant. Then these nano-powders are dispersed into the hosting liquids using magnetic stirrer, or ultrasonic bath. As the two-step method can be used to produce nanofluids in a more economical way, it can be used for a large-scale production of nanofluids. However, the stability of the dispersed nanoparticles in this method is weaker than in the one-step method.

Figure 2-14 is an illustration of these two stabilization methods.

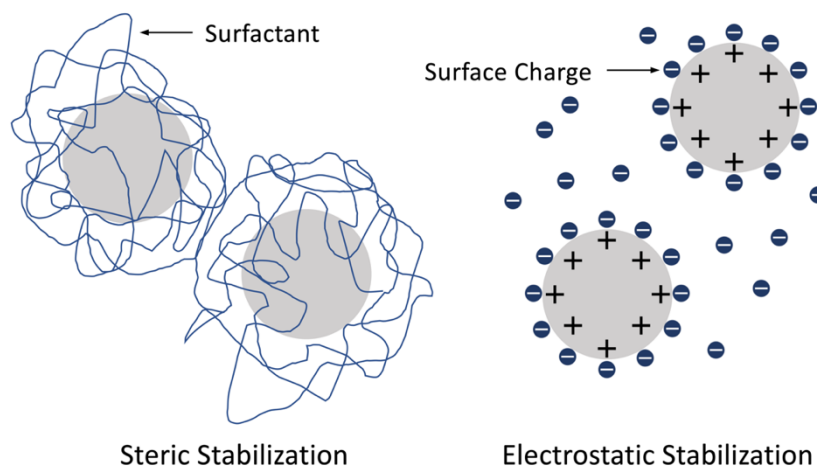


Figure 2-14 Two types of stabilization

Since one of the key requirements for the nanofluids is their stability, extra attention should be paid to improve their dispersing stability. According to the Derjaguin-Landau-Verwey-Overbeek (DLVO) theory, the total forces acting between two particles in the host liquid is the sum of the van der Waals attraction and the electrostatic repulsion due to the surface charge on the particles. Following this, the electrostatic stabilization may help to enhance the dispersing stability of the particle. Another stabilization process is the steric stabilization,

which improves the dispersing stability by decreasing the active area of the surface of the particle, i.e., by surface modification with surfactants: Oleic Acid, which is a widely used surfactant, was firstly used for production of the mineral-oil-based nanofluids by Lee and Kim (2012) [77]. Another surfactant, Cetyl Trimethyl Ammonium Bromide (CTAB), was used by Atiya (2015) to treat TiO<sub>2</sub> particles and to prepare mineral oil-based TiO<sub>2</sub> nanofluids [78].

#### **2.4.2 Polarisation and Charging of Particles**

As discussed in the previous section, the main aim of developing nanofluids is to improve the dielectric strength of the fluids and the cooling performance. Therefore, the discussion of the mechanisms which govern the behaviour of nanoparticles is given in this section.

The enhancement of thermal conductivity of nanofluids has been studied, and four possible reasons for this enhancement have been summarised by Choi (2002) [79] and Eastman (2004) [80] as follow:

- The Brownian motion of the nanoparticles, which enables the direct solid to solid heat transport by the moving particles, is considered to enhance the thermal conductivity of the nanofluids. The calculations based on the Stokes-Einstein formula and the water-based nanofluids show that the thermal diffusion is much faster than the Brownian diffusion [79]. However, in [81], the microscopic motion, induced by both the Brownian motion and the interparticle forces, is declared to result in the additional heat transfer in the nanofluids. The Brownian motion is also supposed to play an important role in particle clustering, which is considered as another reason for enhancement in the thermal conduction.
- Nanoparticle clustering, which can have a major effect on the thermal conductivity by creating paths of lower thermal resistance. On one hand, both the cluster size, and the particle arrangement within the cluster can influence this enhancement. On the other hand, the cluster size and particle arrangement are also linked with the solid agglomeration, which produces a negative effect on the nanofluids' stability.
- Liquid layering, which exists at the liquid-solid interface, can enhance the thermal conductivity due to the fact that the atomic structure of the liquid layer is more ordered than the atomic/molecular structure of the bulk of the liquid. The ordered

structure typically leads to the higher thermal conductivity, like in the case of crystalline solids.

- Nature of the heat transport in nanoparticles, which originates from the ballistic phonon effect among the nanoparticles: the ballistic phonons initiated in one particle can reach a neighbouring particle as the particles constantly move due to the Brownian motion, which leads to the short distance between two neighbouring particles.

Apart from the reasons listed above, Lee (2006) has proved that the surface charge also affects the heat transfer experimentally [82]. However, there is still no complete description of the heat transfer enhancement mechanism(s) in the nanofluids. As presented above, many factors and mechanisms have been discussed. However, the complex structure of both the particle and particle-liquid interface, resulted in complications with the development of a general theory describing the heat enhancement in nanofluids.

Another major parameter which can be improved by adding nanoparticles is the dielectric strength of the liquid.

A model of the development of pre-breakdown streamers in mineral-oil-based nanofluids was proposed by O'Sullivan (2007) [83][84] and furtherly developed by Hwang (2008) in [85]. In this model, the dielectric strength of the nanofluids is increased as electrons produced by the field ionisation is captured by the conductive particles in the mineral oil, leading to the reduction in the mobility of the electrons, and correspondingly to the reduction in the streamer velocity. This model introduces a relaxation time constant as follows:

$$\tau = \frac{2\varepsilon_1 + \varepsilon_2}{2\sigma_1 + \sigma_2} \quad 2-38$$

where  $\sigma_1$  and  $\sigma_2$  are the electrical conductivities of the host liquid and the conductive particles, respectively.  $\varepsilon_1$  and  $\varepsilon_2$  are dielectric permittivities of the host liquid and the conductive particles, respectively.

To capture electrons, the relaxation time must be shorter than the propagation time of the streamer, which enables the capture process illustrated in Figure 2-15. It can lead to complete avoidance of the electric breakdown.

As shown in Figure 2-15, the conductive particle is polarised in the external electric field. The charge carriers with high mobility (the electrons) are trapped on the surface of the particle until the particle is fully charged, this charge is known as the saturation charge. Since the charge carriers with high mobility (the electrons) are captured by larger particles with low mobility (saturated particles), the propagation of the streamer(s) is halted, leading to the higher electric strength of the nanofluids.

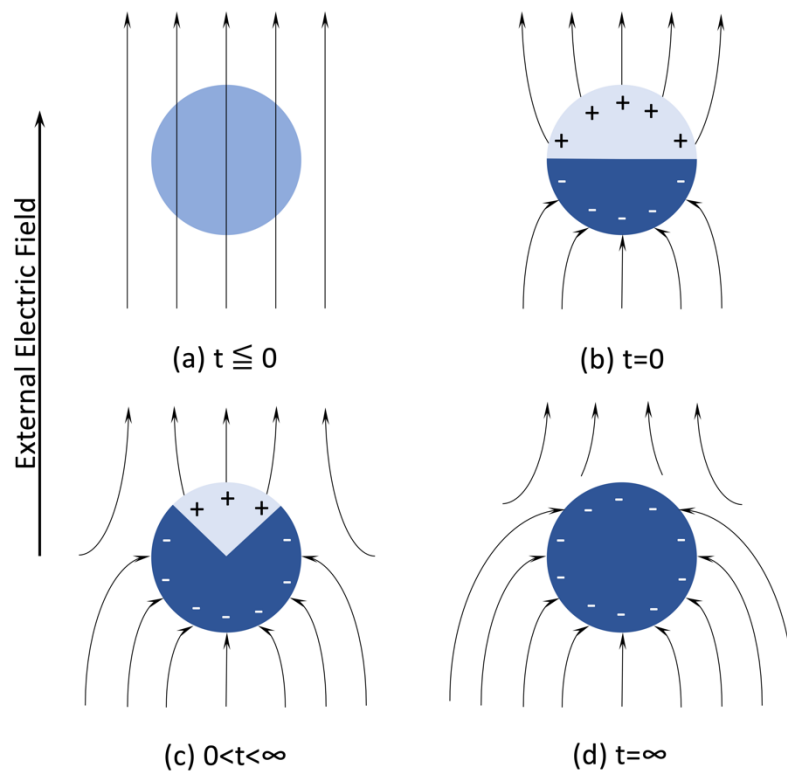


Figure 2-15 Surface charge distribution of a conductive particle at different moments in time after application of the electric field from (a)  $t \leq 0$ , till full the end of the field relaxation process (d)  $t = \infty$ .

However, some experimental results are not in agreement with the predictions from this model. On one hand, the dielectric strength of the mineral-oil-based nanofluids with SiC particles could be even lower than that of the pure mineral oil while the relaxation time for the SiC nanofluid(s) is much shorter than the time scale of the streamer development [86]. On the other hand, the oil-based nanofluids with TiO<sub>2</sub> particles has much longer, sub-s relaxation time, however these nanofluids can provide greater dielectric strength than the pure dielectric host liquids [87]. Apart from the contradiction from the experiment results, there are also defects of the assumption about the electron involved in this model: the mean free path of electrons in dielectric liquids is of the order of 10 Å [88], which could limiting the capture process proposed illustrated in Figure 2-15.

Considering the limitation of the relaxation time model, Du (2011) introduced another model describing the dielectric strength of nanofluids based on semi-conductive particles [73][74]. In Du's work, the concept of the 'electron trap', which is typically used in semiconductor models, has been used to describe the development of breakdown in nanofluids. The electron traps can be distinguished into two categories: deep traps and the shallow traps, defined by the energy required for an electron to escape from each trap.

For TiO<sub>2</sub> particles, the presence of the shallow trap can be detected by their photocatalytic activity [89]. In this case, the electron with high velocity can be captured by these shallow traps and then released rapidly by turning into a slower electron. After repeated trapping and de-trapping acts, the velocity of electrons is reduced, preventing the propagation of the streamer, and leading to the higher breakdown strength of the nanofluids [73].

However, Aljure (2014) pointed out in [90] that the simulation results support neither the relaxation model by O'Sullivan (2007, 2008) [83][84], nor the electron trap model by Du (2011, 2012) [73][74]. Moreover, the experimental results in [91] showed that the electron trapping model was not applicable to mineral oil based nanofluids with ZnO particles.

Du (2015) also used the bubble theory for the explanation of the higher breakdown strength of the nanofluids with BN particles [92]: the charge injection near the electrode may cause the Joule heating, leading to the development of gas bubbles near the electrode. Since the gas breakdown in such bubbles can lead to formation of a conductive plasma channel, which results in the complete breakdown, an increased thermal conductivity of the nanofluids with

BN particles can accelerate the dissipation of the Joule heat, preventing formation of the bubble(s) and thus leading to the enhancement of the breakdown strength of the nanofluid.

By now, the general theories of explaining enhancements in the dielectric strength of the nanofluids are still required. This is because lacking the theory guidance causes not only the difficulties in explaining the discovered aspects brought by the nanofluids but also the difficulties in the synthesis of new type nanofluids. Moreover, the theory lacking decreases the confidence in promoting the nanofluids into practical applications as the potential risks of the nanofluids are hard to predict without the theory guidance.

## **2.5 Summary**

This chapter presents the background information and analysis of fundamentals and practical methodologies related to the research conducted in the framework of this thesis.

The review of dielectric liquids and their applications in electric systems is presented in the first section. Three types of dielectric liquids: mineral oils, synthetic esters, and natural esters, were considered and their chemical composition and properties were analysed. Mineral oils, which are the most widely used insulating liquids, are facing significant challenges like strict environmental and safety requirements and regulations. In recent years environmentally friendly dielectric liquids - synthetic and natural ester liquids have been developed and now these liquids are used in different practical electric systems as liquid insulators. However, their electrical and dielectric properties are not fully known and these factors as well as some of their physical properties such as higher viscosity limit their wider use in the power and pulsed power industries. Therefore, better understanding of the physical processes and breakdown mechanisms in these liquids stressed with the external electric field can help engineers in selection and coordination of insulating liquids. Also, further information on the physical processes in such liquids can stimulate the development of nanofluids with specific parameters and characteristics

Understanding of conduction mechanisms in the dielectric liquids is fundamental for the interpretation of the experimental results obtained in the present study. Thus, these conduction

and charge injection and generation processes in the dielectric liquids have been reviewed in Section 2.2.

The review included of the processes of generation of charge carriers in the dielectric liquids and the behaviour of the charge carriers in the dielectric liquids stressed with the external electric field.

The mobility of charge carriers is discussed along with the charge re-distribution processes at the liquids-electrode interface, this information is required for the analysis of the experiment results obtained in this study.

In Section 2.3, two methods of measurement of the mobility were introduced: the ToF method and the SCLC method. These two methodologies enable the measurement of the mobility of charge carriers to be conducted under a wide range of the electric field magnitudes. The EHD effect was also discussed in this section, the EHD will be used in further analysis of the behaviour of the dielectric liquids stressed with the electric field.

Finally, Chapter 2 made an introduction to nanofluids which is an important objective of the present research project. The nanofluids are considered as promising liquids for the use in electrical and high voltage systems due to their proven ability to hold higher voltages. The dielectric strength of these nanofluids depends on concentration and type of nanoparticles: for example, in [21], both TiO<sub>2</sub> and BN particles were selected to prepare nanofluids whose concentration ranged from 0.0006% to 0.1% (b/w), and the results showed that It was found that in most cases, the optimal concentration of these two types of nanoparticles are between 0.0006% and 0.004% (b/w). All these aspects provide an opportunity for practical applications of nanofluids in high voltage systems, especially in some specific applications with restricted space or weight requirements. However, the practical utilisation of nanofluids is still facing challenges due to lack of experimental data and theoretical model(s).

Based on the literature review conducted in this chapter, it can be stated that various insulating liquids have been developed for different applications over the years. Among them are mineral oils, ester liquids, and nanofluids. It is noticed that the use of these liquids in different practical applications strongly rely on the understanding of the conduction, the EHD and breakdown processes within these liquids. As these processes are defined by the behaviour of

the charge carriers, the conduction processes. In this case, mobility of charge carriers and the EHD behaviour of the insulating liquids were selected as the main research objectives of the present study.

## Chapter 3 MATHEMATICAL MODEL OF PARTICLE CHARGING IN DIELECTRIC LIQUIDS

---

As introduced in Section 2.4, a nanofluid can be developed by dispersing poorly conductive sub- $\mu\text{m}$  particles in a dielectric liquid. In some practical applications, nanofluids are used in high voltage systems as insulating liquids. Thus, it is crucial to understand the behaviour of dispersed solid particles in nanofluids.

In this work, a model based on a solid particle surrounded by a liquid stressed with a uniform electric field is developed to investigate the charging processes and forces acting on this particle. The modelling work and corresponding analysis aim to explore the transient electric field in poorly conductive particles immersed in dielectric fluid stressed with the suddenly applied electric field  $E_0$  ( $t \geq 0$ ). This external field results in polarisation and redistribution of the bounded and free charges in the particle(s) and in the fluid (the Maxwell-Wagner relaxation process). To simplify the modelling work, it assumes that there is no net free charge in the system and all the positive and negative charges are identical, i.e., same mass, volume, and shape, except their polarity. A transient electric field was used to analytically obtain the electric force acting between two particles in the fluid via the dipole-dipole approximation.

The results of this modelling work include analytical expressions for the transient electric field in and around the particle, the transient charge distribution across the particle-liquid interface, and electric forces acting between two particles in a poorly conductive fluid. With a wide range of parameters related to different insulating fluids and particles used in the present work, these expressions have been utilised to simulate the interfacial charge distribution, the electric field distribution, and the force as functions of the relative permittivities and electrical conductivities of both particles and fluids. The obtained analytical results will be applied in explaining the electrohydrodynamic motion in nanofluids studied in Chapter 7 and will help in further analysis of the behaviour of small-scale particles in insulating liquids stressed with the externally applied DC field.

## **3.1 Particles in Dielectric Liquid: Development of Mathematical Model**

Due to the difference between relative permittivities and electric conductivities of the dispersed particles and the hosting liquid, the charge accumulation occurs across the particle-liquid interfaces once they are stressed with the external electrical field. This section starts with the modelling of an individual particle placed in dielectric liquid. Then this model is expanded to describe the Coulomb force between two particles immersed in the liquid stressed with the external electric field.

### **3.1.1 Electric Response of Single Particle**

In 1873, James Clerk Maxwell published his book “*A Treatise on Electricity and Magnetism*” [86], in which he introduced a way of describing the electric conduction in dielectrics based on a linear multi-layered capacitor model: in this model, the space between two parallel plane electrodes is filled with several of layers of poorly conductive materials with different relative permittivities and conductivities. Maxwell pointed out that when this multi-layered capacitor is stressed with the external voltage, the charge accumulation occurs across the interfaces formed by these different layers. Karl Willy Wagner (1914) [93][94], extended Maxwell’s model into the AC domain and this transient polarisation process is now called ‘Maxwell-Wagner polarisation’.

In the Maxwell-Wagner polarisation model, the charge accumulation at the interface starts to occur once this interface is stressed with the external electric field, and the charge reaches its saturated value after a specific time. This time called ‘Maxwell-Wagner relaxation time’ depends not only on the relative permittivities and conductivities of the materials but also on the geometrical factors [95]. Therefore, specific equation(s) which provide the Maxwell-Wagner relaxation time for each specific topology geometry are required for the modelling of the polarisation processes. In the present work, the Maxwell-Wagner relaxation time was obtained for a single spherical particle located in a poorly conductive media stressed with the uniform electric field. A schematic diagram of a single particle model is given in Figure 3-1.

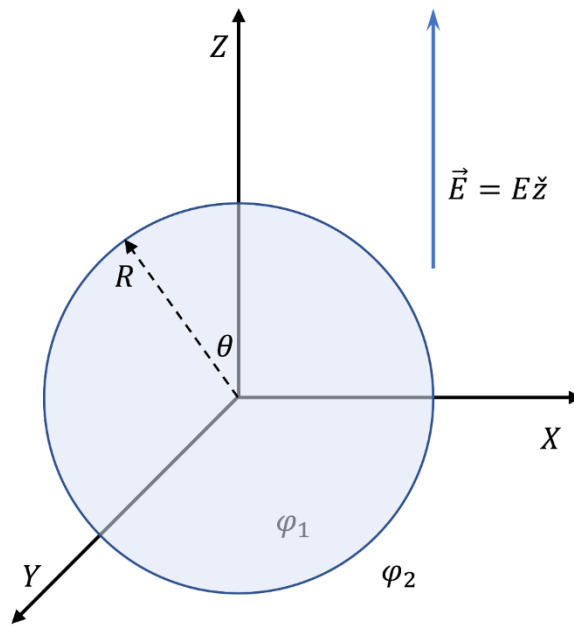


Figure 3-1 Single Particle in Dielectric Liquid.  $\vec{E}$  represents the uniform electric field whose direction is parallel to the Z-axis,  $R$  is the radius of the sphere,  $\theta$  is the polar angle,  $\varphi_1$  and  $\varphi_2$  is the electric potential inside and outside the sphere, respectively.

In Figure 3-1, a spherical particle with radius  $R$ , dielectric permittivity  $\epsilon_1$ , and electric conductivity  $\sigma_1$ , is immersed in the dielectric liquid, with dielectric permittivity  $\epsilon_2$ , and electric conductivity  $\sigma_2$ . A uniform electric field  $E$  along the Z-axis is applied at time  $t = 0$ , leading to the initiation of the charge accumulation process at the particle-liquid interface. This charge accumulation process completes when the charge reaches its steady-state value.

Using the assumption that there is no net free charge in the system, electrostatic potential  $V$ , is governed by the Laplace's equation:

$$\vec{E} = -\nabla V \quad 3-1$$

$$\nabla^2 V = 0 \quad 3-2$$

The general solution of the Laplace's equation for the axisymmetric spherical model can be expressed by the Legendre polynomials with corresponding coefficients. The general solution of the electric potential inside and outside the sphere was given by T. B. Jones [96]:

$$\varphi_1 = A(t)r \cos \theta \quad \text{for } r \leq R \quad 3-3$$

$$\varphi_2 = -E_0 f(t)r \cos \theta + B(t)r^{-2} \cos \theta \quad \text{for } r \geq R \quad 3-4$$

where,  $A(t)$  and  $B(t)$  are unknown time dependent coefficients.  $E_0$  is the magnitude of the external uniform electric field, and  $f(t)$  is the step function ( $f(t) = 0$  for  $t < t_0$ , and  $f(t) = 1$  for  $t > t_0$ ) which describes the application of the external step field.

By applying the relationship presented by Equation 3-1, the normal component of the induced electric field inside and outside of the sphere can be obtained as follows:

$$\vec{E}_{r1} = -A(t)\cos\theta\hat{r} \quad \text{for } r \leq R \quad 3-5$$

$$\vec{E}_{r2} = Ef(t)\cos\theta + 2B(t)r^{-3}\cos\theta\hat{r} \quad \text{for } r \geq R \quad 3-6$$

where,  $\hat{r}$  is the unit vector. However, the coefficients  $A(t)$  and  $B(t)$  are still unknown. To find them, additional boundary conditions should be introduced. The detailed mathematical derivation of expressions for  $A(t)$  and  $B(t)$  is given in Appendix I, the final expressions for  $A(t)$  and  $B(t)$  are:

$$A(t) = -3E \left[ \frac{\varepsilon_2}{\varepsilon_1 + 2\varepsilon_2} \exp\left(-\frac{t}{\tau}\right) + \frac{\sigma_2}{\sigma_1 + 2\sigma_2} \left(1 - \exp\left(-\frac{t}{\tau}\right)\right) \right] \quad 3-7$$

$$B(t) = ER^3 \left[ \frac{\varepsilon_1 - \varepsilon_2}{\varepsilon_1 + 2\varepsilon_2} \exp\left(-\frac{t}{\tau}\right) + \frac{\sigma_1 - \sigma_2}{\sigma_1 + 2\sigma_2} \left(1 - \exp\left(-\frac{t}{\tau}\right)\right) \right] \quad 3-8$$

where,

$$\tau = \frac{\varepsilon_1 + 2\varepsilon_2}{\sigma_1 + 2\sigma_2} \quad 3-9$$

is the Maxwell-Wagner relaxation time. According to Equation 3-7 and 3-8, the radial component of the electric field can also be presented as:

$$\vec{E}_{r1} = 3E \left[ \frac{\varepsilon_2}{\varepsilon_1 + 2\varepsilon_2} \exp\left(-\frac{t}{\tau}\right) + \frac{\sigma_2}{\sigma_1 + 2\sigma_2} \left(1 - \exp\left(-\frac{t}{\tau}\right)\right) \right] \cos\theta \hat{r} \quad 3-10$$

$$\vec{E}_{r2} = Ef(t)\cos\theta + 2E \frac{R^3}{r^3} \left[ \begin{array}{l} \frac{\varepsilon_1 - \varepsilon_2}{\varepsilon_1 + 2\varepsilon_2} \exp\left(-\frac{t}{\tau}\right) \\ + \frac{\sigma_1 - \sigma_2}{\sigma_1 + 2\sigma_2} \left(1 - \exp\left(-\frac{t}{\tau}\right)\right) \end{array} \right] \cos\theta \hat{r} \quad 3-11$$

Based on the electric field obtained above, the surface charge can then be calculated by the Gauss Law. For this spherical model, the charge on two hemispheres was obtained: on the half-sphere above the X-Y plane and on another half-sphere below the X-Y plane. The total charge on the sphere is zero as this model assumes zero net free charge on the particle, thus two hemispheres have equal but opposite charges on their surfaces. Therefore, the calculation of the surface charge density requires either of two hemispheres, and the following procedure is based on the hemisphere above the X-Y plane:

$$\begin{aligned}
 Q &= \oiint \vec{D} \cdot d\vec{S} \\
 &= \oiint (\vec{D}_{r1} - \vec{D}_{r2}) \cdot d\vec{S} && \text{for } \theta \in [0, \frac{\pi}{2}] && 3-12 \\
 &= \oiint (\vec{E}_{r1}\epsilon_1 - \vec{E}_{r2}\epsilon_2) \cdot d\vec{S}
 \end{aligned}$$

which yields the surface charge density  $\rho$ :

$$\rho = \vec{E}_{r1}\epsilon_1 - \vec{E}_{r2}\epsilon_2 \quad \text{for } \theta \in [0, \frac{\pi}{2}] \quad 3-13$$

The opposite hemisphere of the particle below the X-Y plane has the same charge distribution but the charge has an opposite polarity.

### 3.1.2 Forces Acting on Particles in Liquids

As discussed in the literature review, a typical nanofluid is a colloid with a good stability in terms of suspension of dispersed particles. The particles in nanofluids with a weak stability can aggregate and precipitate due to the gravity.

Once a nanofluid is stressed with an external electric field, the forces induced by the external field result in the EHD motion of the liquid, and the motion of the particles suspended in this nanofluid. The behaviour of the dispersed particles is affected by both the EHD motion of the fluid and the charge (re)distribution across the particle-fluid interface. Considering these factors, two main categories of forces that govern the motion of the particles can be identified: the drag force and the Coulomb force acting on the charged particles.

The drag force, which is also called fluid resistance or fluid friction, is caused by the relative motion of the particles in the fluid. This force is given as:

$$F_D = \frac{1}{2}\rho v^2 A C_D \quad 3-14$$

where,  $\rho$  is the fluid density,  $v$  is the particle's relative velocity to the fluid,  $A$  is the cross-sectional area of the particle, and  $C_D$  is a dimensionless coefficient depending on both the shape of the particle and the Reynolds number.

Apart from the drag force, the Coulomb force generated by the external field and other charged particles can also affect the particle's dynamics.

For the particle with a non-zero net charge, the Coulomb force acting on the particle can be attributed to the presence of the external field and other particles. In this case, the critical problem for the force determination is the evaluation of the net charge on the particles, which is beyond the scope of the present model.

In the previous section, the polarisation process associated with a single particle in the external electrical field was analysed. An analytical solution for the surface charge distribution on the particle was obtained. This solution assumes that there is no net free charge on/near the particle, which may not always be the case in different practical applications. However, the obtained results, i.e., the surface charge distribution, can be used to calculate the polarisation charge on individual particles, which contributes to the total Coulomb force acting on two polarised particles.

On the other hand, for two particles with zero net charge, the dipole-dipole interaction defines the forces between these two particles. Therefore, a mathematical description of these forces can be developed according to the dipole-dipole interaction. This dipole-dipole analysis leads to a straightforward analytical solution for the force acting between two polarised particles.

In this chapter, the force acting between two particles was obtained for two polarised particles with zero net charges.

### 3.1.3 Coulomb Force Acting between Two Particles

The dipole-dipole interaction method is used in the present work to obtain the force acting between two particles with zero net charges. In *< Classical Electrodynamics >* [97], the image method has been introduced to solve the dipole-dipole problem. Although this method was developed based on a conducting object, it can be extended into dielectrics with further conditions. The detailed mathematical procedure is presented in this section.

First, the dipole moment of a single particle needs to be calculated.

The polarisation of a single particle in the dielectric liquid in the external electric field is presented in Figure 3-2. As shown in the left bottom corner of Figure 3-2, multiple individual dipoles are formed by the accumulated charges at the interface between the particle and the liquid. This is because the surface charge induced by the uniform electric field along the Z-axis is symmetrically distributed in the X-Y plane. Therefore, to obtain the dipole moment of a single particle, the total moment of the induced dipoles inside the circle shown in the upper left of Figure 3-2 can be calculated. To simplify this analysis, only the space within the first quadrant within the X-Y plane is considered. The total moment of a single particle is then four times the moment calculated for a single quadrant due to the Z-axis rotational symmetry of the charge distribution.

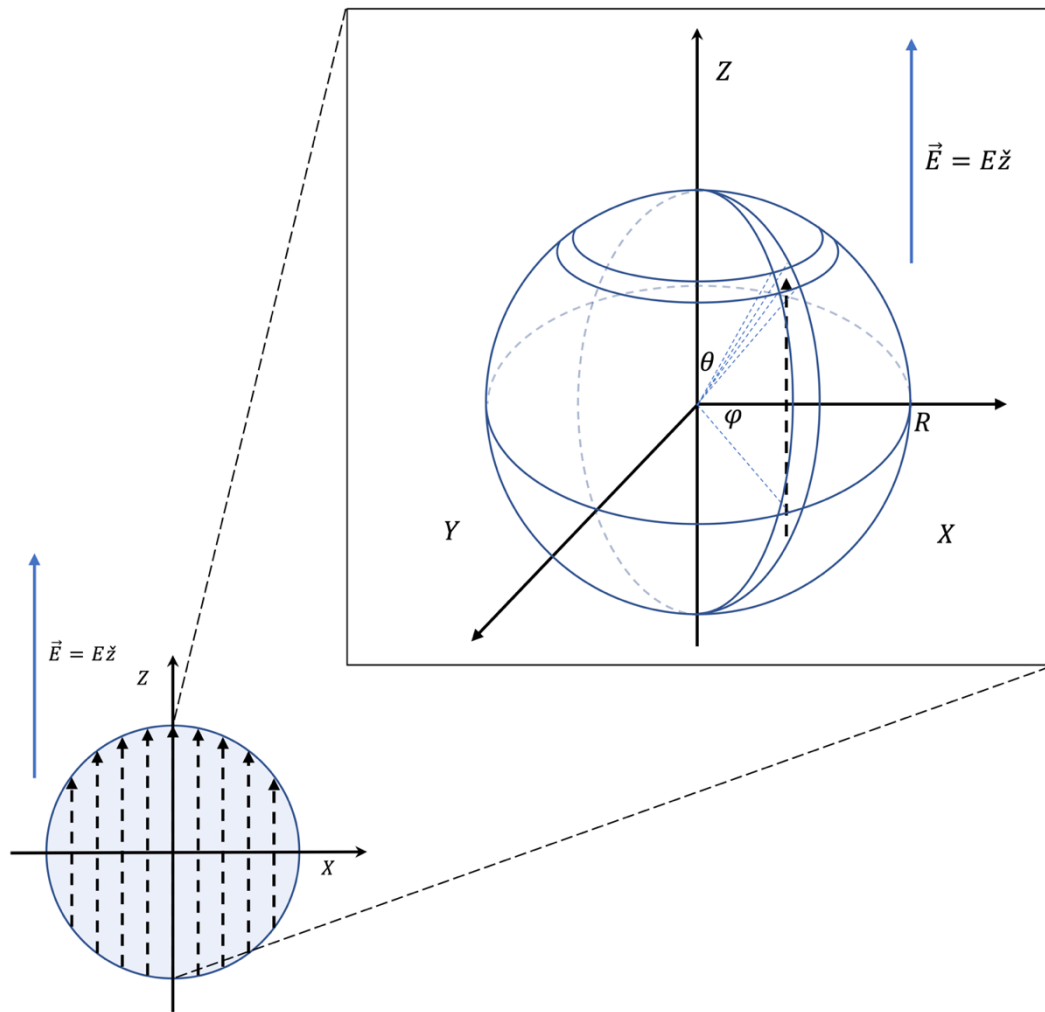


Figure 3-2 Polarisation of a Single Particle in the uniform external field. The 2D graph in the bottom-left corner of the figure illustrates the multiple individual dipoles inside the sphere as arrows. The 3D graph in the upper-right corner of the figure illustrates the parameters required by the model: radial distance  $R$ , polar angle  $\theta$ , and azimuthal angle  $\varphi$ .

The induced charge within a unit area can be expressed as:

$$dQ = \rho dA \quad 3-15$$

where,  $\rho$  is the surface charge density,  $A$  is the unit area, and  $Q$  is the accumulated charge.

According to Figure 3-2, the unit area  $dA$  can be expressed as:

$$dA = R^2 \sin\theta d\phi d\theta \quad 3-16$$

Equation 3-16 yields the dipole moment of an individual dipole inside the particle:

$$dP = l\rho(r, \theta, \phi)dA \quad 3-17$$

where,  $l$  is the distance between two unit areas and equals to  $|2R\cos\theta|$ . With the surface charge distribution obtained by Equation 3-13, the dipole moment within this space can be expressed as:

$$\begin{aligned}
 P = \frac{4\pi}{3} R^3 \left\{ 3E\varepsilon_1 \left[ \frac{\varepsilon_2}{\varepsilon_1 + 2\varepsilon_2} \exp\left(-\frac{t}{\tau}\right) + \frac{\sigma_2}{\sigma_1 + 2\sigma_2} \left(1 - \exp\left(-\frac{t}{\tau}\right)\right) \right] \right. \\
 - 2E\varepsilon_2 \left[ \frac{\varepsilon_1 - \varepsilon_2}{\varepsilon_1 + 2\varepsilon_2} \exp\left(-\frac{t}{\tau}\right) + \frac{\sigma_1 - \sigma_2}{\sigma_1 + 2\sigma_2} \left(1 - \exp\left(-\frac{t}{\tau}\right)\right) \right] \\
 \left. - E\varepsilon_2 f(t) \right\} \quad 3-18
 \end{aligned}$$

giving the total dipole moment of a single particle:

$$\begin{aligned}
 P = \frac{16\pi}{3} R^3 \left\{ 3E\varepsilon_1 \left[ \frac{\varepsilon_2}{\varepsilon_1 + 2\varepsilon_2} \exp\left(-\frac{t}{\tau}\right) + \frac{\sigma_2}{\sigma_1 + 2\sigma_2} \left(1 - \exp\left(-\frac{t}{\tau}\right)\right) \right] \right. \\
 \left. - 2E\varepsilon_2 \left[ \frac{\varepsilon_1 - \varepsilon_2}{\varepsilon_1 + 2\varepsilon_2} \exp\left(-\frac{t}{\tau}\right) + \frac{\sigma_1 - \sigma_2}{\sigma_1 + 2\sigma_2} \left(1 - \exp\left(-\frac{t}{\tau}\right)\right) \right] \right. \\
 \left. - E\varepsilon_2 f(t) \right\} \quad 3-19
 \end{aligned}$$

With the obtained dipole moment of a single particle, the force based on the dipole-dipole interaction can then be analysed with the DID model [98].

In the DID model, a pair of dielectric spheres A and B with the same dielectric permittivity  $\varepsilon_1$  are placed in the medium with the dielectric permittivity  $\varepsilon_2$ . The radius of sphere A is  $a$ , and  $b$  for sphere B. The distance between the centres of these two spheres is  $r$ . The dipole moment induced by the external electric field  $\vec{E}$  for sphere A and B are  $p_{a0}$ , and  $p_{b0}$ , respectively.

It is assumed that these two spheres are placed within the effective range where the dipole moment  $p_{a0}$  of the sphere A can induce an image dipole  $p_{b1}$  in sphere B, and vice versa. Then dipole  $p_{b1}$  induces a new image dipole  $p_{a2}$  on sphere A. Following this, a set of infinite series image dipoles can be induced in sphere A, and B which can be presented as:

$$\frac{P_{aTrans}}{P_{a0}} = (b \sinh \alpha)^3 \times \sum_{n=1}^{\infty} \left[ \frac{(-\delta)^{2n-2}}{(b \sinh n\alpha + a \sinh (n-1)\alpha)^3} + \frac{(-\delta)^{2n-1}}{(r \sinh n\alpha)^3} \right] \quad 3-20$$

$$\frac{P_{aLongi}}{P_{a0}} = (b \sinh \alpha)^3 \times \sum_{n=1}^{\infty} \left[ \frac{(2\delta)^{2n-2}}{(b \sinh n\alpha + a \sinh (n-1)\alpha)^3} + \frac{(2\delta)^{2n-1}}{(r \sinh n\alpha)^3} \right] \quad 3-21$$

Parameter  $\alpha$  satisfies:

$$\cosh \alpha = \frac{r^2 - a^2 - b^2}{2ab} \quad 3-22$$

and parameter  $\delta$  is defined as:

$$\delta = \frac{\epsilon_1 - \epsilon_2}{\epsilon_1 + \epsilon_2} \quad 3-23$$

where subscript *Trans* denotes a transverse field, which is perpendicular to the line joining the centres of two spheres, while subscript *Longi* denotes a longitudinal field, which is parallel to the line joining the centres of two spheres, as presented in Figure 3-3:

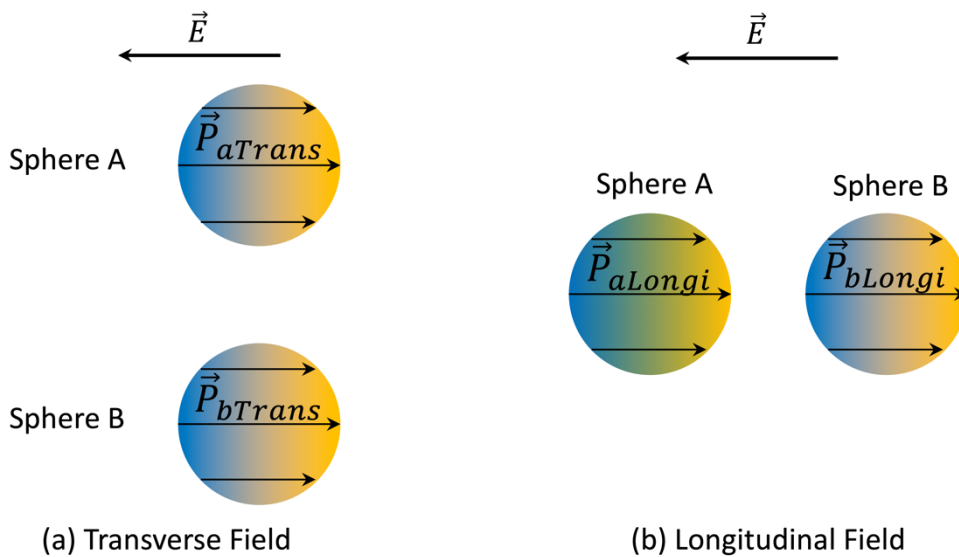


Figure 3-3 Illustration of Transverse Field and Longitudinal Field, the arrows inside the spheres indicate the direction of the dipole moment of the particle.

It should be noted that the total dipole moment obtained by Equations 3-20, and 3-21 is based on the image method, which is applicable to the conductors rather than dielectrics. However, this limitation has been overcome by Yu, K., [98] by introducing a new factor,  $\delta$  (as seen in Equation 3-23): when  $\delta \rightarrow 1$ , namely there is a high contrast between the relative permittivity of the particle and the fluids, the model reduces to a conducting particle model, and the approximation are expected to be good. However, the numerical simulation results obtained in [98] show that even for a moderate difference in relative permittivities of particles and the liquid ( $\delta = 1/3$ ), the analytic results from the DID model agree well with the numerical results for the separation between  $1.5(a + b)$  and  $3(a + b)$ , where  $a$  and  $b$  are radii of the two spheres.

Also, the distance between two spheres affects the accuracy of the approximation in the DID method. According to [98], the results obtained by Equation 3-20, and 3-21 can be modified by changing the term  $n$  within the equations as: (a),  $n = 1$ , the result has a single term, turning into a point-dipole (PD) model; (b),  $n = 1$  to  $n = 2$ , these equations represent the DID model; (c), for  $n = \infty$  the equations represent multiple-induced-dipole (MID) model.

In this case, the PD approach should be used to model the electrostatic interaction between two spheres with a large separation [99]. As the separation decreasing, the point-dipole model becomes invalid, and the multiple-induced-dipole model should be used. However, it is stated in [98] that for the separation larger than  $1.3(a + b)$ , where  $a$  and  $b$  are radii of the two spheres, the results from the DID model almost coincides with the results from the MID model.

Based on the total dipole moment achieved above, the force between two spheres can then be given by the following equations:

$$F_{Trans} = \frac{E_0}{2} \frac{\partial}{\partial r} (P_{aTrans} + P_{bTrans}) \quad 3-24$$

$$F_{Longi} = \frac{E_0}{2} \frac{\partial}{\partial r} (P_{aLongi} + P_{bLongi}) \quad 3-25$$

With the obtained dipole moment for two spheres, the forces between the two spheres can be obtained by Equation 3-24 and 3-25, and the results of this analysis are presented and discussed in the next section.

## **3.2 Simulation Results and Discussions**

The developed model was used to obtain the surface charge distribution on particles immersed in a dielectric fluid stressed with a step field and the force acting between two particles. These results are presented in Section 3.2.1 and 3.2.2. The parameters of the model, i.e., physical properties of the particles and liquids, were selected to represent practical particles and liquids used in the present work. The particles include TiO<sub>2</sub>, and BN particles, while the liquids used in this analysis are the MIDEL 7131 Synthetic Ester, the MIDEL eN 1204 Natural Ester, and the Shell Diala B Mineral Oil. The model was implemented in Python 3.7.

### **3.2.1 Maxwell-Wagner Relaxation Time**

To model BN and TiO<sub>2</sub> particles, their properties, including their electrical conductivity (obtained in [100][101]), and relative permittivity (obtained in [102][103]), are required. All these parameters are listed in Table 3-1. The relative permittivity of the liquids (obtained in [104]) required for modelling are also listed in Table 3-1. The electrical conductivity of the dielectric liquids was obtained in the present work.

As shown in Table 3-1 the electrical parameters of the SE and the NE are similar to each other. In this case, the analysis of the forces in esters was conducted based on the NE only. Modelling of particle's behaviour in mineral oils was based on the MO parameters given in Table 3-1.

Table 3-1 Parameters for Simulation

		Electrical Conductivity (S/m)	Relative permittivity
<b>Particle</b>	<b>TiO<sub>2</sub></b>	$10^{-11}$	~ 60
	<b>BN</b>	$10^{-13} - 10^{-15}$	~ 6
<b>Dielectric Liquid</b>	<b>SE</b>	$4.5 \cdot 10^{-12}$	~ 3.2
	<b>NE</b>	$5 \cdot 10^{-12}$	~ 3.2
	<b>MO</b>	$7.5 \cdot 10^{-14}$	~ 2.2

Using parameters in Table 3-1 with Equation 3-9, which describes the Maxwell-Wanger relaxation time, the relaxation time of the TiO<sub>2</sub> and BN particles immersed in a dielectric liquid was obtained and given in Table 3-2.

Table 3-2 Maxwell-Wagner Relaxation Time

	<b>Esters</b>	<b>Mineral Oil</b>
<b>TiO<sub>2</sub></b>	29.40 s	56.18 s
<b>BN</b>	10.87 - 10.97 s	368.33 - 609.82 s

From Table 3-2, it can be seen that for the same particles, the relaxation time in the ester fluid is always shorter than the relaxation time in the MO, which can be attributed to the much lower electrical conductivity of the MO.

Moreover, the relaxation time of the BN particles in the MO is one order of magnitude longer than the relaxation time of all the other samples. This difference stems from the significantly lower electric conductivity of both the BN particles and the MO.

It can also be found in Table 3-2 that the calculated relaxation time for the BN particle is presented as a time range rather than a specific value. This range is due to the variation in the parameters available from the literature.

### **3.2.2 Surface Charge Distribution**

Using the relaxation time obtained in Section 3.2.1, a detailed simulation of the surface charge distribution was obtained and presented and discussed in this section.

Using parameters given in Table 3-1 with Equations 3-10, 3-11, and 3-13, the surface charge distribution on a single particle was obtained. Figure 3-4 is an example of the modelled surface charge distribution on a single  $\text{TiO}_2$  particle immersed in the ester fluid and stressed with the electric field with a magnitude of  $10^6 \text{V/m}$  for 200 s. This electric field strength was selected to match the experimental parameters used in this research, the details of which are presented in Section 4.3. The simulating time (200 s) was set to allow the surface charge on the sample to reach its quasi-steady state.

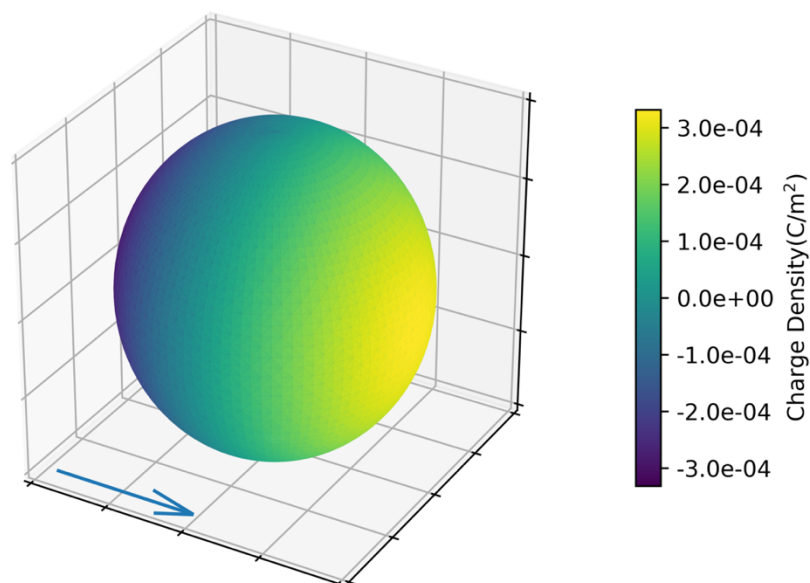


Figure 3-4 Surface Charge Distribution on a Single  $\text{TiO}_2$  Particle in the uniform electric field with magnitude of  $10^6 \text{V/m}$  at  $200^{\text{th}}$  second after the voltage switch on, the blue arrow indicates the direction of the electric field.

It can be found from Figure 3-4 that, under the assumption that both the positive and negative charge carriers have the same mobility and density, the highest surface charge density is observed on two poles of the sphere. Moreover, the surface charge density distribution follows a rotational symmetry in the direction of the external electric field, presented by the blue arrows in Figure 3-4. This conclusion also can be reached based on Equations 3-10, 3-11, and 3-13. Therefore, the following modelling focuses on the relaxation time rather than the surface charge distribution.

The surface charge of the sphere can also be obtained by Equations 3-10, 3-11, and 3-13, and the results of this modelling are presented and discussed below (the half surface with only positive/negative charge):

$$Q = 3\pi R^2 E \frac{\varepsilon_1 \sigma_2 - \varepsilon_2 \sigma_1}{\sigma_1 + 2\sigma_2} \left(1 - \exp\left(-\frac{t}{\tau}\right)\right) \quad 3-26$$

According to Equation 3-26, it can be found that the charging process on the surface of the particle is an exponential process, i.e., the surface charge grows exponentially in time. In this case, it can be stated that the charge will reach its quasi-steady state after a specific transient period. Mathematically, this transient period can be defined by the time constant  $\tau$  (the Maxwell-Wagner relaxation time) which governs the exponential growth: this time reaches  $\sim 63\%$  of its saturation value at time  $t = \tau$ ;  $\sim 95\%$  at  $t = 3\tau$ , and  $\sim 99\%$  at  $t = 5\tau$ . In this study, the duration of the transient period is defined as  $t = 5\tau$ , which is referred to as the ‘transient time’ in the following analysis.

Using Equation 3-26, the charge on the half-sphere can then be calculated based on different physical models, which are given in Figure 3-5, Figure 3-6, and Figure 3-7, respectively.

In Figure 3-5, the surface charge on the half surface of the particle is obtained based on a single  $\text{TiO}_2$  particle with a 200 nm radius under  $10^6 \text{V/m}$  electric field. 200 nm was selected as the simulation radius because the radius of the particles used in the experimental part of this work is  $\sim (150 - 250)$  nm. The obtained particle dimensions are discussed in Section 4.1.3.

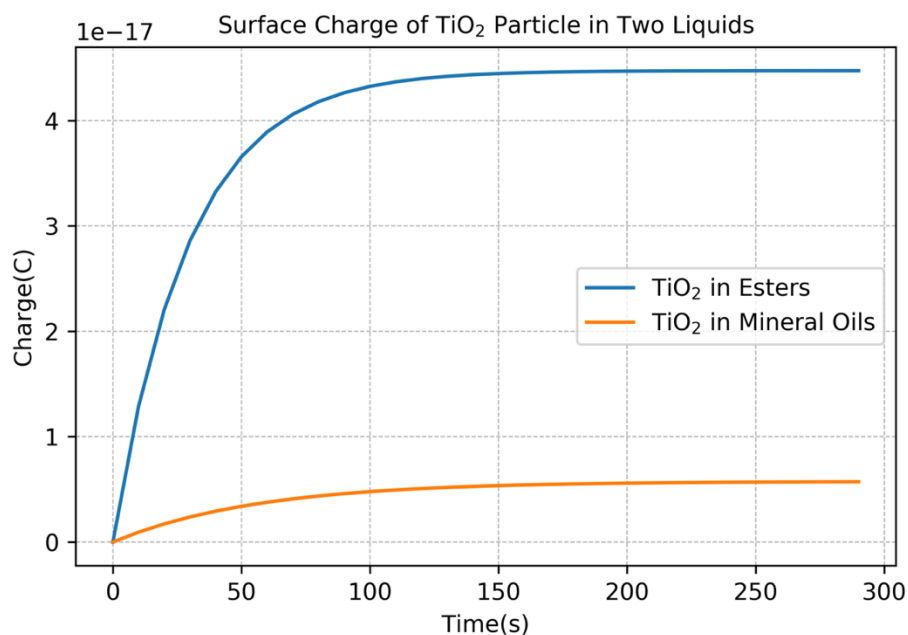


Figure 3-5 Surface Charge on TiO<sub>2</sub> particle immersed in the ester liquid and the mineral oil. The radius of TiO<sub>2</sub> particle is 200 nm, the magnitude of the externally applied field is 10<sup>6</sup>V/m.

It can be found from Figure 3-5 that the surface charge on the TiO<sub>2</sub> particle immersed in the ester fluid in the quasi-steady state is much higher than that in the mineral oil. According to the Maxwell-Wagner relaxation times  $\tau$  listed in Table 3-2, the transient time of the TiO<sub>2</sub> particles in the ester fluid is 147.00 s, which corresponds to the surface charge of  $4.43 \cdot 10^{-17}$  C. The transient time for the TiO<sub>2</sub> particle in the MO is 280.90 s, which corresponds to the surface charge of  $0.57 \cdot 10^{-17}$  C.

The simulation results for a single BN particle are presented in Figure 3-6. Two lines in this figure correspond to the surface charge on the BN particles with the minimum and maximum electrical conductivity obtained in the literature.

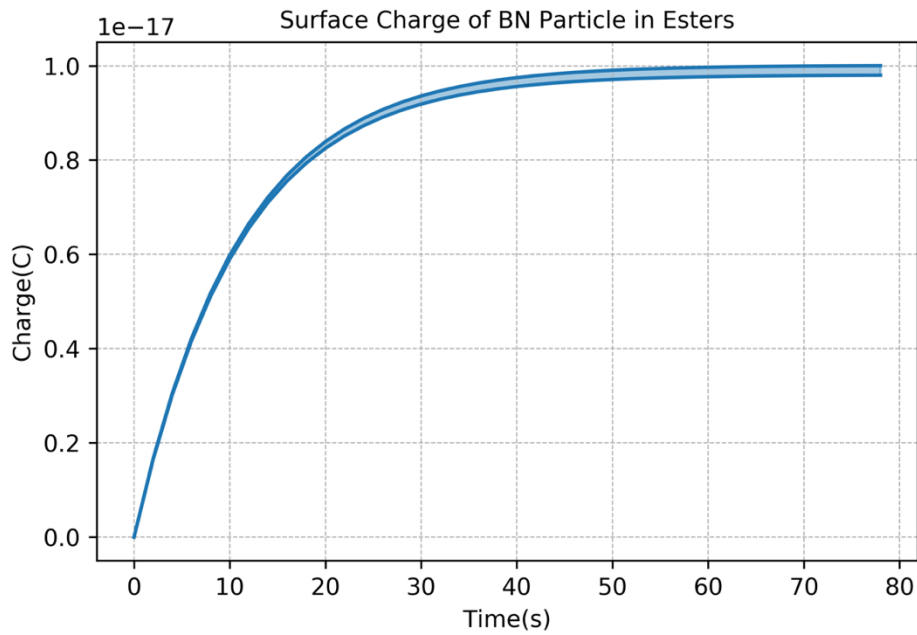


Figure 3-6 Surface Charge on a single BN particle in the ester fluid. The radius of the BN particle is 200 nm, the magnitude of the electric field is  $10^6 \text{ V/m}$ . The blue region indicates the surface charge variations due to the electrical conductivity variations of the BN particle. The upper line corresponds to the electrical conductivity of  $10^{-13} \text{ S/m}$ , and the lower line corresponds to the electrical conductivity of  $10^{-15} \text{ S/m}$ , [101].

The surface charge on the BN particle presented in Figure 3-6 was obtained using the same parameters as in the case of  $\text{TiO}_2$ -particles: the radius of the BN particle is 200 nm, and the electric fields strength is  $10^6 \text{ V/m}$ . The transient time and the corresponding surface charge of the BN particles in esters were obtained using the parameters listed in Table 3-2, i.e.,  $\tau$  is from 54.35 s to 54.85 s, and  $q$  is from  $0.97 \cdot 10^{-17} \text{ C}$  to  $0.99 \cdot 10^{-17} \text{ C}$ .

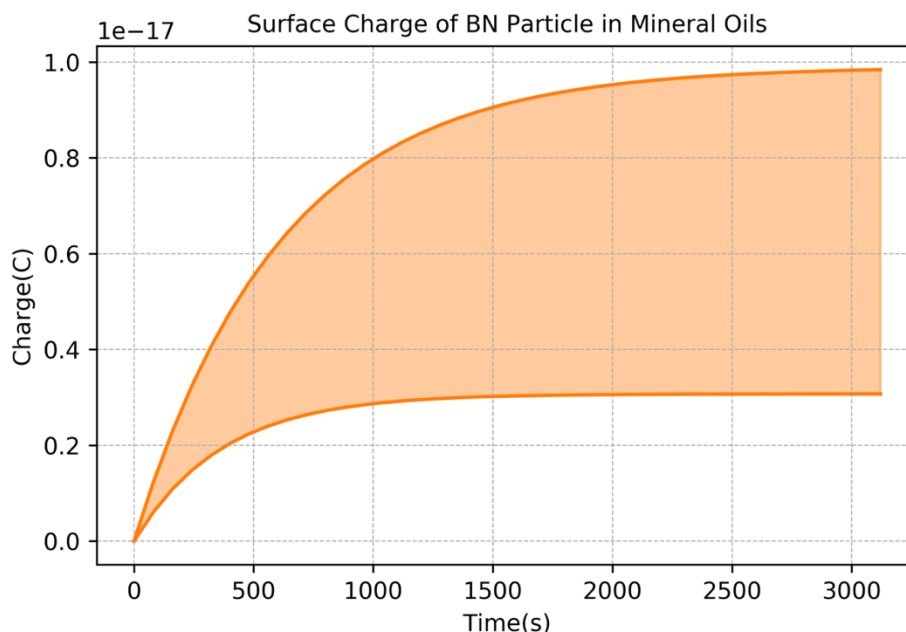


Figure 3-7 Surface charge on a single BN particle in the mineral oil. The radius of the BN particle is 200 nm, the magnitude of the electric field is  $10^6 \text{ V/m}$ . The orange region indicates the surface charge variations due to the electrical conductivity variations of the BN particle. The upper line corresponds to the electrical conductivity of  $10^{-13} \text{ S/m}$ , and the lower line corresponds to the electrical conductivity of  $10^{-15} \text{ S/m}$ , [101].

The transient time and the corresponding surface charge of the BN particles in the mineral oil are 1841.65 to 3049.10 s and  $0.30 \cdot 10^{-17}$  to  $0.98 \cdot 10^{-17} \text{ C}$ , respectively. The transient time of the BN particles in the mineral oil is about two orders of magnitude longer than the transient time of the BN particles in the esters.

For the surface charge in quasi-steady state, the results of these two simulations (Figure 3-5 to Figure 3-7) have shown that the surface charge on the BN particle in the esters and mineral oils are much lower than the surface charge formed on  $\text{TiO}_2$  particle.

The results obtained in this section demonstrate the symmetry of the surface charge distribution. The surface charge of an individual particle has been obtained by Equation 3-26.

However, this mathematical model relies on several assumptions, leading to a less accurate representation of the practical particles and hosting fluids. For example, if the simulated charge is close to an elementary charge, the interactions between electrons should be considered. Therefore, these limitations must be considered when using the developed model to describe the experimental results.

To model the behaviour of particles in the fluid stressed with the external electric field, the force acting on the particle should be obtained and analysed. In this model, the forces acting on the immersed particles include buoyancy, gravity, drag force due to the particle's motion in the fluid, and the electric force, all of which have been introduced in Section 3.1.2.

The electric force in this model stems from two sources: the Coulomb force resulting from the applied electric field when the net charge on the single particle is not zero, and the Coulomb force resulting from the neighbouring charged particle. In this modelling work, it is assumed that the net charge on the particle is zero; the electrical force hence equals the Coulomb force generated by the neighbouring particle only. Furthermore, the analytical expression for this Coulomb force between two particles in the transverse field and longitudinal field is presented by Equations 3-24, and 3-25. The force due to the transverse field is a repulsing force, while the force due to the longitudinal field is an attractive force. An illustration of these two forces is shown in Figure 3-8.

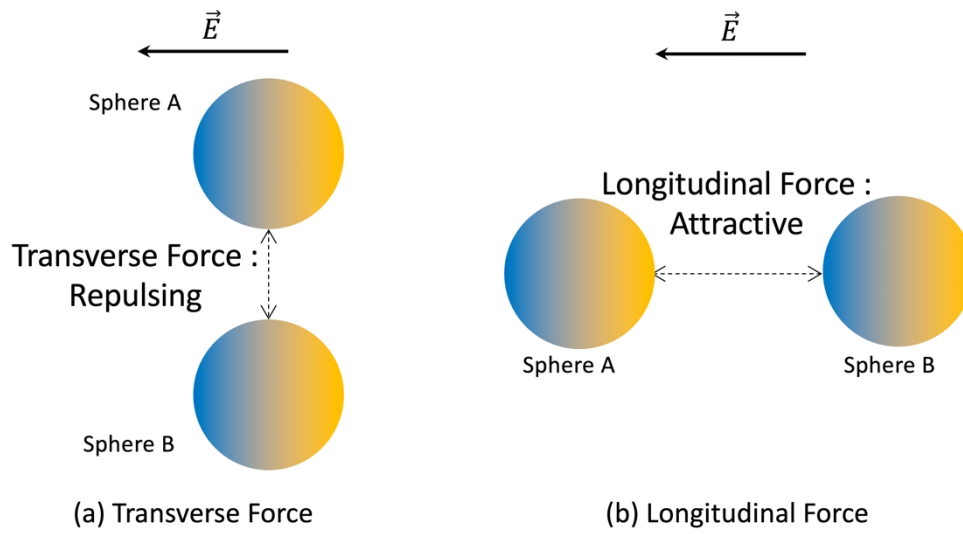


Figure 3-8 Illustration of Transverse Force and Longitudinal Force.

To solve Equations 3-24 and 3-25, they should be rewritten to enable programming. This programming was performed using Python 3.7 environment. Combination of Equations 3-19 to 3-23 gives a new equation for transverse  $F_{Trans}$ , and longitudinal  $F_{Longi}$  forces:

$$F_{Trans} =$$

$$\begin{aligned} & \frac{3P_a E\gamma}{2} \sum_{n=1}^{\infty} \left[ \frac{b^3 \left(R - \frac{1}{R}\right)^2 \left(R + \frac{1}{R}\right) \times (-\delta)^{2n-2}}{[b(R^n + R^{-n}) + a(R^{n-1} - R^{1-n})]^3} \right. \\ & \left. - \frac{b^3 \left(R - \frac{1}{R}\right)^3 [bn(R^n + R^{-n}) + a(n-1)(R^{n-1} + R^{1-n})] \times (-\delta)^{2n-2}}{[b(R^n + R^{-n}) + a(R^{n-1} - R^{1-n})]^4} \right] \\ & + \frac{3P_a E\gamma}{2} \sum_{n=1}^{\infty} \left[ \frac{b^3 \left(R - \frac{1}{R}\right)^2 \left(R + \frac{1}{R}\right) \times (-\delta)^{2n-1}}{r^3 (R^n - R^{-n})^3} \right. \\ & \left. - \frac{b^3 n \left(R - \frac{1}{R}\right)^3 \times (-\delta)^{2n-1}}{r^3 (R^n + R^{-n})^3} \right] \\ & + \frac{3P_b E\gamma}{2} \sum_{n=1}^{\infty} \left[ \frac{a^3 \left(R - \frac{1}{R}\right)^2 \left(R + \frac{1}{R}\right) \times (-\delta)^{2n-2}}{[a(R^n + R^{-n}) + b(R^{n-1} - R^{1-n})]^3} \right. \\ & \left. - \frac{a^3 \left(R - \frac{1}{R}\right)^3 [an(R^n + R^{-n}) + b(n-1)(R^{n-1} + R^{1-n})] \times (-\delta)^{2n-2}}{[a(R^n + R^{-n}) + b(R^{n-1} - R^{1-n})]^4} \right] \\ & + \frac{3P_b E\gamma}{2} \sum_{n=1}^{\infty} \left[ \frac{a^3 \left(R - \frac{1}{R}\right)^2 \left(R + \frac{1}{R}\right) \times (-\delta)^{2n-1}}{r^3 (R^n - R^{-n})^3} \right. \\ & \left. - \frac{a^3 n \left(R - \frac{1}{R}\right)^3 \times (-\delta)^{2n-1}}{r^3 (R^n + R^{-n})^3} \right] \end{aligned}$$

3-27

$F_{Longi} =$

$$\begin{aligned}
 & \frac{3P_a E \gamma}{2} \sum_{n=1}^{\infty} \left[ \frac{b^3 \left(R - \frac{1}{R}\right)^2 \left(R + \frac{1}{R}\right) \times (2\delta)^{2n-2}}{[b(R^n + R^{-n}) + a(R^{n-1} - R^{1-n})]^3} \right. \\
 & \left. - \frac{b^3 \left(R - \frac{1}{R}\right)^3 [bn(R^n + R^{-n}) + a(n-1)(R^{n-1} + R^{1-n})] \times (2\delta)^{2n-2}}{[b(R^n + R^{-n}) + a(R^{n-1} - R^{1-n})]^4} \right] \\
 & + \frac{3P_a E \gamma}{2} \sum_{n=1}^{\infty} \left[ \frac{b^3 \left(R - \frac{1}{R}\right)^2 \left(R + \frac{1}{R}\right) \times (2\delta)^{2n-1}}{r^3 (R^n - R^{-n})^3} - \frac{b^3 n \left(R - \frac{1}{R}\right)^3 \times (2\delta)^{2n-1}}{r^3 (R^n + R^{-n})^3} \right] \quad 3-28 \\
 & + \frac{3P_b E \gamma}{2} \sum_{n=1}^{\infty} \left[ \frac{a^3 \left(R - \frac{1}{R}\right)^2 \left(R + \frac{1}{R}\right) \times (2\delta)^{2n-2}}{[a(R^n + R^{-n}) + b(R^{n-1} - R^{1-n})]^3} \right. \\
 & \left. - \frac{a^3 \left(R - \frac{1}{R}\right)^3 [an(R^n + R^{-n}) + b(n-1)(R^{n-1} + R^{1-n})] \times (2\delta)^{2n-2}}{[a(R^n + R^{-n}) + b(R^{n-1} - R^{1-n})]^4} \right] \\
 & + \frac{3P_b E \gamma}{2} \sum_{n=1}^{\infty} \left[ \frac{a^3 \left(R - \frac{1}{R}\right)^2 \left(R + \frac{1}{R}\right) \times (2\delta)^{2n-1}}{r^3 (R^n - R^{-n})^3} - \frac{a^3 n \left(R - \frac{1}{R}\right)^3 \times (2\delta)^{2n-1}}{r^3 (R^n + R^{-n})^3} \right]
 \end{aligned}$$

where,

$$R = \frac{r^2 - a^2 - b^2 + \sqrt{(a+b-r)(a+b+r)(a-b+r)(a-b-r)}}{2ab} \quad 3-29$$

$$\gamma = \frac{d\alpha}{dr} = \frac{2r}{\sqrt{(a+b-r)(a+b+r)(a-b+r)(a-b-r)}} \quad 3-30$$

A specific distance range for the particle separation is required to keep the computational accuracy: the longer separation leads to smaller contribution to the Coulomb force from another particle in the complete expression for external force.

On the other hand, the shorter separation between two particles increases the modelling time significantly. In addition, the surface charge distribution can be disrupted significantly by the shorter distance between two particles, decreasing the accuracy of computational procedure. Therefore, separation  $r$  used in this work is fixed at  $1.2(a + b)$  and  $2(a + b)$ , the intervals at which the DID model is applicable. Correspondingly, term  $n$  equals 2 in these simulations.

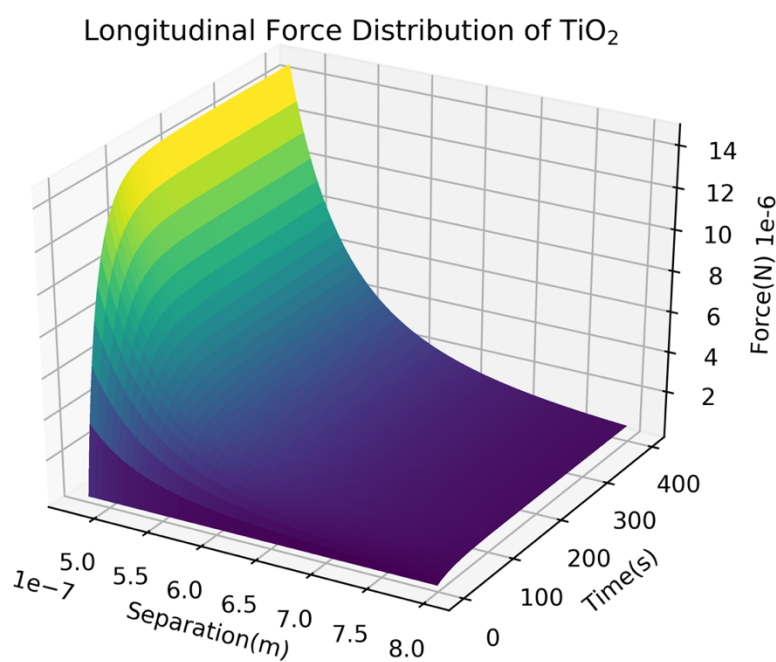


Figure 3-9 Longitudinal Force between two TiO<sub>2</sub> particles in esters; the particle radius is 200 nm, the electric field strength is 10<sup>6</sup>V/m.

Figure 3-9 shows the obtained longitudinal force between two  $\text{TiO}_2$  particles immersed in the ester fluid, with a radius of 200 nm. The applied field strength is  $10^6 \text{V/m}$ , the field is applied for 400 s.

The force increases initially and then, after  $\sim 200$  s, remains quasi-constant, which agrees with the relaxation time obtained from the dipole moment simulation based on a single particle (as shown in Table 3-2). This is not surprising as the dipole moment of the particle includes only the time variable affecting the DID induced force. It can also be found from Figure 3-9 that the force increases when the particles approach each other, and this increase is particularly significant for the shorter separation between the particles.

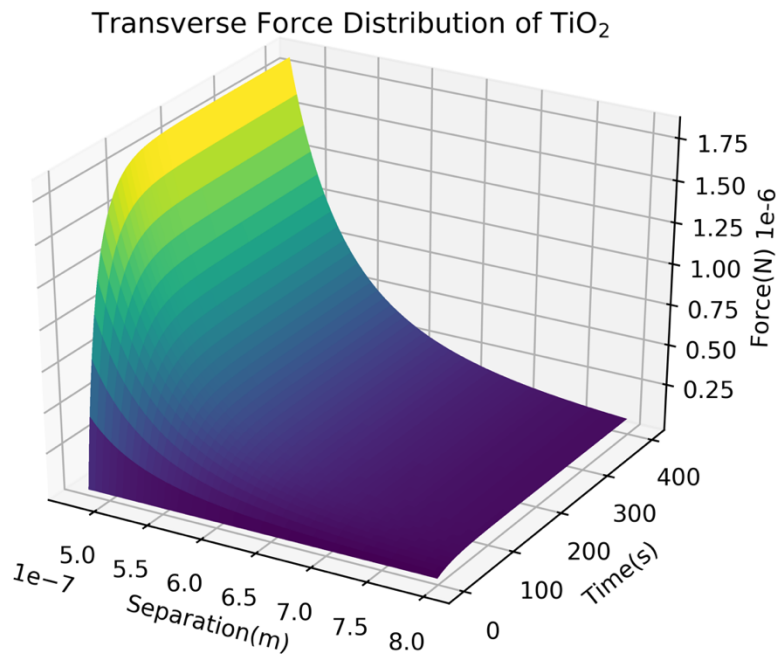


Figure 3-10 Transverse Force between two  $\text{TiO}_2$  particles in esters. The particle radius is 200 nm, the electric field strength is  $10^6 \text{V/m}$ .

Comparing with the results presented in Figure 3-9, the transverse force given in Figure 3-10 retains the same characteristics in terms of the force's functional behaviour with both time and separation. However, the transverse force is approximately one order of magnitude lower than the longitudinal force under the same conditions, indicating the dominant role of the longitudinal force in the Coulomb force affecting the dynamic of the particles. As an attraction force, the longitudinal force can potentially result in aggregation of the particles, which is undesirable and will damage the stability of the nanofluids. Therefore, the following analysis was conducted using the longitudinal force between two particles.

As presented by Equations 3-27 to 3-30, the variables affecting the force include the separation between the particles, the radius of the particle, external electric field (applying time/field strength) and the particle/fluids parameters (relative permittivity and electric conductivity). Thus, only a single variable was considered an independent parameter in each simulation in the present modelling work. The results of each simulation are shown as 2D graphs in the followings.

The first variable studied is the separation between two particles: the radius of each particle is 200 nm, the electric field strength is  $10^6 V/m$ , simulation time was selected as 400 s, which means the force has reached its quasi-steady state, as shown in Figure 3-9.

Figure 3-11 illustrates the longitudinal forces acting between two  $TiO_2$  particles in both esters and the mineral oil at 400<sup>th</sup> s after application of the electric field. The force acting between the  $TiO_2$  particles in ester fluid is  $\sim 7$  times greater than the force acting between these two particles in the mineral oil, which is caused by the higher surface charge on each particle in the ester compared with the particle in the mineral oil.

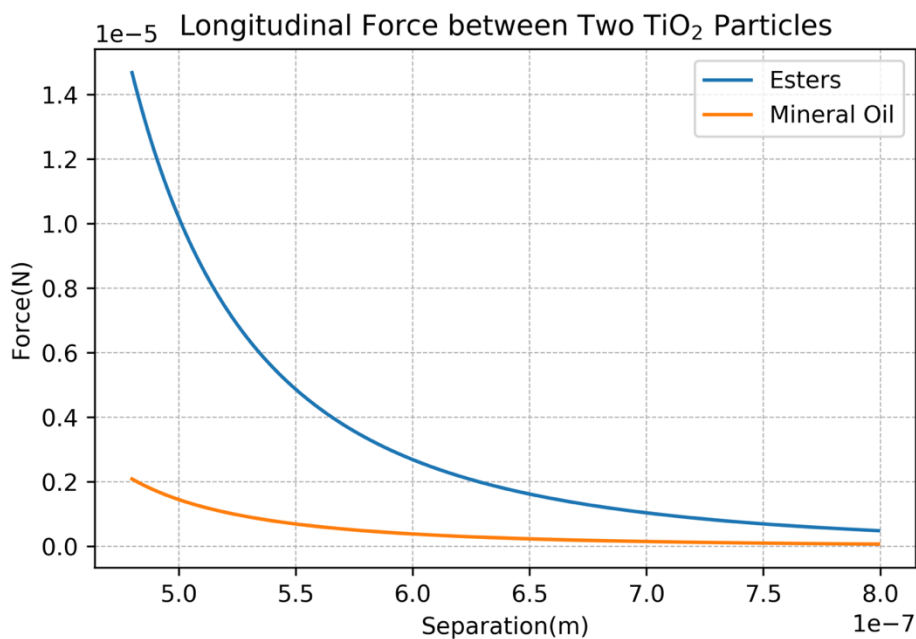


Figure 3-11 Force acting on TiO<sub>2</sub> particle in two liquids at the 400<sup>th</sup> second after application of the field, the radius of the particle is 200 nm, the electric field strength is  $10^6 V/m$ .

The force between two BN particles was also obtained and shown in Figure 3-12. The particle radius and the electric field strength remain the same as in the modelling of TiO<sub>2</sub> particles: 200 nm and  $10^6 V/m$ . However, the time selected for the BN particle is 4000 s after application of the electric field. According to the results shown in Figure 3-7, the relaxation time which is required to reach its quasi-steady state is much longer for the BN particles than for other particles.

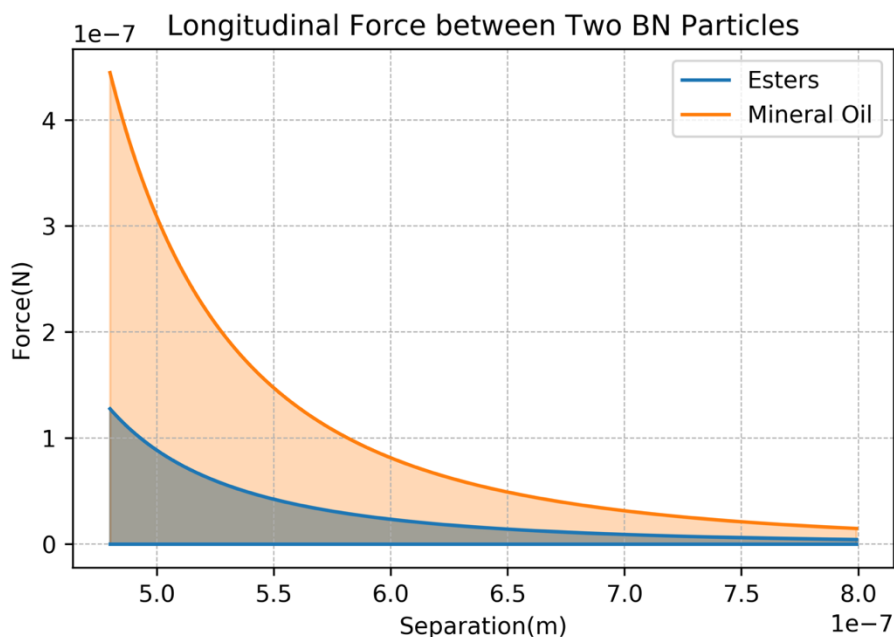


Figure 3-12 Force acting between two BN particles in esters and mineral oils at the 4000<sup>th</sup> s after application of the field. The radius of the two BN particle is 200 nm, the magnitude of the electric field is  $10^6 V/m$ . The blue/orange region indicates the surface charge variations due to the electrical conductivity variations of the BN particles. The upper line of the blue/orange region corresponds to the electrical conductivity of  $10^{-13} S/m$  [101].

Due to variations in the electric conductivity of the BN particles, Figure 3-12 also presents the obtained force in regions, which corresponds to different electrical conductivities of the BN particles: the upper line of the region corresponds to the maximum force obtained with the electrical conductivity of  $10^{-13} S/m$  for the BN particles.

It can be seen that the main difference between Figure 3-11, and Figure 3-12 is the magnitude of the obtained force: the maximum value of the longitudinal force acting between two BN particles is approximately two orders of magnitude lower than the force acting between two  $TiO_2$  particles under the same condition. Also, the results in Figure 3-12 indicates that the force acting between two BN particles in mineral oils could be higher than that in ester liquids.

The second variable simulated in this section is the particle's radius: the modelling of the longitudinal forces was conducted with different particle radiuses but with the same particle separation distance and the same electric field strength.

Before the further simulation, it must be pointed out that particle separation refers to the centre-centre separation, which is the distance between the centres of two particles. However, the purpose of using various particle radiuses is to investigate the effect of the particles dimensions on the Coulomb force acting between them. Therefore, the separation between two particles in the present simulation is defined as the surface-surface separation, i.e., the distance between the surfaces of these two particles. In the following simulations, the surface-surface separation is fixed at 150 nm.

Figure 3-13 shows the modelling results for the  $\text{TiO}_2$  particles: the force acting between two  $\text{TiO}_2$  particles with the radius ranging from 100 nm to 300 nm. It can be concluded that for a given surface-surface separation, the force acting between two particles increases with the particle's size, which is due to an increase in the total charge on the particle.

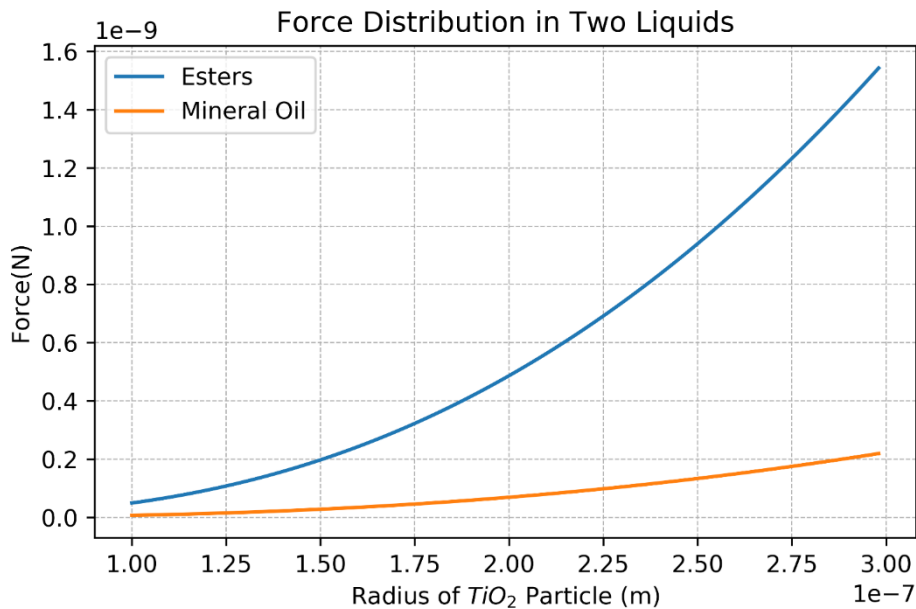


Figure 3-13 Force acting between two  $\text{TiO}_2$  particles with different radiuses,  $t = 400$  s, the surface-surface separation is 150 nm, the electric field strength is  $10^6 \text{V/m}$ .

Figure 3-14 provides the force acting between two BN particles with their radiuses ranging from 100 nm to 500 nm. This force has the same functional behaviour as the force presented in Figure 3-13, i.e., large particles induce larger longitudinal forces between them.

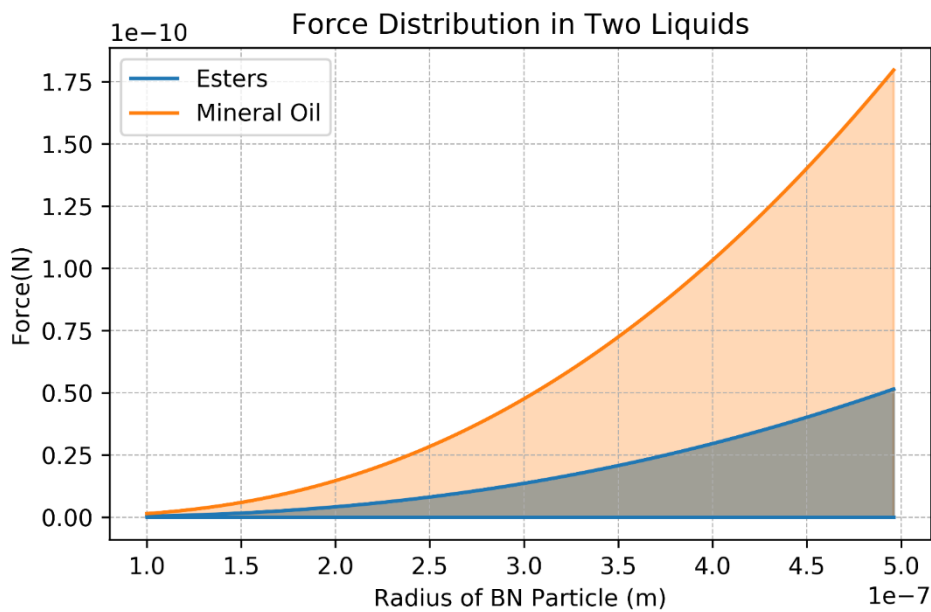


Figure 3-14 Force acting between two BN particles with different radiuses,  $t = 4000$  s, the surface-surface separation is 150 nm, the electric field strength is  $10^6 V/m$ . The blue/orange region indicates the surface charge variations due to the electrical conductivity variations of the BN particles. The upper line of the blue/orange region corresponds to the electrical conductivity of  $10^{-13} S/m$  [101].

According to the modelling conducted in this section using particles with various radiuses, it can be stated that the attraction force acting between two  $TiO_2$  particles is always higher than the force acting between two BN particles in both liquids.

### 3.3 Summary

In this chapter, the analytical model which provides the surface charge distribution and corresponding Coulomb force acting between two particles has been developed. This model was used to investigate the forces acting on different particles immersed in the esters and the mineral oil. The results of this systematic investigation are presented in this chapter.

Based on the Maxwell-Wagner relaxation theory, an analytical model of the charge accumulation process at the particle-liquid interface has been developed. This model provides the surface charge distribution on the individual particle in the external electric field.

However, it should be noted that this model was developed based on the vital assumption: there is no free space charge in the vicinity of these particles. Thus, the positive and negative charges have the same surface density and distributed identically in each particle.

Using the surface charge distribution and the assumption mentioned above, the single particle model has been used to obtain the Coulomb force acting between two particles immersed in a liquid stressed with the external electric field. The longitudinal force was obtained: this force can potentially cause the aggregation of the particles in the liquid. The obtained results allow for investigation of the factors affecting the longitudinal force between two particles: the radius of particles, the separation between two particles, and most importantly, the physical parameters of the particles and hosting liquids. It was found that the longitudinal force acting between two TiO<sub>2</sub> particles is higher than the force acting between two BN particles in both esters and mineral oils.

As introduced in Section 3.1.2, the forces that govern the particles' behaviour in the liquid can be divided into four main categories: gravity, buoyancy, drag force, and Coulomb force. The latter two forces play the dominant role when the hosting liquid is stressed with a high electric field. The analysis of the Coulomb force (longitudinal force) presented in this chapter will be used to explain the experimental results provided in Chapter 7.

# Chapter 4 EXPERIMENTAL AND DATA ANALYSIS

## METHODOLOGIES

---

This chapter presents the methodology of the development and characterisation of nanofluids used in the present work and the rationale for selecting specific dielectric liquids and nanoparticles for these nanofluids.

This chapter also presents the experimental systems used in the present work for measuring the mobility of charge carriers, including the test cells, low voltage and high voltage power supplies, diagnostic, and control devices. The arrangement and general description of the experimental set-ups are presented.

## **4.1 Nanofluids: Development and Particle Size**

### **Examination**

This main research objective of the present work is to investigate the particle's dynamic behaviour in nanofluids and to obtain the mobility of charge carriers in the nanofluids. This knowledge and information will help in further understanding of the dielectric properties of nanofluids, making contribution to their wider use in practical high voltage power and pulsed power applications. This section presents the methodology used to develop nanofluids, starting with selection of solid particles, their treatment and characterisation, and ending with measurements of particle size distribution in the developed nanofluids.

#### **4.1.1 Properties of the Raw Materials**

Two types of particles were selected for development of nanofluids: Titanium Dioxide ( $\text{TiO}_2$ ) and Boron Nitride (BN) particles. As can be seen from Table 3-1, there is a significant difference between relative permittivities and electric conductivities of these two types of particles. Thus, it may be expected that these particles will behave differently in the dielectric fluids when stressed with the external electric field.

The hosting liquids were selected to represent three different categories of insulating liquids which are used in power and pulsed power applications, i.e., synthetic ester liquids, natural ester liquids and traditional mineral oil.

MIDEL 7131, which is selected to represent the Synthetic Esters, was developed in the 1970s and is currently manufactured by M&I Materials Ltd. This fluid is used as a liquid insulator in power transformers and has significant advantages over traditional mineral oils – it has a high fire point, thus providing better fire safety. It is an environmentally friendly, biodegradable liquid.

MIDEL eN 1204, made from rapeseed and canola, is also manufactured by M&I Materials Ltd. It is selected to represent the Natural Esters in this research. As a recently developed insulation fluid, MIDEL eN 1204 is currently available on the market and designed to be used as a liquid insulator in high voltage systems.

Also, Shell Diala B transformer oil, which satisfies the traditional Mineral Oil grade requirements, was used to develop nanofluids to compare the EHD motion of particles and the mobility of charge carriers in the ester-based and mineral-oil-based nanofluids [105].

The basic characteristics of the pure liquids used in this study are provided in Table 4-1 [105] [106] [107].

Table 4-1 Physical Parameters of the ester liquids and mineral oil

	<b>MIDEL 7131 (SE)</b>	<b>MIDEL eN 1204 (NE)</b>	<b>Shell Diala B (MO)</b>
<b>Relative Permittivity</b>	~ 3.2	~ 3.2	~ 2.2
<b>Electric Conductivity (S/m<sup>2</sup>)</b>	$4.5 \cdot 10^{-12}$	$5 \cdot 10^{-12}$	$7.5 \cdot 10^{-14}$
<b>Density at 20 °C (g/mL)</b>	0.97	0.92	0.89
<b>Viscosity at 20 °C (mm<sup>2</sup>/sec)</b>	70	85	26

#### 4.1.2 Development of Nanofluids

The surfaces of nanoparticles should be modified to improve the suspension stability before dispersing these particles into the pure dielectric liquids. In this research, the oleic acid was used as a surfactant for the surface treatment according to the method described in [108]. The details of this treatment are described below.

- 1 g of powder consisting of TiO<sub>2</sub> or BN nanoparticles and 100 mL of ethanol were well mixed during 15 mins by magnetic stirring and then kept in a water bath at 60 °C for 1 hour.
- After this treatment, 0.25 g oleic acid was added to the mixture. To ensure the particles are well covered with the oleic acid, the mixtures were stirred for 15 min by the magnetic stirrer. After that, the mixture was placed in an ultrasonic bath to assist the process of covering particle' surfaces with the oleic acid.
- After 2 hours of sonication, the mixtures were washed with ethanol three times in the centrifuge to remove the redundant oleic acid. Finally, the liquids were placed in an oven for 24 hours at 60 °C. After that, grinding procedure was used to obtain powders consisting of the surface modified TiO<sub>2</sub> or BN nanoparticles.

The nanofluids were produced using these surface modified nanoparticles: the nanoparticles were mixed with the hosting liquids using the magnetic stirring and sonication processes. Each process which lasted for 15 min was repeated four times. During each cycle, the sample was placed in cool water for 20 – 30 min to avoid overheating due to the sonication.

In this research project, nanofluids with two concentrations of TiO<sub>2</sub> or BN particles were prepared: 0.005% and 0.1% by weight (b/w). The nanofluids with 0.005% b/w concentration were investigated in several papers, and it was reported that the nanofluids with this concentration could provide an enhanced dielectric strength [21]. The Nanofluid with 0.1% b/w concentration was selected to demonstrate the EHD behaviour and to obtain the mobility of charge carriers in the nanofluid with a significantly higher concentration of particles, as compared with the nanofluid with the 0.005% b/w concentration.

Before conducting each mobility measurement, the nanofluid samples were treated with ultrasound again to avoid the aggregation of particles in these samples during the storage.

### 4.1.3 Particle Size Distribution in Nanofluids

It is important to establish the actual size distribution of the particles in the developed nanofluids. A Malvern Zetasizer NANO ZSP from Malvern Panalytical Ltd. was used to obtain the particle size distribution in the prepared nanofluids. The principle of operations of the Malvern Zetasizer is based on the Dynamic Light Scattering (DLS) method, which is discussed in brief here.

In the case of colloids, the particles dispersed in liquid are subject to the Brownian motion. The diffusion of spherical particles in fluids in the conditions of low Reynolds numbers (which are typically less than one) can be quantitatively described by the Stokes-Einstein equation:

$$D = \frac{k_B T}{6\pi\eta D_H} \quad 4-1$$

where  $D$  is the diffusion coefficient,  $k_B$  is the Boltzmann's constant,  $T$  is the absolute temperature,  $\eta$  is the fluid viscosity, and  $D_H$  is the hydrodynamic radius of the spherical particle. It should be noted that the Stokes-Einstein equation includes the hydrodynamic radius which is the radius of the particle and surrounding fluid which moves together with the particle. In the present study, the hydrodynamic radius of particle includes a linear dimension of the particle, surfactant molecules attached to the surface of the particle, and liquid molecules attached to the particle's surface/surfactant molecules.

When a sample of colloidal fluid is subjected to the laser beam, the scattering of the beam caused by the dispersed particles is recorded by the detectors. As the particles dispersed in the liquid are in continuous movement due to the Brownian motion, the intensity of the scattered light is affected by the particles' motion during the measurement: for smaller particles, more intensive motion can induce fast fluctuations in the intensity of the scattered light; while larger particles which move slower, lead to a less intensive fluctuations in the intensity of scattered light. With the help of the autocorrelation function, the intensities of scattered light can be transformed into diffusion constant  $D$ , used in the Stokes-Einstein

equation (Equation 4-1) and the particle size distributions can then be obtained. Figure 4-1 illustrates the basic principle of the DLS methodology.

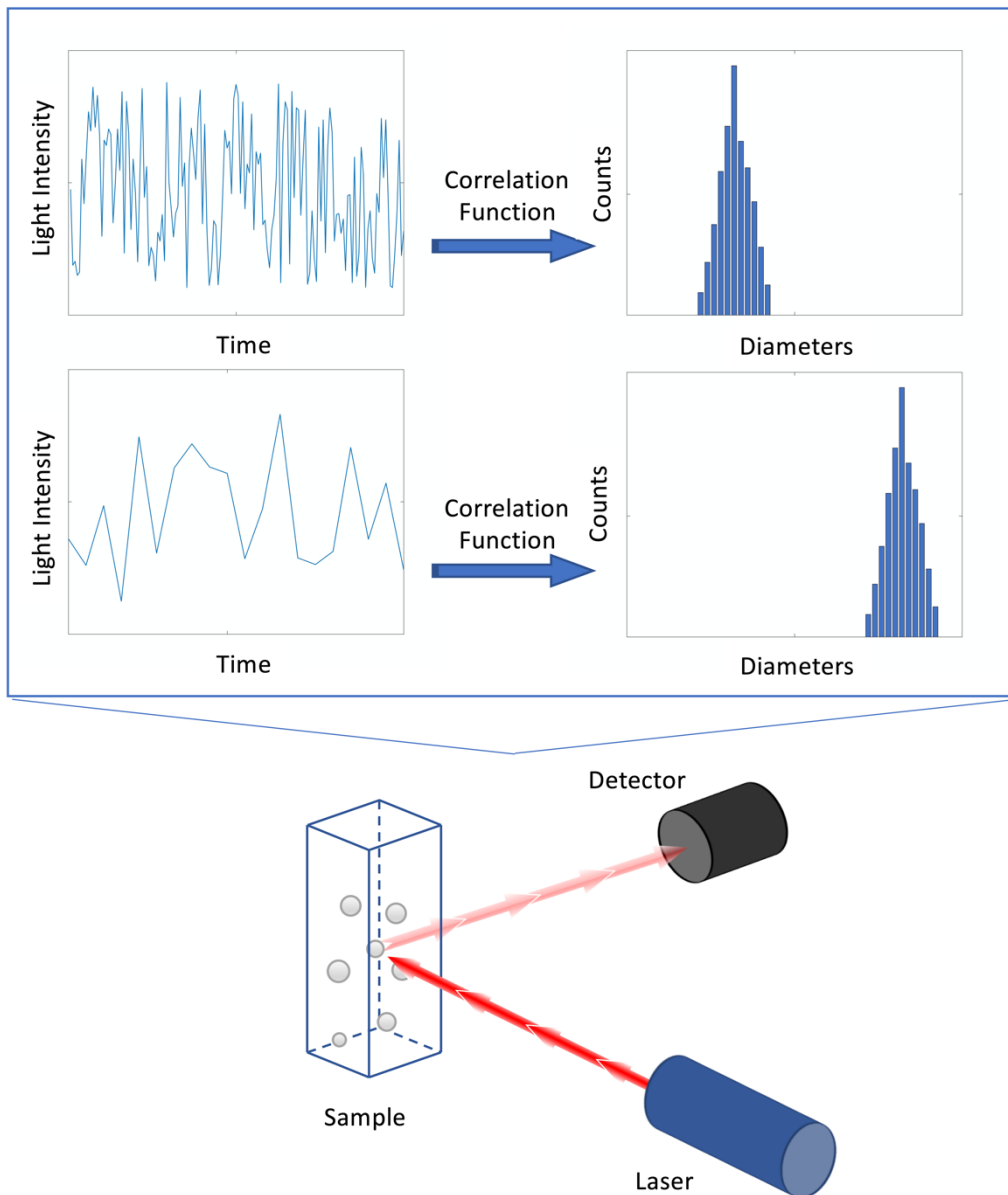


Figure 4-1 Basic Principles of the DLS

The DLS method requires information on the refractive index and absorption coefficient of particles in the colloidal solutions, these parameters for the fluids used in this study are listed in Table 4-2 and Table 4-3:

Table 4-2 Relative Index of the Liquids used in this study (Data source: [109][110])

	<b>MIDEL 7131</b>	<b>MIDEL eN1204</b>	<b>Shell Diala B</b>
<b>Refractive Index at 20 °C</b>	1.455	1.475	1.48

Table 4-3 Refractive Index and Absorption Coefficient of Particles (Data source: [111][112][113][114][115][116])

	<b>TiO<sub>2</sub></b>	<b>BN</b>
<b>Refractive Index</b>	2.42	1.65
<b>Absorption Coefficient</b>	$6 \cdot 10^{-4}$	$6 \cdot 10^{-4}$

Although this method for measurement of particles with dimensions ranging from 0.1 nm to 10  $\mu\text{m}$ , the DLS method has some limitations. Two of them are particularly relevant to the presented study: the sedimentation process and the multiple light scattering. Stability of the MO based nanofluids is significantly weaker than stability the ester based nanofluids s due to the low viscosity of the MO. The second limitation is multiple light scattering (light beam is

scattered by multiple particles), which typically affects highly concentrated samples of nanofluids. Due to these two reasons, to measure the particle size distribution in the nanofluids with 0.1% b/w concentration of particles, these samples were diluted before the DLS measurements.

Furthermore, to prevent sedimentation in the samples, all samples were treated in the ultrasonic bath before the DLS tests. The DLS tests were repeated five times for each sample, and three individual samples of each nanofluid were used.

Figure 4-2 presents the averaged size distribution of the TiO<sub>2</sub> particles in the SE, the NE, and the MO based nanofluids. Figure 4-3 presents the averaged size distribution of the BN particles in these three liquids. The averaged results were calculated from the three individual samples.

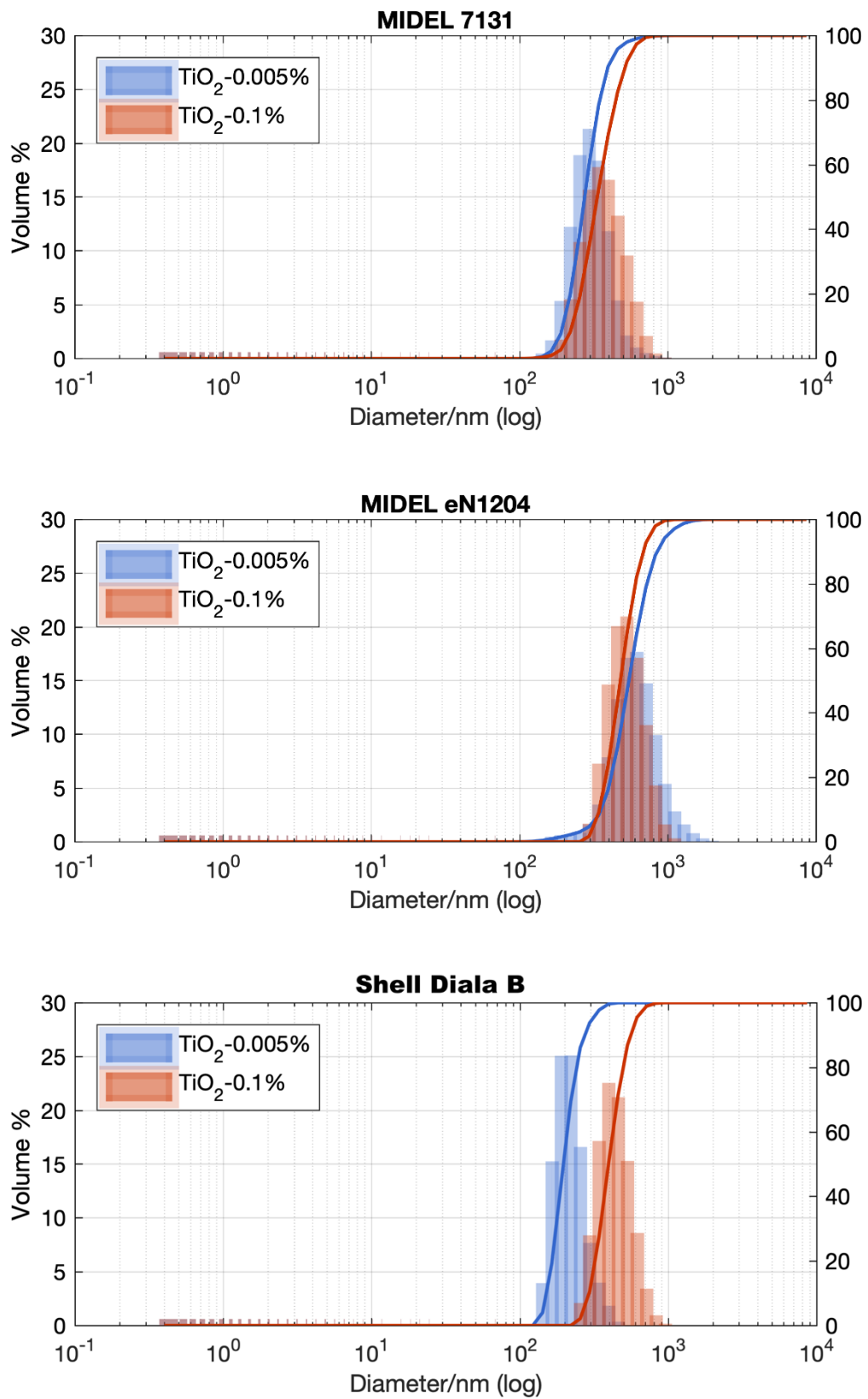


Figure 4-2 Size Distribution of TiO<sub>2</sub> particles in the nanofluids used in the present study

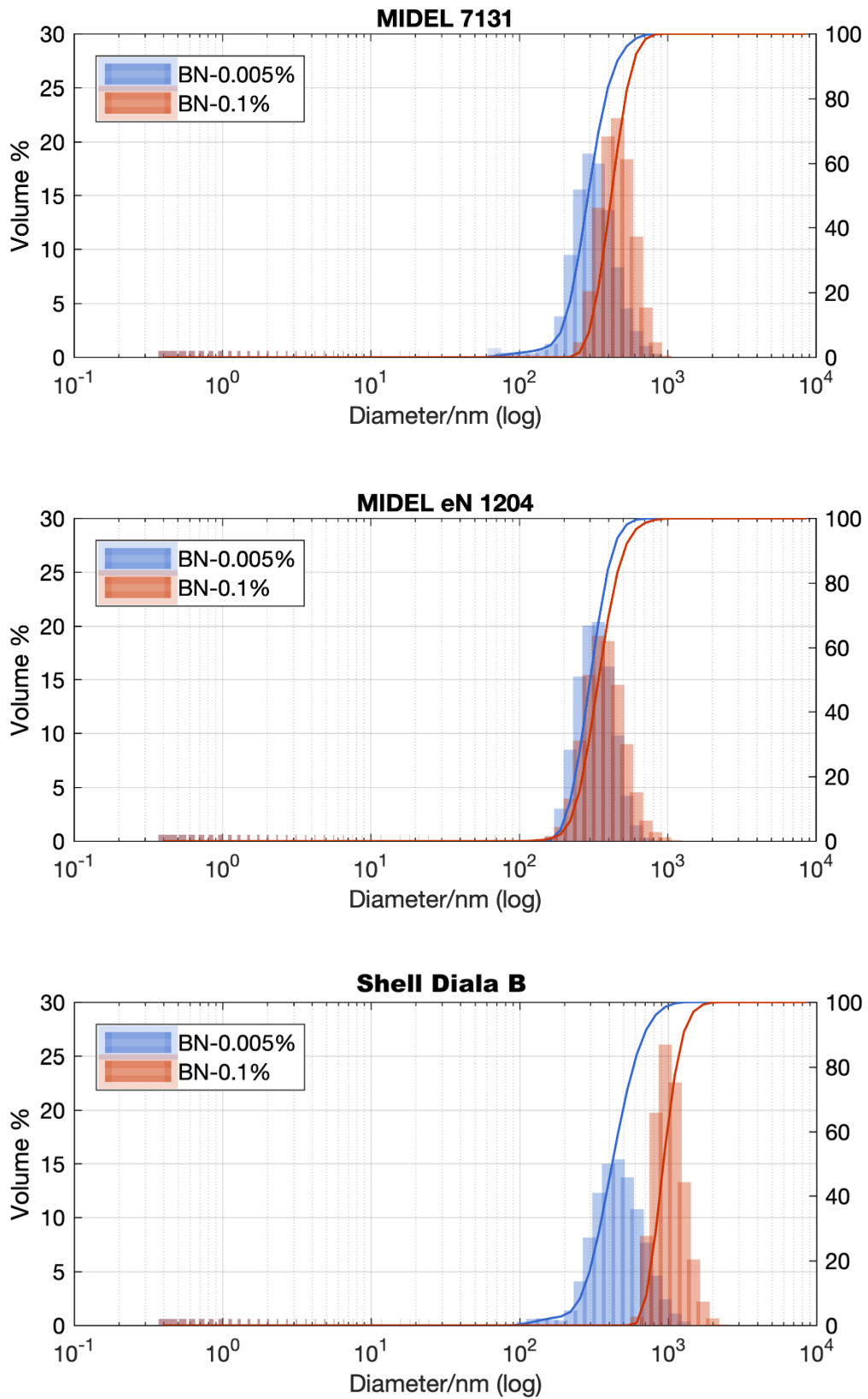


Figure 4-3 Size Distribution of BN particles in the nanofluids used in the present study

The height of each vertical bar in Figure 4-2 and Figure 4-3 represents the portion (indicated by the left y-axis) of the particles with the corresponding diameter range. Solid curves represent the cumulative size distribution of the particles in the prepared nanofluids.

It was found that typically, particles have larger dimensions in the nanofluids with 0.1% b/w concentration of the particles compared with the nanofluids with 0.005% b/w concentration of the particles (for nanofluids prepared using the same particles and hosting liquids). This finding shows the negative effects of the particle concentration on the particle dispersion. Furthermore, for the nanofluids prepared using the same particles but different hosting liquids, the overlap between particle distribution peaks representing two nanofluids with different concentrations increases with the viscosity of the hosting fluids. Such a trend indicates that the viscosity of the hosting liquid plays an important role in the particle dispersion.

The average size (diameter) of the particles in the nanofluids used in the present study is given in Table 4-4. Each value is the average value of three independent measurements (fresh samples were used for each measurement). The uncertainty is the standard deviation in the average diameter of particles.

Table 4-4 Average Diameter of Particles

Type of Particles	Concentration, b/w	Average diameter (nm)		
		SE	NE	MO
<b>TiO<sub>2</sub></b>	0.005%	293.03±38.79	539.02±55.44	221.05±39.47
	0.1%	359.30±60.64	513.56±60.52	441.97±76.78
<b>BN</b>	0.005%	332.06±42.17	337.16±27.36	487.10±74.24
	0.1%	465.23±42.24	389.15±52.46	1042.30±142.01

It is shown in Table 4-4 that the average diameter of the dispersed particles is in the range of ~ (200 - 550) nm except for the BN particles in the mineral oil (the nanofluid with 0.1% b/w concentration of the BN particles). However, as indicated by Equation 4-1, the particle's radius obtained by the Malvern Zetasizer is the hydrodynamic radius, which is larger than the physical radius of the particle. Therefore, all other samples of the developed nanofluids can be considered as nanofluids with an average radius of particles of ~ 100 nm.

## **4.2 Design of Experimental System: Instruments**

The main elements of the experiment system include the power supply(ies), test cell(s), current and voltage diagnostic devices, video monitoring system. The power supply(ies) and current/voltage diagnostic systems are presented and discussed in this section, while the test cells used in this study with corresponding experimental arrangements are discussed in Section 4.3.

### **4.2.1 Power Supplies and Control System**

This research project used two different power sources: the AU series HV DC power supply for generation high voltage with magnitude of more than 1 kV. The output of the Keithley 617 electrometer was used to generate the voltages within  $\pm 100$  V range.

The AU-60 series HV power supply from Matsusada Precision Inc. produces DC voltage ranging from 0 kV to 60 kV. Two power suppliers: the AU-60P5, and the AU-60N5, were used in this research to generate HV DC voltage of positive polarity and negative polarity, respectively.

To ensure the safety and synchronisation between the power supply(ies) and the diagnostic system, the power supply(ies) was remotely controlled by the LabVIEW software via a DAQ card from National Instruments: the digital output ports of the DAQ card were connected to the control pins of the power supply used in each specific test, as illustrated in Figure 4-4.

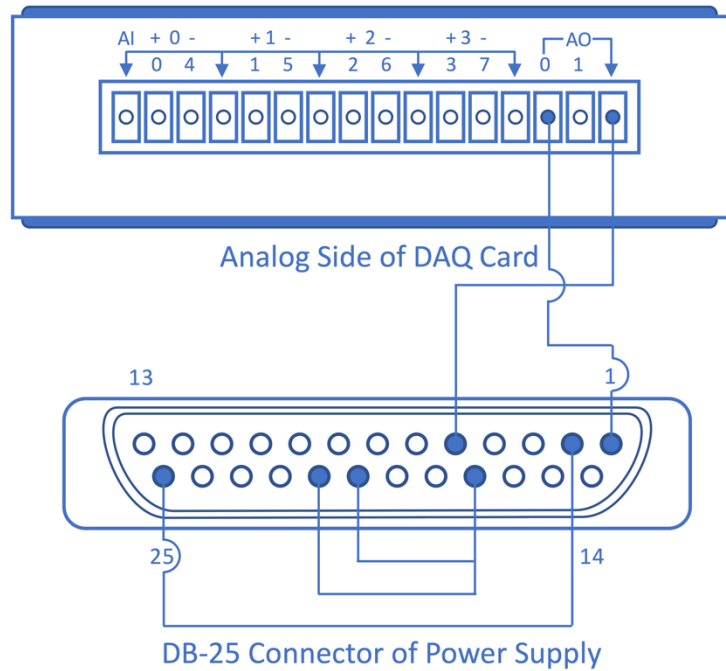


Figure 4-4 Pin Connection between DAQ Card and Power Supply

However, the AU series power supplies are not capable of producing stable output voltage with magnitude below 1 kV. Therefore, to generate DC voltage with magnitude  $< 1\text{ kV}$  (few hundreds of volts), the Keithley 617 electrometer was used.

The Keithley 617 electrometer can produce DC voltage ranging from  $-102\text{ V}$  to  $102\text{ V}$  with  $50\text{ mV}$  steps. The Keithley 617 electrometer was controlled remotely by the LabView software through the GPIB card produced by Prologix, LLC. Under this arrangement, the Keithley 617 electrometer can be used to suddenly change the polarity of in the output voltage, generating a voltage signal with reverse polarity. This function enables the reverse-polarity method to be utilised in obtaining the mobility of charge carriers in the dielectric liquids.

#### **4.2.2 Experimental Design: Electric Current Measurements**

The main experimental parameter, obtained by both, the ToF method and the SCLC method, is the electric current passing through the liquids. The magnitude of the current in the present study was typically within the pA - nA range. Such low magnitude currents were measured using two methods: the direct current measurements by the Keithley 6514 electrometer and current measurements facilitated by the current viewing resistor (current shunt).

In the direct current tests, the Keithley 6514 electrometer was used as a virtual ground to measure the current directly: the electrometer was remotely controlled using a self-developed program in the LabVIEW environment via an RS232/USB interface cable, and the current data was saved in the computer by the LabVIEW software.

The SCLC method requires a highly divergent electric field developed in the test cell with the point-plane electrode configuration, the current in this case was obtained using the current viewing resistor. The magnitude of current passing through the shunt resistor was in the nA range. Thus, the voltage drop across this resistor was amplified using the INA 114 operational amplifier (Texas Instrument Inc). The amplified voltage signal was monitored using the digitising oscilloscope, Tektronix TBS 1102B. Figure 4-5 illustrates the amplifier's pin configuration and the relevant circuit connections. The voltage waveforms registered by the oscilloscope were stored as CSV files, enabling accurate measurements of the amplified voltage (current through the current viewing resistor).

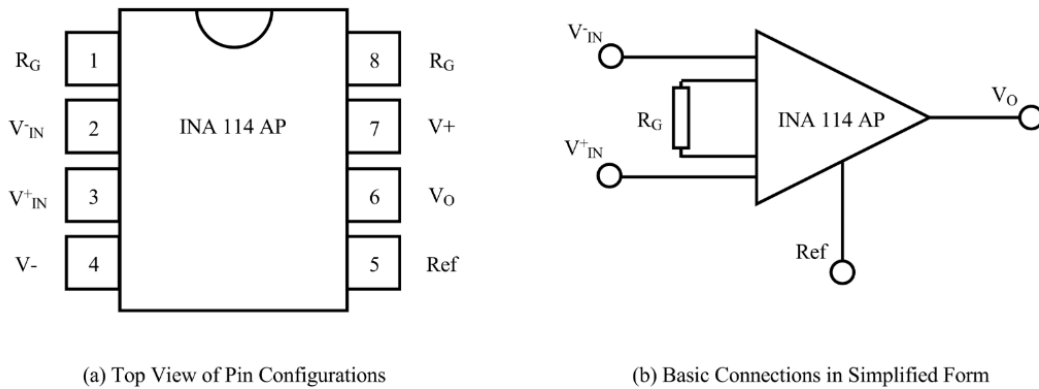


Figure 4-5 Schematic Diagrams of the INA 114 AP Amplifier

To ensure the reliability of the current measurements, the practical gain of the amplifier was obtained using the portable calibration system, Fluke 515A. This voltage source produces a DC voltage signal in the  $\mu V$  range. To calibrate the operational amplifier, the DC voltage output from the Fluke 515A voltage source was amplified by the operational amplifier and registered by the digitising oscilloscope. By increasing the input voltage from 0 to 1 mV in a  $50 \mu V$  step, the calibration curve (the output voltage as a function of the input voltage) was obtained, and the practical gain of the amplifier was calculated by fitting a straight line to the measured data using the least-square fitting method. The calibration tests were conducted in triplicate, and the results are shown in Figure 4-6, which presents the obtained input-output voltage curves and the fitting lines.

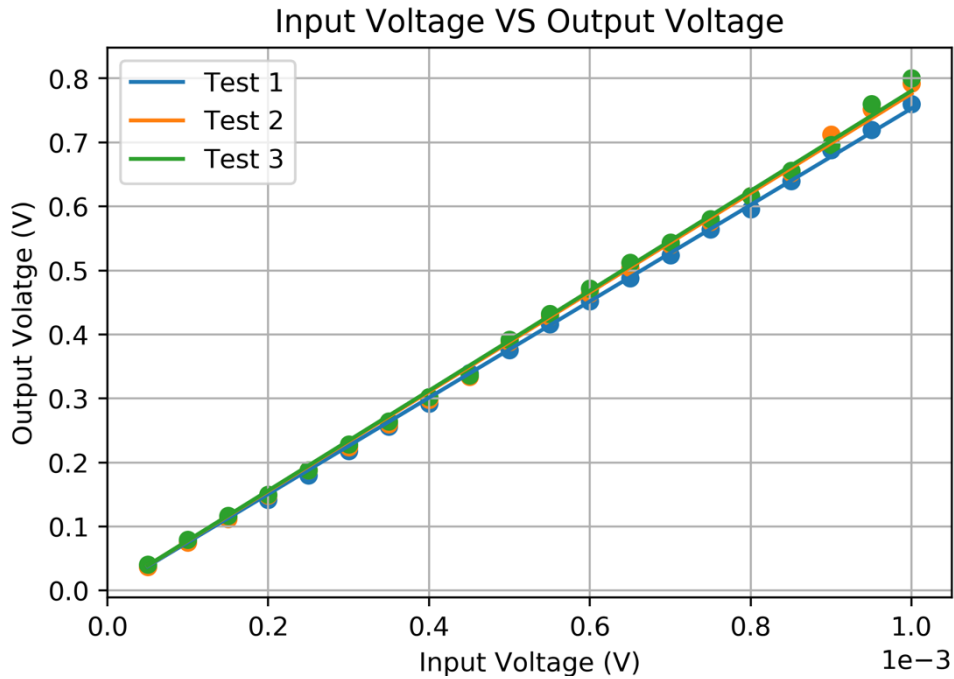


Figure 4-6 Calibration of the operational amplifier. The output voltage as a function of input voltage (solid symbols); solid lines are fitting lines obtained by the least-square fitting method; three solid lines indicate the experiment data obtained from three individual tests.

The obtained practical gain of the operational amplifier is  $770.05 \pm 30.04$ .

### 4.2.3 Experimental Design: Optical Instruments

The EHD motion of particles in nanofluids stressed with the electric field was investigated using a stand-alone CCD camera and a CCD camera attached to the optical microscope. The matrix used in the CCD camera has a dimension of 1/2.3 inch and it is a 14-megapixel matrix (maximum, long time exposure regime). Thus, two optical approaches for characterisation of the EHD particle motion were used.

In the first approach, a CCD camera was placed above the test cell, and the motion of particles and fluid was observed directly. An LED light source was located under the test cell to ensure

sufficient brightness, which allows for observations of the movement of particles in the test cell.

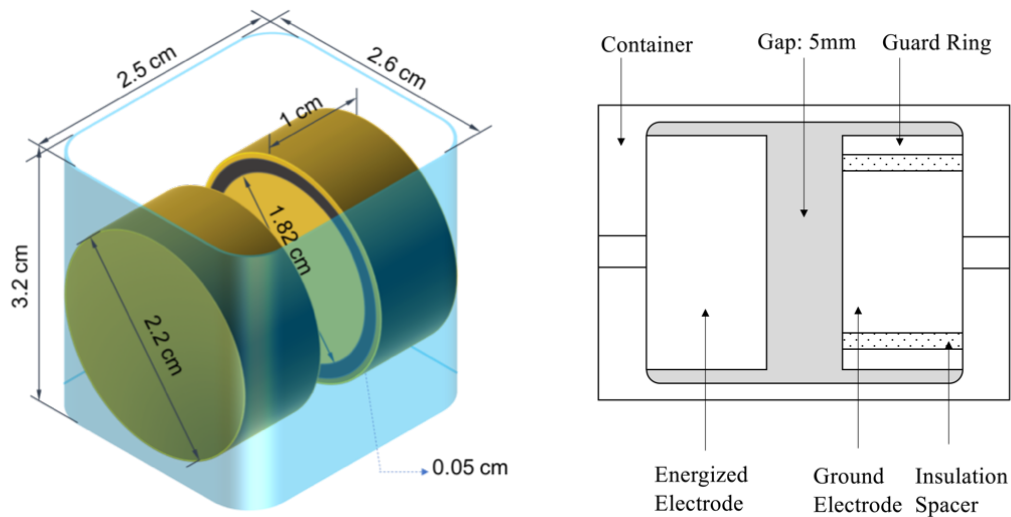
In the second approach, a CCD camera was attached to the microscope, which provided desirable magnification. However, only a specific, restricted area in the test cell was observed. It can be operated at a lower resolution of 1280x720 but at the 720 frames per second which help to record the movement of particles/fluid. The M1000-D optical microscope (Swift Optical Instruments) was equipped with 4xD, 10xD, 40xD, and 100xD objectives. Due to the limitation of the focusing length, only the 4xD objective was used for the micro-scale observations. By presenting the final image on a 17-inch computer monitor, the total magnification of 156.4 times ( $17 \times 2.3 \times 4$ ) was achieved. Two areas were investigated under the microscope: the area close to the electrodes and the area in the centre of the test cell, which allowed for detailed visualisations of the movement and collective behaviour of the suspended particles.

## **4.3 Test Cells**

Four test cells were used in the present project, which underpinned different experimental methodologies. Two custom-built test cells were used to investigate the electrohydrodynamic behaviour of nanofluids and the electric current measurement. Two other test cells (one of them is a standard test cell, and another one was a custom-built test cell) were used to conduct investigation of the mobility in pure dielectric liquids stressed with uniform and nonuniform electric fields, respectively.

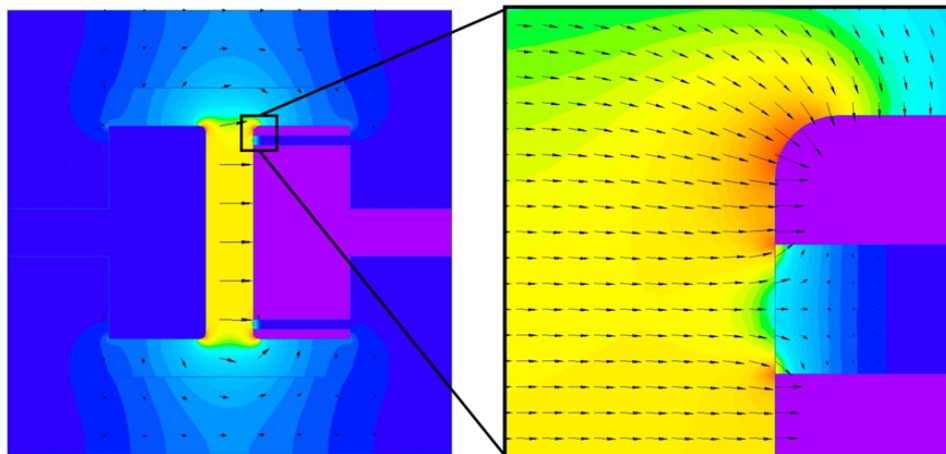
### **4.3.1 Test Cell with a Guard-Ring Electrode**

The test cell with a guard ring electrode was designed and developed to investigate the EHD movement in fluids using the CCD camera and the microscope and to measure the conduction current through the tested liquids. As illustrated in Figure 4-7(a) and (b), this test cell consists of a rectangular PTFE container and two parallel stainless-steel electrodes. One electrode includes the grounded guard-ring around the current sensing electrode according to the ASTM-D257.



(a)

(b)

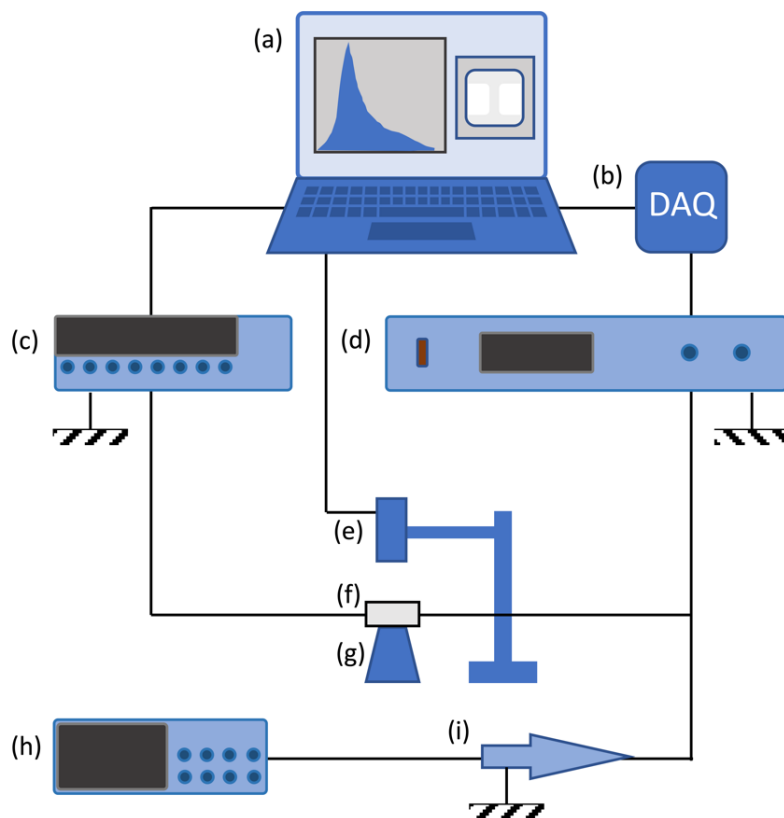


(c)

Figure 4-7 (a) Schematic 3D view of the guard ring test cell's inner part. (b) Schematic cross-section of the guard ring test cell (top view). (c) Simulation of the electric field distribution within the test cell (QuickField software). Arrows indicate the direction of the electric field. The parameters used in this modelling are provided in Appendix II.

The guard-ring structure provides a quasi-uniform electric field between the ground (current sensing) electrode and the energised electrode. The electric field distribution with a zoom-in view of the electrode edge is shown in Figure 4-7 (c).

The schematic diagram of the experimental setup, which includes the guard ring structured test cell, is illustrated in Figure 4-8.



- |   |  |
|---|--|
| (a): Laptop                                       | (e): Digital Camera                            |
| (b): DAQ Card<br>(NI USB-6000 )                   | (f): Test Cell                                 |
| (c): Electrometer<br>(Keithley 6514 )             | (g): LED Light Source                          |
| (d): Power Supply<br>(Matsusada Precision AU-60 ) | (h): Oscilloscope<br>(Tektronix TBS 1102 )     |
|   | (i): High Voltage Probe<br>(Tektronix P6015A ) |

Figure 4-8 System arrangement consisting of the guard ring structured test cell.

Figure 4-8 shows the power supply controlled via LabVIEW installed on the laptop. The electrometer which serves as a virtual ground ((c) in Figure 4-8) is also controlled by the LabVIEW code via a USB port. The LabView code was developed for data acquisition and power control, allowing data to be transferred from the electrometer to the PC for further processing. The current values acquired by the electrometer were saved as CSV files.

Figure 4-8 also shows a link between the laptop and the digital camera, allowing remote observation of the fluid under the test during HV tests. Besides, this arrangement enables recording of videos, these video files were saved after each test for further analysis. An LED light was located under the test cell to provide a clear image of the fluid, particularly in the case of nanofluids. The voltage applied to the test cell was monitored by the high voltage probe and recorded by the oscilloscope.

### **4.3.2 Transparent Test Cell with Parallel Disk Electrodes**

To obtain the dynamic behaviour of particles in the liquids, their movement was studied using the optical microscope equipped with the CCD camera (micro-level monitoring). This analysis of the particles' motion was conducted in the transparent test cell made of Perspex (PMMA), as shown in Figure 4-9.

This test cell is equipped with two parallel brass electrodes, as shown in Figure 4-9 (a) and (b). The electric field in the test cell was simulated using the QuickField software, the obtained field distribution with a zoom-in view of the edge of the electrode is shown in Figure 4-9 (c).

Since this test cell was designed for the micro-scale monitoring of particles, the material and dimensions of the test cell were adapted to fit the microscope. The diameter of the cylindrical electrodes was set at 10 mm, which was within the focal length of the microscope, ensuring clear observation of the liquid at any depth. As the micro-scale method is aimed at the investigation of the dynamics of particles in the fluids, the gap length between two electrodes was set at 15 mm, which is longer than the inter-electrode gap length in the guard ring structured test cell (5 mm), leaving this large space between the two electrodes for observation of the movement of particles.

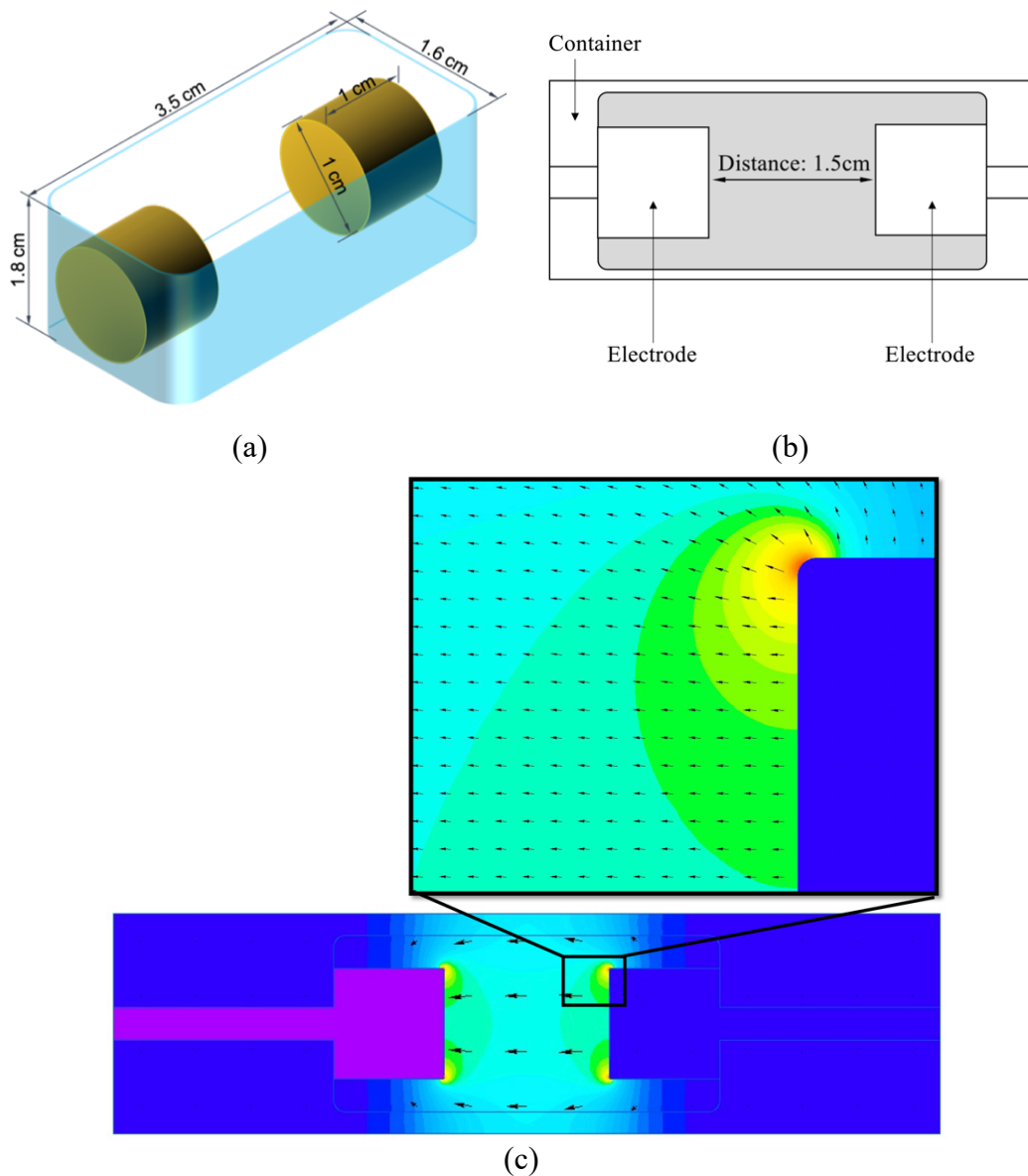


Figure 4-9 (a) Schematic 3D view of the transparent test cell. (b) Schematic cross-section of the transparent test cell. (c) Electric field distribution within the test cell (simulated using the QuickField software). The parameters used in this modelling are provided in Appendix II.

The diagram of the test system consisting of the transparent test cell is shown in Figure 4-10.

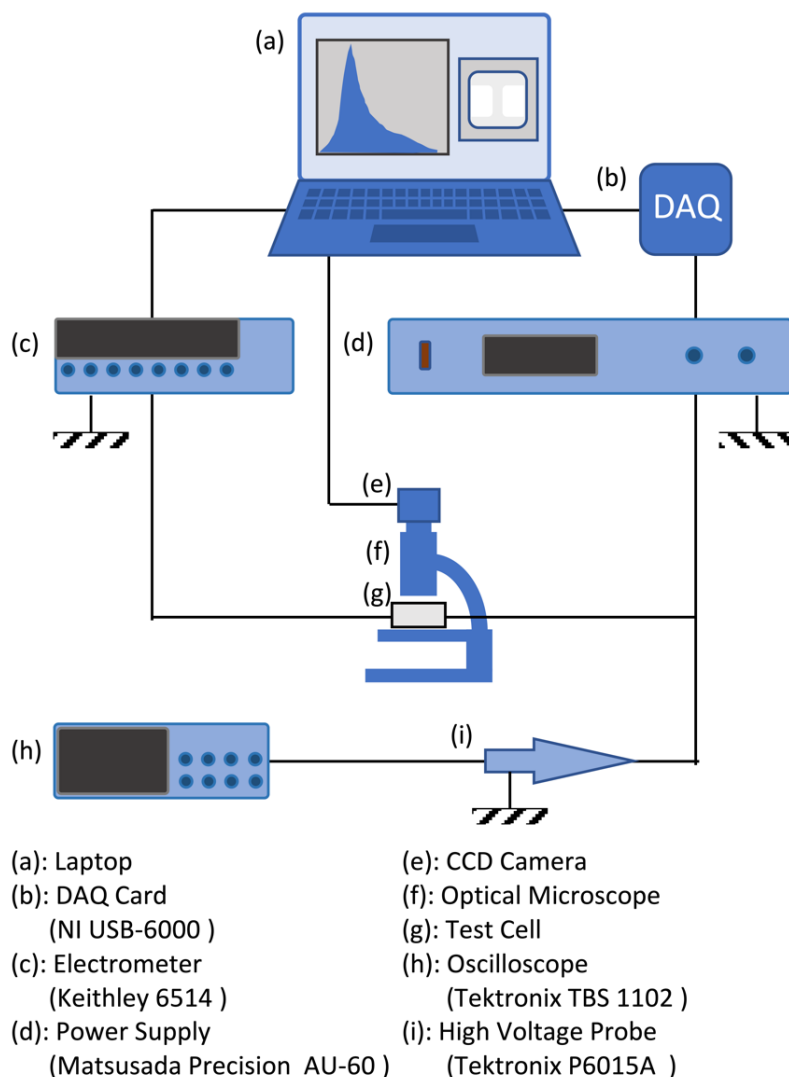


Figure 4-10 Schematic diagram of the system with the transparent test cell.

Comparing with the test system which includes the guard ring electrode test cell shown in Figure 4-8, the only difference in the test schematics shown in Figure 4-10 is the CCD equipped microscope which is used to observe nanoparticles in the liquids. Using this test system, the micro-scale video recordings, and images of the nanofluids were obtained. The videos obtained using the CCD camera were saved on the laptop for further analysis.

### 4.3.3 Coaxial Test Cell

A type 4536A oil test cell manufactured by the H. TINSLEY & CO Ltd was used for DC measurements with voltages below 100 V. A 3D view and the cross-sectional view of this test cell are given in Figure 4-11 (a) and (b), respectively.

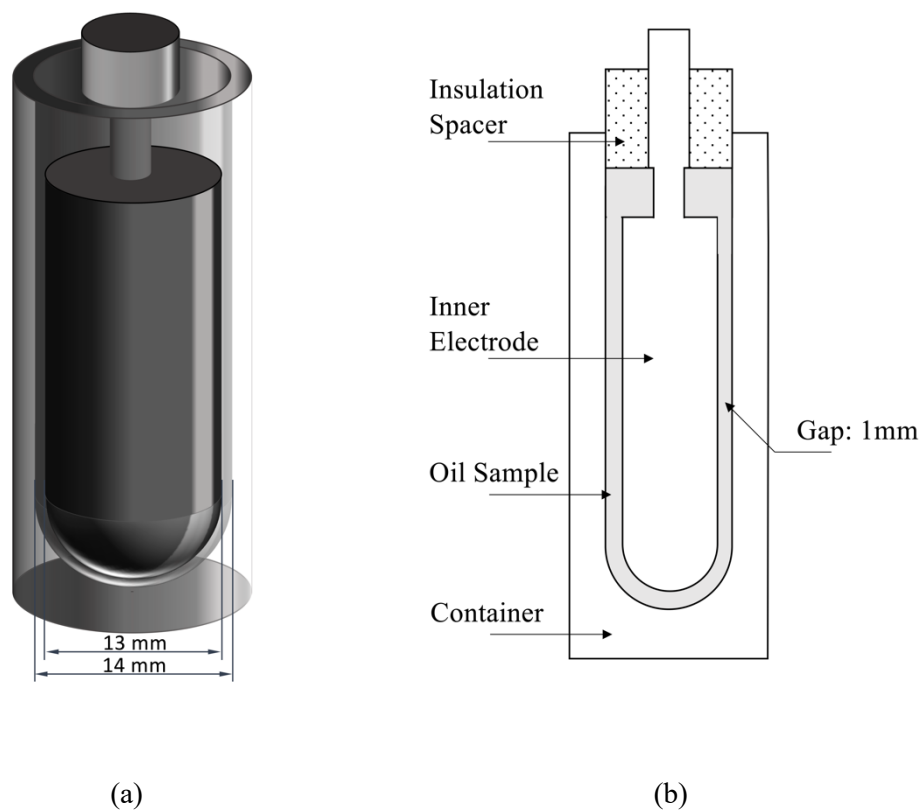


Figure 4-11 (a) Schematic 3D View of the Coaxial Test Cell, the diameter of the inner electrode is 13 mm and the inner diameter of the container is 14 mm. (b) Schematic cross-section of the Coaxial Test Cell.

The electrodes of this test cell are made of stainless steel. There is a PMMA-made insulation spacer between the cell container and the inner electrode. The inner electrode has a cylindrical

profile with a hemisphere as the lower end. The radius of the cylinder and the hemisphere is 13 mm. The inner radius of the outer electrode is 14 mm, providing a 1mm separation between these two electrodes. Due to a high “electrode area / electrode separation” ratio, the electric field within the gap is a quasi-uniform electric field.

The central electrode the coaxial test cell was energised using the voltage output from the Keithley 617 electrometer. The details of the experimental arrangement are provided in Figure 4-12.

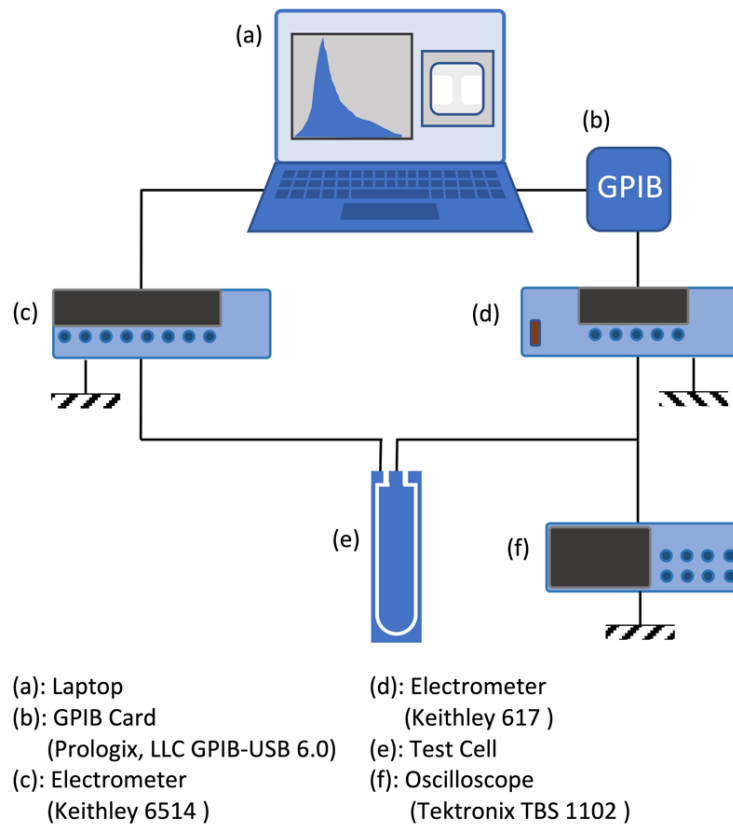


Figure 4-12 Test System with the Coaxial Test Cell

As shown in Figure 4-12, the Keithley 617 is controlled using the developed LabVIEW code via the GPIB card, enabling the power supply to change the polarity of the applied voltage in the reverse polarity tests suddenly. The LabVIEW code controls the Keithley 6154 electrometer enabling the application of the voltage to the central electrode and electric current measurement during the test. Since the test voltage in these measurements was below 100 V, the voltage applied on the test cell can be monitored by the oscilloscope directly.

#### 4.3.4 Test Cell with Needle-Plane Electrodes

Sections 4.3.1 to 4.3.3, introduced three test cells that provide a nominally uniform (low divergence) electric field. In this section, a test cell which provides a highly diverged electric field is discussed. The details of this test cell are given in Figure 4-13.

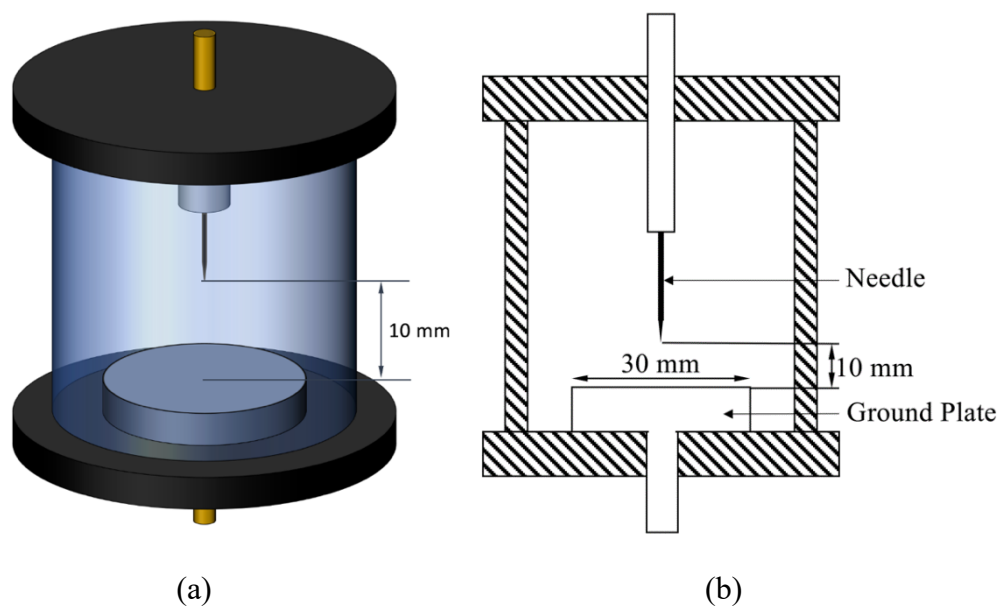


Figure 4-13 (a) Schematic 3D view of the needle-plane test cell. (b) Schematic cross-section of the needle-plane test cell.

In Section 2.3.2, the SCLC method in obtaining of the mobility of charge carriers was introduced. This method is based on the space charge limited current, which is governed by the space charge developed in the vicinity of the needle electrode. The Needle-Plane test cell was designed and developed to achieve the space charge saturated regime in the highly diverged electric field near the needle tip. To increase the field divergence, and to replicate the point-plane configuration used in the mathematical approximation in [62], the gramophone needle was sharpened to obtain a tip radius of 20  $\mu\text{m}$ , as shown in Figure 4-14.



Figure 4-14 Sharpened tip of the gramophone needle used as the HV electrode

As shown in Figure 4-14, the radius of the needle tip was measured as  $\sim 20$  micrometres. This radius value is used in the study of the electric field distribution. The diagram of the measurement system based on the needle-plane test cell is shown in Figure 4-15.

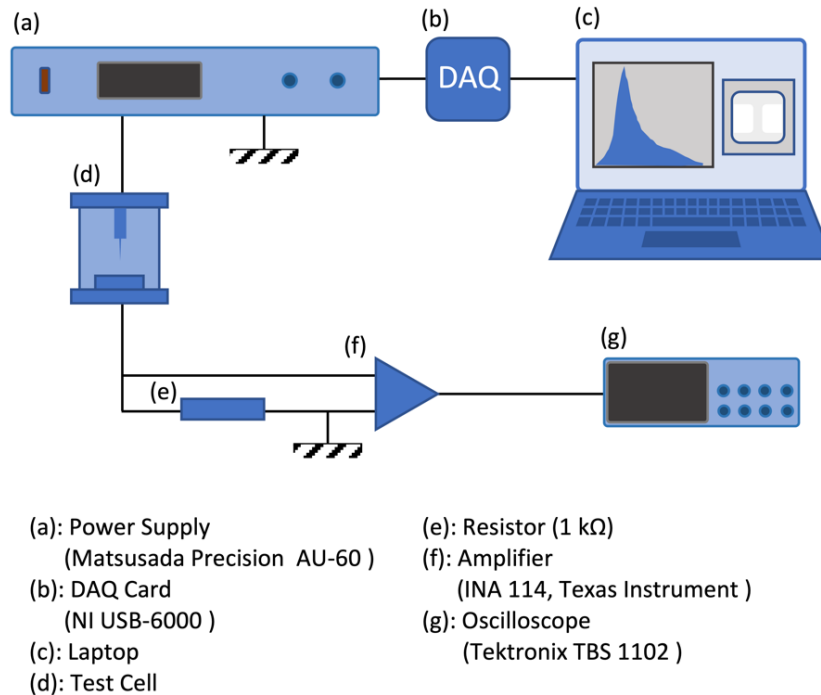


Figure 4-15 Test System with the needle-plane test cell

As discussed in Section 4.2.2, the current measurements in the case of the point-plane test cell were conducted using the current sensing resistor to avoid potential damage to the diagnostic equipment in the case of spark breakdown. The operational amplifier with the gain of  $770.05 \pm 30.04$  is used to amplify the voltage drop across the current viewing resistor. The selection of the 1 k $\Omega$  viewing resistor is based on the arrangements developed by Jing (2016) [21]. The voltage waveforms were registered by the oscilloscope and saved as CSV files for further analysis. The current through the liquid in the point-plane test cell was obtained by dividing the voltage across the resistor by the resistor's nominal value.

## 4.4 Summary

In this chapter, the experimental methods and methodologies used in the present thesis have been introduced and discussed. These methods include methods of preparation of nanofluids,

characterisation of particle size in nanofluids, experimental setups, and data analysis and processing methods.

The properties of the raw materials (liquids and solid particles) used in preparation of the nanofluids have been presented. The particles used in this research are TiO<sub>2</sub> and BN particles. The liquids used in this research project are MIDEAL 7131 synthetic ester, MIDEAL eN1204 natural ester, and the mineral oil that conforms to the Shell Diala B specification. Nanofluids with two concentrations of particles have been developed: 0.005% b/w concentration and 0.1% b/w concentration. 0.005% b/w concentration was selected due to its proven ability to enhance the dielectric strength of nanofluids. In comparison, the higher 0.1% b/w concentration of particles in the nanofluids was selected to study the enhanced effect of the electric field on the EHD behaviour of the nanofluids. Examination of the size distribution of the dispersed particles was conducted, and it was found that majority of the dispersed particles have dimensions of a few hundreds of nanometres, except the case of the highly concentrated mineral oil-based nanofluid with BN particles. The obtained average size of the particles in the nanofluids was used to develop the mathematical model(s) to analyse the experiment results.

This chapter presents the experimental setups used in this study. The components of these systems include different power supplies (Matsusada AU-60 and Keithley 617), the electrometer (Keithley 6514), voltage monitoring system(s) (Tektronix P6015A High voltage Probe and TBS1102 oscilloscope), visualisation instruments (digital camera and optical microscope equipped with the CCD camera), and the controlling system (LabVIEW software and codes, NI USB 6000 DAQ card, and Prologix GPIB-USB card). The specific arrangements of the test setups which are based on these components are discussed in this chapter.

Three custom-built test cells, together with one commercially available test cell were used to measure the mobility of charge carriers and to study the EHD behaviour of nanofluids. The guard ring test cell and the transparent test cell were used for both normal observation and micro-level observation of the nanofluids. The guard ring test cell, together with the coaxial test cell, and the needle-plane test cell, are designed to measure the mobility of charge carriers under different electric field strengths.

The raw data obtained from the experiments require processing to obtain reliable results. The principles of data filtering and uncertainty calculations are presented in this chapter. More specific parameters involved in the data processing will be presented and discussed in the following chapters with corresponding data.

## Chapter 5 MOBILITY OF CHARGE CARRIERS: UNIFORM ELECTRIC FIELD

---

This chapter presents the study focussed on obtaining the mobility of charge carriers in the dielectric liquids stressed with a uniform electric field. The ‘Time of Flight’ method is used to obtain the mobility of charge carriers in the ester liquids and in the mineral oil. As discussed in Chapter 2, there are two practical methods that can be used to conduct the ToF tests: the Reverse-polarity Method, and the Single-polarity Method. The measurements of ToF according to the reverse-polarity method were conducted in the coaxial test cell, while the single-polarity method was implemented in the plane-plane test cell with the guard-ring topology. Thus, ToF’s were obtained in electric fields ranging from 40 kV/m to 1200 kV/m, which allowed for the investigation of potential dependency of the mobility of charge carriers on the field strength. ToF and mobility of charge carriers were obtained in the pure dielectric liquids: MIDEL 7131 (synthetic ester), MIDEL eN1204 (natural ester), and Shell Diala B (mineral oil). Also, the charge carrier density in these dielectric liquids was evaluated. These results will help in further understanding the behaviour of the nanoparticles in nanofluids stressed with DC voltage, which will be discussed in Chapter 7.

## **5.1 Experimental Procedure**

Three dielectric liquids, MIDEAL 7131 (synthetic ester), MIDEAL eN1204 (natural ester), and Shell Diala B (mineral oil), were used in this study. Samples of these liquids were subjected to the DC voltage stress in two test cells: the coaxial test cell, and the plane-plane cell with the guard-ring topology, whose details are presented in Sections 4.3.3 and 4.3.1, respectively. Two ToF measuring methods were employed to obtain the mobility of charge carriers: the reverse-polarity method and the single-polarity method. These two methods have been presented and discussed in detail in Section 2.3.1.

### **5.1.1 Reverse-Polarity Method**

The coaxial test cell was used in the reverse-polarity tests. The narrow gap (1 mm) between the two electrodes offers a quasi-uniform electric field. The schematic diagram of this test cell and the relative instrument arrangement are presented in Figure 4-12 in Section 4.3.3.

In the reverse-polarity tests, the Keithley 617 electrometer was used to provide DC voltages using its internal power supply function. Three voltage levels were selected for these tests: 40 V, 60 V, and 80 V, which correspond to the field values of 40, 60 and 80 kV/m.

The reverse-polarity method involves application of a negative step DC voltage to the central electrode of the coaxial test cell for 30 mins, then the polarity of the applied voltage is suddenly reversed, and the liquid sample in this test cell is stressed with a positive DC voltage for another 30 mins. The conduction current through the liquid was measured using the Keithley 6514 electrometer with the data acquisition rate of 2 current readings per second.

For each fluid tested under specific voltage, three individual tests were conducted to ensure measurement reliability. A fresh sample of liquid was used in each individual test. After each ToF test, the test cell was cleaned with ethanol and lint-free tissue to remove residual oil or ester liquid from the surface of the inner electrode and the internal surface of the test cell.

### **5.1.2 Single-Polarity Method**

One of the main objectives in this research project is to investigate and establish the potential dependency of the mobility of charge carriers on the electric field strength. To achieve this objective, the test system, which consists of the coaxial test cell, and the Keithley 617 electrometer, has to be replaced as this system is not capable of delivering sufficiently higher electric field strength. Thus, to measure the mobility of charge carriers under higher electric field strength (400 – 1200 kV/m) the plane-plane test cell and the AU-60 power supply were used, this system is presented in Figure 4-8, Section 4.3.1.

However, due to operational limitations, the polarity of the output high voltage generated by the AU-60 power supply cannot be changed suddenly, which is required in the reverse-polarity method. Thus, ToF measurements in the plane-plane test energised by the AU-60 power supply were performed using the single-polarity method.

The single-polarity ToF measurements were performed by stressing the plane-plane test cell with a DC step voltage for 60 minutes. The electric current through the liquid under the test was measured directly by the Keithley 6514 electrometer which served as a virtual ground. The data acquisition rate was 2 current readings per second. Three voltage levels of both polarities:  $\pm 2$  kV,  $\pm 4$  kV, and  $\pm 6$  kV, were selected for these single-polarity ToF tests. Three individual tests were carried out for each type of fluid stressed with the required voltage level. Like in the reverse-polarity method, each liquid sample used in the single-polarity method was a fresh sample of specific liquid, and the same cleaning procedures was used after each test.

According to the introduction in Section 2.3.1, the single-polarity method requires a correction coefficient to obtain an accurate value of the mobility. This correction coefficient can be obtained from the reverse-polarity method: two ToF intervals can be determined in individual reverse-polarity tests by identifying the appearance time of two current peaks. The first current peak is formed by the motion of charge carriers travelling a distance shorter than the inter-electrode gap. The second current peak appears due to the charge carriers travelling the distance equals to the inter-electrode gap. The correction coefficient can then be calculated using Equation 2-25 in Section 2.3.1. In this section, the correction coefficients were

calculated for each type of fluids and the results of this analysis are presented in Section 5.2.1, 5.2.2, and 5.2.3.

## **5.2 Reverse-Polarity Method**

The measured and digitally processed electric current-time graphs and obtained mobility values for three tested liquids: MIDEL 7131, MIDEL eN 1204 and Shell Diala B are presented and discussed in this section. Also, the correction coefficient obtained for each dielectric liquid is presented.

### **5.2.1 Mobility of Charge Carriers in Synthetic Ester**

Prior to further discussion of these results, the methodology of digital processing and analysis of the raw current data is provided at the beginning of this section.

Figure 5-1 (a) shows an original current in the SE obtained under 40 V stress with the reverse-polarity method. As can be seen from Figure 5-1 (a), there are two distinct current peaks in the current-time graph. These peaks occur in two time intervals, 0 – 10 min and 30 – 40 min. According to Section 2.3.1, the second ToF interval, i.e. the time interval between the moment of the voltage polarity reversing and the time moment which corresponds to second current peak, can be used in Equation 2-24 to calculate the mobility of charge carriers directly. This time interval is marked by a rectangular box in Figure 5-1 (a). Therefore, the measurement of the ToF, i.e., obtaining the time of appearance of the peak current, becomes the key factor in obtaining the mobility of charge carriers.

In Figure 5-1 (a), the data point which corresponds to the maximum current that occurs within the 30 – 60 min time interval is labelled by ‘A’. Correspondingly, the time interval between the moment of the voltage polarity reversal (30<sup>th</sup> min in the current-time graph) and the moment indicated by point A is the second ToF interval required for calculating the mobility of charge carriers. To achieve a better time resolution of point A in Figure 5-1 (a), a zoom in view of the interval marked by the rectangular box is presented in Figure 5-1 (b).

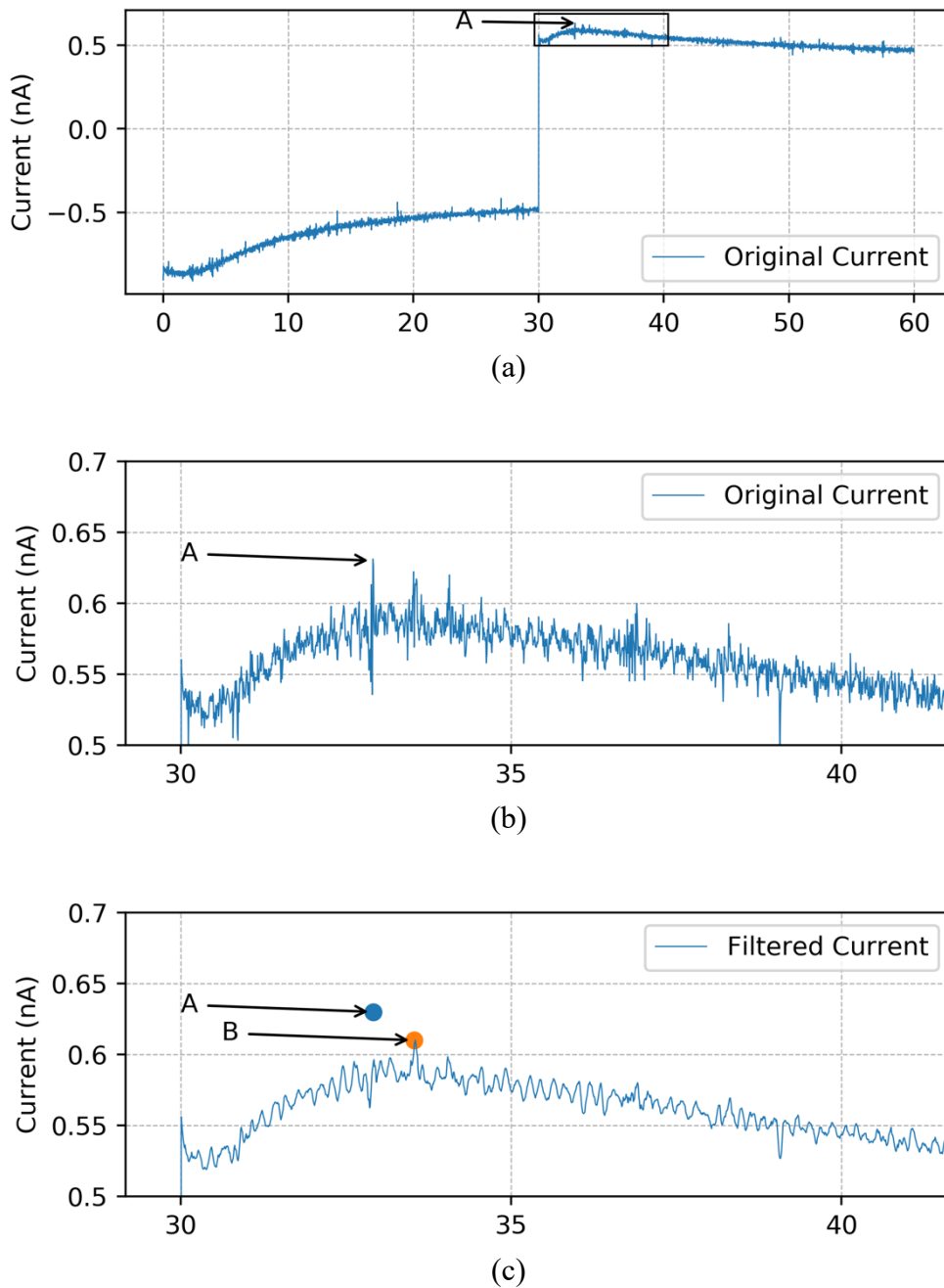


Figure 5-1 (a) The raw current in the SE stressed with 40 V (single test); (b) A zoom-in view of the current -time section marked by the rectangular box in (a), point A is the maximum current spike; (c) Filtered current-time graph originally presented in (b), point B is now represent the maximum current in this filtered waveform, point A is the maximum current spike observed in the original un-filtered current-time plot.

Figure 5-1 (b) shows multiple spikes in the current-time curve. The maximum current indicated by point A is also a spike. The current peak in the ToF method corresponds to the moment of arrival of the majority of charge carriers to the opposite electrode. Considering the physical meaning of the current peak, an uncertainty in the direct selection of point A for the ToF identification can be introduced. This is due to multiple factors, which result in the maximum current at point A, include the arrival of the majority of the charge carriers, and current spike(s) of different nature. The raw current-time graphs should be digitally filtered to remove outliers to avoid misrepresentation of the current peak. The filtered current corresponds to the moment of arrival of the majority of charge carriers to the opposite electrode, and thus allows for clear(er) identification of the time of flight.

The current-time wave presented in Figure 5-1 (c) is the result of filtering of the raw data presented in Figure 5-1 (b). The filter used in this procedure was the Savitzky-Golay (SG) filter, as introduced in Section 0, of which the polynomial order was set at 2, and the window length was set at 9.

An orange dot labelled 'B' in Figure 5-1 (c) represents the maximum current in the filtered current-time characteristics. For comparison, point A, which represents the maximum current spike in the original un-filtered current-time graph, is also shown as a blue dot in Figure 5-1 (c). Therefore, point B represents not only the current spike but also can be used in identification of the maximum current in the current-time characteristics shown in Figure 5-1 (c).

As discussed in Section 0, the current can be filtered smoother by increasing the window length using the SG filter. However, it was found that further smoothing does not produce more accurate identification of the time moment which corresponds to the peak current. On the other hand, the longer window length causes a higher risk of over filtering, which results in the distortion in the original current waveform. Thus, the filter window should be strictly controlled in the filtering procedure. Besides, as various liquids were used in this research, the filtering parameters should remain the same in all tests to ensure consistency of the filtering procedure and the obtained results.

Based on these two findings, various window lengths and polynomial orders were tested with all current waveforms obtained in the reverse-polarity tests. Based on this procedure, the

filtering parameters were selected as follows: the filtering window length was set at 9 data points; the polynomial order was set at 2.

With the procedure described above, the current plots for the SE stressed with 40 V, 60 V, and 80 V were filtered and they are shown in Figure 5-2.

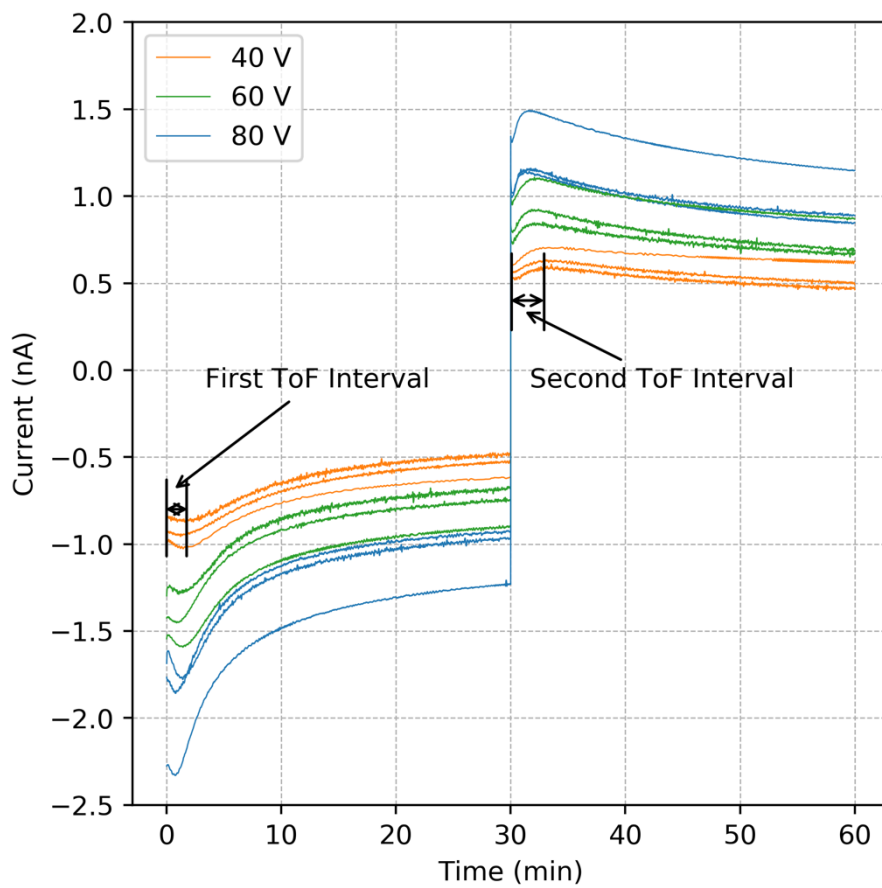


Figure 5-2 Current-time graphs in the SE obtained by the reverse-polarity method. 1<sup>st</sup> and 2<sup>nd</sup> ToF time intervals are schematically shown in this figure.

Each line in Figure 5-2 corresponds to an individual ToF test. As can be found from Figure 5-2, the current peaks occur early (in relation to time zero, i.e., the moment of voltage application) for higher voltages, which indicates that the travelling time for the charge carriers is decreasing with an increase in the applied electric field. To present this tendency quantitatively, the ToF values obtained from the current graphs are listed in Table 5-1.

Table 5-1 ToF intervals of the SE

	First ToF (s)			Second ToF (s)		
Tested Voltage	40 V	60 V	80 V	40 V	60 V	80 V
Test 1	90.0	72.0	67.0	213.5	167.0	105.0
Test 2	94.5	68.0	41.5	190.0	143.5	95.5
Test 3	112.5	54.5	40.5	266.5	124.5	94.5

As shown in Table 5-1, in each individual test, both the first and second ToF intervals decrease with an increase in the applied voltage. Before conducting further analysis, it must be pointed out that the repeatability of the current amplitude shown in Figure 5-2 is low, i.e., the current plot obtained under 80V in Test 1 differs significantly from the two from Test 2 and 3, respectively: the amplitude of the second current peak in Test 1 under 80 V is ~40% higher than the amplitude of the second current peaks in Tests 2 and 3. However, the second ToF obtained under 80 V in Test 1 is only 9.95% higher than that in Test 2 and 11.11% higher than that in Test 3. Since the focus of this experiment is the mobility of charge carriers in the liquids, the ToF results presented in Figure 5-2 can be used for obtaining the mobility values in the present work.

According to Section 2.3.1, the second ToF interval can be used in Equation 2-24 to calculate the mobility of charge carriers in the liquids. The results of these calculations are presented in Table 5-2.

Table 5-2 Mobility of Charge Carriers in the SE

Applied Voltage	40 V	60 V	80 V
Calculated Mobility ( $\times 10^{-10} \text{m}^2/(\text{V}\cdot\text{s})$ )	1.12	1.15	1.27
Uncertainty ( $\times 10^{-10} \text{m}^2/(\text{V}\cdot\text{s})$ )	$\pm 0.40$	$\pm 0.34$	$\pm 0.15$

The uncertainty values in Table 5-2 were calculated following the methodology presented in Section 0. Type A uncertainty in the mobility is the uncertainty in the ToF intervals obtained via three individual tests. Considering a relatively small sample size (three tests), this Type A uncertainty was calculated at 95% confidence level using the student distribution. For the 95% confidence interval, the student t-parameter which is related to the two-sided distribution and two degrees of freedom, of which the factor is 4.303. The Type B uncertainty stems from the uncertainty in the clock of the LabVIEW and the voltage source, the Keithley 617 electrometer. The uncertainty values presented in Table 5-2 are the combined Type A and Type B uncertainties, which were obtained by Equation III-1.

It can be seen from Table 5-2 that the mobility increases with the applied voltage. However, as uncertainties in the mobility values overlap with each other, this increase may not be considered a statistically significant increase.

In [117], Mahidhar (2020) presents the mobility measurements conducted in MDEL 7131 using the reverse-polarity method. These results show that the mobility of charge carriers in MDEL 7131 ranges from  $\sim 0.5 \cdot 10^{-9} \text{m}^2/(\text{V}\cdot\text{s})$  to  $\sim 1.1 \cdot 10^{-9} \text{m}^2/(\text{V}\cdot\text{s})$  under the electric field ranging from 12.5 kV/m to 100 kV/m, which approximately one order of magnitude higher than the results presented in this section. However, the temperature of the liquid in [117] was 30 C°, which is higher than the temperature of liquids in the present tests ( $\sim 20 \text{C}^\circ$ ). Thus, the higher mobility reported in [117] can be attributed to the higher test temperature.

As mentioned in Section 5.1.2, the mobility measurements under higher electric field, 400 kV/m – 1200 kV/m, were conducted using the single-polarity method. In this case, the

correction coefficient for obtaining mobility values is required. This coefficient was defined in Section 2.3.1 by Equation 2-25. Using Equation 2-25 and the ToF intervals presented in Table 5-1, the correction coefficients for the SE were calculated, and their values for different voltage levels are given in Table 5-3.

Table 5-3 Correction Coefficient for the SE

Tested Voltage	40 V	60 V	80 V
Correction coefficient	0.44	0.45	0.50
Uncertainty	±0.11	±0.06	±0.27

Table 5-3 shows that the values of the correction coefficient are almost the same for all three applied voltages. However, further confirmation of this finding is required for other liquids. This analysis will be presented in the following section.

### 5.2.2 Mobility of Charge Carriers in Natural Ester

The filtered current-time plot for the MIDEL eN1204 is shown in Figure 5-3. As introduced in the previous section, the filtering process was performed using the same parameters (window length: 9, polynomial order: 2) for all tested liquids. However, as it can be seen in Figure 5-3, some current spikes are remaining in the filtered current graph, for example, in the 0-10 min interval of the current-time graph obtained under 80 V. These current peaks (outliers) were removed before identification of the current peak used for obtaining ToF values. The removing procedure was conducted as follow: if the magnitude of current reading,  $i$ , is more than 120% higher than the magnitude of current reading  $i + 1$  and  $i - 1$ , then this current reading,  $i$ , will be replaced as the mean of the reading  $i + 1$  and  $i - 1$ .

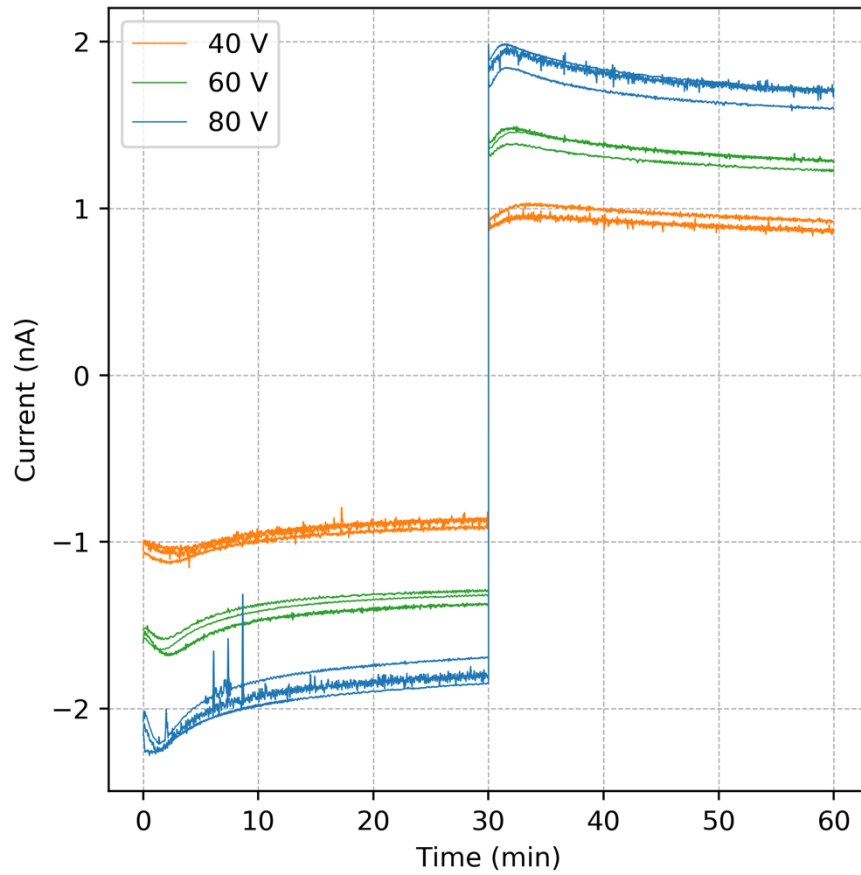


Figure 5-3 Current-time graphs in the NE obtained using the reverse-polarity method

The ToF values obtained from these current plots are presented in Table 5-4.

Table 5-4 ToF values for the NE

Tested Voltage	First ToF (s)			Second ToF (s)		
	40 V	60 V	80 V	40 V	60 V	80 V
<b>Test 1</b>	155.5	110.5	56.0	256.5	152.0	89.0
<b>Test 2</b>	149.5	85.0	62.0	222.5	147.0	96.0
<b>Test 3</b>	121.5	73.5	65.0	180.5	93.5	86.0

As can be seen from the results presented in Table 5-4, both the first and second ToF intervals decrease with an increase in the applied voltage. This tendency agrees with the tendency found for the SE fluid presented in Table 5-1.

Following the same calculation procedure introduced in the previous section, the mobility of charge carriers was obtained using the ToF intervals presented in Table 5-4. The obtained results and corresponding uncertainty values are presented in Table 5-5.

Table 5-5 Mobility of Charge Carriers in the NE

<b>Tested Voltage</b>	<b>40 V</b>	<b>60 V</b>	<b>80 V</b>
<b>Mobility (<math>\times 10^{-10} \text{m}^2/(\text{V}\cdot\text{s})</math>)</b>	1.13	1.27	1.38
<b>Uncertainty (<math>\times 10^{-10} \text{m}^2/(\text{V}\cdot\text{s})</math>)</b>	$\pm 0.40$	$\pm 0.64$	$\pm 0.16$

It can be seen from Table 5-5 that the obtained mobility increases with an increase in the applied voltage, while the corresponding uncertainty intervals overlap with each other. A similar tendency was found for the SE fluid in the previous section, indicating that there is no statistically significant increase in the mobility of charge carriers with an increase in the applied field in both the NE and SE fluids.

The correction coefficient for the NE was also obtained using Equation 2-25 and the ToF values presented in Table 5-4. The obtained correction coefficient values for the NE with the corresponding uncertainties are listed in Table 5-6.

Table 5-6 Correction Coefficient of the NE

<b>Applied Voltage</b>	<b>40 V</b>	<b>60 V</b>	<b>80 V</b>
<b>Correction Coefficient</b>	0.65	0.70	0.68
<b>Uncertainty</b>	±0.10	±0.27	±0.12

From Table 5-6, it can be seen that the correction coefficient for the NE under different voltages remains quasi-constant, this tendency also has been reported for the SE in the previous section. The values of the correction coefficient for the NE show a statistically significant difference compared with the correction coefficients for the SE. In this case, it can be suggested that the correction coefficient in the SE is only defined by the charged species in the fluid rather than the electric field strength. This conclusion is important as it ensures the validity of the application of the correction coefficient in higher electric fields in the tests conducting in accordance with the single-polarity method. To verify this conclusion furtherly, the correction coefficients for the mineral oil were obtained, and they are presented in the following section.

### **5.2.3 Mobility of Charge Carriers in Mineral Oil**

Figure 5-4 shows the filtered current plot of the Shell Diala B obtained using the reverse-polarity method.

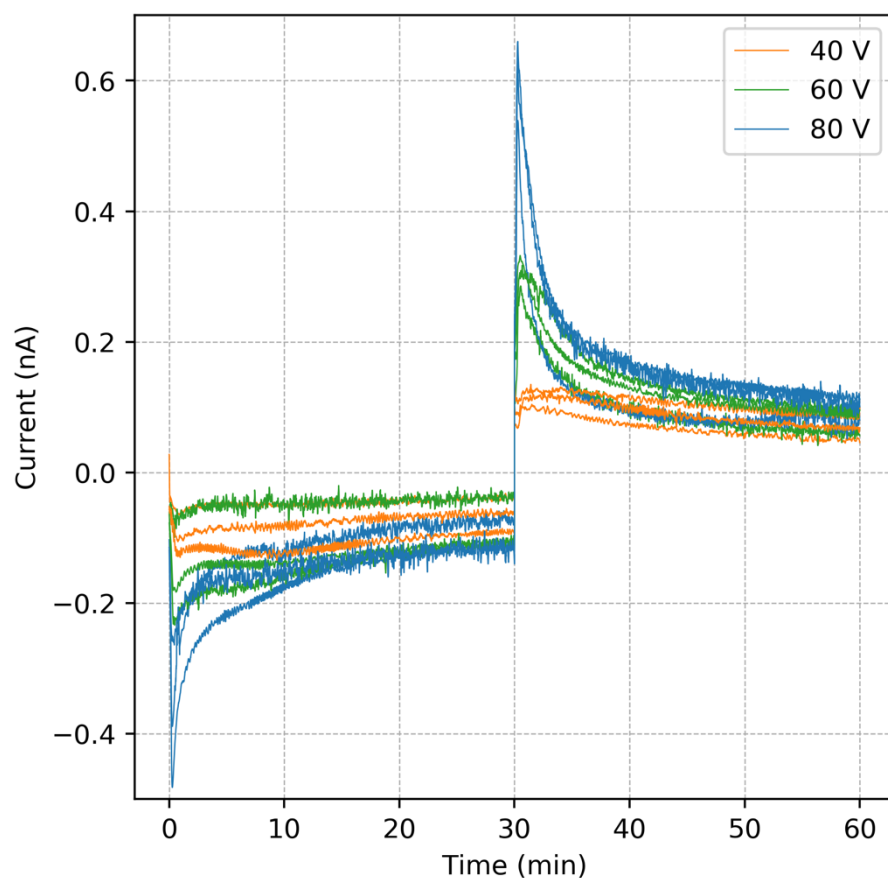


Figure 5-4 Current-time graphs in the MO obtained by the reverse-polarity method

The filtering conditions for the current waveform in the MO were the same as in the two previous two cases for the SE and the NE fluids: the window length was set at 9 data points, and the polynomial order was set at 2.

From Figure 5-4, it can be seen that the shape of the current peaks in the MO is much sharper than the current peaks observed in both the SE and the NE. In addition, the conduction current in the MO (which was  $< 0.2$  nA, as shown in Figure 5-4) is much lower than the current obtained in both the SE ( $\sim (0.5 - 1)$  nA, as shown in Figure 5-2) and the NE ( $\sim (1 - 2)$  nA, as shown in Figure 5-3).

Apart from the differences mentioned above, the current peak positions (which correspond to the ToF intervals) in the MO are also much shorter than the ToF intervals in both esters. Table 5-7 shows the ToF intervals for the MO obtained using the reverse-polarity method.

Table 5-7 ToF intervals for the MO

Applied Voltage	First ToF Interval (s)			Second ToF Interval (s)		
	40 V	60 V	80 V	40 V	60 V	80 V
Test 1	80.5	28.5	13.5	91.0	33.5	18.5
Test 2	70.0	25.0	13.5	83.5	28.5	16.0
Test 3	70.5	31.0	15.0	82.0	39.5	16.0

The mobility of charge carriers in the MO was obtained using the ToF intervals presented in Table 5-7 using Equation 2-25. These values are given in Table 5-8 together with their uncertainties.

Table 5-8 Mobility of Charge Carriers in the MO

Tested Voltage	40 V	60 V	80 V
Calculated Mobility ( $\times 10^{-10} \text{m}^2/(\text{V}\cdot\text{s})$ )	2.92	4.93	7.43
Uncertainty ( $\times 10^{-10} \text{m}^2/(\text{V}\cdot\text{s})$ )	$\pm 0.34$	$\pm 1.63$	$\pm 1.30$

Compared with both ester liquids used in the present work, the mobility of charge carriers in the MO increases significantly with an increase in the applied voltage. Besides, the mobility of charge carriers in the MO is also higher than that in the esters under the same voltage level. Potential reasons for the different behaviour are discussed in detail in Section 5.4.

The correction coefficients of the MO were calculated using Equation 2-25 with the ToF intervals listed in Table 5-7, and the obtained results are listed in Table 5-9.

Table 5-9 Correction Coefficient of the MO

<b>Applied Voltage</b>	<b>40 V</b>	<b>60 V</b>	<b>80 V</b>
<b>Correction Coefficient</b>	0.86	0.84	0.83
<b>Uncertainty</b>	±0.06	±0.12	±0.05

The correction coefficients of the MO are almost the same for all three levels of the applied voltage, which is similar to the case of the ester liquids. However, the coefficients of the MO are different from the coefficients obtained for both ester liquids, which provides further confirmation that the correction coefficient is governed by the nature of the fluid rather than by the applied voltage, ensuring the validity of its application in the single-polarity method.

### **5.3 Single-Polarity Method**

One of the aims in this study is to investigate the potential dependency of the mobility of charge carriers on the applied field strength. Thus, different test cells were used in this study to meet the requirements of the tests under different magnitudes of electric field. Due to the operational limitations of the power supply used in the tests, the measurement of the mobility of charge carriers in dielectric liquids under higher electric field were conducted only using

the single-polarity method and the plane-plane test cell. In this section, the ToF intervals and corresponding mobility values obtained under higher electric field strength (400 – 1200 kV/m) are presented and discussed. The correction coefficients obtained in Sections 5.2.1 to 5.2.3 were used to ensure the accuracy of the results obtained by the single-polarity method.

### **5.3.1 Mobility of Charge Carriers in Synthetic Ester**

Figure 5-5 and Figure 5-6 show the current-time graphs obtained in the MIDEL 7131 (SE) fluid under positive voltage and negative energisation, respectively.

A surprising feature of the current-time graphs shown in Figure 5-5 and Figure 5-6 is the presence of two current peaks in each current waveform. To distinguish these two current peaks, the “First” current peak refers to the current peak that occurs early after the application of voltage, and the “Second” current peak refers to the current peak that occurs after the “First” peak. To represent the second peak more clearly, a log scale is used for the time axis in Figure 5-5 and Figure 5-6.

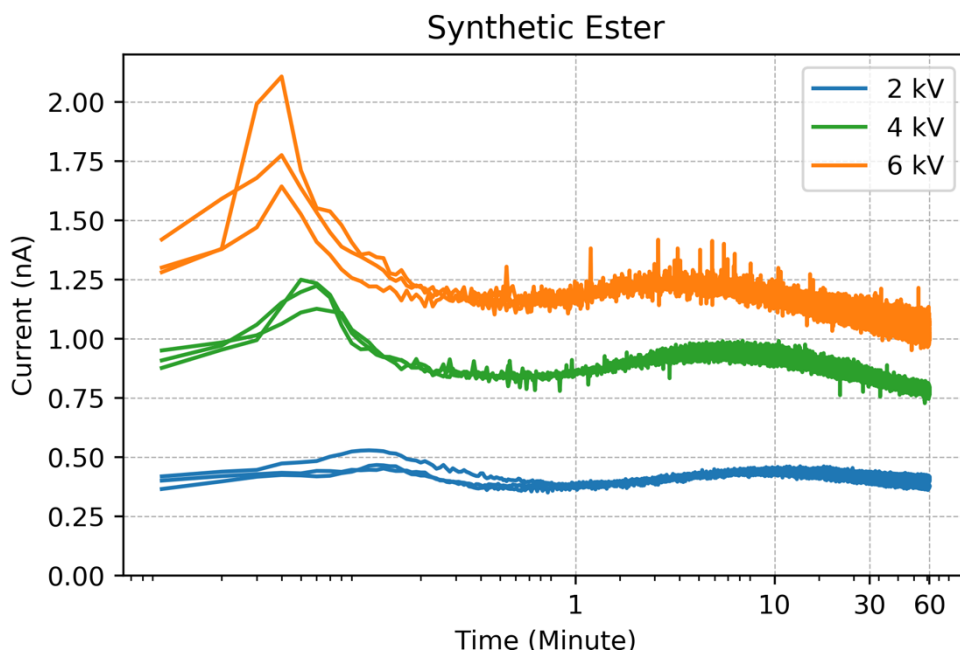


Figure 5-5 Current-time graphs in the SE under positive voltage obtained by the single-polarity method

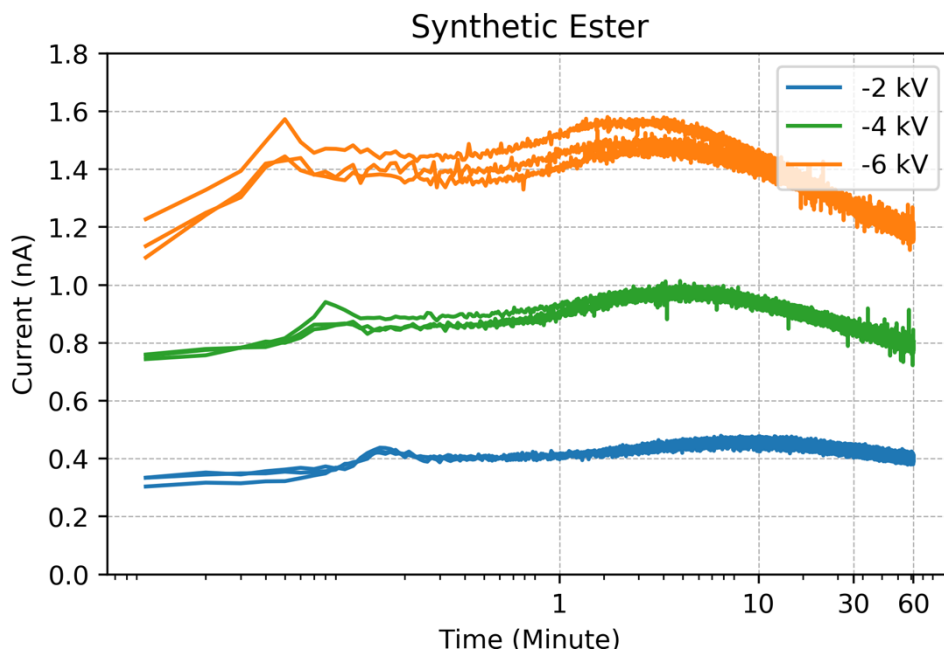


Figure 5-6 Current-time graphs in the SE under negative voltage obtained by the single-polarity method

The first current peak reflects the motion of charge carriers due to the application of the step voltage. The time of appearance of the first current peak is the ToF interval used to calculate the mobility of the charge carriers in the SE. The second current peak, which was not observed in previous reverse-polarity tests, is observed in all single-polarity tests with the SE. The magnitude of the second current peak in the case of negative energisation is even higher than the magnitude of the first current peak in the SE (as shown in Figure 5-6).

From Figure 5-5 and Figure 5-6, it can be found that the second current peaks in the case of higher voltages appear early. The magnitude of the second current peak in the case of a higher voltage level is also higher. Both of these aspects suggest the link between the formation of the second current peak and the electric field strength. The main difference between the reverse-polarity tests and the single-polarity tests is the field strength: the electric field strength in the single-polarity tests ranges from 400 kV/m to 1200 kV/m, while the strength of the field in the reverse-polarity tests ranges from 40 kV/m to 80 kV/m, which is about one order of magnitude lower than the single-polarity test. Therefore, potential reason for the appearance of the second current peak can be attributed to the higher electric field strength, and a detailed discussion on this will be presented in Section 5.3.3.

However, further understanding of the nature of the second current peak requires additional experimental tests, especially in the case of the mineral oil, which is significantly different from the ester liquids in terms of its chemical ingredients.

According to the current graphs shown in Figure 5-5 and Figure 5-6, the ToF intervals of the SE can be obtained using the time of appearance of the first current peak. The results are shown in Table 5-10.

Table 5-10 ToF intervals of the SE under positive and negative voltage

Applied Voltage	ToF Intervals (s)			ToF Intervals (s)		
	+2 kV	+4 kV	+6 kV	- 2 kV	- 4 kV	- 6 kV
<b>Test 1</b>	6.0	3.5	2.5	8.0	5.5	3.0
<b>Test 2</b>	6.5	3.0	2.5	9.5	5.0	3.0
<b>Test 3</b>	6.0	3.5	2.5	8.0	6.0	3.5

As discussed in Section 2.3.1, a correction coefficient is required to obtain the mobility of charge carriers in the single-polarity method. The application of this coefficient is described by Equation 2-26. In this Chapter, the correction coefficients for all three liquids have been obtained and presented in Section 5.2.1 to 5.2.3. In this case, the mobility of charge carriers was obtained using the ToF intervals and the corresponding correction coefficients by Equation 2-26. The results are shown in Table 5-11.

Table 5-11 Mobility of Charge Carriers in the SE

Applied Voltage	+2 kV	+4 kV	+6 kV
<b>Calculated Mobility (<math>\times 10^{-9} \text{m}^2/(\text{V}\cdot\text{s})</math>)</b>	0.95	0.88	0.78
<b>Uncertainty (<math>\times 10^{-9} \text{m}^2/(\text{V}\cdot\text{s})</math>)</b>	$\pm 0.17$	$\pm 0.20$	$\pm 0.12$
Tested Voltage	- 2 kV	- 4 kV	- 6 kV
<b>Calculated Mobility (<math>\times 10^{-9} \text{m}^2/(\text{V}\cdot\text{s})</math>)</b>	0.69	0.54	0.62
<b>Uncertainty (<math>\times 10^{-9} \text{m}^2/(\text{V}\cdot\text{s})</math>)</b>	$\pm 0.17$	$\pm 0.13$	$\pm 0.14$

The obtained mobilities are presented in Table 5-11 with their uncertainties. The uncertainty calculation procedure in this section remains the same as the procedure described in Section 5.2.1.

From the results presented in Table 5-11, it can be seen that the mobility of charge carriers obtained under different voltage levels remain almost the same for the same voltage polarity. In addition, all mobilities obtained under the positive voltage are higher than the mobilities obtained under the negative voltage. In [118], Aljure (2019) found that in the needle-plane configuration stressed with a positive DC voltage, the currents are mainly dependent upon the Zener molecular ionisation mechanism and the mobility of the positive ions, while the electron multiplication and electron attachment process play only a secondary role. However, for the same configuration under a negative DC voltage, the current is mainly dependent upon electron multiplication and attachment processes, with Zener molecular ionisation providing the seed of quasi-free electrons. In this case, it can be expected that the main charge carriers produced under positive polarity could be different from the main charge carriers produced under the negative polarity, resulting in the difference in the mobility of charge carriers between the positive and negative polarities. However, the reason behind the higher mobilities from the positive voltage still requires further investigation.

The mobility of charge carriers presented in Table 5-11 is approximately one order of magnitude higher compared with the mobilities of charge carriers presented in Table 5-2 (in Section 5.2.1), which were obtained in the lower electric fields (40 - 80 kV/m). The increase in the mobility values can be attributed to the significantly higher electric fields (400 - 1200 kV/m) used in these tests.

### **5.3.2 Mobility of Charge Carriers in Natural Ester**

Figure 5-7 and Figure 5-8 show the current-time plots for the MIDEL eN1204 under positive and negative polarity, respectively.

From Figure 5-7 and Figure 5-8, it can be found that there are also two current peaks in each current wave in the NE, which is similar to the current peaks in the SE as described in Section 5.3.1. The behaviour of the second current peak found in the NE also has similarities with the second current peak found in the SE, i.e., the second current peaks in the NE stressed

with higher voltages appear early. Since the NE has chemical properties similar to the SE, (as discussed in Section 2.1.3), the similar behaviour of the current found in the SE and the NE fluids is not surprising.

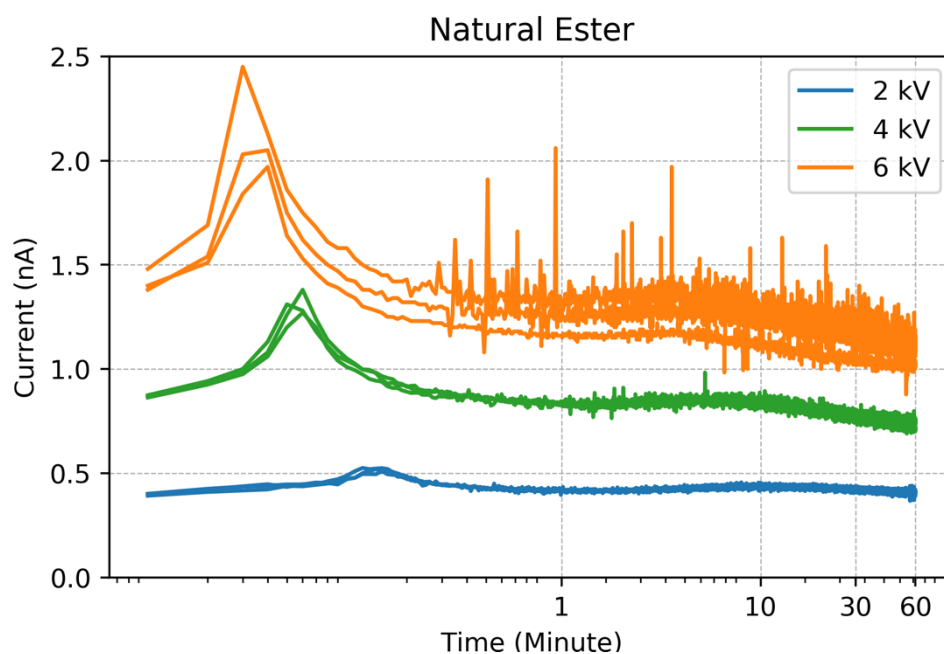


Figure 5-7 Current-time graphs in the NE under positive voltage obtained by the single-polarity method.

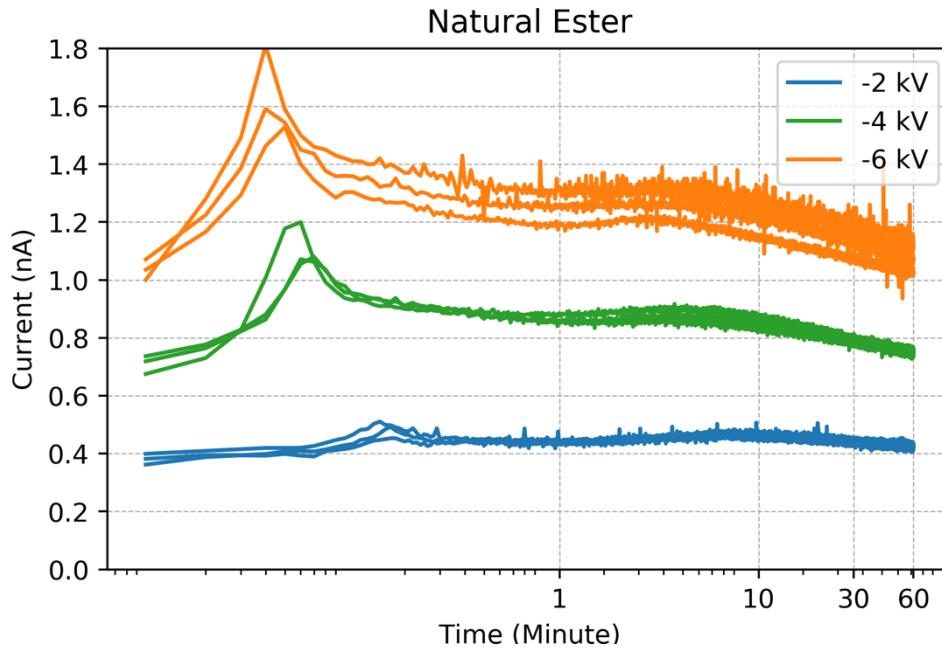


Figure 5-8 Current-time graphs in the NE under negative voltage obtained by the single-polarity method.

The ToF intervals in the NE were also obtained using the first current peaks in the current-time graphs. The obtained results are shown in Table 5-12.

Table 5-12 ToF intervals in the NE under Positive and Negative Voltage

Applied Voltage	ToF Intervals (s)			ToF Intervals (s)		
	+2 kV	+4 kV	+6 kV	- 2 kV	- 4 kV	- 6 kV
<b>Test 1</b>	7.5	3.0	2.5	8.0	3.5	3.0
<b>Test 2</b>	8.0	3.5	2.0	9.0	3.5	2.5
<b>Test 3</b>	8.0	3.5	2.5	9.0	4.0	2.5

Using the ToF obtained using the first current peak and the correction coefficients for the reverse-polarity method, the mobility of charge carriers was obtained by Equation 2-26. The results of this analysis are presented in Table 5-13.

Table 5-13 Mobility of Charge Carriers in the NE

Applied Voltage	+2 kV	+4 kV	+6 kV
<b>Calculated Mobility (<math>\times 10^{-9} \text{m}^2/(\text{V}\cdot\text{s})</math>)</b>	1.07	1.26	1.20
<b>Uncertainty (<math>\times 10^{-9} \text{m}^2/(\text{V}\cdot\text{s})</math>)</b>	$\pm 0.12$	$\pm 0.25$	$\pm 0.32$
Tested Voltage	-2 kV	-4 kV	-6 kV
<b>Calculated Mobility (<math>\times 10^{-9} \text{m}^2/(\text{V}\cdot\text{s})</math>)</b>	0.97	1.14	1.05
<b>Uncertainty (<math>\times 10^{-9} \text{m}^2/(\text{V}\cdot\text{s})</math>)</b>	$\pm 0.16$	$\pm 0.21$	$\pm 0.24$

From Table 5-13, it can be seen that the mobility of charge carriers obtained under different voltage levels remains almost constant for the same voltage polarity, which is similar to the results obtained for the SE. However, although the mobility of charge carriers in the NE obtained under positive voltage is higher than those obtained under the negative voltage, the difference in the mobility values obtained under opposite polarities is not statistically significant.

### 5.3.3 Mobility of Charge Carriers in Mineral Oil

Figure 5-9 and Figure 5-10 show the current as a function of time in the Shell Diala B stressed with positive and negative voltages, respectively.

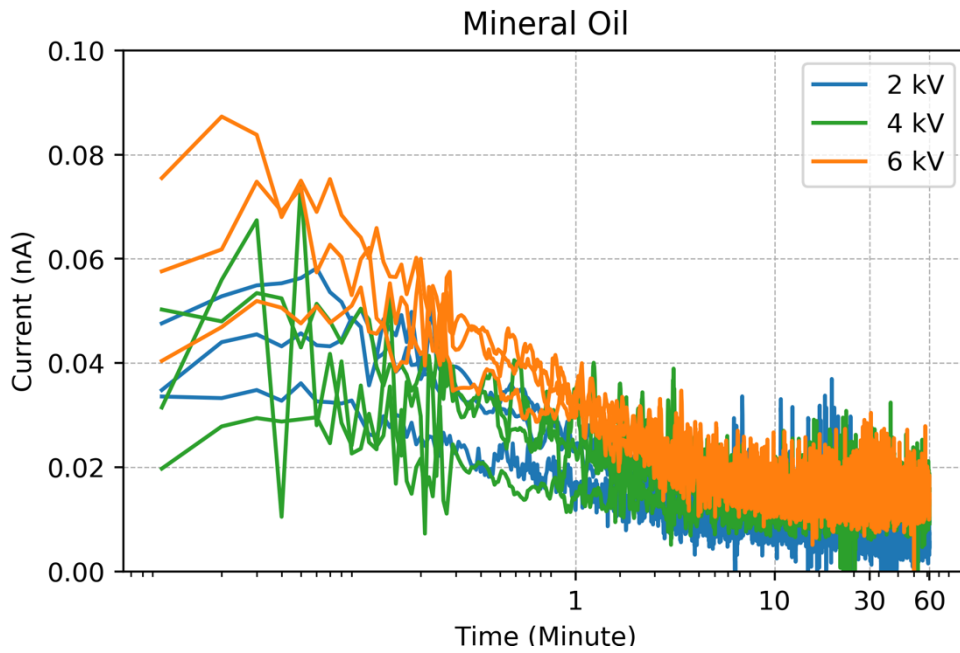


Figure 5-9 Current-time graphs in the MO under positive voltage obtained by the single-polarity method

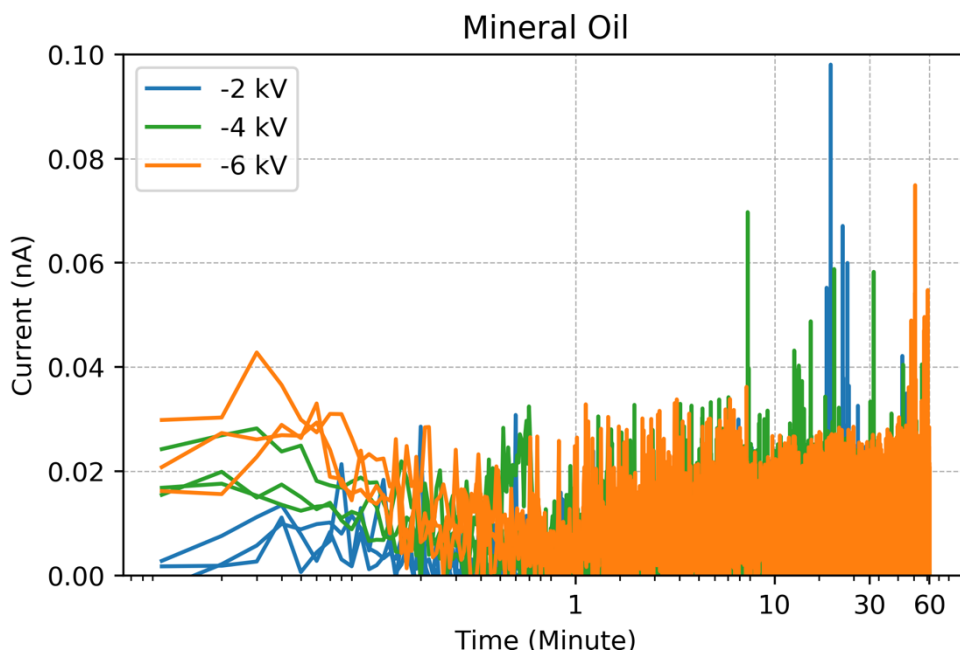


Figure 5-10 Current-time graphs in the MO under negative voltage obtained by the single-polarity method

Compared with the current plots obtained for two ester liquids presented in Sections 5.3.1 and 5.3.2, the current-time graph for the MO displays two different features.

1. Only single current peak was observed in each individual current plot for the MO, while two current peaks were obtained in each individual current plot for both esters. Since the chemical composition of the MO differs significantly from the chemical composition of both esters, and the second current peak observed in both esters is linked with the electric field strength, the possible reason for the appearance of the second current peak in esters can be attributed either to a higher degree of molecule dissociation or to a stronger molecule polarisation in the case of higher electric fields.

However, in Section 2.2.2, it has been proved that the increase in the molecule dissociation rate due to an increase in the field strength is weak. It hence can be concluded that the second peak found in the esters originates from the molecule polarisation.

Despite the complex chemical structure and composition of all three liquids used in this research, the main molecular structures of mineral oil include paraffin and naphthene, while the main molecular structures of the esters consist of several ester linkages (-COOR), as presented in Section 2.1.2 and 2.1.3. Since the ester linkages (-COOR) are polar functional chemical groups, the molecules of esters are hence more polar than the molecules of mineral oils [119]. Therefore, the second current peak observed in the current-time graphs for ester liquids could be attributed to the molecular polarisation process in the higher electric field: the reorientation of the polarised molecules may induce an additional current, which manifests itself as the second current peak in the current-time graph. However, this explanation still requires further investigation and confirmation.

2. The second difference between the current-time plot for the MO and the current-time plots for the esters are a lower signal-to-noise ratio in the case of the MO current-time plots. This difference can be attributed to a significantly lower conduction current in the MO ( $< 0.02$  nA) compared with the current in the ester liquids ( $\sim 0.4 - 1.4$  nA).

Using the current plots presented in Figure 5-9 and Figure 5-10, the ToF intervals which correspond to the observed current peaks were obtained. The results are shown in Table 5-14.

Table 5-14 ToF intervals of the MO under Positive and Negative Voltage

Applied Voltage	ToF Intervals (s)			ToF Intervals (s)		
	+2 kV	+4 kV	+6 kV	- 2 kV	- 4 kV	- 6 kV
Test 1	3.5	4.5	2.0	2.5	1.5	2.0
Test 2	5.0	2.0	1.5	5.0	2.0	1.5
Test 3	3.0	3.0	2.0	2.5	1.5	2.5

Unlike the ToF intervals obtained for the ester liquids (Table 5-10 and Table 5-12), the ToF intervals for the MO obtained under higher voltages are not always shorter than those obtained under lower voltage levels. For example, the ToF intervals obtained under +2 kV from Test 1 and Test 3 are shorter than the ToF intervals obtained for higher voltages, +4 kV from Test 1. The main reason for this discrepancy is the relatively low data acquisition rate (time intervals between two consecutive data points) of the electrometer compared with the ToF intervals for the MO. As discussed in Section 5.1.2, the data acquisition rate of the Keithley 6514 electrometer used in this measurement is 2 data reading per second. Therefore, for the longest ToF intervals obtained for the MO which is 5 s (under +2 kV from Test 2), only 10 data points were recorded. Thus, to obtain an accurate time resolution of the current peak, a higher data acquisition rate(s) should be used. It is expected that an increase in time resolution in the current measurements should provide a better resolution of the current peaks.

The obtained ToFs were used to calculate the mobility of charge carriers in the MO used in the present study. The results of this analysis are presented in Table 5-15.

Table 5-15 Mobility of Charge Carriers in the MO

<b>Tested Voltage</b>	<b>+2 kV</b>	<b>+4 kV</b>	<b>+6 kV</b>
<b>Calculated Mobility (<math>\times 10^{-9} \text{m}^2/(\text{V}\cdot\text{s})</math>)</b>	2.74	1.67	1.92
<b>Uncertainty (<math>\times 10^{-9} \text{m}^2/(\text{V}\cdot\text{s})</math>)</b>	$\pm 1.50$	$\pm 1.36$	$\pm 0.62$
<b>Tested Voltage</b>	<b>-2 kV</b>	<b>-4 kV</b>	<b>-6 kV</b>
<b>Calculated Mobility (<math>\times 10^{-9} \text{m}^2/(\text{V}\cdot\text{s})</math>)</b>	3.18	3.18	1.76
<b>Uncertainty (<math>\times 10^{-9} \text{m}^2/(\text{V}\cdot\text{s})</math>)</b>	$\pm 2.79$	$\pm 1.12$	$\pm 0.90$

Table 5-15 shows that the mobility of charge carriers in the MO is higher than that in both esters: the SE and the NE (as seen in Table 5-11 and Table 5-13, respectively). Besides, the uncertainty in the mobility values for the MO is much higher than that for the ester liquids.

Therefore, to obtain better accuracy in determination on the ToF intervals under different applied voltages, the data acquisition rate of the electrometer should be higher. It is expected that an increase in the time resolution in current measurements will lead to a better resolution of the current peaks and thus to an improved accuracy in the mobility values. However, the mobility of charge carriers obtained in the present study, as shown in Table 5-15, still can be used in evaluation of the injected space charge in different liquids, which will be discussed in the next section.

## 5.4 Discussion and Summary

The mobilities of charge carriers in the SE, the NE, and the MO have been obtained using the reverse-polarity and the single-polarity methods. These methods enable the mobility

measurements to be carried out under different electric field strengths. Figure 5-11 shows the mobility as a function of the electric field strength.

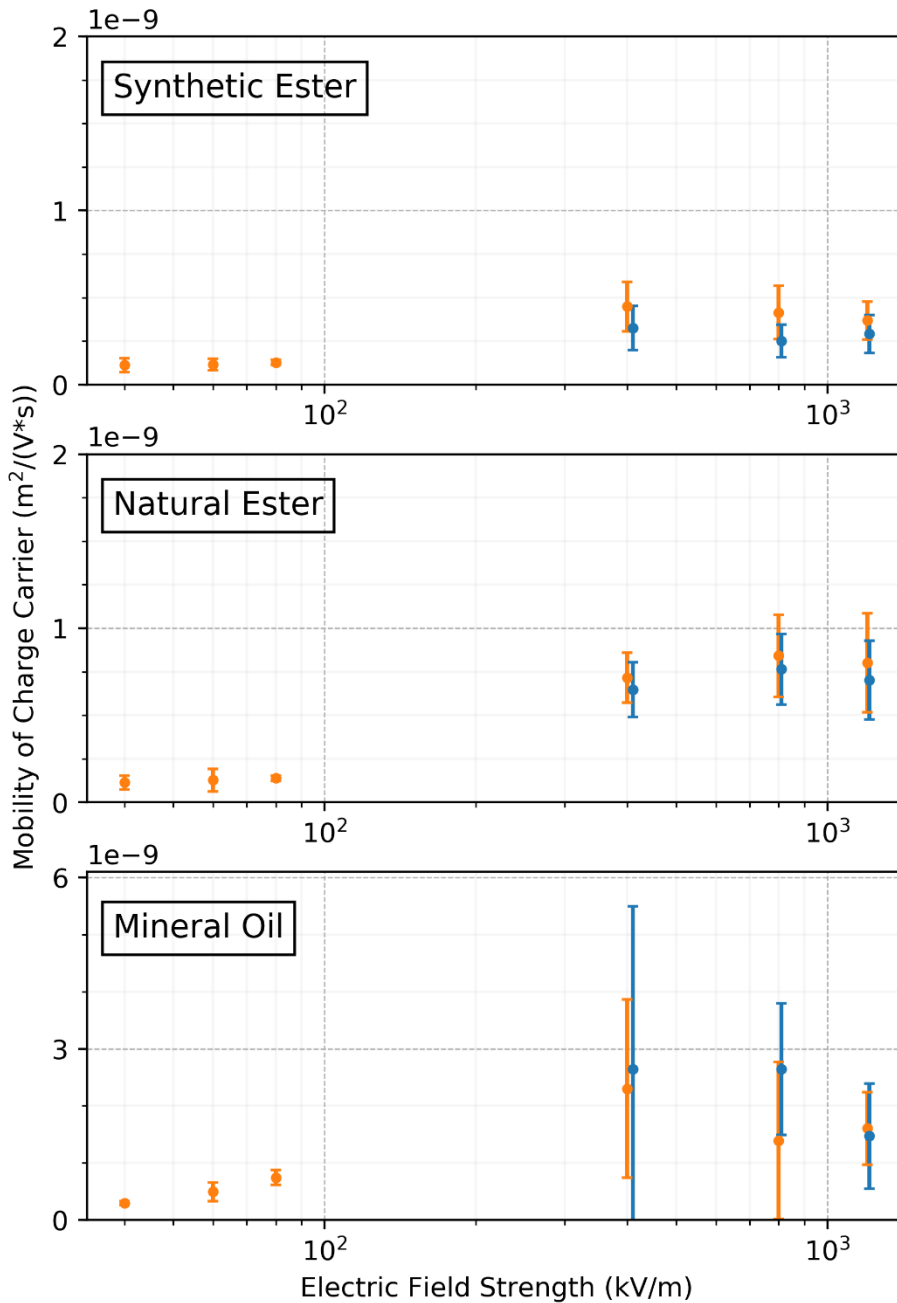


Figure 5-11 Mobility of Charge Carriers vs Electric Field Strength. The orange dots indicate the mobility measured under positive voltage; The blue dots indicate the mobility

obtained under the negative polarity. Error bars indicate the uncertainty in the mobility values (obtained based on the 95% confidence level).

The error bars in Figure 5-11 represent the corresponding uncertainty in the mobility values. Since both positive and negative energisation was used in the single-polarity method, the corresponding mobility values are presented in different colours: the orange dots indicate the data measured under positive voltage while the blue dots indicate the negative polarity data.

Figure 5-11 shows a positive correlation between the mobility of charge carriers and the electric field strength for all three liquids. The potential reason for this positive correlation is the EHD movement of fluids stressed with an external electric field.

As discussed in Section 2.3.3, the EHD velocity of the liquid stressed with the electric field can be estimated from the energy viewpoint: since the fluid motion is caused by the electric field, the kinetic energy of the fluid can be assumed to be proportional to the electrostatic energy of the electric field, which yields:

$$\frac{1}{2}\varepsilon E^2 \propto \frac{1}{2}\rho v^2 \quad 5-1$$

where  $\varepsilon$  is the dielectric permittivity of the liquid;  $E$  is the electric field strength; and  $\rho$  and  $v$  are the density and the velocity of the liquid, respectively. According to Equation 5-1, it can be found that the fluid motion velocity is proportional to the electric field strength:

$$v \propto E\sqrt{\varepsilon/\rho} \quad 5-2$$

From Equation 5-2, it can be concluded that the electric field with a higher strength generally leads to a higher EHD velocity of the fluid. As discussed in Section 2.3.3, not only the electric field but also the liquid motion can stimulate the movement of the charge carriers in dielectric liquids. Since measurements of the mobility using the ToF method relies on the motion of the charge carriers in liquids, the effect of the EHD on the measurement results is unavoidable.

In this case, the obtained mobility is called the ‘apparent mobility’, which can be increased by the EHD due to the higher electric field.

It also should be noticed that there are other factors affecting the velocity of the EHD motion of the fluid, including its viscosity, permittivity, and density. Since the viscosity of the MO is significantly lower than that of both esters (as shown in Table 4-1 in Section 4.1.1), the impact of the motion of the liquids on the mobility values can be higher for the MO compared with the esters, resulting in the increasing of the mobility values in the MO (as shown in Table 5-8 in Section 5.2.3).

Also, the configuration of the test cell plays an important role in the formation of the EHD movement. Further investigation of the potential effect of these factors on the apparent mobility of charge carriers under different energisation regimes is required.

Although the EHD effect is complicated and beyond the scope of this work, the apparent mobility obtained in this study provides valuable information on electrical conductivity and charge motion in the mineral oil and the ester liquids. The obtained results can be used in different practical applications that require information on the mobility of charge carriers in the analysis of the dielectric behaviour of insulating liquids.

Apart from the mobility of charge carriers, another important parameter – space charge density, can also be obtained from the experimental results presented in this chapter.

According to Equations 2-6 and 2-7, the current density  $J$  can be expressed as a product of the mobility of charge carriers  $\mu$ , the average charge of the charge carriers  $q$ , the field strength  $E$ , and the numbers of charge carriers per unit volume  $n$  :

$$J = n\mu qE \quad 5-3$$

On the other hand, the current density can also be expressed as a function of the electrical conductivity  $\sigma$  and the field strength  $E$  :

$$J = \sigma E \quad 5-4$$

Combination of Equations 5-3 and 5-4 provides the relationship between the electrical conductivity and the mobility of charge carriers:

$$\sigma = nq\mu \quad 5-5$$

In Equation 5-5, the product of  $nq$  provides the space charge density (charge per unit volume) in the dielectric liquids. Using the experimental results obtained and presented in this chapter, it can be found that the mobility values obtained in the same electric field have the same order of magnitude for all three liquids. However, as can be found from the results shown in Table 4-1, the electrical conductivity  $\sigma$  of the MO is two orders of magnitude lower than that of the ester liquids. In this case, according to Equation 5-5, it can be concluded that the space charge density in the MO is lower than that in the ester liquids under the same electric field strength.

This lower space charge density in the mineral oil compared with the ester liquids for the same energisation conditions can be attributed to the difference in the molecular structure of the ester liquids and the mineral oil. As introduced in Section 2.1.2 and 2.1.3, the molecules of the ester liquids contain ester linkages (-COOR), while molecules of typical mineral oils are composed of hydrocarbons. According to Koopman's theorem, the energy required for the ionisation of a molecular system equals the orbital energy of the molecule's typical Highest Occupied Molecular Orbital (HOMO). Thus, the orbital energy of the HOMO from the molecule can be used to estimate the threshold level of energy required for an electron to be removed from the molecule.

In [120], Wang et al. (2018) simulated the energy variation in the HOMO of liquid molecules under an external electric field. In their paper, it was found that the externally applied electric field may result in larger orbital energy changes in the molecules of ester liquids than that in the molecules of mineral oil. This indicates a higher probability for ester molecules to lose an electron(s) in the electric field compared with the mineral oil molecules. Such an analytical conclusion is consistent with the experimental results obtained in the present study, i.e., the

space charge density in the MO is lower than that in the ester liquids under the same electric field strength.

In this chapter, two methodologies of the ToF measurement have been used to obtain the mobility of charge carriers in three dielectric liquids. Based on these results and the corresponding analysis, two main conclusions have been reached:

Firstly, there is a positive correlation between the measured mobility of charge carriers and the corresponding field strength. The reason for this correlation is the EHD effect in the liquid stressed with an external electric field as the EHD motion of the bulk of the fluid is linked with the electrostatic energy in the liquid.

Secondly, based on the relation between the mobility of charge carriers in the liquids and the corresponding space charge density of the liquids (Equation 5-5), the mobilities obtained in three liquids lead to the conclusion that the space charge density in the MO is about two orders of magnitude lower than that in the SE and the NE. As the research objectives of this work include not only pure liquids but also the nanofluids, this conclusion on the space charge density can facilitate analysis of the charge distribution in the nanofluids, which will be presented and discussed in Chapter 8.

Further investigation of the mobility of charge carriers was conducted in the present work using a strongly non-uniform electric field. The results obtained using the SCLC method are presented and discussed in Chapter 6.

# Chapter 6 MOBILITY OF CHARGE CARRIERS: NON-UNIFORM ELECTRIC FIELD

---

The mobility of charge carriers in the pure liquids in virtually uniform electric field obtained under the field magnitudes ranging from 40 kV/m to 1200 kV/m using the ToF method was presented and discussed in Chapter 5.

However, in many practical topologies employed in different power and pulsed power high voltage systems, insulating liquids are stressed with highly non-uniform electric fields. A typical example of such highly divergent electric field is the field generated in a point-plane electrode topology. The maximum field at the tip of the point (needle) electrode is significantly higher than the nominal ‘average’ field in the gap obtained by dividing the applied voltage by the inter-electrode gap. This high electric field leads to the development of the space charge in the inter-electrode gap filled with an insulating fluid. This space charge redistributes the electric field in the gap. Thus, the space charge governed electric field may affect the breakdown voltage in the point-plane topology. Also, the current injected into the gap may lead to potential thermal effects such as the formation of pre-breakdown gas cavities due to the Joule heating of the fluid which may affect the breakdown strength of this liquid-filled gap.

In this chapter, the mobility of charge carriers has been investigated using the SCLC method in the conditions of a highly divergent electric field. The obtained mobility and the electric field in the point plane topology are presented and discussed in this Chapter.

## 6.1 Experimental Procedure

The SCLC method is used to obtain the mobility of charge carriers in the conditions of a highly non-uniform electric field in the Needle-Plane test cell. The principle of the SCLC method was introduced in Section 2.3.2, the point-plane test cell used in this Chapter was discussed in Section 4.3.4. The dielectric liquids used in the SCLC tests are the MIDEL 7131 Synthetic Ester, the MIDEL eN 1204 Natural Ester, and the Shell Diala B Mineral Oil, whose details can be found in Table 4-1 in Section 4.1.1.

According to Section 2.3.2, the mobility of charge carriers can be obtained by analysing the current-voltage squared ( $I-V^2$ ) curve, which should be a straight line in the case of the complete space charge saturated regime of conduction in dielectric liquids. This conduction regime corresponds to the third phase in the I-V graphs in Figure 2-8 in Section 2.2.2. The space charge saturated phase of conduction can be described by the Fowler-Nordheim mechanism, in which the conduction current is presented as a function of the applied voltage in  $\ln(I/V^2)$  vs  $1/V$  coordinates. Using the experimental  $I-V^2$  curves, the mobility of charge carriers can then be obtained by Equation 2-32.

In the present chapter, I-V characteristics of the insulating fluids have been obtained using two ranges of the applied voltages: from 1 kV to 40 kV and from 1 kV to 15 kV.

The first voltage range, 1kV - 40 kV, was used to obtain the conduction current using the current sensing resistor: a voltage drop across this resistor with a value of 1 k Ohm was measured. The plane electrode was virtually grounded using this current viewing resistor. The voltage drop across this resistor was amplified by an INA 114 amplifier and then registered by the Tektronix TBS 1102B oscilloscope. The details of the measuring procedure are presented in Figure 4-15 in Section 4.3.4.

The schematic diagram of the test circuit in which the current was measured using the current viewing resistor is shown in Figure 6-1.

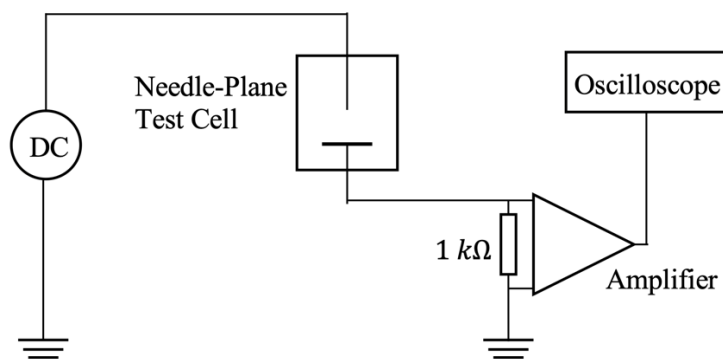


Figure 6-1 Schematic diagram of the current measurement circuit with the current sensing resistor.

The needle-electrode was stressed with the DC voltage, raised in steps of 1 kV from 1 kV to 40 kV. The voltage signal across the current viewing resistor was obtained and saved into a CVS file at each voltage step. Five measurements of the voltage across the current viewing resistor were conducted at each voltage step.

The gain of the amplifier was  $770.05 \pm 30.04$ . As discussed in Section 4.2.2, the actual voltage drop across the current viewing resistor,  $V_c$ , was calculated for each voltage step by multiplied the registered voltage across the resistor by the gain of the amplifier. Then, the conduction current was obtained using the Ohms law. All I-V curves were measured in triplicate using fresh samples of insulating liquids in each test. The surfaces of both electrodes and the test cell were cleaned with ethanol and lint-free tissue after each test.

Although the current-sensing resistor was used for the voltages from 1 kV to 40 kV, it was found that the measured voltage drops across this resistor was virtually constant for applied voltages less than  $\sim 10$  kV. This is because the current through the liquids (and through the current viewing resistor) for such applied voltages was below  $\sim 2$  nA and could not be resolved by the current viewing resistor and the operational amplifier.

Thus, to measure conduction lower currents,  $< 2$  nA, the test cell was virtually grounded through the Keithley 6514 electrometer. In this case, the current was measured directly by the electrometer; however, for safety reasons, the applied voltage was limited by 15 kV to avoid potential breakdown events in the test cell, which could damage the electrometer.

The input of the electrometer was connected to the plane electrode of the point-plane test cell. Figure 6-2 shows the schematic diagram of the current measurement system using the Keithley 6514 electrometer, which served as a virtual ground in the circuit.

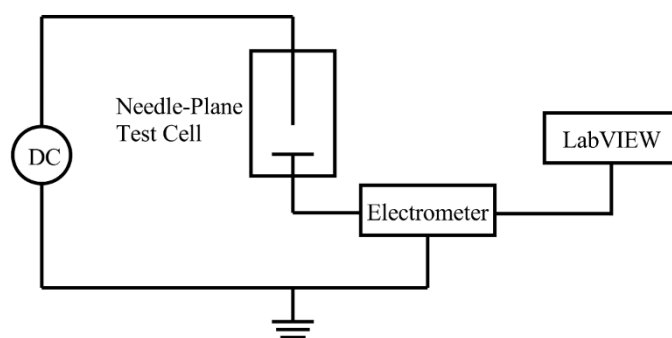


Figure 6-2 Schematic Diagram of Current Measurement Circuit with the Electrometer

Controlled by the LabVIEW code, the Keithley 6514 electrometer provided current reading at the fixed rate of 2 readings per second. The duration of each test was 30 min, which is long enough to ensure the current through the liquids to reach its steady-state condition. The measurements under the same voltage level were repeated three times for each sample. Then the test cell was cleaned and filled with a fresh sample of insulating liquid.

The limitation of this method is a relatively low ( $< 15$  kV) level of the applied voltage. This voltage was not exceeded to minimise potential risk of breakdown events in the tested liquids.

However, this voltage range is sufficient to compliment the voltage range used in the measurements with the current-sensing resistor.

## **6.2 Space Charge Saturation Regime of Conduction and Mobility of Charge Carriers**

As discussed in Section 2.3.2, the mobility of charge carriers can be obtained from the  $I-V^2$  graphs when the space charge in the liquid under the test is saturated. In this section, the experimental current-volt (I-V) characteristics for each tested liquid are presented. Using these I-V characteristics, the Fowler-Nordheim graphs for each liquid were plotted, which allow for the identification of the space charge saturated regions in these graphs. The least squares method was used to plot fitting lines in the Fowler-Nordheim graphs to identify the space charge saturation region, which is described by the  $I-V^2$  dependency. The functional dependency of current on voltage squared in this region is then illustrated to obtain the mobility of charge carriers by Equation 2-32.

### **6.2.1 Mobility of Charge Carriers in Synthetic Ester**

The experimental I-V plots for the SE obtained by the direct current measurements using the electrometer and by the current viewing resistor are presented in Figure 6-3 (a) and (b) respectively. In the current-voltage curve obtained by the current-sensing resistor, every data point in Figure 6-3 (a) represents an average value of three individual tests. In each test, the current measurements were conducted five times for each voltage level. Thus, the average current values shown in Figure 6-3 (a) were calculated using 15 current readings in total. The current measured using the electrometer is shown in Figure 6-3 (b), each data point in Figure 6-3 (b) represents an average value of current obtained in three individual tests. Error bars in this figure represent 95% confidence intervals for current values.

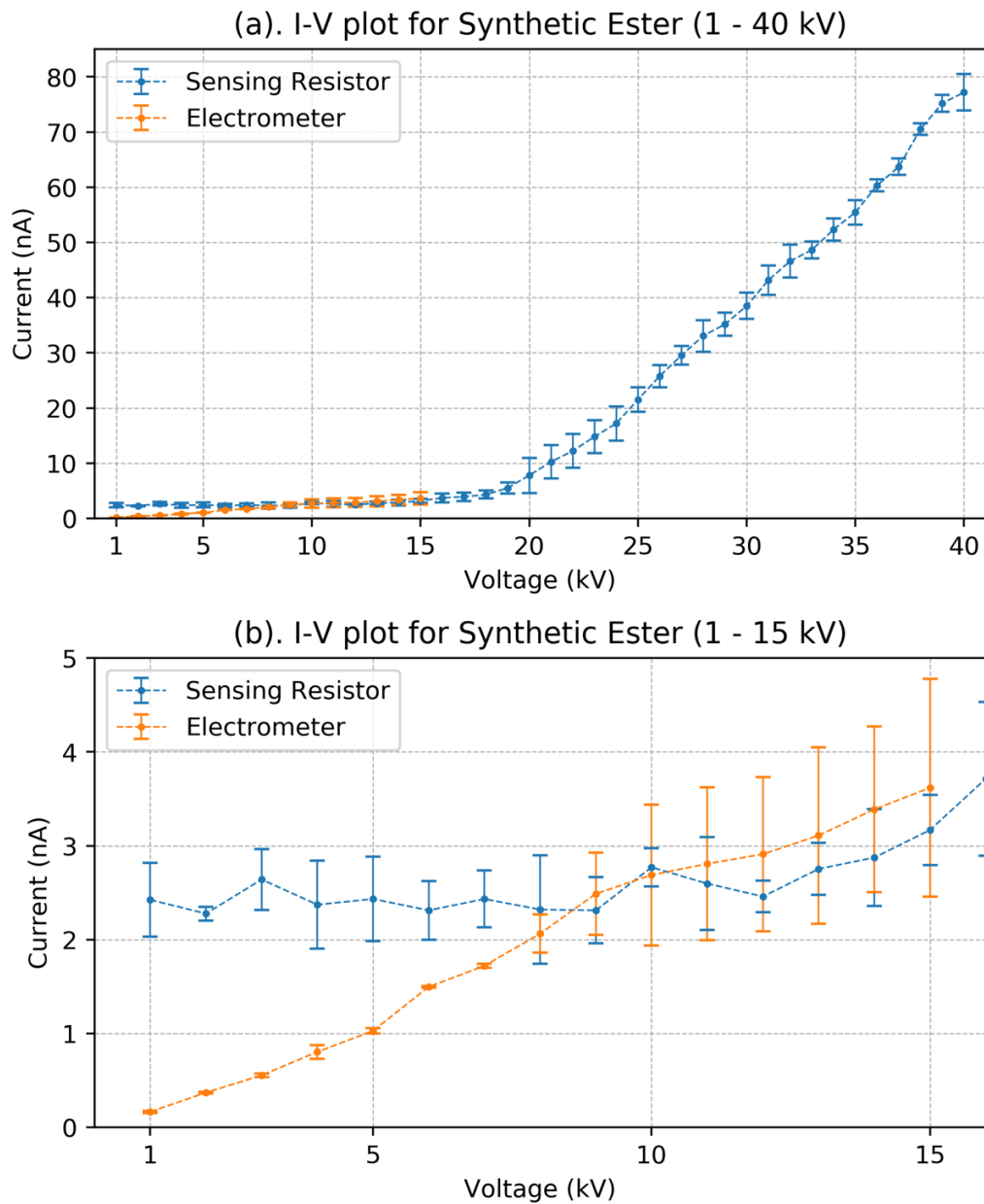


Figure 6-3. I-V plot for the SE: (a) Voltage ranging from 1kV to 40 kV, (b) A zoom-in view for voltages 1kV – 15 kV. The orange dots: current measurements by the electrometer; the blue dots - current measurements by the current-sensing resistor. Error bars indicate 95% confidence intervals.

As shown in Figure 6-3 (b), for the voltages below ~ 15 kV, the current obtained by the current-sensing resistor remains almost constant. In contrast to the current-sensing resistor

method, the I-V curve obtained by the electrometer for voltages below 15kV shows the linear ohmic behaviour, which can be attributed to the higher accuracy of the current measurements carried out by the electrometer for currents below  $\sim (2 - 3)$  nA. Thus, the complete I-V characteristic for the SE can be obtained by merging current values obtained by the electrometer in the range 1 kV - 12 kV and the current values obtained by the sensing resistor for 13 kV – 40 kV. Using this combined I-V characteristic, the Fowler-Nordheim (F-N) graph for the SE was plotted. This graph is presented in Figure 6-4 (a).

As introduced in Section 2.2.2, the Fowler-Nordheim plot has three distinct conduction regions, which can be identified in Figure 6-4 (a): 1 kV – 17 kV refers to Region I, 18 kV – 27 kV refers to Region II, and 28 kV – 40 kV refers to Region III. Practically, the identification of the border between Region I and Region II is straightforward: there is a turning point between these two regions. For the border between Region II and III, it is conducted according to the nature of the region II reflected by Equation 2-14, i.e., the current-voltage relationship is given by a straight line in coordinates  $\ln(I/V^2)$  vs  $1/V$ . Following this, the least squares method was introduced in the border identification; initially several borders were selected approximately. Then the least squares method was applied to these borders and the border whose fitting coefficient is closest to 1 was selected as the border between Region II and Region III. Figure 6-4 (b) and Figure 6-4 (c) are zoom-in views of Region II and Region III, respectively.

Region I (1 kV– 17 kV) is the region that represents the Ohmic conduction due to the intrinsic charge carriers which are present in the fluid at low values of the applied voltage, i.e., high values of  $1/V > 0.059$  ( $\text{kV}^{-1}$ ).

Region II (18 – 27 kV) in the F-N graph represents the conduction which is governed by the charge injection and corresponds to the values of  $1/V$  from  $\sim 0.037$  ( $\text{kV}^{-1}$ ) to  $\sim 0.056$  ( $\text{kV}^{-1}$ ).

Region III (28 – 40 kV) in the F-N graph represents the conduction in the case of complete space charge saturation current where  $\ln(I/V^2)$  values show a quasi-constant behaviour. Region III corresponds to the high values of the applied voltage, i.e., low values of  $1/V$ ,  $< 0.036$  ( $\text{kV}^{-1}$ ).

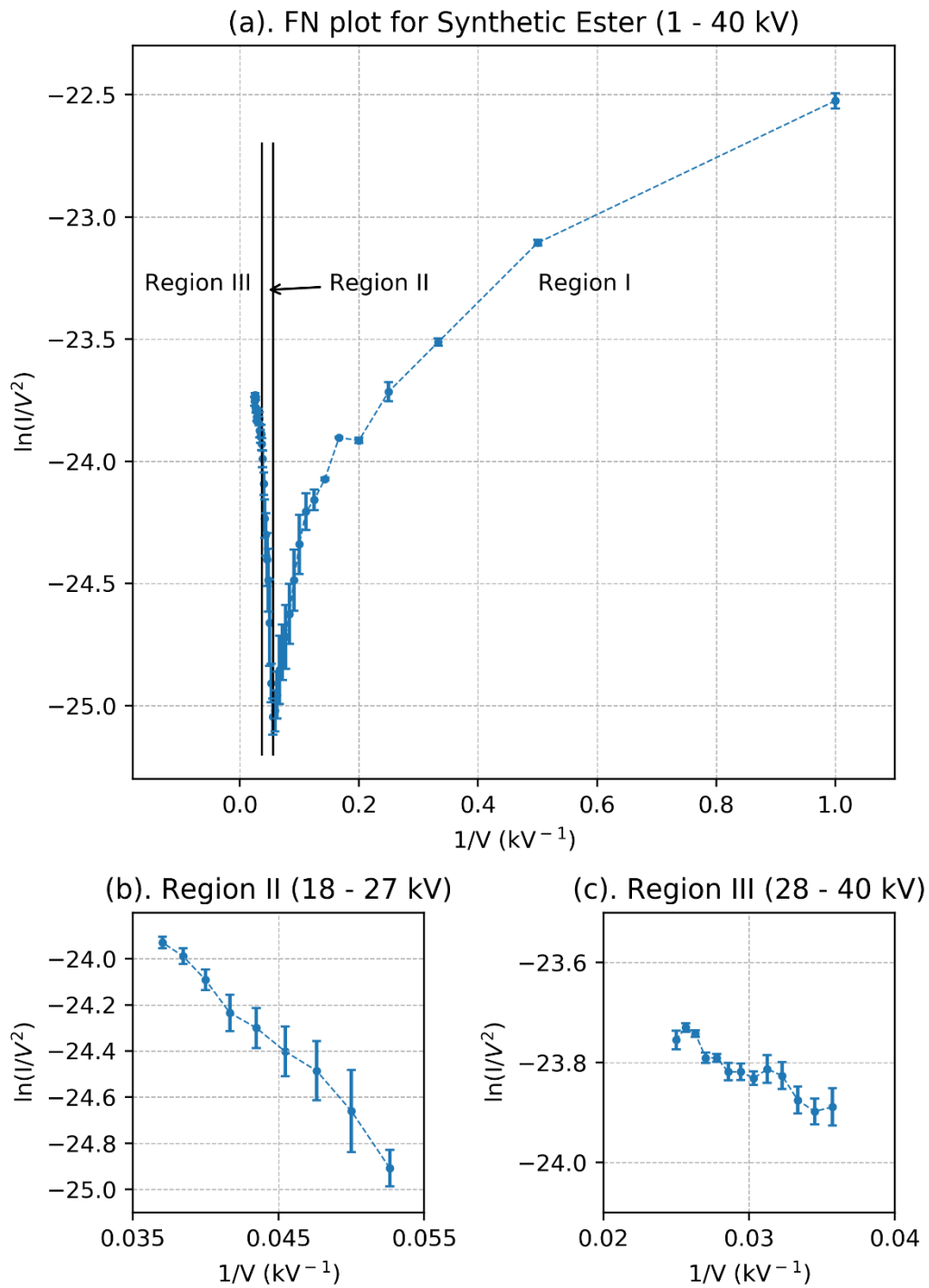


Figure 6-4 Fowler-Nordheim (FN) plot for the SE, (a) FN plot for the SE from 1kV- 40 kV, (b) A zoom-in of Region II, (c) A zoom-in of Region III. Error bars indicate 95% confidence intervals.

Using Equation 2-32, the mobility of charge carriers can be obtained from the  $I-V^2$  characteristics of the liquid when the current is a space charge saturated current, which corresponds to Region III in the F-N graph. As Region III for the SE is found to be between 28 kV and 40 kV as shown in Figure 6-4 (c), the  $I-V^2$  plot for the SE for this range of voltages, from 28 kV to 40 kV, is shown in Figure 6-5.

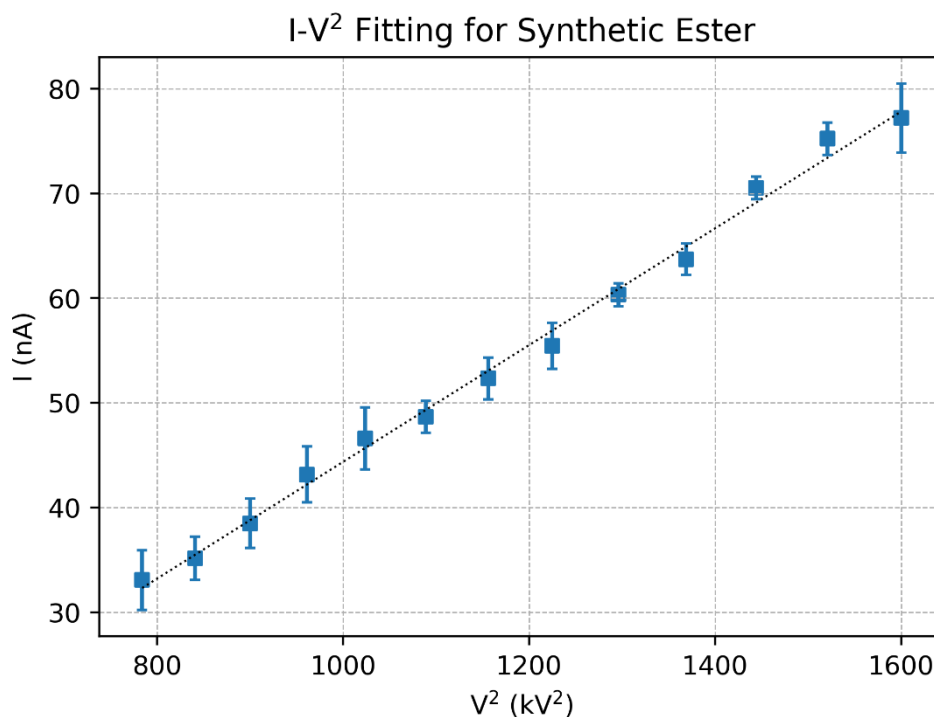


Figure 6-5.  $I-V^2$  Plot for the SE: Experimental data (blue dots, each dot is an average of 15 current values) and the best fit line (dotted line) based on the least-square fitting. Error bars indicate 95% confidence intervals.

In Figure 6-5, the experimental current values are shown as blue dots. Each value is an average of 15 current measurements. The experimental data in the  $I-V^2$  coordinates in Figure 6-5 were fitted with a straight line using the least squares method. The goodness of the coefficient ( $R^2$ ) of the fitting line is 0.972. Thus, the experimental data can be fitted with a straight line in the

I-V<sup>2</sup> coordinates, which confirms the complete space charge saturation regime of the current. The slope of this straight line in the I-V<sup>2</sup> coordinates was used to obtain the mobility of charge carriers according to Equation 2-32. It was found that the mobility of charge carriers in the SE is  $(5.04 \pm 1.17) \cdot 10^{-9} \text{ m}^2/(\text{V} \cdot \text{s})$ .

## **6.2.2 Mobility of Charge Carriers in Natural Ester**

The experimental current-volt (I-V) curves of the NE are presented in Figure 6-6 (a) and (b). The current values obtained for the NE have been processed in the same way as in the case of the SE: the current values obtained by the current-sensing resistor were averaged using the data from three individual tests in which five values of current were obtained for each voltage level (15 current readings in total). Every data point from the electrometer in Figure 6-6 represents an averaged conduction current from three individual tests. Error bars in Figure 6-6 show the 95% confidence intervals.

As introduced in Section 6.1, there is a transition between the current values obtained by the current viewing resistor and the electrometer. For low voltages (below this transition level), the Ohmic behaviour in the I-V curves is observed only in the case of the measurements performed by the electrometer. Compared with the I-V characteristic of the SE (Figure 6-3 (a) and (b)), the current in the NE (Figure 6-6 (a) and (b)) is higher under the same voltage level.

The complete I-V characteristic for the NE was obtained by merging the current values obtained by the electrometer in the 1 – 10 kV range with the current values obtained by the electrometer in the range from 11 kV – 40 kV. The F-N graph for the NE developed using this combined I-V characteristic is shown in Figure 6-7 (a).

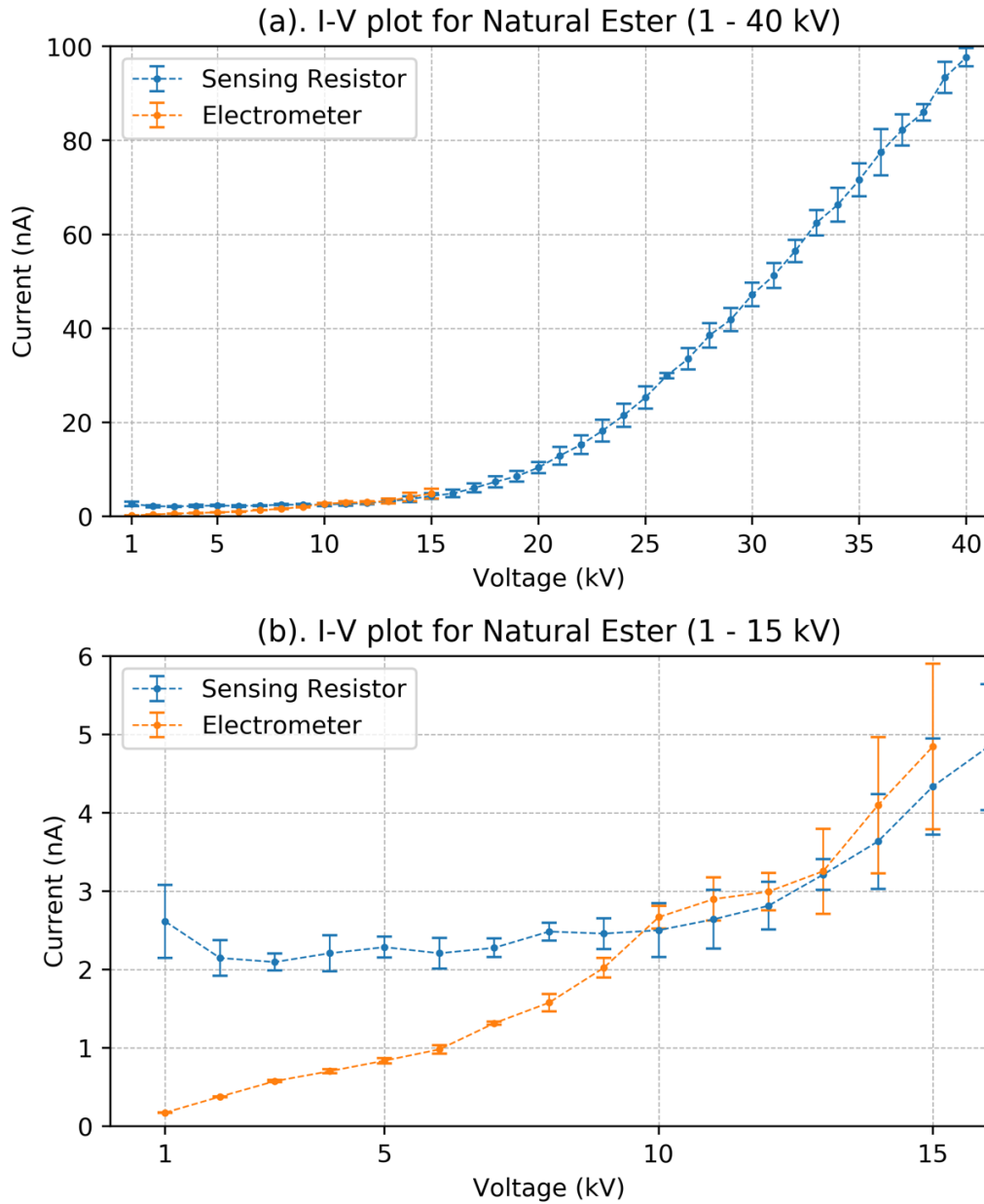


Figure 6-6 I-V plot for the NE: (a) Voltage ranging from 1kV to 40 kV, (b) A zoom-in view for voltages 1kV – 15 kV. The orange dots: current measurements by the electrometer; the blue dots - current measurements by the current-sensing resistor. Error bars indicate 95% confidence intervals.

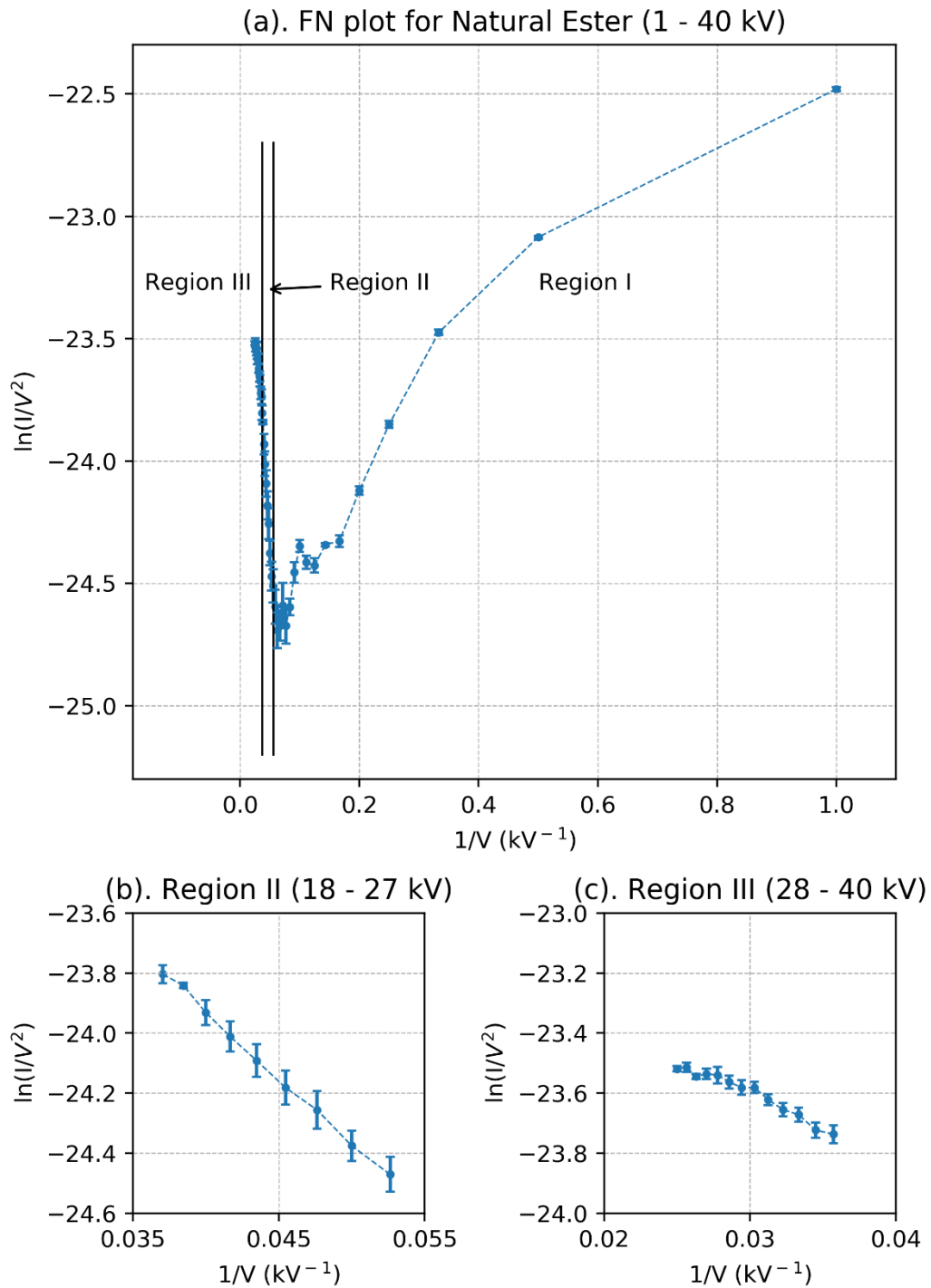


Figure 6-7 Fowler-Nordheim (F-N) graph for the NE, (a) F-N graph for the NE from 1-40 kV, (b) A zoom-in view of Region II, (c) A zoom-in view of Region III. Error bars indicate the 95% confidence intervals.

In Figure 6-7 (a), three distinct regions in the F-N graph for the NE can be identified: Region I, 1 – 17 kV; Region II, 18 – 27 kV, and Region III, 28 – 40 kV. The relative values of  $1/V$  are above  $\sim 0.059$  ( $\text{kV}^{-1}$ ) in Region I;  $\sim 0.037$  ( $\text{kV}^{-1}$ ) to  $\sim 0.056$  ( $\text{kV}^{-1}$ ) in Region II, and below  $\sim 0.036$  ( $\text{kV}^{-1}$ ) in Region III. It is found that these three conduction regions identified in the NE and the SE are the same, which can be attributed to the similarity in their chemical composition. To present the details of Region II and Region III of the NE, the zoom-in plots of these two regions are shown in Figure 6-7 (b) and Figure 6-7 (c), respectively.

As introduced in the previous section, Region I of the F-N graph (1 – 17 kV for the NE) represents the Ohmic conduction due to intrinsic charge carriers in the fluid. Region II (18 – 27 kV for the NE) represents the conduction that is governed by the charge injection.

Region III in the F-N graph (28 – 40 kV for the NE) represents the conduction in the case of the complete space charge saturation regime where the obtained current shows a quasi-constant behaviour in  $\ln(I/V^2)$  coordinates. The  $I-V^2$  part of this region can be used to calculate the mobility of charge carriers using Equation 2-23. Region III for the NE, which represents the  $I-V^2$  part, is shown in Figure 6-8. A straight line representing the least square fitting to the experimental  $I-V^2$  data is also included in Figure 6-8.

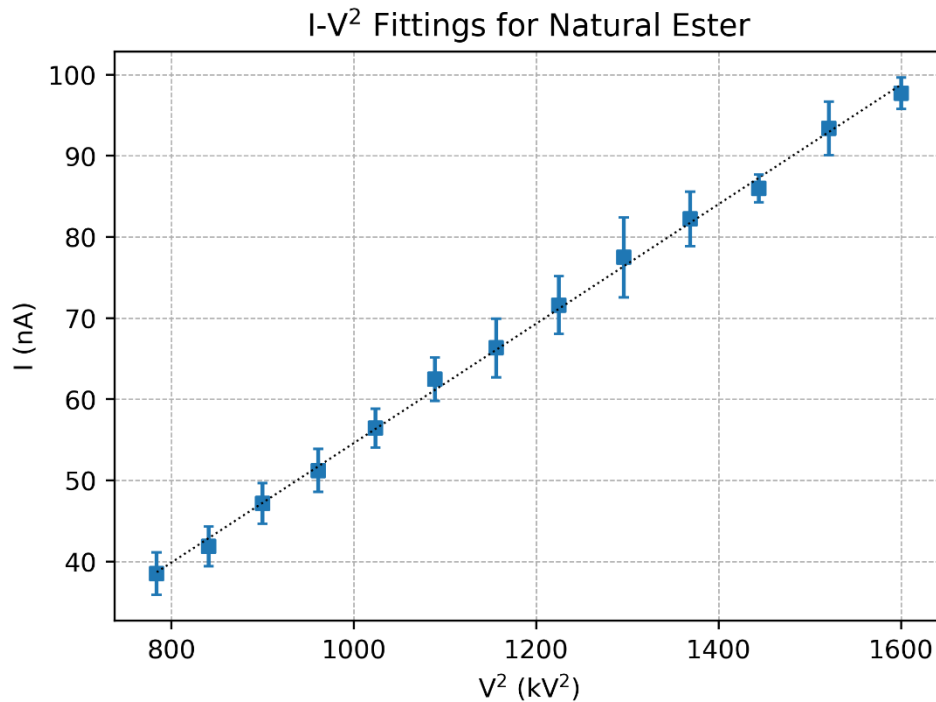


Figure 6-8. I-V<sup>2</sup> Plot for the NE. The blue dots represent experimental current data (average value of 15 readings). The dotted line is the least-square fitting to the experimental data. Error bars indicate 95% confidence intervals.

In Figure 6-8, the blue dots represent the experimentally obtained current, each point is an average of 15 current readings in total. The goodness of fit coefficient ( $R^2$ ) of the least square fitting line in Figure 6-8 is 0.993. Using the slope of this fitting line and Equation 2-32, the mobility of charge carriers in the NE was obtained and found to be:  $(5.96 \pm 0.72) \cdot 10^{-9} \text{ m}^2/(\text{V} \cdot \text{s})$ .

### 6.2.3 Mobility of Charge Carriers in Mineral Oil

Figure 6-9 (a) and (b) shows the experimental I-V characteristics of the MO obtained by both methods, using the electrometer and the current-sensing resistor.

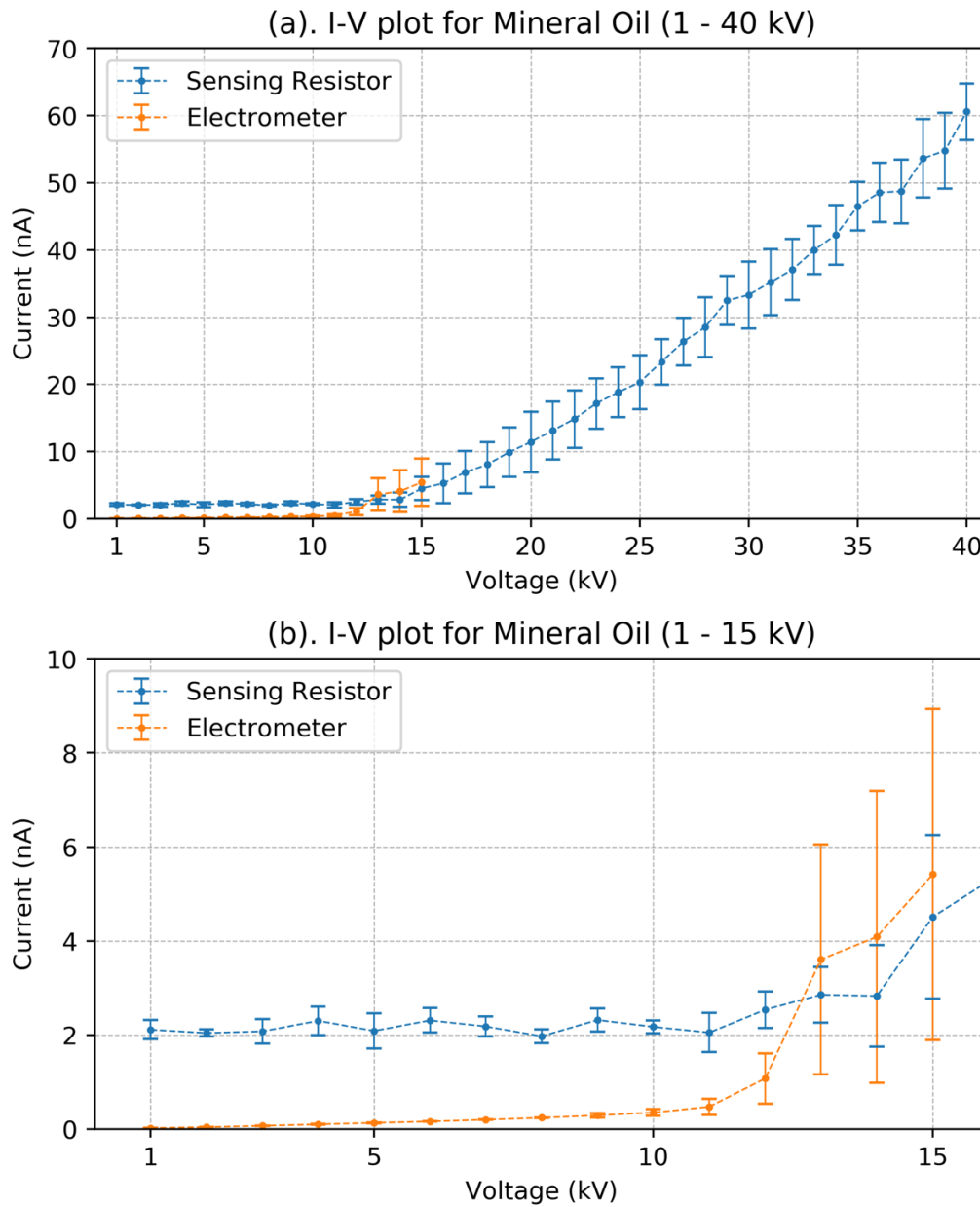


Figure 6-9. I-V plot for the MO: (a) Voltage ranging from 1kV to 40 kV, (b) A zoom-in view for voltages 1kV – 15 kV. The orange dots: current measurements by the electrometer; the blue dots - current measurements by the current-sensing resistor. Error bars indicate 95% confidence intervals.

For the current obtained by the current-sensing resistor, every data point in Figure 6-9 represents an averaged current reading from three individual tests and was calculated using 15 current measurements in total. For the current values obtained by the electrometer, every data point in Figure 6-9 represents the current value which is an average of three individual tests. The error bars show the 95% confidence intervals.

Due to the low electric conductivity of the MO, the current in the MO is lower than in both esters fluids under the same voltage, which is shown in Figure 6-9 (a). According to Figure 6-9 (b), 13 kV is the critical voltage for the MO, below which the ohmic behaviour of the current in the tested liquid can only be resolved using the electrometer. Following the same procedure presented in two previous sections, a new combined I-V characteristic for the MO consisting of the current values obtained by the electrometer for 1 kV to 13 kV and by the sensing resistor between 14 kV to 40 kV was obtained. Based on this new I-V characteristic, the F-N graph for the MO was plotted and is given in Figure 6-10.

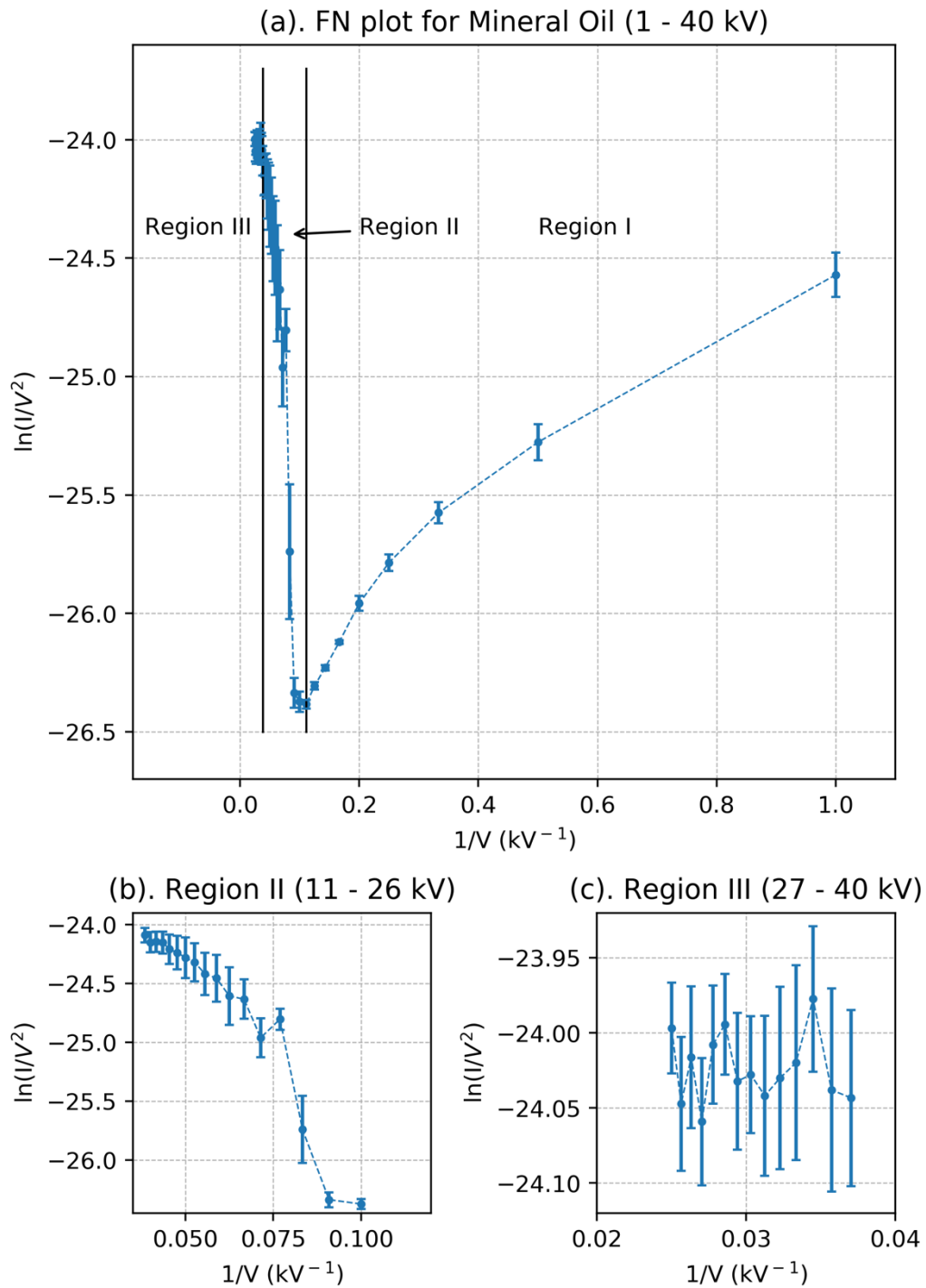


Figure 6-10 Fowler-Nordheim (F-N) graph for the MO, (a) FN plot for the SE from 1kV-40 kV, (b) A zoom-in of Region II, (c) A zoom-in of Region III. Error bars indicate 95% confidence intervals.

In Figure 6-10 (a), three distinct regions in the F-N graph for the MO can be identified: Region I, 1 – 10 kV; Region II, 11 – 26 kV, and Region III, 27 – 40 kV. The relative values of  $1/V$  are above  $0.1 \text{ (kV}^{-1}\text{)}$  in Region I;  $\sim 0.091 \text{ (kV}^{-1}\text{)}$  to  $\sim 0.038 \text{ (kV}^{-1}\text{)}$  in Region II, and below  $\sim 0.037 \text{ (kV}^{-1}\text{)}$  in Region III. There is a significant difference between the F-N graph for the MO and F-N graphs for two esters presented before. The voltage range of Region I for the MO (1 – 10 kV) is smaller than that of the esters (1 – 17 kV). This difference shows that the charge injection threshold for the MO is lower than for the ester liquids. To present the details of Region II and Region III, the zoom-in plots of these two regions are shown in Figure 6-10 (b) and Figure 6-10 (c), respectively.

Using Equation 2-32, the mobility of charge carriers in the MO can be obtained from the space charge saturated  $I-V^2$  characteristics, which corresponds to Region III in the FN plot. As Region III for the MO is found to be 27 - 40 kV as shown in Figure 6-10 (c), the  $I-V^2$  plot for the MO for this range of voltages is given in Figure 6-11.

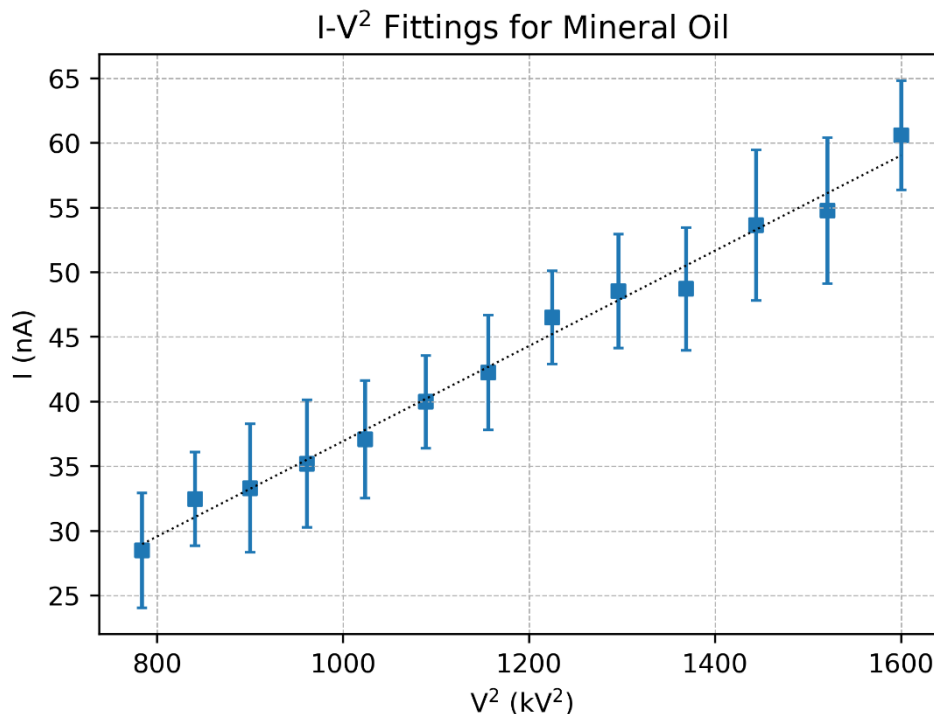


Figure 6-11  $I-V^2$  Plot for the MO: Experimental data (blue dots, each dot is an average of 15 current values) and the best fit line (dotted line) based on the least-square fitting. Error bars indicate 95% confidence intervals.

In Figure 6-11, the experimental current values are shown as blue dots. Each value is an average of 15 current measurements. The goodness of the fit coefficient ( $R^2$ ) of the least square fitting line in Figure 6-11 is 0.988. The slope of this straight line in the  $I$ - $V^2$  coordinates was used to obtain the mobility of charge carriers using Equation 2-32. It was found that the mobility of charge carriers in the MO is  $(4.55 \pm 0.82) \cdot 10^{-9} \text{ m}^2/(\text{V} \cdot \text{s})$ .

## **6.3 Space Charge Governed Electric Field**

As discussed at the beginning of this chapter, the introduction of the SCLC method into this study is based on two considerations: one is that the SCLC method enables the mobility of charge carriers to be obtained in a much higher electric field ( $>10^4 \text{ kV/m}$ ), supporting the investigation of potential dependency of the mobility on the field strength. Another consideration is related to practical applications, i.e., highly non-uniform electric fields in practical electrical systems, which requires the study of the effect of injection of charges on the field strength re-distribution in the liquid. The analysis of the field strength in the Needle-Plane topology is based on the assumption of the full space charge saturation regime, which is a different approach compared with the case of the uniform electric field. The space charge is injected into the liquid into the vicinity of the needle HV electrode. In [62], theoretical analysis of the field in the vicinity of the needle tip is provided, which results in redistribution of the field in the needle-plane gap.

### **6.3.1 The Field Strength of the Needle Tip**

As discussed in Section 2.3.2, the electric field distribution in the point plane topology will be governed by the space charge injected into the liquid. In [62], it is assumed that the conduction current is the steady-state current and the mobility of the charge carriers is assumed to be independent from the field strength, also it is assumed that the diffusion current is assumed to be negligible with respect to the conduction current. Following this, the analytical expression for the field along the central axis of the point-plane configuration in the case of the space charge saturation is given as [62]:

$$E(v) = \frac{\sqrt{\rho^2(2 - \rho)^2 E_p^2 - Av \left[ \rho(2 - \rho) + v(1 - \rho) - \frac{v^2}{3} \right]}}{(v + \rho)(2 - v - \rho)} \quad 6-1$$

where,  $v = x/a$ , and  $\rho = r/2a$ ,  $a$  is the sum of the needle tip radius and the distance between the point at the needle tip to the plane electrode,  $x$  is the distance from the needle tip to the plane electrode, and  $r$  is the radius of the tip apex, the details of these parameters can be found in Figure 2-13 in Section 2.3.2.

In this analysis, the radius of the tip apex  $r$  is 20  $\mu\text{m}$  (as shown in Figure 4-14). Since the distance between the point at the needle tip and the plane electrode is 10 mm (Figure 4-13), which is three orders of magnitude longer than the radius of the tip apex  $r$ , the value for  $a$  is taken as 10 mm.

The factor  $A$  in Equation 6-1 can be calculated using the current  $I$ , the relative permittivity of the liquids  $\epsilon_r$ , and the mobility  $\mu$  of the charge carriers in the liquids:

$$A = \frac{2I}{\pi a \epsilon_r \epsilon_0 \mu} \quad 6-2$$

Term  $E_p$  in Equation 6-1 can be approximated as the electric field strength at the point apex. The value for  $E_p$  can be obtained by fitting the experimental current and corresponding voltage data using Equation 2-31 in Section 2.3.2.

In this research, the mobility of charge carriers and the I-V characteristic in all three liquids (SE, NE, and MO) were obtained and discussed in Section 6.2. Thus, the approximation for  $E_p$  was conducted using the following procedure: for each specific liquid, i.e., the SE, the NE, or the MO, the mobility of charge carriers and the experimental I-V characteristic which corresponds to Region III of the F-N graph were used in Equation 6-1. Thus, field  $E(v)$  can be expressed using two independent variables from Equation 6-1:  $E_p$  and  $v$ . With this new expression for  $E(v)$  and a numerical range set for  $E_p$ , the voltage drop between the needle tip and the ground plate can be obtained by Equation 2-31. Then the numerical value of  $E_p$ , which

yields the minimum Mean Squared Error (MSE) between the calculated and the experimental voltage drops, is selected as a nominal of  $E_p$  for this system

Using experimental I-V characteristics obtained in three independent tests, three nominal values of  $E_p$  were obtained for each liquid, their averaged values with uncertainties are listed in Table 6-1. Each uncertainty was calculated as a 95% confidence interval using the Student distribution (t factor of 4.303 for 95% confidence interval).

Table 6-1  $E_p$  values of the three liquids

	<b>Synthetic Ester</b>	<b>Natural Ester</b>	<b>Mineral Oil</b>
$E_p$ (kV/m)	43295.392 ±3827.939	36742.871 ±2128.070	16295.009 ±8531.354

The results in Table 6-1 show the statistically significant difference in  $E_p$  values obtained for two esters and the mineral oil:  $E_p$  values for two ester liquids are more than twice higher than the  $E_p$  value for the mineral oil. This indicates significantly higher electric field strength in the vicinity of the needle electrode in the ester liquids compared with the mineral oil under the same voltage. These results can be used in the design of electrical insulation in high voltage power or pulsed power system.

### **6.3.2 Field Distribution in the Point-Plane Topology**

Using  $E_p$  and the mobility of charge carriers presented in Section 6.3.1 and Section 6.2, respectively, the electric field strength distribution along the central axis of the point-plane topology can be obtained by Equation 6-1. The electric field strength varies with the current and the electric field distribution was obtained using different I-V characteristics from Region III for each liquid. The resulting field distribution for the SE, the NE, and the MO are shown in Figure 6-12, Figure 6-13, and Figure 6-14 respectively.

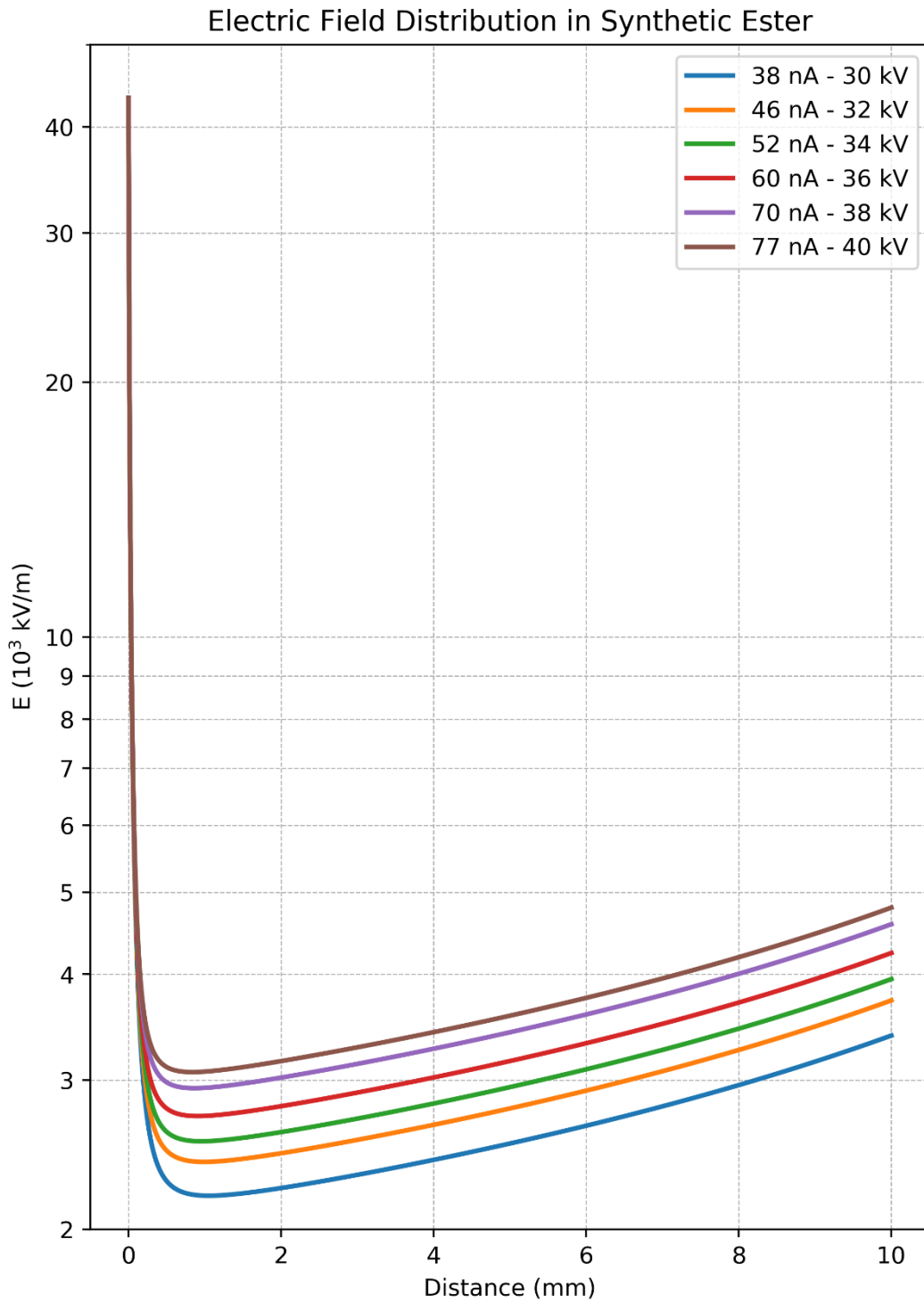


Figure 6-12 Electric field strength along the central axis of the needle-plane configuration based on different I-V characteristics of the Synthetic Ester. A distance of 0 mm corresponds to the needle tip (anode), and a distance of 10 mm corresponds to the grounded plane (cathode); the field strength at the needle tip ( $E_p$ ) was set at 43295.392 kV/m.

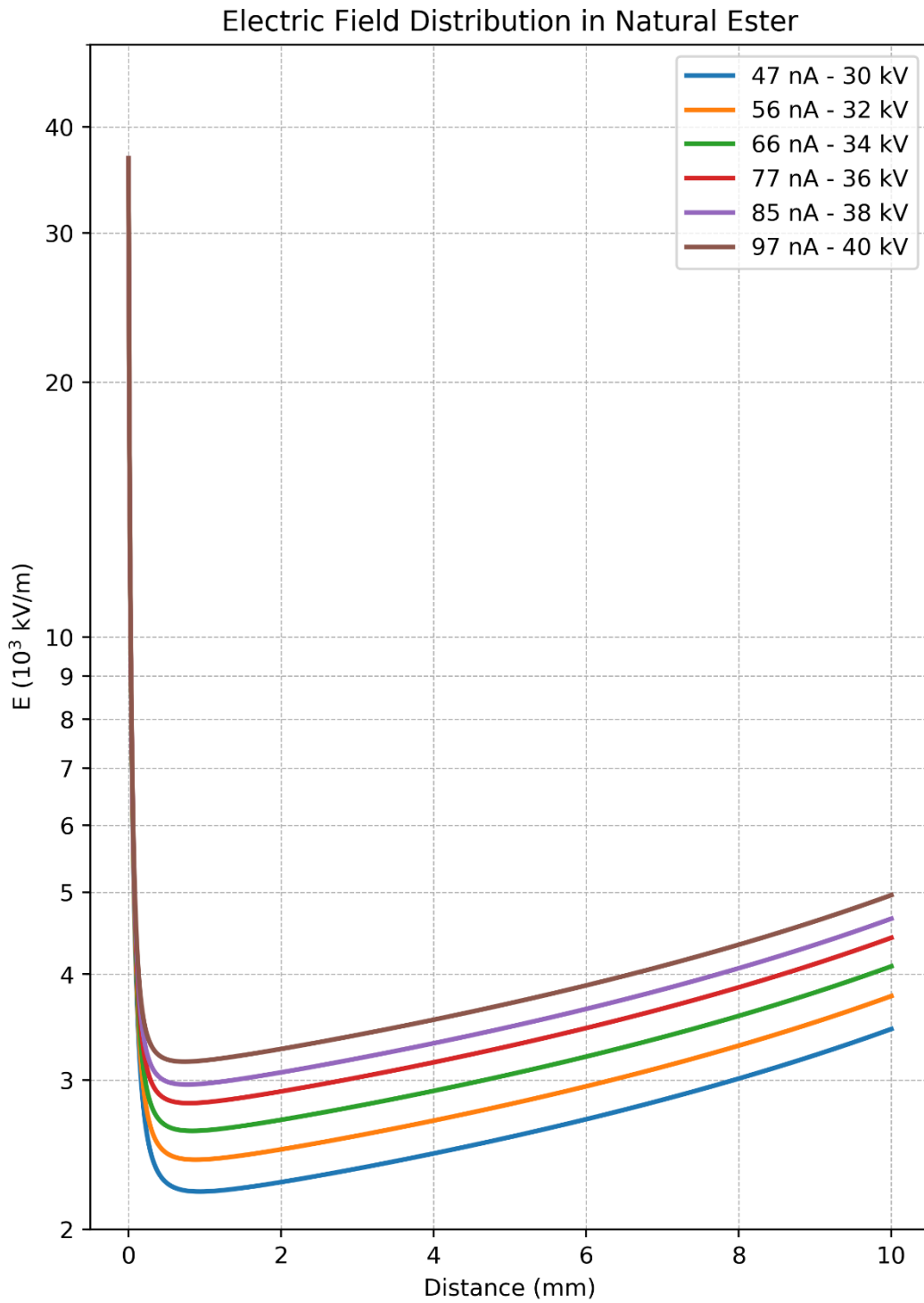


Figure 6-13 Electric field strength along the central axis of the needle-plane configuration based on different I-V characteristics of the Natural Ester. A distance of 0 mm corresponds to the needle tip (anode), and a distance of 10 mm corresponds to the grounded plane (cathode); the field strength at the needle tip ( $E_p$ ) was set at 36742.871 kV/m.

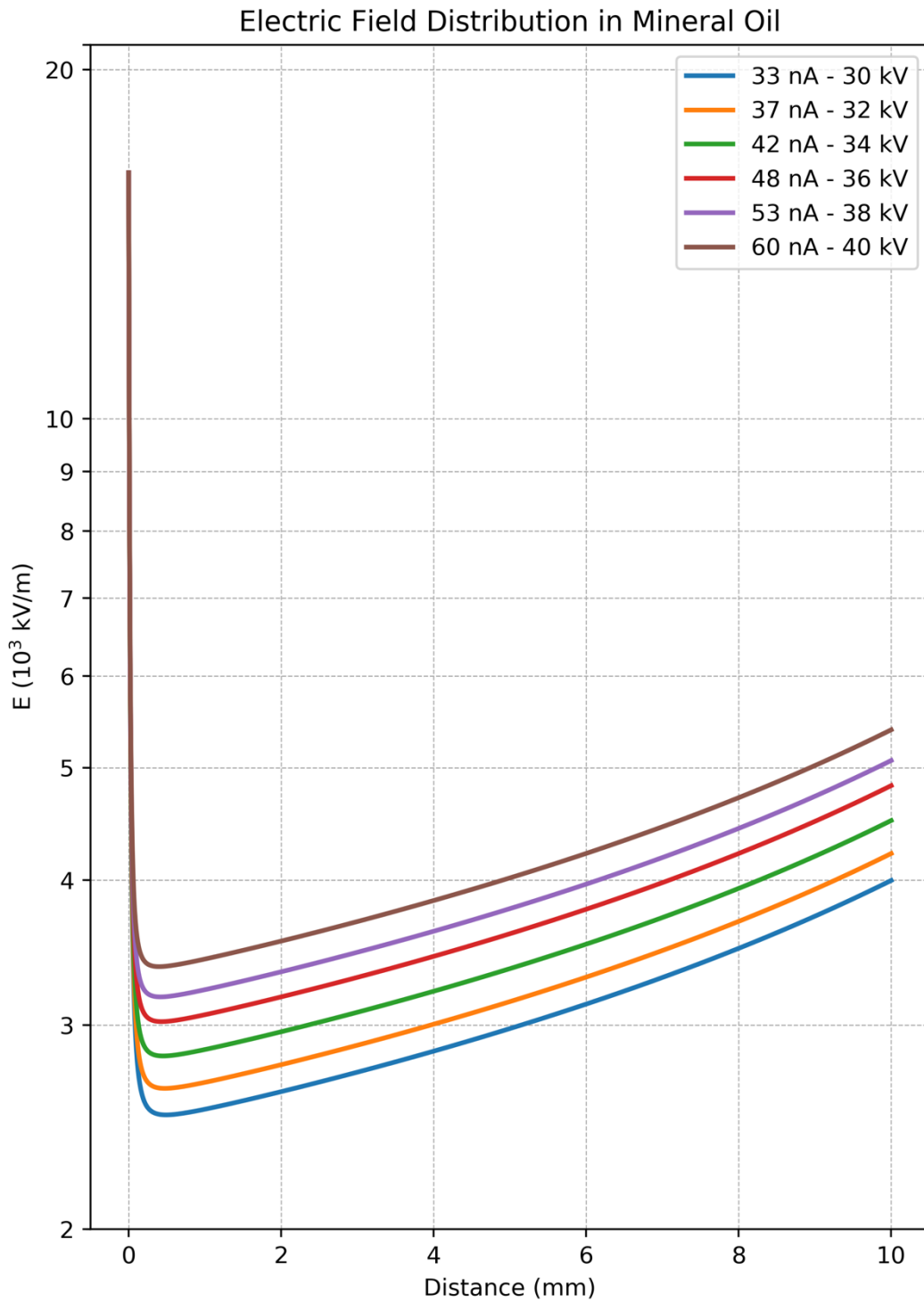


Figure 6-14 Electric field strength along the central axis of the needle-plane configuration based on different I-V characteristics of the Mineral Oil. A distance of 0 mm corresponds to the needle tip (anode), and a distance of 10 mm corresponds to the grounded plane (cathode); the field strength at the needle tip ( $E_p$ ) was set at 16295.477 kV/m.

It can be seen from Figure 6-12, Figure 6-13, and Figure 6-14 that the electric field strength drops quickly when the distance from the tip increases. Although the electric field strength near the needle tip in the MO is significantly lower than that for the esters, the field strength in the middle of the gap is similar for all three liquids:  $\sim (2 - 5) \cdot 10^9$  kV/m.

As introduced at the beginning of this chapter, one of the aims of this investigation is to establish potential dependency of the mobility on the electric field. This analysis requires not only the mobility which is obtained from experiments but also the relative electric field strength. Since the main effect on the  $I-V^2$  curves in the SCLC method is provided by the charge carriers near the needle tip, the electric field strength in the vicinity of the tip is used in the analysis.

The field distribution in the point-plane topology filled with different liquids presented in this section also provides the baseline reference data for the direct comparison between the liquids in the Needle-Plane configuration. These results can be used for analysis of the breakdown voltage in high voltage electrical power systems.

## **6.4 Discussion and Summary**

In this chapter, the conduction currents in the SE, NE, MO under DC voltage in the range from 1 kV to 40 kV have been obtained using the Needle-Plane electrode topology. Based on the I-V characteristics obtained, the Fowler-Nordheim graphs for all three liquids have been plotted to identify the voltage range where the space charge saturated regime is achieved. The mobility of charge carriers was obtained based on the  $I-V^2$  characteristics in the space charge saturated regime of conduction.

Using the obtained mobilities, the electric field distribution along the central axis in the needle plane electrode configuration was obtained and presented for three liquids. These results can be used to evaluate the breakdown voltages in the case of highly divergent fields in liquid dielectrics.

The positive correlation between the mobility of charge carriers and the electric field strength has been established and discussed in Section 5.4 in the previous chapter. The mobility of

charge carriers in the three dielectric liquids (the SE, NE, and MO) was obtained in Section 5.4 using the ToF method and found to be  $\sim (1 - 7) \cdot 10^{-9} \text{ m}^2/(\text{V}\cdot\text{s})$  at  $(4 - 8) \cdot 10^6 \text{ kV/m}$  and  $\sim (1 - 3) \cdot 10^{-9} \text{ m}^2/(\text{V}\cdot\text{s})$  at  $(0.4 - 1.2) \cdot 10^8 \text{ kV/m}$ . The mobility of charge carriers in the three dielectric liquids (the SE, NE, and MO) obtained by the SCLC method in the present Chapter is  $\sim (4 - 6) \cdot 10^{-9} \text{ m}^2/(\text{V}\cdot\text{s})$  at  $(1.6 - 4.3) \cdot 10^9 \text{ kV/m}$ . These mobility values also demonstrate a positive correlation with the field strength.

The results obtained using the ToF method prove that the charge density in the ester liquids is higher than that in the MO, which is discussed in Section 5.4. The mobility of charge carriers in the liquids obtained by the SCLC method has the same order of magnitude as in the case of the mobility obtained by the ToF method. At the same time, the electrical conductivity of the MO ( $7.5 \cdot 10^{-14} \text{ S/m}^2$ ) is about two orders of magnitude lower than that of the ester liquids ( $4.5 \cdot 10^{-12} \text{ S/m}^2$  for the SE;  $5 \cdot 10^{-12} \text{ S/m}^2$  for the NE). Thus, according to Equation 5-5 in Section 5.4, the results of the SCLC measurements are also in agreement with the conclusion that the space charge density in the esters is higher than that in the mineral oil. This difference can be attributed to the different molecular structures, which have been explained in Section 5.4.

In this research, both the ToF and the SCLC methods have been used to obtain the mobility of charge carriers under various electric fields. Implementing the SCLC method has significantly extended the range of the electric fields from  $\sim 1.2 \cdot 10^8 \text{ kV/m}$  to  $\sim (1.6 - 4.3) \cdot 10^9 \text{ kV/m}$ . At the same time, although the SCLC method of obtaining mobility differs from the ToF method, the conclusions derived from both methods are in good agreement with each other, which enhances the credibility of the obtained results.

To achieve comprehensive understanding of the mobility behaviour, the mobility values for esters and mineral oils reported in the literature are presented in Table 6-2.

Table 6-2 Mobility of charge carriers from literature data

Method	Author	Liquid	Field Strength (kV/m)	Mobility (m <sup>2</sup> /(V•s))
SCLC	Butcher [121]	Univolt 61 (MO)	~ 10,000	$2.9 \cdot 10^{-7}$
	Li [122]	Karamay 25# (MO)	~ 7,600-9,600	$2.9 \cdot 10^{-9}$
	Jing [123]	Diala S3 (MO)	N/A	$1.2 \cdot 10^{-7}$
		MIDEL 7131 (SE)		$1.4 \cdot 10^{-7}$
		Rapeseed Oil (NE)		$1.3 \cdot 10^{-7}$
Atten [124]	Mineral Oil	N/A	$1.6 \cdot 10^{-7}$	
ToF	Chen [125]	Diala S3 (MO)	70	$7.5 \cdot 10^{-10}$
	Yang [126]	Mineral Oil A	2.5 - 100	$7.1 \cdot 10^{-10}$
		Mineral Oil B		$2.5 \cdot 10^{-9}$
		Mineral Oil C		$4.6 \cdot 10^{-10}$
	Zadeh [127]	Mineral Oil	~ 4 - 200	$2.6 \cdot 10^{-9}$
		Natural Ester		$1.7 \cdot 10^{-10}$
	Lv [128]	Karamay 25# (MO)	150	$1.5 \cdot 10^{-9}$
	Mahidhar [117]	MIDLE 7131 (SE)	12.5 - 100	$\sim (0.5-1.1) \cdot 10^{-9}$
TO335 (MO)		$\sim (1-2.2) \cdot 10^{-9}$		

From Table 6-2, it can be found that the mobility obtained by the SCLC method is typically higher than the mobility obtained by the ToF method. For example, the mobility obtained by the SCLC method is  $\sim 10^{-7} \text{ m}^2/\text{Vs}$  except for the result from [126] (a detailed discussion of this result is presented in the discussion section of this chapter). On the other hand, the mobilities obtained by the ToF method are typically below  $2.6 \cdot 10^{-9} \text{ m}^2/(\text{V}\cdot\text{s})$  [127]. The main reason for this difference is the higher electric field strength in the SCLC method than in the ToF method. As the SCLC method assumes that the space charge in the tested liquids is saturated, it requires a higher electric field strength for successful SCLC measurements. This contrasts with the ToF measurements, which are typically conducted under significantly lower electric field to minimise the electrohydrodynamic effects.

Besides, as shown in Table 6-2, the mobility obtained in the Karamay 25# mineral oil by Li (2018) [122] is  $2.6 \cdot 10^{-9} \text{ m}^2/(\text{V}\cdot\text{s})$ , which is significantly lower than the mobilities obtained in mineral oils using the SCLC method by other researchers:  $\sim (1.2\text{-}2.9) \cdot 10^{-7} \text{ m}^2/(\text{V}\cdot\text{s})$  [121] [123] [124]. The main reason for this lower mobility could be the configuration of the test cell used in [126]. To review all results obtained by the SCLC method, the test cell configurations and equations used to calculate the mobility in the SCLC method are summarised and presented in Table 6-3.

The terms in equations shown in Table 6-3 are defined as follows:  $I$  is the current through the tested liquids,  $\epsilon_0$  and  $\epsilon_r$  is the vacuum permittivity and relative permittivity, respectively.  $V$  is the voltage across the tested liquids, and  $d$  is the distance between the needle and the electrode plane,  $\mu$  is the mobility of charge carriers in the liquids.

Table 6-3 Equations for obtaining the mobility by the SCLC method

Author	Equation	Test Cell Configuration	Configuration Details
Butcher [121]	$I = 0.71\epsilon_0\epsilon_r\mu \frac{V^2}{d}$	Needle-Plane	Needle Tip Radius: 10 $\mu\text{m}$ Separation: 10 mm
Li [122]	$I = 0.33\epsilon_0\epsilon_r\mu \frac{V^2}{d}$	Plane-Plane	Plane diameter: 25 mm Separation: 10 mm
Jing [123]	$I = 2\epsilon_0\epsilon_r\mu \frac{V^2}{d}$	Needle-Plane	Needle Tip Radius: 8 $\mu\text{m}$ Separation: 5 mm
Atten [124]	$I = 4.02\epsilon_0\epsilon_r\mu \frac{V^2}{d}$	Needle-Plane	Needle Tip Radius: 3 $\mu\text{m}$ Separation: 12 mm

It can be seen from Table 6-3 that the Plane-Plane configuration was only utilised in [122]. This is because that the Needle-Plane configuration typically requires a lower voltage level than the Plane-Plane configuration to achieve the same maximum electric field strength due to the highly divergent electric field near the needle tip. Therefore, compared with the Plane-Plane configuration, the Needle-Plane configuration is more widely used in the mobility measurement by the SCLC method.

The numerical factors in the equations shown in Table 1.3 differ from each other. This can be attributed to the different considerations on describing the development of the space charge. The formula from [121] is taken from [61], this equation was used for liquid hydrogen, nitrogen, and oxygen. The formula used in [122] stems from the Mott-Gurney (MG) law, which was more used with solids [129]. The formula utilised in [123] is based on the Poisson equation [60]. However, this formula was developed based on the gas model, where the ionisation mechanism differs from that in the dielectric liquids.

Compared with the equations given in [121] to [123], the equation provided in [124] was developed with the consideration on the field distortion due to the space charge near the needle tip, which is closer to the conditions of the present research and hence was selected for the analysis in the present work.

However, regardless of the specific equations used to obtain the mobility, the mobility of charge carriers provides important information on the conduction processes in the dielectric liquids and the field distribution in the case of noticeable space charge effects. Thus, it is critically important to study the mobility of charge carriers. It provides vital information on the behaviour of charge carriers in the mineral oil and ester liquids and can help to establish a theory/analytical model which describes breakdown behaviour of the liquids in highly divergent electric fields. Also, the mobility of charge carriers will be used in estimation of the Joule heating effects in the dielectric liquids, which is essential for their health monitoring and analysis of their ageing.

In this chapter, the mobility of charge carriers in three dielectric liquids was obtained using the point-plane electrode topology. The obtained results confirm two conclusions derived in Chapter 5, in which the mobility was measured using the ToF method:

- There is a positive correlation between the mobility of charge carriers and the applied field strength for both esters and mineral oils.
- The space charge density in the esters is higher than the space charge density in the mineral oil under the same electric field.

The research on the mobility of charge carriers in pure dielectric liquids has been delivered using two methods: the ToF method and the SCLC method. Compared with other published data, which are typically based only on a single method (ToF or SCLC), the combination of these two methods allows the mobility measurements to be conducted in a wide range of electric fields, i.e., from 40 kV/m to 80 kV/m, from  $4 \cdot 10^2$  kV/m to  $1.2 \cdot 10^3$  kV/m, and from  $\sim 1.6 \cdot 10^9$  kV/m to  $\sim 4 \cdot 10^9$  kV/m.

Thus, this range of electric fields helps to obtain the dependency of the mobility of charge carriers on the field magnitude. The corrective coefficient in the modified single-polarity

method was introduced for the first time in this research, which helps to increase an accuracy of the single-polarity method.

As mentioned in Chapter 2, nanofluids also attract the attention of researchers and practitioners. Thus, the mobility and the EHD effects in the nanofluids developed in this study using the pure liquids and BN and TiO<sub>2</sub> particles have also been investigated in this research. In the following two chapters, Chapter 7 and Chapter 8, the investigation on the nanofluids is presented: the dynamic behaviour of nanoparticles stressed with the electric field and the mobility of charge carriers in nanofluids.

# Chapter 7 ELECTROHYDRODYNAMIC PROCESSES IN NANOFLUIDS

---

The mobility of charge carriers under various electric fields was investigated in three pure dielectric liquids and the results of this study are presented and discussed in Chapters 5 and 6. As mentioned in Chapter 2, one of the aims of the present work is to investigate the behaviour of particles in nanofluids which may offer improved dielectric strength and thermal conductivity compared with pure liquids. To investigate the mechanisms which may lead to higher breakdown strength of nanofluids, the dynamics of dispersed particles in nanofluids stressed with the external electric field, and the mobility of charge carriers in nanofluids were investigated.

The dynamics of particles in nanofluids stressed with an external electric field was studied in this chapter. Two types of particles, TiO<sub>2</sub> and BN, were selected to produce nanofluids using the following host liquids: MIDEAL 7131, MIDEAL eN1204, and Shell Diala B. The nanofluids with two concentrations of particles, 0.005% b/w, and 0.1% b/w were prepared and studied.

The investigation of the particles' dynamics was conducted by a direct observation of nanoparticles using a CCD camera and a micro-scale observation of using an optical microscope equipped with a CCD camera. The direct optical observation was conducted using a CCD camera located above the test cell with an open top, allowing for an investigation of the motion of particles and their precipitation on the electrodes. The micro-scale observation allowed for a more accurate and detailed analysis of the particle dynamics in the centre of the test cell and in the areas close to the electrodes. Thus, the specific aspects of particle movement have been investigated and established. The modelling results obtained in Chapter 3 and the results obtained in Chapter 5 and 6 were used in the analysis of the particle behaviours in this chapter.

## 7.1 Experimental Procedure

Investigation of the particle behaviour in nanofluids stressed with the external electric field were conducted by the direct observation method using a CCD camera located above the guard-ring test cell filled with nanofluid and stressed with the DC external field, and by the micro-scale observation method, using an optical microscope equipped with the CCD camera, nanofluids in this method were located in the transparent test cell which was located under the lenses of the microscope.

### 7.1.1 Test Cell with a Guard-Ring Electrode

The test plane-plane cell with the guard-ring topology was used for the direct observations of the movement of particles. The schematic diagram of the Plane-Plane test cell, energisation and optical arrangements are provided in Figure 4-7 in Section 4.3.1. The AU-60 HV DC power supplies were used to energise the test cell with DC voltage of both polarities. The following voltage levels were used in this study:  $\pm 2$  kV,  $\pm 4$  kV, and  $\pm 6$  kV. The DC voltage was applied to the electrode of the test cell filled with specific nanofluid for 1 hour in each test. During the test, a CCD camera was placed above the test cell to perform direct observation of the behaviour of the particles in nanofluids. The detailed arrangements of this test arrangements are shown in Figure 4-8 in Section 4.3.1.

Nanofluids with particle concentrations of 0.005% b/w and 0.1% b/w were investigated in this study. The preparation procedures of these nanofluids are described in Section 4.1.2, and the rationale for the selection of these concentrations was discussed in Section 4.1.2. It was shown that the lower concentration, 0.005% b/w of TiO<sub>2</sub> particles in the mineral oil increases the breakdown strength of nanofluids [21]. The higher concentration, 0.1% b/w, was selected in this study to investigate the effect of a higher concentration of nanoparticles on their behaviour in the external electric field. The size distribution of the particles in the tested nanofluids is given in Table 4-4 in Section 4.1.3.

For each nanofluid tested under a specific voltage, three individual tests were conducted to ensure statistical analysis of the obtained results. Each individual test was conducted using a

fresh nanofluid. Nanofluids were stored and taken from a sealed container before each test. After each ToF test, the test cell was cleaned with ethanol and lint-free tissue to remove residual nanofluids from the surfaces of both electrodes.

### **7.1.2 Transparent Test Cell with Parallel Disk Electrodes**

The micro-scale observation procedure was implemented using the optical microscope to investigate the dynamics of particles under the external electric field.

The test cell with a transparent body, which is shown in Figure 4-9 (Section 4.3.2), together with the CCD utilised microscope, was used to perform micro-scale observations. Two AU-60 power supplies were used to produce three voltage levels of both polarities:  $\pm 2$  kV,  $\pm 4$  kV, and  $\pm 6$  kV. The arrangement of the complete test system is presented in Figure 4-10 in Section 4.3.2.

Nanofluids with both concentrations of particles, 0.005% b/w and 0.1% b/w were tested in the transparent test cell. During each individual test, the nanofluid samples were stressed with DC voltage for 20 minutes, while the behaviour of the particles was observed by the CCD camera attached to the microscope and videos were recorded. The test cell was cleaned with ethanol and lint-free tissue after each test.

## **7.2 Particle Dynamics in Synthetic-ester-based Nanofluids**

In Section 3.2.2, the surface charge accumulated on TiO<sub>2</sub> and BN particles in different hosting liquids was obtained analytically. Due to the different electrical conductivities and relative permittivities of the TiO<sub>2</sub> and BN particles (as seen in Table 3-1 in Section 3.2.1), the surface charges on these particles with the same hosting liquid are different for these particles. In this section, the nanofluids consisting of the MIDEAL 7131 Synthetic Ester are studied using both methods: direct observation and the micro-scale observation methods. The behaviour of the dispersed TiO<sub>2</sub> and BN particles are presented by images from the videos obtained in each observation method.

### **7.2.1 Direct Observation**

For all measurements delivered with the direct observation, the dispersed nanoparticles were found to be attracted to the electrode with the higher electric potential, which is shown in Figure 7-1 and Figure 7-2. Figure 7-1 presents still images of the SE-based nanofluids with 0.1% b/w concentration of BN and TiO<sub>2</sub> particles. These images are the snapshots from the videos recorded at the 30<sup>th</sup> minute and the 60<sup>th</sup> minute after stressing the nanofluid with an external DC field (voltage). All images in Figure 7-1 show the area in close proximity to the positively energised electrode.

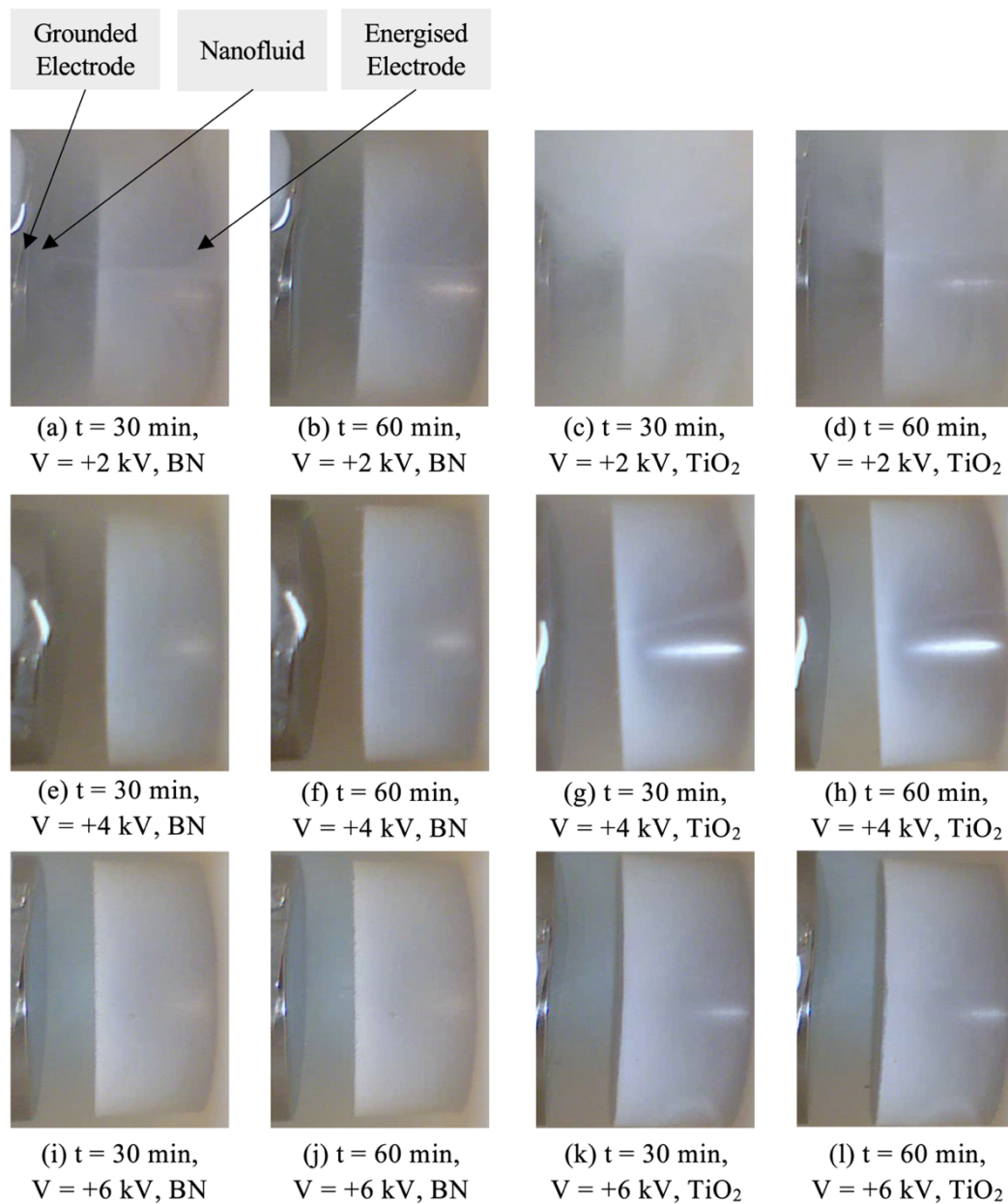


Figure 7-1 Direct observation images of nanofluids with 0.1% b/w concentration of BN and  $\text{TiO}_2$  particles stressed with positive DC voltage.  $t$  is the elapsed after application of DC voltage,  $V$  is the applied voltage, BN or  $\text{TiO}_2$  indicated the type of dispersed particles. The electrode on the right side of each image is the energised electrode, while the opposite electrode is the grounded electrode.

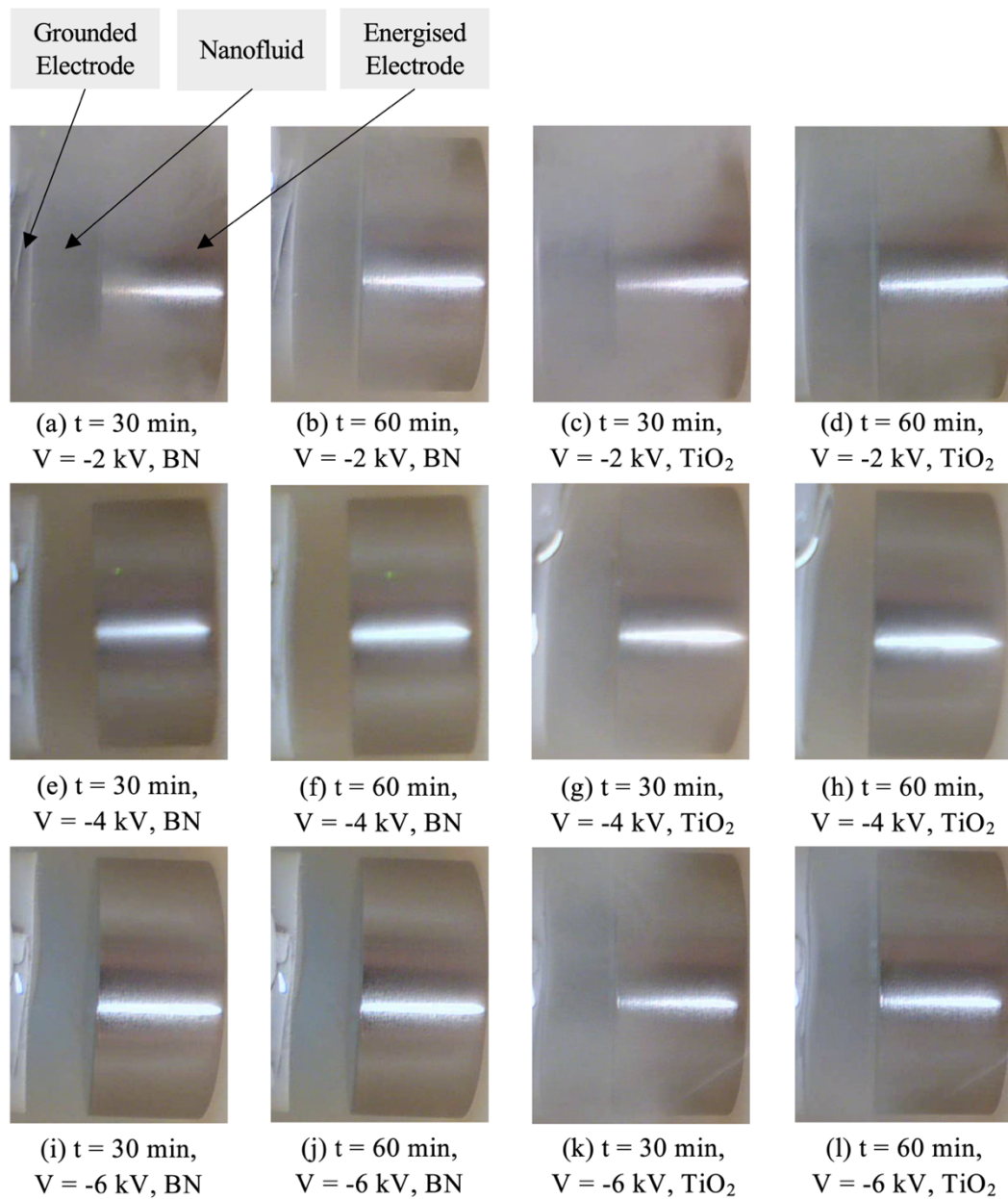


Figure 7-2 Direct observation images of nanofluids with 0.1% b/w concentration of BN and  $\text{TiO}_2$  particles stressed with negative DC voltage.  $t$  is the elapsed after application of DC voltage,  $V$  is the applied voltage, BN or  $\text{TiO}_2$  indicated the type of dispersed particles. The electrode on the right side of each image is the energised electrode, while the opposite electrode is the grounded electrode.

As shown in Figure 7-1, the external electric field results in precipitation of both TiO<sub>2</sub> and BN particles on the HV electrode stressed with positive voltage in all cases: this electrode has the higher potential in all tests shown in Figure 7-1. At the same time, the surface of the grounded electrode, which is shown on the left of each image, remains clean during these 1-hour tests.

The conclusions derived from Figure 7-2 are similar to what was obtained from Figure 7-1: both TiO<sub>2</sub> and BN nanoparticles were precipitated on the grounded electrode, which is shown on the left in each image and has a higher potential compared with a negatively energised HV electrode. At the same time, the surface of the negatively energised electrode remains relatively clean during each 1-hour test.

Besides, the BN particles in nanofluids show a higher precipitation tendency compared with the TiO<sub>2</sub> particles, which can be seen in Figure 7-2 (i) and (k): after being stressed with the same voltage level (-6 kV) for the same duration (30 minutes), the nanofluids with BN particles shown in image (i) is clearer than the nanofluids with TiO<sub>2</sub> particles shown in image (k).

From both Figure 7-1 and Figure 7-2, a summary of the common characteristics between these two figures can be achieved and listed as below:

- 1) Both, TiO<sub>2</sub> and BN nanoparticles precipitated on the electrode with a higher electric potential (energised HV electrode in the case of the positive energisation, and grounded electrode in the case of the negative energisation). Both, TiO<sub>2</sub> and BN nanoparticles were repelled from the electrode with a lower electric potential (energised HV electrode in the case of the negative energisation, and grounded electrode in the case of the positive energisation).
- 2) Precipitation process of both TiO<sub>2</sub> and BN particles can be accelerated by increasing the electric field strength.
- 3) TiO<sub>2</sub> particles demonstrated a lower precipitation tendency compared with BN particles.

The first statement can be explained by two potential reasons. First, the particles in the nanofluids are negatively charged due to the external electric field, which leads to the

movement of the particles towards the electrode with a higher potential (namely moving in the opposite direction of the electric field between the two electrodes). Second, the particles move due to the EHD movement of the nanofluids, and the direction of this movement is always towards the high potential electrode. To support these two hypotheses, several images from the videos are presented in Figure 7-3.

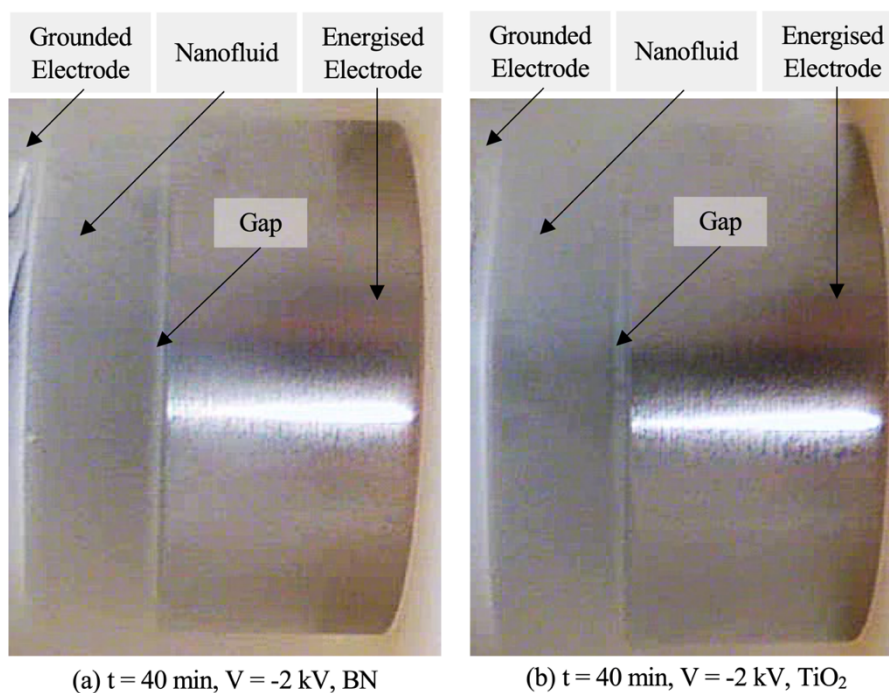


Figure 7-3 Direct observation images of the SE-based nanofluids with 0.1% b/w concentration of BN and TiO<sub>2</sub> particles under negative DC voltages.  $t$  is the time elapsed after application of voltage,  $V$  is the voltage, BN and TiO<sub>2</sub> indicates types of particles in the nanofluid. The electrode presented on the right side of each individual image is the energised electrode. The 'Gap' in each image indicates a part of the inter-electrode gap filled with the nanofluid which has a low concentration of particles (thus looks brighter in these images).

As shown in Figure 7-3, a ‘clear gap’ is formed in the nanofluid at the surface of the negatively charged electrode. This gap is manifestation of a lower concentration of particles in the vicinity of the negative electrode.

Thus, a straightforward explanation of the second statement can be provided: the magnitude of the electric force acting on the (negatively) charged particles is proportional to the field strength, leading to acceleration of the precipitation process in a stronger electric field.

The reason for the weaker precipitation tendency of TiO<sub>2</sub> particles compared with BN particles still requires further investigation: there could be several aspects which can potentially result in such different precipitation tendencies of TiO<sub>2</sub> and BN particles, including the difference in the accumulated/induced charge on these particles: the higher net charge on the individual particle can lead to a stronger Coulomb force pushing the particle in the direction opposite to the direction of the electric field. Moreover, the difference between the dispersion stability of these two types of particles can also induce the different precipitation tendencies. The higher dispersion stability can lead to a lower precipitation rate under the same attraction force from the electrode in this experiment.

The EHD behaviour of the dispersed particles was also studied by the micro-scale observation method. In the next section, the results of the micro-scale observations of the SE-based nanofluids are presented and discussed.

### **7.2.2 Micro-scale observation**

To conduct the detailed study of the dynamics of the particles, the movement of nanoparticles in the SE-based nanofluids was investigated using the micro-scale observation method. The results of this investigation are shown in Figure 7-4.

Figure 7-4 shows the images of nanofluids under +6 kV stress at different moments. Figure 7-4 (a) – (d) are the images of the SE-based nanofluid with 0.1% b/w concentration of TiO<sub>2</sub> particles, while Figure 7-4 (e) - (h) are images of the SE-based nanofluids with 0.1% b/w concentrations of BN particles. The dark areas on the left in the individual image in Figure 7-4 are the surface edges of the grounded electrode, and the dark areas on the right in each image represent concentrated particles in the nanofluids.

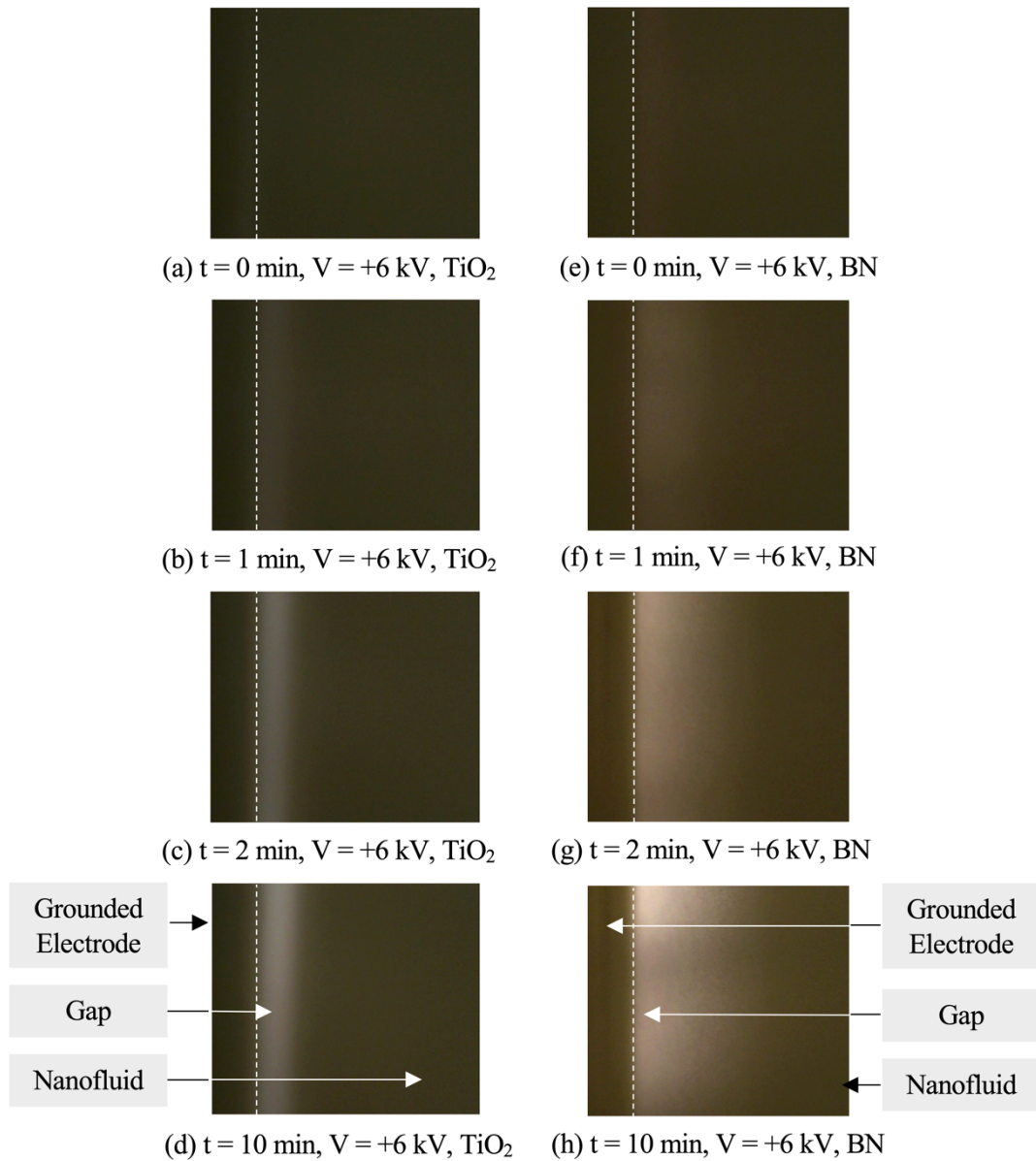


Figure 7-4 Micro-scale observation images of the SE-based nanofluids with 0.1% b/w concentration of BN and  $\text{TiO}_2$  particles under positive DC voltages.  $t$  is the elapsed after application of voltage,  $V$  is the voltage level, BN and  $\text{TiO}_2$  indicates the type of particles. The electrode presented on the left side of each image is the grounded electrode. The white dash line in each image indicates the edge of the electrode surface.

As can be seen from Figure 7-4 (a) - (d), and (e) - (h) respectively, a lower particle density gap appears as time increases, which is in a good agreement with the finding produced by the direct observation method (as shown in Figure 7-3). This gap is a manifestation of a lower concentration of dispersed particles in the vicinity of the grounded electrode. Furtherly, it can be concluded that the low dispersing particle concentration of the nanofluids near the electrode surface is the result of the Coulomb force acting on the negatively charged particles, which confirms the first conclusion obtained in the previous section.

As can be seen from Figure 7-4 that the gap in the nanofluids with  $\text{TiO}_2$  particles is wider than the gap in the nanofluids with BN particles when stressed with the same DC voltage level for the same duration, like Figure 7-4 (d) and (h). To present the difference between the gaps of these two samples clearly, image (d) and (h) in Figure 7-4 are converted into high contrast images with black and white 50% mode, i.e., all pixels in the original image were converted into neither white nor black according to the original lightness of these pixel. The results of this conversion are shown in Figure 7-5.

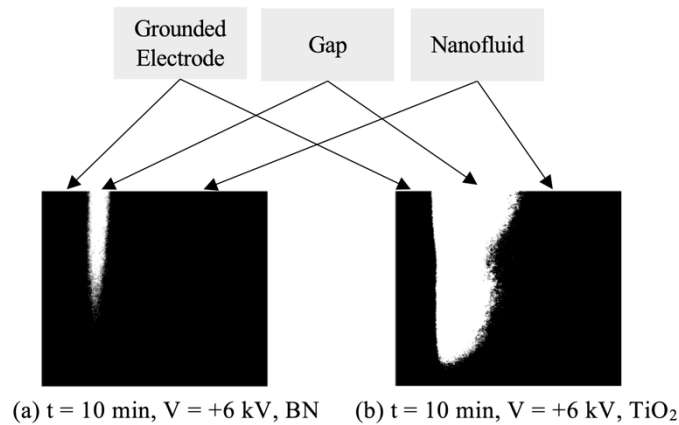


Figure 7-5 Converted micro-scale observation images of the SE-based nanofluids with 0.1% b/w concentration of BN or  $\text{TiO}_2$  particles under positive DC voltages.  $t$  is the time elapsed after the voltage switch on,  $V$  is the voltage level, BN and  $\text{TiO}_2$  indicated the types of particles.

It can be seen that the brighter/clearer part in Figure 7-5 (b) is significantly wider than that in Figure 7-5 (a), which means that the low particle concentration gap formed in the nanofluids with TiO<sub>2</sub> particles is wider than that in the nanofluids with BN particles. This indicates that the impact of the electric field on the BN particles is stronger than the impact on the TiO<sub>2</sub> particles, which agrees with the third feature obtained via the direct observation method, i.e., TiO<sub>2</sub> particles demonstrated a lower precipitation tendency compared with BN particles.

Images obtained by both direct observation and micro-scale methods in the previous section and in this section are based on the nanofluids with 0.1% concentration of particles. During the measurement, images of nanofluids with 0.005% concentration of particles with both these two scales were also obtained, two of which are shown in Figure 7-6.

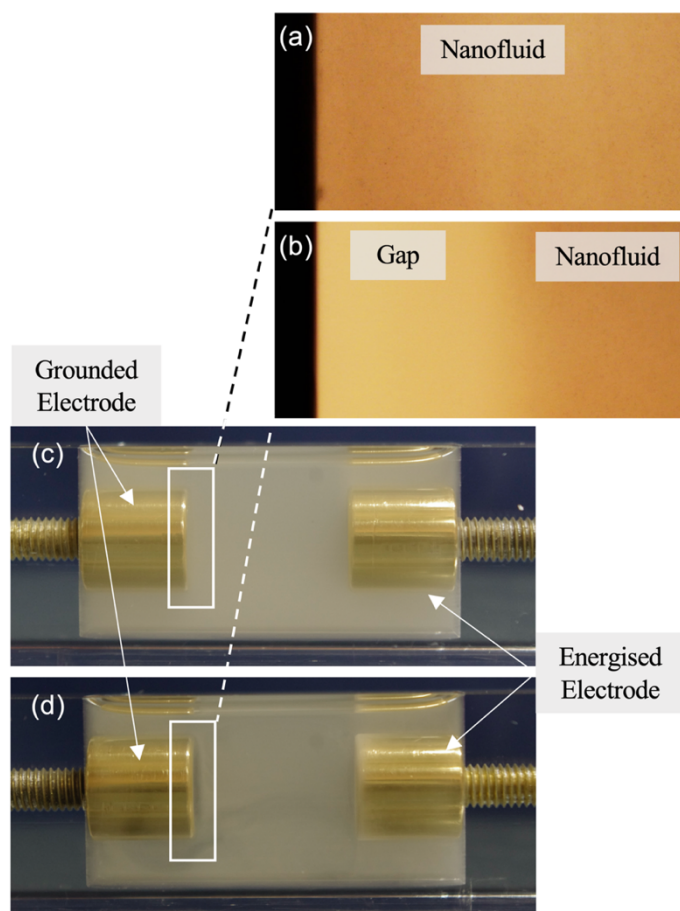


Figure 7-6 Micro-scale observation and direct observation images of the SE-based nanofluids with 0.005% b/w concentration of TiO<sub>2</sub> particles. (a) and (b) is the micro-scale observation images of the nanofluids before and after application of voltage (+ 6 kV), respectively. The dark areas in (a) and (b) are the surfaces of the grounded electrode. (c) and (d) are direct observation images of the SE-based nanofluids before and after application of voltage (+ 6 kV), respectively. The electrode on the left in (c) and (d) is the grounded electrode.

All the images shown in Figure 7-6 are obtained from one individual measurement: the SE-based nanofluids with 0.005% b/w concentration of TiO<sub>2</sub> particles under +6 kV DC stress for 20 minutes.

Both Figure 7-6 (a) and (b), are micro-scale observation images: Figure 7-6 (a) is the image of the nanofluids in the vicinity of the grounded electrode surface before application of

voltage, while Figure 7-6 (b) is the image of the same location after 20 minutes of application of +6 kV DC. The gap observed in the nanofluids with 0.1% b/w concentration of particles, like Figure 7-4, is also visible in Figure 7-6 (b).

Both Figure 7-6 (c) and (d), are direct observation images of the nanofluids: Figure 7-6 (c) is the image of the nanofluid before application of voltage while Figure 7-6 (d) is the image of the nanofluids after 20 minutes application of +6 kV. The electrode on the left in Figure 7-6 (c) and (d) is the grounded electrode.

Analysis of these images show that the nanofluids in the vicinity of the grounded electrode in Figure 7-6 (d) are clearer than in the case of the nanofluids shown in Figure 7-6 (c). Thus, a low particle density is formed similar to the gap seen in Figure 7-1 and Figure 7-2 for the nanofluids with the 0.1% b/w concentration of particles. At the same time, the precipitation of the nanoparticles precipitated on the energised electrode can be clearly observed in Figure 7-6 (d), which is similar to the precipitation process observed in the nanofluids with 0.1% concentration of particles (as seen in Figure 7-1 and Figure 7-2).

Analysis of Figure 7-6 demonstrates that the behaviour of nanoparticles observed in the nanofluids with the 0.005% b/w concentration of particles is similar to the behaviour of the particles in the nanofluids with the 0.1% b/w concentration of particles. The images of the nanofluids with the 0.1% b/w concentration of particles have higher contrast, thus the following analysis of the behaviour of the nanofluids will be based on the images of nanofluids with the with the 0.1% concentration of particles.

In this section, the images obtained using the micro-scale observation method were used to investigate the dynamic behaviour of the nanoparticles and it was shown that the TiO<sub>2</sub> and BN particles are negatively charged under the DC stress. The same conclusion was reached based on the direct observation method. Besides, the higher precipitation tendency of the BN particles compared with the TiO<sub>2</sub> particles was confirmed by the analysis of the micro-scale observation images. However, the reason for this difference in the precipitation tendencies requires further investigation, which will be discussed in Section 7.5.

## **7.3 Particle Dynamics in Natural-ester-based Nanofluids**

In this section, the nanofluids based on the MIDEAL eN 1204 were studied using both the direct observation and the micro-scale observation methods. The electric conductivity, dielectric permittivity and charge carrier density of the NE are like these parameters of the SE, (the SE-based nanofluids were investigated in the previous section). Thus, it is expected that the EHD behaviour of the NE-based nanofluids will be similar to the behaviour of the SE-based nanofluids.

### **7.3.1 Direct Observation**

The direct observation images of the NE-based nanofluids with the 0.1% b/w concentration of BN or TiO<sub>2</sub> particles are shown in Figure 7-7 and Figure 7-8. These images are the snapshots from the videos recorded via the direct observation taken at two moments: at the 30<sup>th</sup> minute and the 60<sup>th</sup> minute after application of voltage. All images in Figure 7-7 and Figure 7-8 show the vicinity of the positive and the negative energised electrode, respectively.

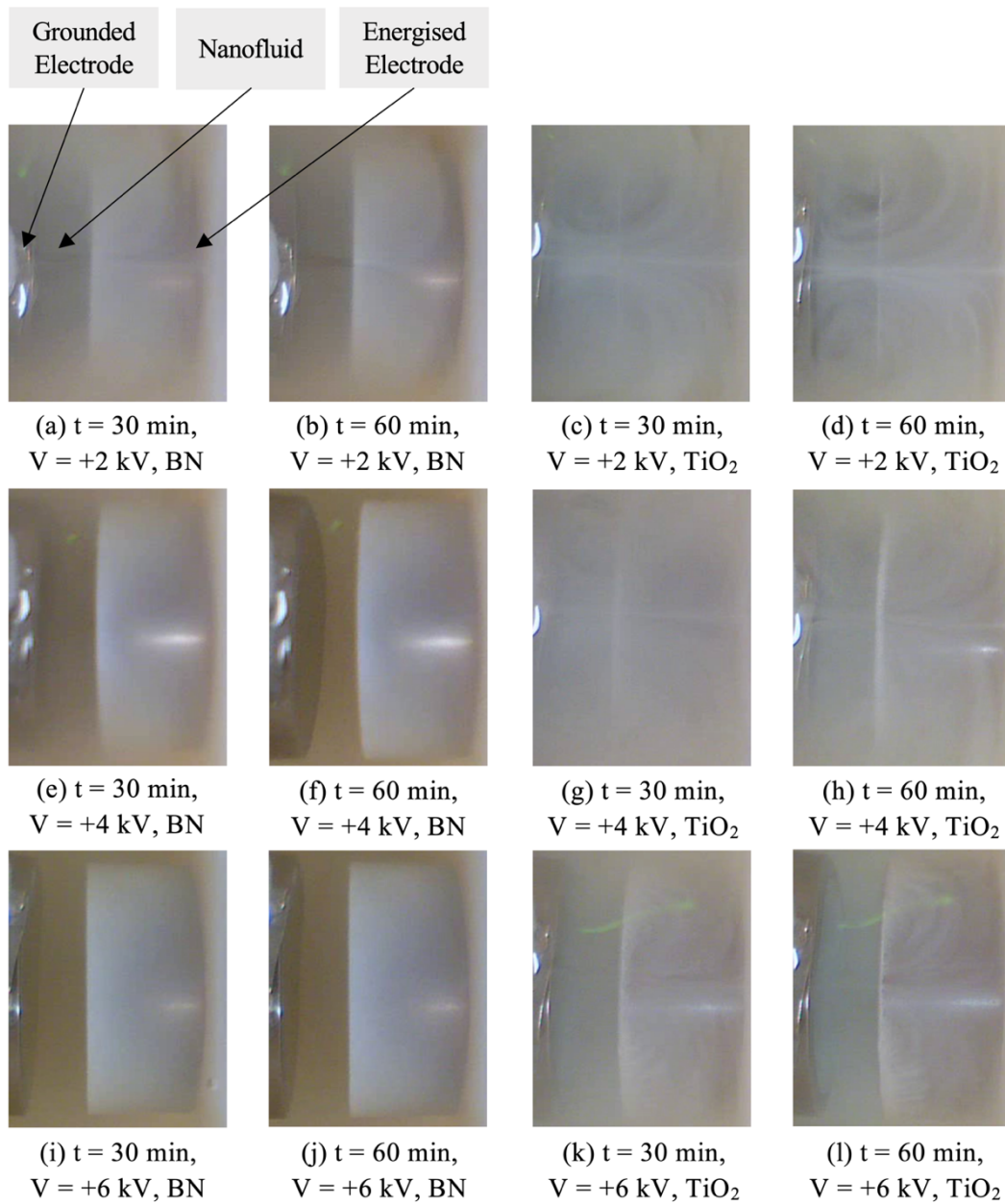


Figure 7-7 Direct observation images of nanofluids with 0.1% b/w concentration of BN and  $\text{TiO}_2$  particles stressed with positive DC voltage.  $t$  is the elapsed after application of DC voltage,  $V$  is the applied voltage, BN or  $\text{TiO}_2$  indicated the type of dispersed particles. The electrode on the right side of each image is the energised electrode, while the opposite electrode is the grounded electrode.

It can be seen that the precipitation tendencies presented in Figure 7-7 are similar to the precipitation tendencies shown in Figure 7-1: both  $\text{TiO}_2$  and BN nanoparticles were precipitated on the positive energised electrode, which is located on the right in each image and has the higher potential compared with the opposite electrode: grounded electrode, the surface of which remains clean during the one-hour test.

The obtained images also demonstrate that an increase in the field strength leads to an acceleration in precipitation of nanoparticles in the NE-based nanofluids. As can be seen from Figure 7-7 (a), (e) - (i), and (c), (g) - (k), the nanofluids between the electrodes become clearer with the higher voltage levels, indicating that more particles were precipitated to the electrode surface due to the higher applied voltages.

Finally, the NE-based nanofluids with  $\text{TiO}_2$  particles show a higher precipitation tendency than the NE-based nanofluids with of BN particles, which is similar to the precipitation tendency of BN and  $\text{TiO}_2$  nanoparticles obtained in the SE based nanofluids reported in the previous section. For example, the NE-based nanofluids with of BN particles, as shown in Figure 7-7, (b), (f), and (g), are clearer than the NE-based nanofluids with  $\text{TiO}_2$  particles, as shown in Figure 7-7 (d), (h), and (l), respectively.

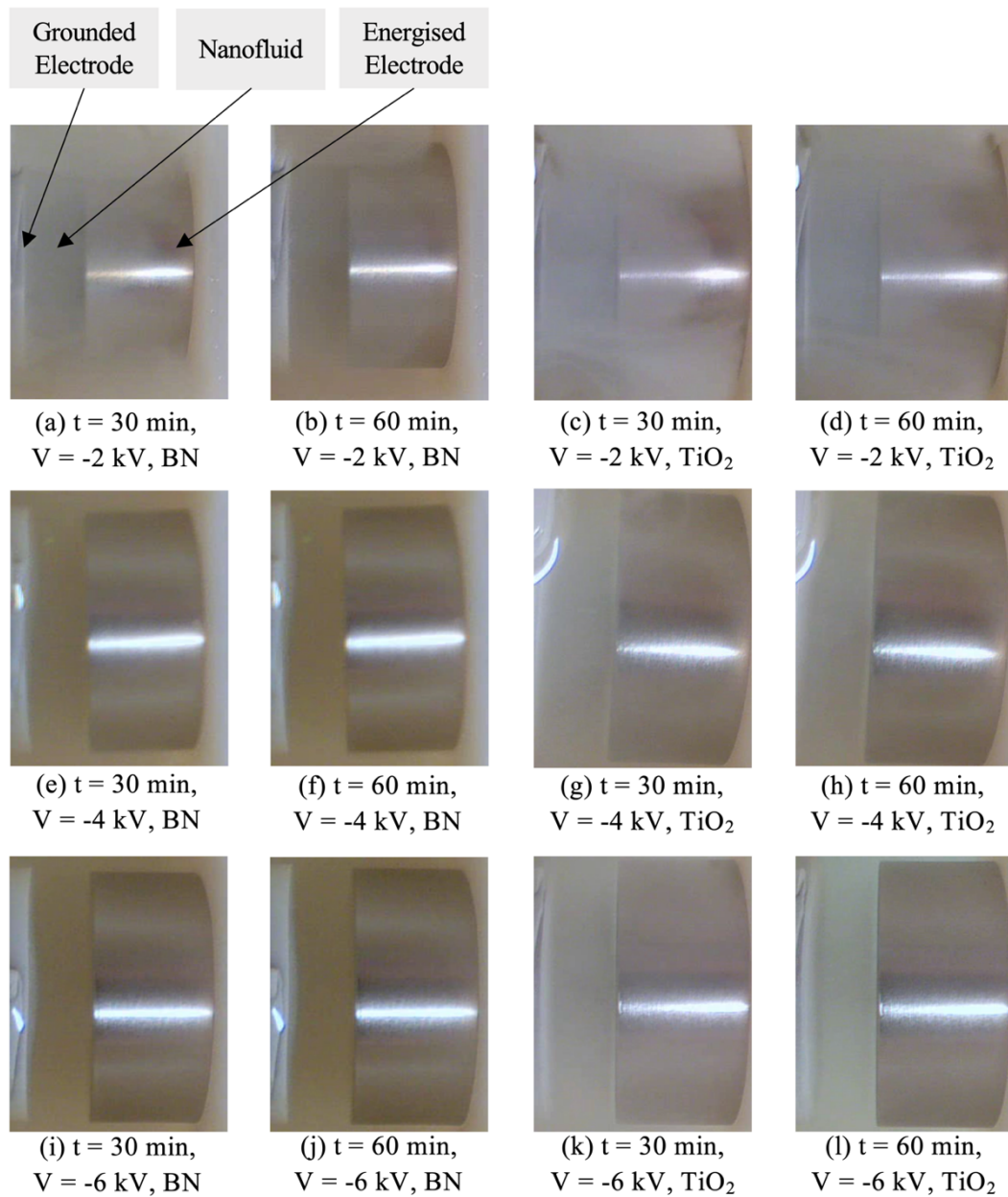


Figure 7-8 Direct observation images of nanofluids with 0.1% b/w concentration of BN and  $\text{TiO}_2$  particles stressed with negative DC voltage.  $t$  is the elapsed after application of DC voltage,  $V$  is the applied voltage, BN or  $\text{TiO}_2$  indicated the type of dispersed particles. The electrode on the right side of each image is the energised electrode, while the opposite electrode is the grounded electrode.

The behaviour of nanoparticles presented in Figure 7-8 is similar to the behaviour of particles presented in Figure 7-2: precipitation of both TiO<sub>2</sub> and BN nanoparticles to the grounded electrode can be seen in each image in Figure 7-8. On the other hand, Figure 7-8 demonstrates a clean surface of the negatively energised electrode, located on the right in each image.

The NE-based nanofluids with BN particles, as shown in Figure 7-8, stressed with the same voltage level and during the same time interval are clearer than the NE-based nanofluids with TiO<sub>2</sub> particle: Figure 7-8 (e) with (g), and Figure 7-8 (i) and (k). This tendency supports the conclusion obtained in Section 7.2.1: the precipitation tendency of the BN particles dispersed in the NE-based nanofluids is higher than the precipitation rate of the TiO<sub>2</sub> particle dispersed in NE-based nanofluids.

Based on the analysis of Figure 7-7 and Figure 7-8, three characteristics found in the SE-based nanofluids were also observed in the NE-based nanofluids:

- 1) Both TiO<sub>2</sub> and BN nanoparticles were precipitated on the electrode with a higher electric potential and repulsed from the electrode with a lower electric potential.
- 2) The higher voltage level (field strength) leads to faster precipitation of both TiO<sub>2</sub> and BN particles in the nanofluids.
- 3) The precipitation tendency of TiO<sub>2</sub> particles is lower compared with BN particles.

From the first and second characteristics, it can be concluded that the particles dispersed in the NE-based nanofluids are negatively charged, the same conclusion was reached for the particles dispersed in the SE-based nanofluids. Further analysis is required to explain the 3<sup>rd</sup> characteristic, which will be presented in Section 7.5.

Apart from the direct observation, the study of the NE-based nanofluids was also conducted using the micro-scale observation method, the results of this study are presented in the following section.

### **7.3.2 Micro-scale Observation**

Figure 7-9 presents two groups of micro-scale observation images, which were taken in two separate tests. Figure 7-9 (a) – (d) are the images of the NE-based nanofluids with 0.1% b/w TiO<sub>2</sub> particles under +6 kV DC stress at different time moments. Figure 7-9 (e) – (h) are the images of the NE-based nanofluids with 0.1% b/w BN particles under +6 kV DC stress at different time moments. The dark space in the left of each image in Figure 7-9 is the surface of the grounded electrode, and the dark space on the right side in each image is the nanofluids.

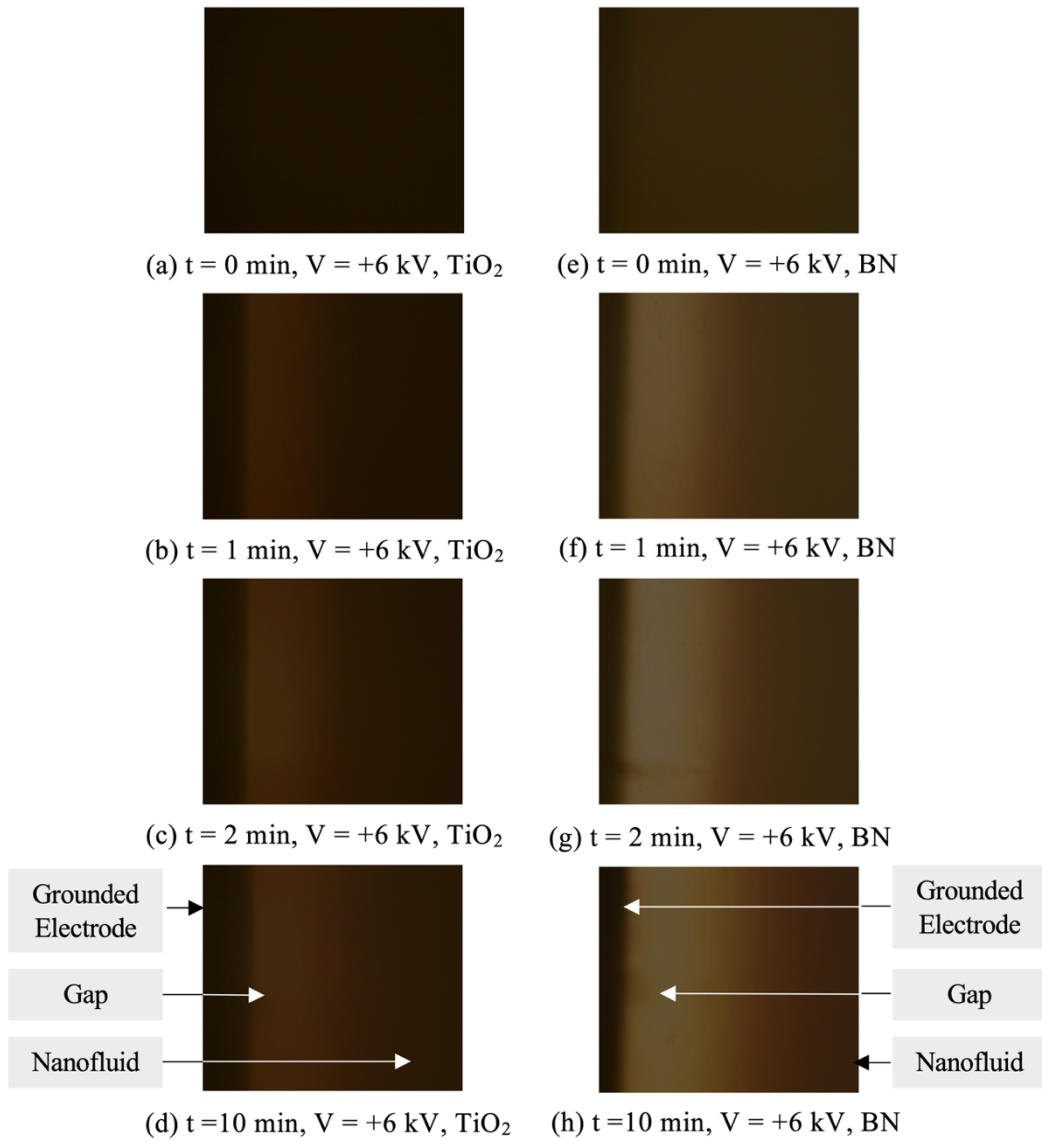


Figure 7-9 Micro-scale observation images of nanofluids consisting of 0.1% b/w concentrated BN/TiO<sub>2</sub> and the NE under positive DC voltages. For (a) - (l),  $t$  is the moment after the voltage switch on,  $V$  is the stressed voltage level, and 'BN/TiO<sub>2</sub>' indicates dispersed particles. The electrode presented on the left side of the individual image is the grounded electrode, one of which is labelled in image (d), (h).

As shown in Figure 7-9, the low particle density space (labelled as ‘Gap’ in Figure 7-9 (d) and (h)) in the nanofluid stressed with the electric field becomes wider with an increase in the voltage magnitude and time of application. This tendency is in agreement with the results obtained by the direct observation method of the NE-based nanofluids, and it confirms that both, TiO<sub>2</sub> and BN nanoparticles are negatively charged in the NE-based nanofluids.

The images shown in Figure 7-9 also confirm that the low particle density space in the NE-based nanofluids with TiO<sub>2</sub> particles is wider than the low particle density space in the NE-based nanofluids consisting with BN particles at the same DC voltage levels and the same duration of DC stress. This tendency is similar to the tendency observed in the SE-based nanofluids, as shown in Figure 7-4. As discussed in the previous section, the larger low particle density space in the NE-based nanofluids with BN particles compared with the NE-based nanofluids with TiO<sub>2</sub> particles indicates a stronger effect of the electric field on the BN particles than on the TiO<sub>2</sub> particles. This finding agrees with the third characteristic obtained by the direct observation method, i.e., the TiO<sub>2</sub> particles demonstrate a lower precipitation tendency compared with the BN particles at the same conditions.

According to the images of the SE-based nanofluids obtained by both the direct observation and the micro-scale observation methods, particles in the NE-based and the SE-based nanofluids behave similarly. This is an expected finding as the NE and SE fluids have similar electrical conductivities and relative permittivities (as shown in Table 4-1 in Section 4.1.1), And furthermore, the results in Chapter 5 and 6 have shown that the mobility of charge carriers in these two esters and the space charge density of these two esters are also similar to each other.

In this case, to investigate the effect of the base liquid on the behaviours of nanofluids, a comprehensive investigation of the nanofluids prepared using different base was conducted and the obtained results are presented in the next section

## **7.4 Particle Dynamics in Mineral-oil-based Nanofluids**

The Shell Diala B has significantly lower electrical conductivity and lower dielectric permittivity compared with both ester liquids. It was shown in Chapters 5 and 6 that the space

charge density of the MO is also lower than that in both esters. Thus, it can be expected that the dynamic behaviour of the MO-based nanofluids will be different from the ester-based nanofluids presented in two previous sections. Moreover, the lower viscosity of the mineral oil also results in a weaker dispersion stability of the particles suspended in the MO-based nanofluid. Both aspects are reflected in the results presented in this section.

#### **7.4.1 Direct Observation**

The direct observation images of the MO-based nanofluids with the 0.1% b/w concentration of BN or TiO<sub>2</sub> particles stressed with positive and negative voltages are presented in Figure 7-10 and Figure 7-12, respectively. All experimental arrangements remain the same as in the previous two sections: the images in Figure 7-10 and Figure 7-12 are the snapshots from the videos recorded using the direct observation method at two moments, at the 30<sup>th</sup> minute and at the 60<sup>th</sup> minute after application of voltage. All images in Figure 7-10 and Figure 7-12 show the local area close to the positive energised electrode.

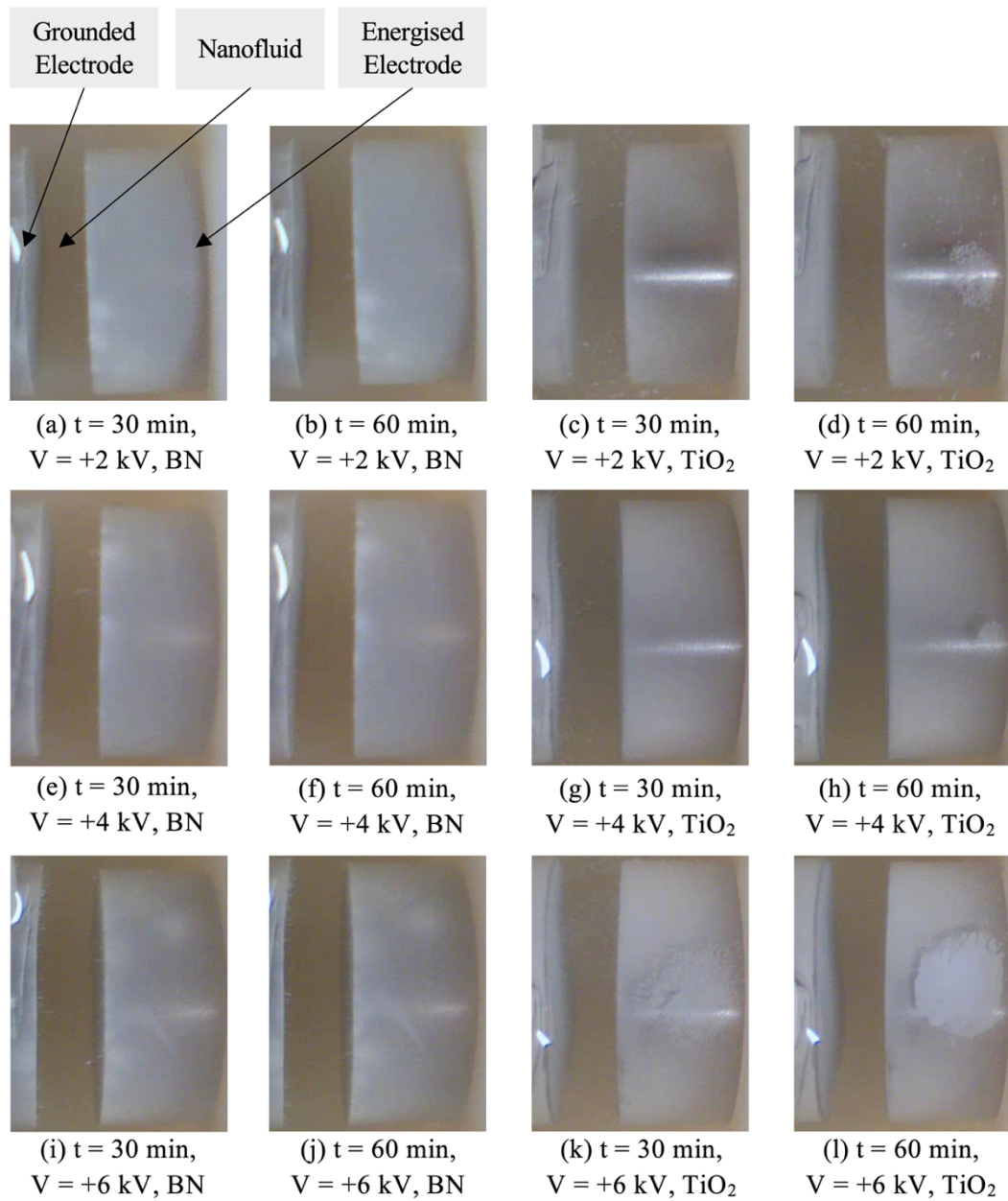


Figure 7-10 Direct observation images of nanofluids with 0.1% b/w concentration of BN and  $\text{TiO}_2$  particles stressed with positive DC voltage.  $t$  is the elapsed after application of DC voltage,  $V$  is the applied voltage, BN or  $\text{TiO}_2$  indicated the type of dispersed particles. The electrode on the right side of each image is the energised electrode, while the opposite electrode is the grounded electrode.

As shown in Figure 7-10, the behaviour of the MO-based nanofluids is significantly different from the behaviour of the ester-based nanofluids: the dispersed particles are attracted to both electrodes in all tests. Besides, the precipitation tendency of both  $\text{TiO}_2$  and BN particles in the MO-based nanofluids is more intensive (faster) than in any of the ester-based nanofluids. For example, as it is shown in Figure 7-10 (a) and (c), the MO-based nanofluids are clearer than the ester-based nanofluids ( Figure 7-7 (a) and (c)) under the same conditions.

Also, it was found that  $\text{TiO}_2$  particles in highly concentrated (0.1% b/w) MO-based nanofluids stressed with DC voltage demonstrated a tendency to agglomerate and to form clusters of particles during the test. These clusters were floating on the surface of the MO-based nanofluids, such clustering was not observed in any other types of nanofluids studied in this research.

Another effect observed in the MO-based nanofluid stressed with high electric field is a formation of particle chains, as shown in Figure 7-10. It can be seen that straight BN and  $\text{TiO}_2$  particle chains were formed during the tests. For example, several straight particle chains are clearly visible in Figure 7-10 (e), (i), and (j). To deliver a clear view of these particle chains, two direct observation images were zoomed in and presented in Figure 7-11.

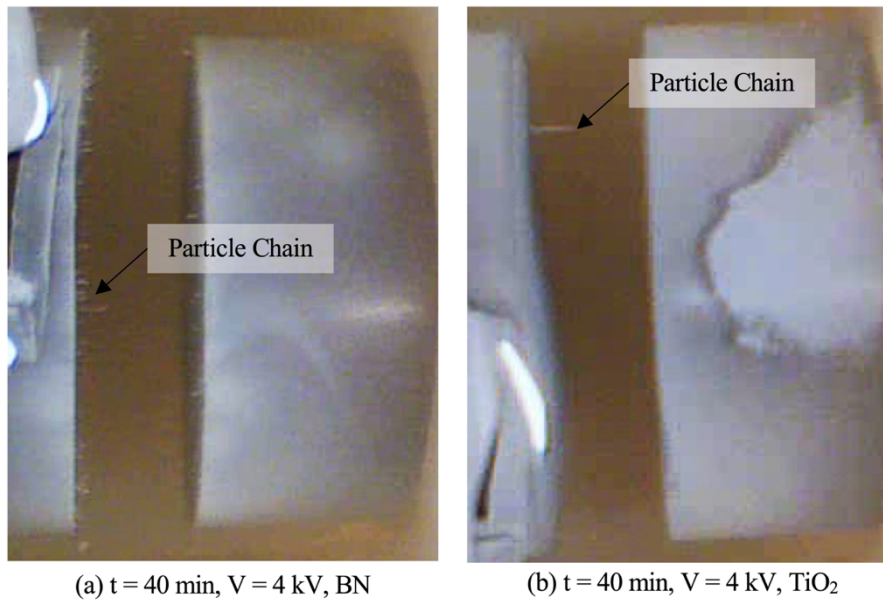


Figure 7-11 Direct observation images of MO-based nanofluids with the 0.1% b/w concentration of BN and TiO<sub>2</sub> particles the under positive DC stress.  $t$  is the time elapsed after application of volatge,  $V$  is the voltage level, BN and TiO<sub>2</sub> indicate the type of particles. The electrode presented on the right side in each image is the energised electrode. The ‘Particle Chain’ label indicates the particle chains formed in the nanofluid.

The straight particle chains are visible in both images in Figure 7-11. It can be seen that all these chains are formed perpendicular to the electrode surface, along the field lines, which stipulates that these chains are formed due to polarisation of the particles in the external electric field.

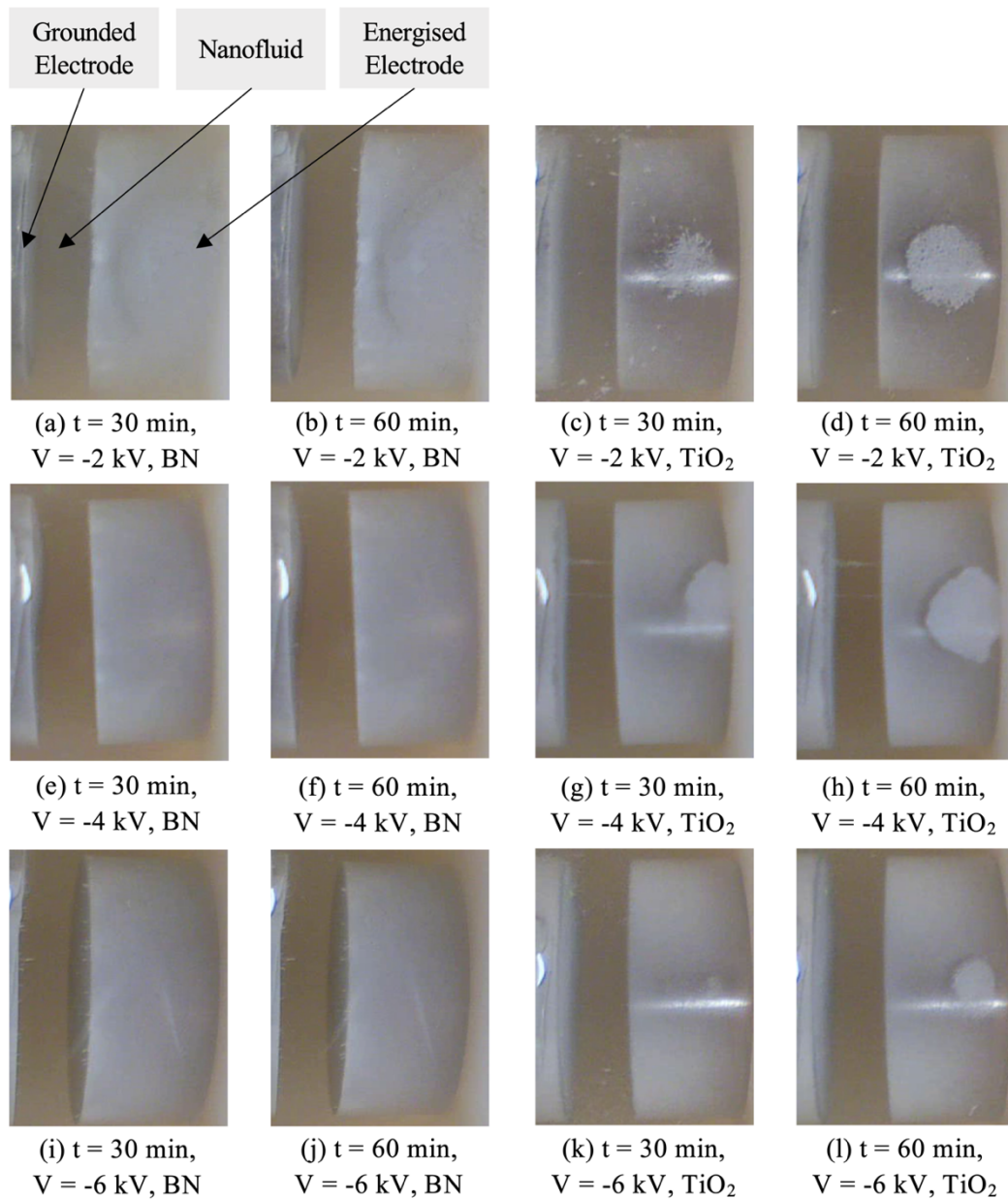


Figure 7-12 Direct observation images of nanofluids with 0.1% b/w concentration of BN and  $\text{TiO}_2$  particles stressed with negative DC voltage.  $t$  is the elapsed after application of DC voltage,  $V$  is the applied voltage, BN or  $\text{TiO}_2$  indicated the type of suspended particles. The electrode on the right side of each image is the energised electrode, while the opposite electrode is the grounded electrode.

The direct observation images of the MO-based nanofluids with 0.1% b/w concentration of BN and TiO<sub>2</sub> particles under negative DC stress are shown in Figure 7-12. This figure shows that the behaviour of the nanofluids stressed with negative voltage is similar to the behaviour of the nanofluids under positive DC stress. Firstly, as all images in Figure 7-12 show, the particles precipitate on both electrodes. Secondly, clusters of floating TiO<sub>2</sub> particles can be formed in the nanofluids under negative DC stress. Finally, the straight particle chains were formed in the nanofluids under negative DC stress. Furthermore, in some cases, these chains of TiO<sub>2</sub> particles formed in the MO-based nanofluids under the negative DC stress cross the entire inter-electrode gap and form ‘particle bridges’, some of which are shown in Figure 7-12 (g), (h). A zoomed-in image of the particle bridges is shown in Figure 7-13.

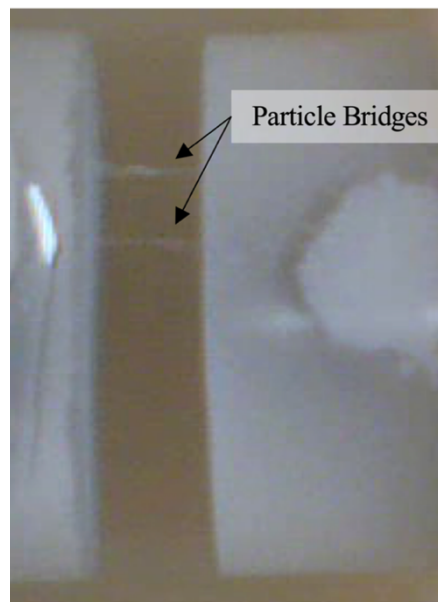


Figure 7-13 Direct observation image of MO-based nanofluids with 0.1% b/w concentration of TiO<sub>2</sub> particles under positive 4 kV DC voltage. The image was taken at the 40<sup>th</sup> minute after application of voltage. The electrode shown on the right side of the image is the energised electrode.

Two particle bridges formed between the electrodes are clearly visible in Figure 7-13. This bridging phenomenon will be discussed in the next section based on the micro-scale images of the nanofluids.

Figure 7-10 to Figure 7-12 show the behaviours of the MO-based nanofluids under DC stress, from which a summary was obtained and presented below:

- 1) TiO<sub>2</sub> and BN nanoparticles in the MO-based nanofluids precipitate on both electrodes in the case of positive and negative DC stress.
- 2) Straight particle chains are formed in the nanofluids with BN and TiO<sub>2</sub> particles. Several parallel particle bridges were observed in the nanofluids with TiO<sub>2</sub> particles.
- 3) The precipitation process is faster in the MO-based nanofluids than the ester-based nanofluids.

The faster precipitation tendency of particles in the MO-based nanofluids can be attributed to the weaker dispersion stability of the MO-based nanofluids. It was found that visually notable precipitation of particles in the MO-based nanofluids with 0.1% b/w concentration of nanoparticles took place within ~ 2 hours after preparation of these nanofluids, while for the ester-based nanofluids sedimentation of the particles started to be visible after more than one week from the preparation date of these nanofluids.

#### **7.4.2 Micro-scale Observation**

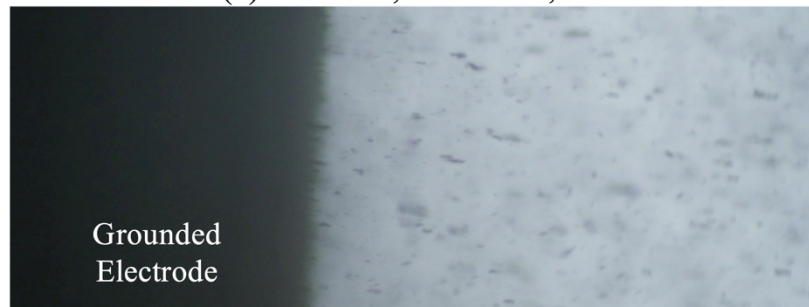
Figure 7-14 and Figure 7-15 present the micro-scale images of the nanofluids under +6 kV stress at different time moments. Figure 7-14 shows the images of the MO-based nanofluids with 0.1% b/w concentration of BN nanoparticles, while Figure 7-15 shows the images of the MO-based nanofluids with 0.1% b/w concentration of TiO<sub>2</sub> particles. The dark areas on the left in each image in Figure 7-14 and Figure 7-15 are the surface edges of the grounded electrode.



(a)  $t = 0$  min,  $V = +6$  kV, BN



(d)  $t = 4$  min,  $V = +6$  kV, BN



(e)  $t = 8$  min,  $V = +6$  kV, BN



(f)  $t = 12$  min,  $V = +6$  kV, BN

Figure 7-14 Micro-scale images of the MO-based nanofluid with 0.1% b/w concentration of BN particles under + 6 kV DC voltage.  $t$  is the time elapsed after application of voltage.

As shown in Figure 7-14, the BN particles suspended in the MO start to assemble into straight particle chains after application of the voltage, these chains are perpendicular to the surface of the electrode, i.e., they are aligned with the direction of the electric field between two electrodes. This tendency is in a good agreement with the structure and location of the particle chains obtained from the direct observation images (as seen from Figure 7-10 to Figure 7-12). Besides, it is also shown in Figure 7-14 that the particle chains increase in their size with an increase in time.

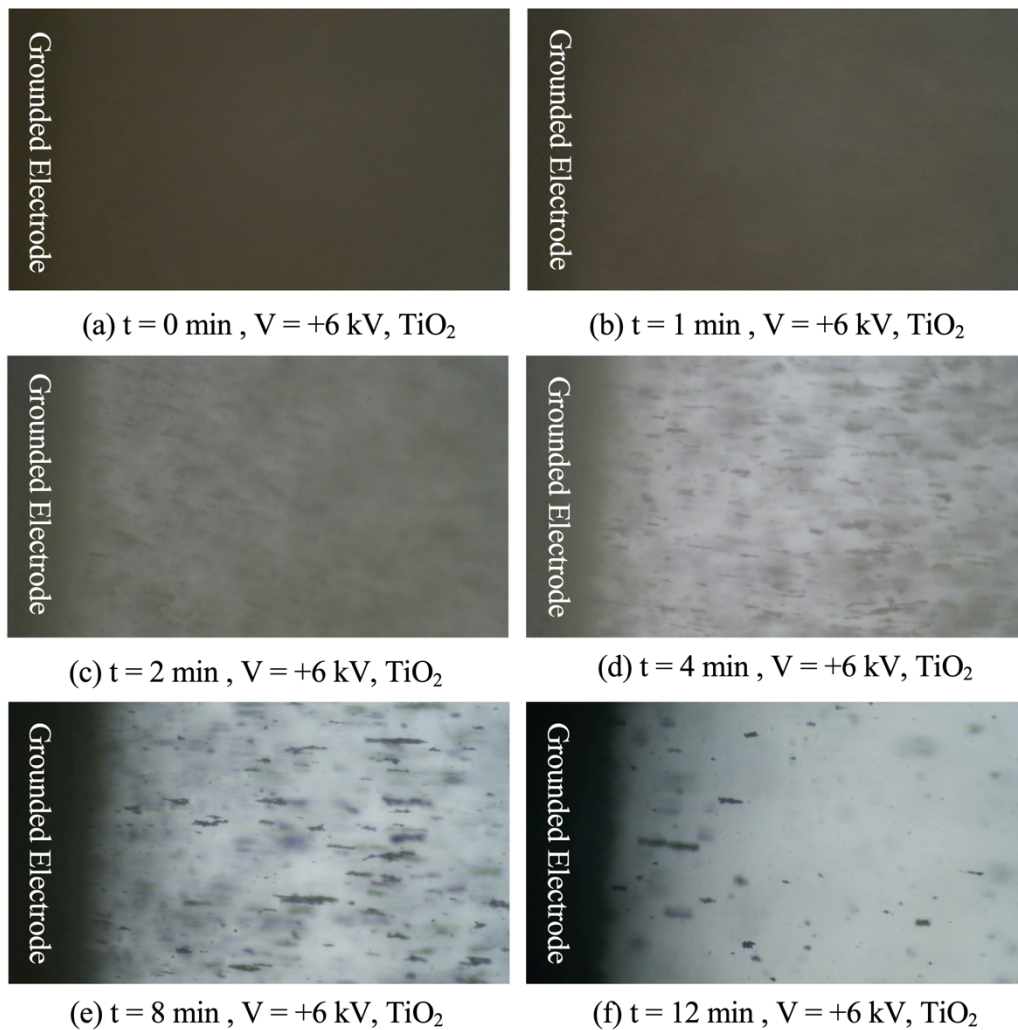


Figure 7-15 Micro-scale observation images of nanofluids consisting of 0.1% b/w concentrated  $\text{TiO}_2$  and the MO under positive 6 kV DC voltages. For image (a) - (f),  $t$  is time elapsed after application of the voltage.

Figure 7-15 shows the formation of the TiO<sub>2</sub> particle chains in the MO-based nanofluids. Firstly, the TiO<sub>2</sub> particle chains are aligned with the direction of the electric field between two electrodes, which agrees with the chain topologies obtained from the direct observation images (as seen in Figure 7-11).

Secondly, compared with the BN particle chains, the TiO<sub>2</sub> particle chains are longer. These longer chains lead to formation of the particle bridges found only in the nanofluids with TiO<sub>2</sub> particles during the direct observation measurement. In [130], Mahmud et al. reported similar ‘particle bridges’ formed between two electrodes under the DC voltage stress. In their research, the fibber-like dust particles made from pressboard were dispersed into mineral oils to simulate the contaminated transform oil. The author observed that the longer fibre-like particles attach to the electrodes first and then elongate towards the opposite electrode under the DC stress. At the same time, smaller particles are attracted to the long fibre-like particles. The particle chains continue to grow and eventually form complete bridges. As Figure 7-15 show that the TiO<sub>2</sub> particle chains are longer than the BN particle chains, it can hence conclude that it is easier to form particle bridges in the nanofluids with the TiO<sub>2</sub> particles rather than with the BN particles.

In this section, the existence of the straight particle chains in the MO-based nanofluids is confirmed by the micro-scale observation images. Besides, it is shown by the images that the direction of both the BN and TiO<sub>2</sub> particle chains is parallel to the external electric field. Finally, it is found that the TiO<sub>2</sub> particle chains are generally longer than the BN particle chains, which results in the formation of the TiO<sub>2</sub> ‘particle bridge(s)’ in the MO-based nanofluids with 0.1% b/w concentration of TiO<sub>2</sub> particles.

Based on the results obtained and presented in this section, it can be stated that the suspended particles become polarised when the nanofluid is stressed with the external electric field. The dynamics of the particles is governed by both the EHD movement of the fluid and by the dipole-dipole interaction between the particles, the latter may lead to the formation of the particle chains and bridges. Polarised particles can form the particle chains along the field lines and these chains attach to the electrode surface. The ‘particle bridge’ can be formed between two electrodes.

## 7.5 Discussion and Summary

The images of nanofluids stressed with DC electric field obtained by the direct observation and the micro-scale observation methods are presented in this chapter. These images provide insight into the dynamic behaviour of the particles in the nanofluids.

For the ester-based nanofluids it was found that:

- (1) both BN and TiO<sub>2</sub> particles are negatively charged under the DC stress.
- (2) BN particles in the esters-based nanofluids precipitate faster than TiO<sub>2</sub> particles.

For the mineral-oil-based nanofluids it was found that:

- (3) BN and TiO<sub>2</sub> particles are polarised under the DC stress, which leads to formation of the straight particle chains in the nanofluids.
- (4) The TiO<sub>2</sub> particle chains are longer than the BN particle chains. The ‘particle bridges’ formed between two electrodes were observed in the MO-based nanofluids with TiO<sub>2</sub> particles. No complete particle bridges were formed in the MO-based nanofluids with BN particles.

Potential reason for results (2) and (4) is not only the surface charge on the particles but also all forces acting on the particle, i.e., the Coulomb force, gravity, buoyance, and the drag force due to the motion of particles in the fluid. For example, more intensive precipitation of TiO<sub>2</sub> particles than BN particles could be a result of their different physical and topological properties: the nominal specific density of TiO<sub>2</sub> particles, 4.23 g/cm<sup>3</sup> is almost twice higher than the nominal specific density of BN particles, 2.1 g/cm<sup>3</sup> although the average diameter of TiO<sub>2</sub> particles in the NE-based and MO-based nanofluids is greater than the average diameter of BN particles, as shown in Table 4-4. Further investigation of these aspects is required.

To explore potential mechanisms which underpin results (1) and (3), an analysis based on the model of polarisation processes (Chapter 3) and the space charge density (Chapter 5 & 6), has been conducted and discussed below.

The surface charge distribution on a single particle placed in the dielectric liquid was obtained in Section 3.2.2. Using Equation 3-10, 3-11 and 3-13 with the relevant parameters, the surface charge distribution on the particles was calculated, and shown in Figure 7-16 and Figure 7-17. The following conditions were used in this analysis.

Firstly, as discussed in Section 3.2.1, the surface charge was calculated based on the Maxwell-Wagner relaxation process, which takes place during specific transient time. The surface charge obtained in Section 3.2.1 show that the transient time (which is defined as five Maxwell-Wagner time constants) for a TiO<sub>2</sub> particle is 147.00 s in esters and 280.90 s in mineral oils. Considering that the duration of the DC stress in the direct and the micro-scale observation methods is 3600 s and 1200 s, respectively, the present analysis assumes that all particles have their saturated surface charge. Thus, the duration of the applied voltage in the present analysis equals to 5 Maxwell Wagner time constants.

Secondly, Equation 3-10, 3-11 and 3-13 determine the linear relationship between the surface charge and the electric field strength. In this case, the simulations were conducted using a single field strength, 800 kV/m, which corresponds to the electric field strength between the two electrodes in the Plane-Plane test cell stressed with 4 kV.

Thirdly, the electrical conductivity and relative permittivity of the SE, the NE, and the MO can be found in Table 4-1 in Section 4.1.1. The electrical conductivity and relative permittivity of the BN and TiO<sub>2</sub> particles can be found in Table 3-1 in Section 3.2.1. Using these values, the surface charge on BN particles was obtained using the maximum and minimum values of the electrical conductivity of these particles and the fluids. The dimensions of the BN and TiO<sub>2</sub> particles are given in Table 4-4 in Section 4.1.3.

Finally, the units of the surface charge density used in Figure 7-16 and are “elementary charge per nanometre squared”, e/nm<sup>2</sup>.

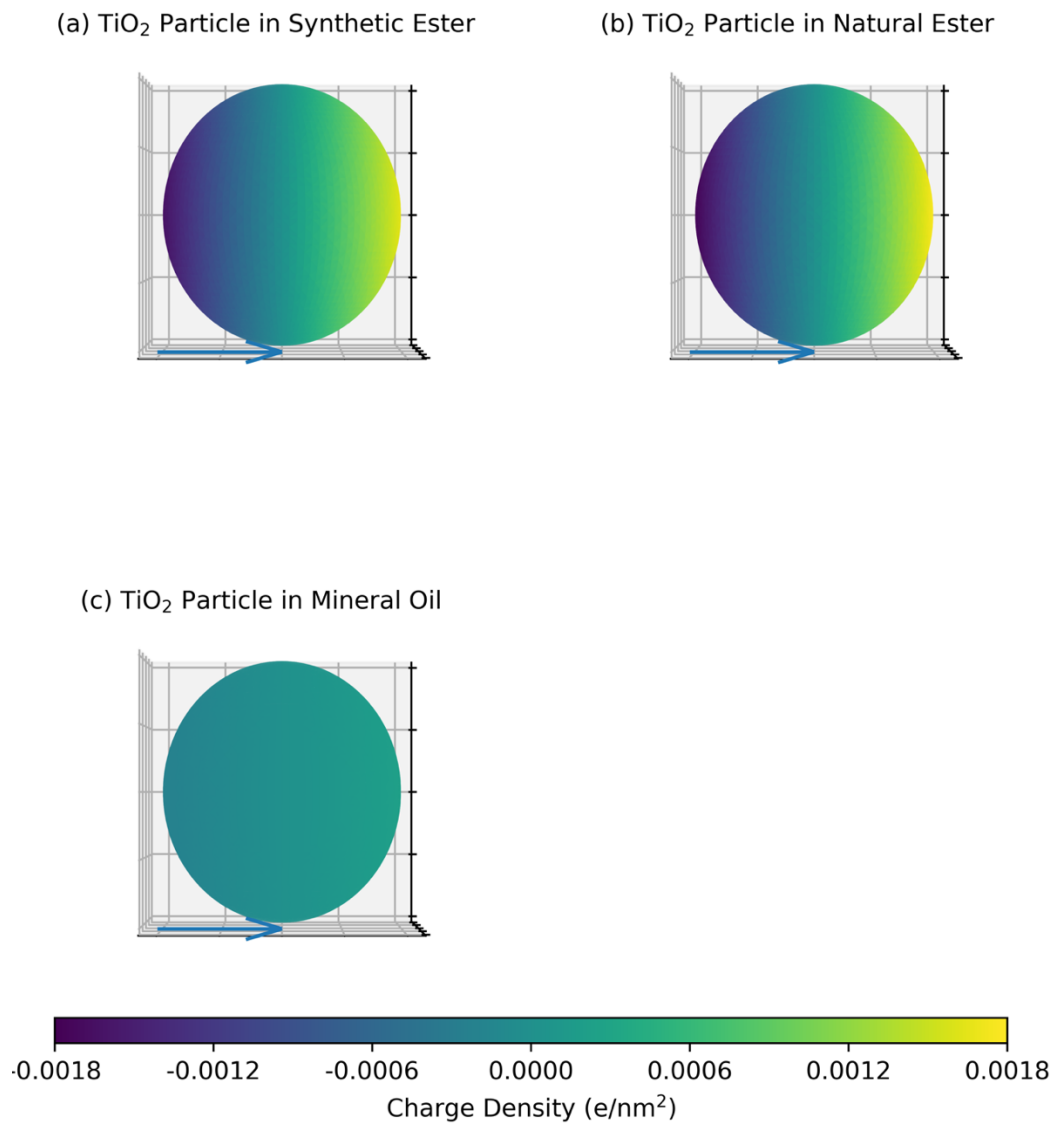


Figure 7-16 Surface charge distribution on individual TiO<sub>2</sub> particle in three dielectric liquids. The electric field strength is 800 kV/m. The duration of the applied field equals to 5 Maxwell Wagner time constants. The blue arrows indicate the direction of the electric field. The colors on the particle surface indicate the relative charge density.

Figure 7-16 shows that the surface charge distribution on a single TiO<sub>2</sub> particle has a rotation symmetry, it is symmetrical in the direction of the external electric field. The highest surface charge density is observed on the poles of the particle. The highest surface charge density on

TiO<sub>2</sub> particles in esters is much higher than that of TiO<sub>2</sub> particles in the mineral oil. The maximum values of the charge densities on TiO<sub>2</sub> particles in different liquids are presented in Table 7-1.

Table 7-1 Maximum Surface Charge Density on TiO<sub>2</sub> Particle

Liquid	Synthetic Ester	Natural Ester	Mineral Oil
Highest Charge Density (e/nm <sup>2</sup> )	~ 0.0017	~ 0.0018	~ 0.0002

Thus, based on these simulation results, the following conclusion can be derived: for the TiO<sub>2</sub> particles under the same external electric field, the accumulated surface charge on TiO<sub>2</sub> particles in ester is approximately one order of magnitude higher than that TiO<sub>2</sub> particle in the mineral oil. Based on this conclusion, a potential mechanism for the different charge states of the TiO<sub>2</sub> particle in esters and mineral oils can be proposed as follows.

Generally, the positive and negative charge carriers in the dielectric liquids can be considered as the positively and negatively charged molecules, respectively. According to the mathematical model developed in this research, the positive/negative charges are distributed on the two half-spheres of the particle. This distribution characteristic can be applied to the scenario in the mineral-oil-based nanofluids well: the positively charged molecules and negatively charged molecules are distributed on the two poles of the particles equally, leading to the polarised state of the particle in the nanofluids.

However, for the ester-based nanofluids, the results presented in Chapter 5 and 6 show that the charge density in the ester is approximately one order of magnitude higher than that in the mineral oils. The higher space charge density in esters is explained by the simulation in [120] which show that it is easier for ester molecules to release electrons than for the mineral oil molecules. In this case, it can be expected that the negative charge accumulated on the particle

in the ester-based nanofluids is not only the negatively charged molecules but also electrons, while the positive charge is still defined by only positively charged molecules. Correspondingly, the difference between the constituent of the positive accumulated charge and the negative accumulated charge could cause a different accumulating efficiency, i.e., there could be more negative charge accumulated on the particle than the positive charge, leading to the net negative charge on the particle in the ester.

In particular, as the results in Table 7-1 show, the accumulated charge on the particle in the ester is approximately one order of magnitude higher than that on the particle in the mineral oil, which can furtherly amplify the net negative charge on the particle in the ester, resulting in the negatively charged particles in the ester.

From Figure 7-17, it can be seen that the surface charge distribution on a single BN particle shows the same characteristics in the case of TiO<sub>2</sub> particles: the surface charge density demonstrates a rotation symmetry in the direction of the external electric field, and the highest surface charge density occurs at the poles of the particle.

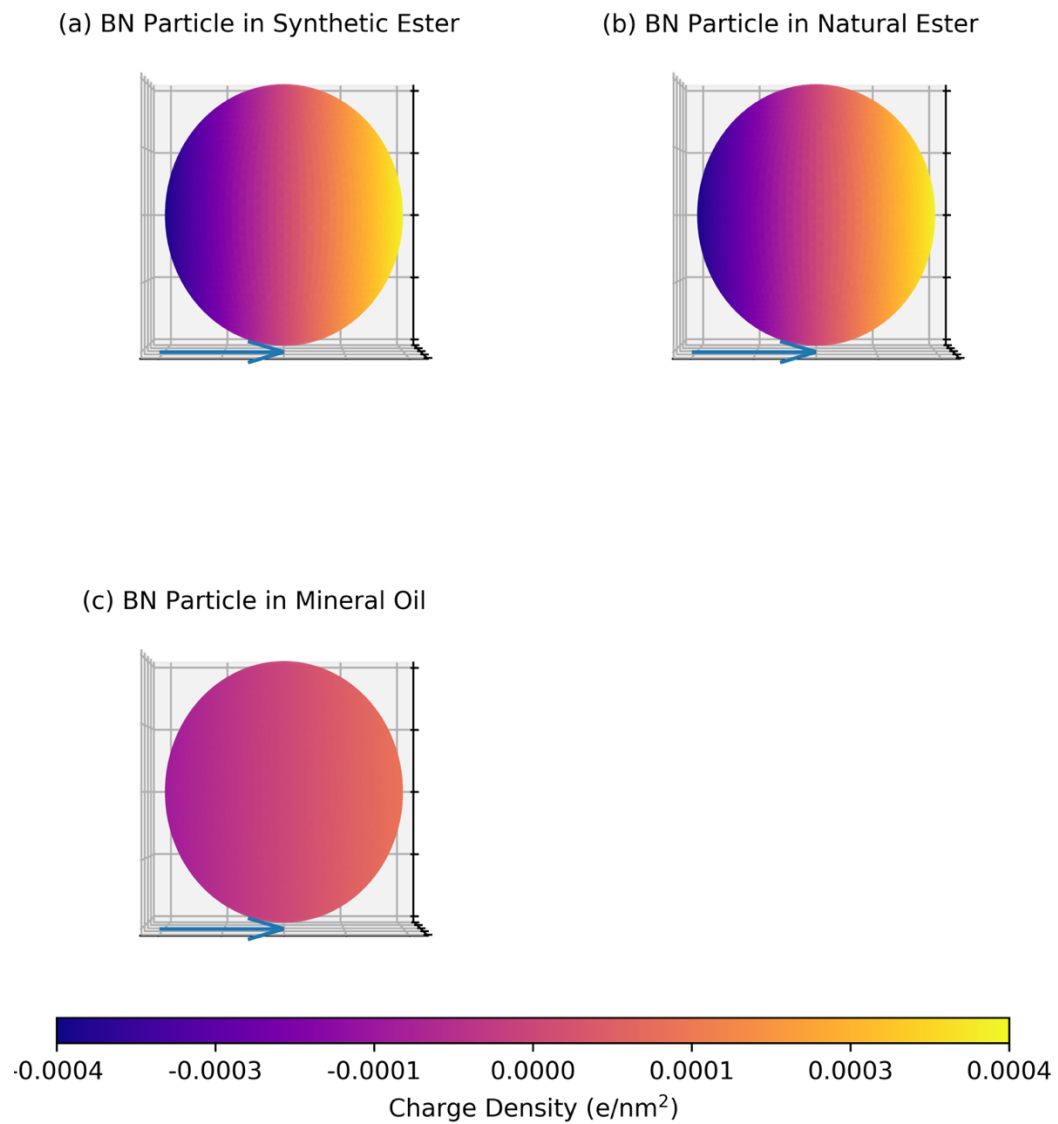


Figure 7-17 Surface charge distribution on individual BN particle in three dielectric liquids. The electric field strength is 800 kV/m. The duration of the applied field equals to 5 Maxwell Wagner time constants. The blue arrows indicate the direction of the electric field. The colors on the particle surface indicate the relative charge density.

The results in Figure 7-17 show that that the maximum surface charge density on BN particles in esters is significantly higher than that on BN particles in mineral oils.

Therefore, the mechanisms similar to those used to explain the charging processes of TiO<sub>2</sub> particles can be proposed to explain the experiment results in the case of the BN particles: the potential negative net charge on BN particle in the ester is amplified by significantly higher accumulated charge on BN particle in the ester- compared with the charge on the BN particle in the mineral-oil, leading to the net negatively charged BN particles in the esters, but only polarised BN particles in the mineral oils.

In this chapter, both the direct observation and the micro-scale observation were utilised to investigate the dynamic behaviours of the nanofluids under the DC voltage stress. The TiO<sub>2</sub> and BN particles are dispersed with the SE, the NE, and the MO, respectively, to achieve the nanofluids being studied in this research. The results of these investigations show that both the TiO<sub>2</sub> and BN particles are negatively charged in the esters under the DC stress. However, TiO<sub>2</sub> and BN particles are polarised only (no net charge) in the mineral oils under the DC stress. This is due higher electron capture ability of these two particles as compared with the ester molecules, but lower electron capture ability as compared with the mineral oil molecules.

## Chapter 8 CONDUCTION CURRENT AND MOBILITY OF CHARGE CARRIERS IN NANOFUIDS

---

In Chapters 5 and 6, the conduction current and the mobility of charge carriers in three dielectric liquids (the synthetic and natural esters and the mineral oil) were obtained in the electric field from  $\sim 10$  kV/m to  $\sim 10 \cdot 10^8$  kV/m. A positive correlation between the mobility of the charge carriers and the electric field strength was established for all three tested liquids. Besides, the obtained results show that the space charge density in the ester liquids is significantly higher (about one order of magnitude) than that in the mineral oil under the same applied electric field.

The mobility of charge carriers and the EHD movement of particles was also investigated in nanofluids. In Chapter 7, the EHD behaviour of nanoparticles in the nanofluids was investigated using the direct and micro-scale observation methods. The results of this study demonstrated that both  $\text{TiO}_2$  and BN particles are negatively charged in the ester-based nanofluids but only polarised in the mineral-oil-based nanofluids.

Further investigations of the nanofluids are required to obtain their dielectric properties. Thus, it is necessary and important to characterise the electric conduction processes in these nanofluids. The results of these investigations will help to provide recommendations for practical use of nanofluids as insulating liquids in high voltage systems and apparatuses in different power and pulsed power applications. Therefore, the electric conduction current and the mobility of charge carriers in the nanofluids were investigated in the present chapter. This chapter presents and discusses the obtained experimental results on the conduction processes in the nanofluids with 0.1 % b/w and 0.005% b/w concentrations of  $\text{TiO}_2$  and BN particles. The DC electric current and the mobility of charge carriers in the nanofluids have been obtained, and these characteristics have been compared with the same parameters obtained in pure liquids.

## **8.1 Experimental Procedure**

The ToF measurements were conducted to facilitate the analysis of the mobility of charge carriers in the nanofluids. The prepared nanofluids were subjected to the DC stress in the test cell with the guard-ring structure. The single-polarity method was used to measure the time of flight.

### **8.1.1 Tests Conducted in the Guard-Ring Test Cell**

Nanofluids with 0.005% b/w and 0.1% b/w concentrations of TiO<sub>2</sub> and BN particles were tested in this study. The preparation procedure of these nanofluids and the rationale for selection of these specific concentrations of BN and TiO<sub>2</sub> particles were presented in Section 4.1.2. The lower concentration of TiO<sub>2</sub> nano-particles, 0.005% b/w, is proved to increase the breakdown strength of nanofluids [21]. The higher concentration, 0.1% b/w, was selected to investigate the effect of higher concentration of solid nanoparticles on the behaviours of these nanoparticles in the external electric field. The size distribution of the TiO<sub>2</sub> and BN nanoparticles in the developed nanofluids were obtained and presented in Table 4-4 in Section 4.1.3.

The single-polarity measurements were conducted by applying a DC step voltage to the test cell with the guard-ring topology. The schematic diagram of the test cell and the experimental test system arrangement were presented in Figure 4-8 in Section 4.3.1. During the individual test, all nanofluids were stressed with DC voltage for 60 minutes. The electric current passing through the test cell was measured by the Keithley 6514 electrometer, and the data acquisition rate was two current readings per second.

Three DC voltage levels of both polarities:  $\pm 2$  kV,  $\pm 4$  kV, and  $\pm 6$  kV, were selected for these single-polarity ToF tests. Three individual tests were carried out for each type of nanofluid stressed with a specific voltage level. Each individual test was conducted using a fresh sample of specific nanofluid, the prepared nanofluids were stored in a sealed storage container. After each ToF test, the test cell was cleaned with ethanol and lint-free tissue to

remove residual fluid from the internal surface of the test cell and the surface of the two electrodes.

## **8.2 Experimental Results: Nanofluids with TiO<sub>2</sub> Particles**

The results obtained using nanofluids consisting of the TiO<sub>2</sub> particles are presented in this section. The electric current passing through the nanofluids stressed with different voltage levels was obtained by the single-polarity method and the mobility of the charge carriers was obtained and analysed. The current through the pure liquids (no suspended particles) and the mobility of charge carriers in the pure dielectric liquids obtained from Section 5.3.1 to 5.3.3. are presented in this chapter as the reference.

### **8.2.1 Electric Current and Mobility of Charge Carriers in Synthetic-ester-based Nanofluids**

The conduction current passing through the MIDEAL 7131 Synthetic Ester based nanofluids with 0.005% b/w and 0.1% b/w concentrations of TiO<sub>2</sub> particles, and through the pure SE liquid stressed with DC voltage is shown in Figure 8-1 and Figure 8-2. The conduction current in the pure SE fluid was obtained and discussed in Section 5.3.1. This current as a function of time is shown in Figure 8-1 and Figure 8-2 for the reference purposes. Each current line in Figure 8-1 represents the value from three individual tests.

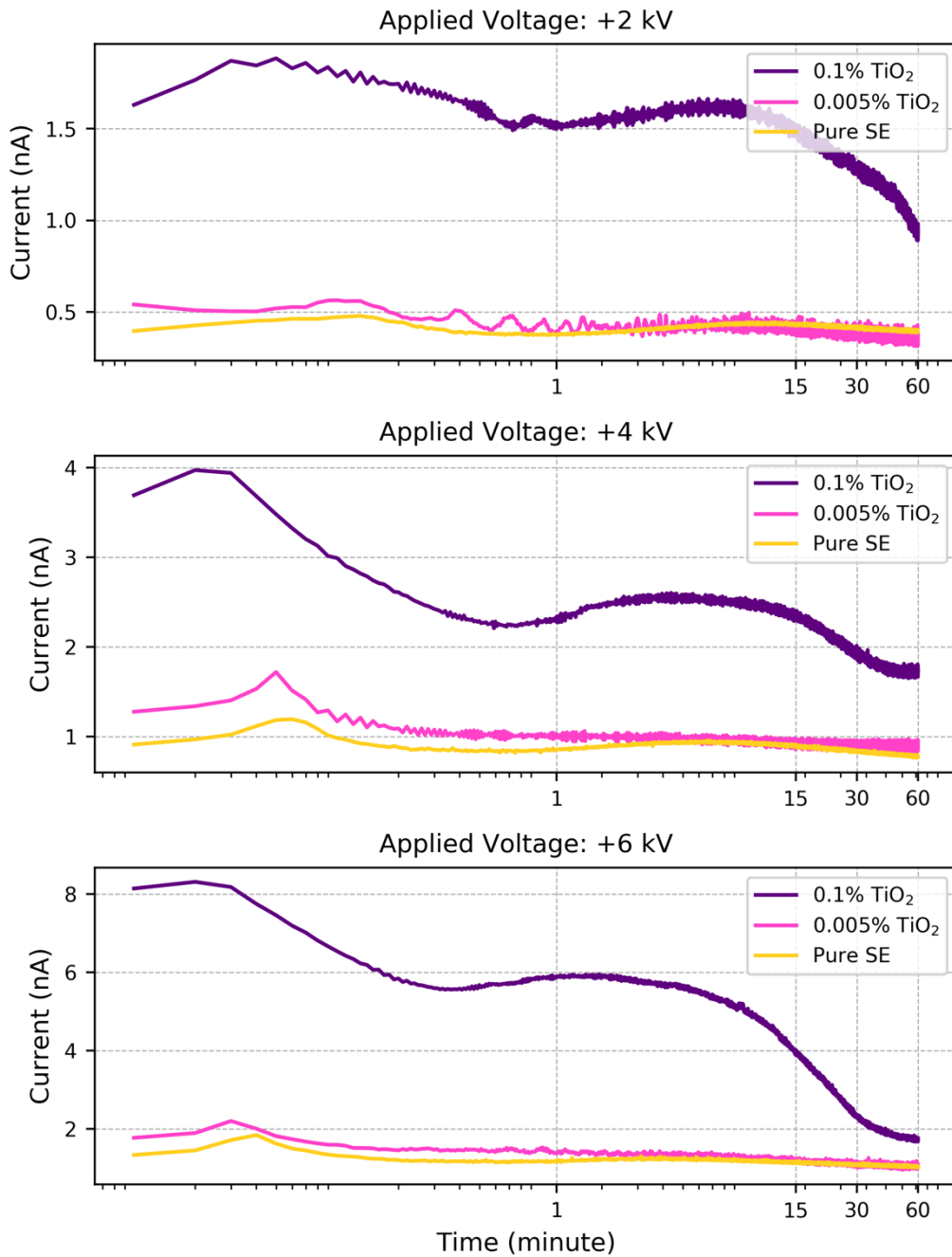


Figure 8-1 Current through the SE-based nanofluids with 0.1% b/w and 0.005% b/w concentrations of TiO<sub>2</sub> particles (positive DC voltage). Each individual current line is an average of three individual tests. The current through the pure SE is shown as a reference.

Figure 8-1 shows that the electric current through the SE-based nanofluids with 0.1% b/w concentration of TiO<sub>2</sub> particles is significantly higher than the current through both the pure SE and the SE-based nanofluid with 0.005% concentration of TiO<sub>2</sub> particles under the same voltage level.

The current values fluctuate during the 60-minute measurement interval. In this research, it was found that the nanofluids with 0.1% concentration took much longer time (generally more than 3 hours) than the dielectric liquids to reach the quasi-steady state. In this case, it is impossible to use the conduction current for the current analysis in this study. To quantify the difference between the currents in the prepared nanofluid, the current obtained at the end of each test (i.e., between the 59<sup>th</sup> and 60<sup>th</sup> min of measurements) was used. This current is referred to as the ‘Final Current’. Thus, the current obtained between the 59<sup>th</sup> and 60<sup>th</sup> min of application of the DC stress was used to calculate the average “Final Current” value for each sample, the obtained “Final Currents” for each nanofluids studied in this section are shown in Table 8-1.

Table 8-1 Final current for the SE-based nanofluids (positive energisation)

Liquid	Final Current (nA)		
	+2 kV	+4 kV	+6 kV
Pure Synthetic Ester	0.397±0.002	0.780±0.001	1.033±0.004
SE-based Nanofluid (0.005% b/w TiO <sub>2</sub> particles)	0.358±0.004	0.895±0.006	1.041±0.008
SE-based Nanofluid (0.1% b/w TiO <sub>2</sub> particles)	0.938±0.004	1.726±0.011	1.895±0.006

The uncertainty in Table 8-1 was calculated according to the procedure presented in Section 0. Type A uncertainty evaluation method was used to calculate the standard deviation at the 95% confidence level using the sample size of 360 data points. Type B evaluation was used to obtain the uncertainty associated with the voltage source. The uncertainties provided in Table 8-1 are combined uncertainties which were obtained by Equation III-1 in Section 0 using both evaluation types: A and B.

As shown in Table 8-1, the final current through the SE-based nanofluids with 0.005% b/w concentration of the TiO<sub>2</sub> particles is like that through the pure SE fluid under the same voltage level. On the other hand, the final currents through the SE-based nanofluids with 0.1% b/w concentration of the TiO<sub>2</sub> particles are ~ (1.8 - 2.2) times higher than the final currents through the pure SE fluid under the same DC voltage. The difference between the final currents through the SE-based nanofluids with 0.1% b/w concentration of the TiO<sub>2</sub> particles and the pure SE fluid decreases when the voltage level increases. Based on the current plots and the EHD behaviours of the nanoparticles obtained in the previous chapter, it can be concluded that the higher currents through the SE-based nanofluids with 0.1% b/w concentration of the TiO<sub>2</sub> particles can be attributed to the motion of the TiO<sub>2</sub> particles. A detailed discussion of this effect is presented in Section 8.4.

From Figure 8-1, two current peaks, which were found in the pure dielectric liquids, are also present in these two nanofluids. Like the description in Section 5.3.1, the ‘first current peak’ refers to the peak which appears early in the test, and the ‘second current peak’ refers to the peak that appears after the first one. To resolve the second peak more clearly, time axis in the current plots is presented in the log scale. According to Section 5.3.1, the time to appearance of the first current peak is the ToF interval, which is used to calculate the charge carrier mobility according to Equation 2-26 in Section 2.3.1.

In addition, as introduced in Section 2.3.1, a correction coefficient is introduced in calculations of the mobility of charge carriers in the single-polarity method. The application of this coefficient is described by Equation 2-26 in Section 2.3.1. However, the measurement of the correction coefficient for the nanofluids was obstructed because the particles in the nanofluids can form a closed-circuit easily in the coaxial test cell (the gap distance between the two electrodes is only 1 mm). Therefore, for the nanofluids, the correction coefficient used in the mobility calculation is followed the correction coefficient of the relative hosting liquids. In this case, the correction coefficient of the SE presented in Section 5.2.1 was selected as the

correction coefficient for the SE-based nanofluids. In this Section, the mobility of charge carriers in the nanofluids was calculated following the same procedure as described in Section 5.3.1. The obtained mobilities and their uncertainties are presented in Table 8-2.

Table 8-2 Mobility of charge carriers in the tested liquids under positive DC voltage

Liquid	Mobility ( $\times 10^{-9} \text{ m}^2/(\text{V}\cdot\text{s})$ )		
	+2 kV	+4 kV	+6 kV
Pure Synthetic Ester	0.95±0.17	0.88±0.20	0.78±0.12
SE-based Nanofluid (0.005% b/w TiO <sub>2</sub> particles)	1.26±1.08	1.26±0.59	0.98±0.14
SE-based Nanofluid (0.1% b/w TiO <sub>2</sub> particles)	2.20±1.13	1.60±0.67	1.30±0.19

The Type A uncertainty in the mobility calculation is related to the ToF intervals obtained in three individual tests. Considering the small sample size (three tests), the Type A uncertainty was calculated at the 95% confidence level using the two-sided, two degrees of freedom Student distribution parameters.

The Type B uncertainty in the calculation stems from the uncertainty of the clock of the LabVIEW and the voltage source. The uncertainty given in Table 8-2 is the combined uncertainty which includes uncertainties of both Type A and Type B. This combination was delivered by Equation III-1 in Section 0.

The obtained mobility of charge carriers in three types of liquids are given in Table 8-2, which shows that the mobility decreases with a decrease in the concentration of nanoparticles in the tested liquid. The mobility is highest for the SE-based nanofluid with a 0.1% b/w

concentration of TiO<sub>2</sub> nanoparticles and the lowest for the pure SE. This tendency can be seen at all three tested voltage levels. Further discussions on the mechanisms behind this characteristic will be presented in Section 8.4.

Moreover, it was found that the uncertainties in the obtained mobility values for the nanofluids with 0.005% b/w and 0.1% b/w concentrations of TiO<sub>2</sub> nanoparticles decrease with an increase in the applied voltage. This is the result of short ToF values, which are close to data acquisition rates, i.e., the ToFs of all three individual tests of the nanofluids with 0.1% b/w concentration of TiO<sub>2</sub> nanoparticles stressed with +6 kV are 1.5 s, which corresponds to 3 current acquisition intervals (the electrometer returns only three current measurements within 1.5 s). Thus, the accuracy in resolution of the current peaks in the time domain is limited by the data acquisition rate, resulting in that the Type A uncertainty of the ToF was zero in this case.

The conduction current through the nanofluids was also obtained under negative DC energisation. The current-time characteristics under negative voltage stress is presented in Figure 8-2.

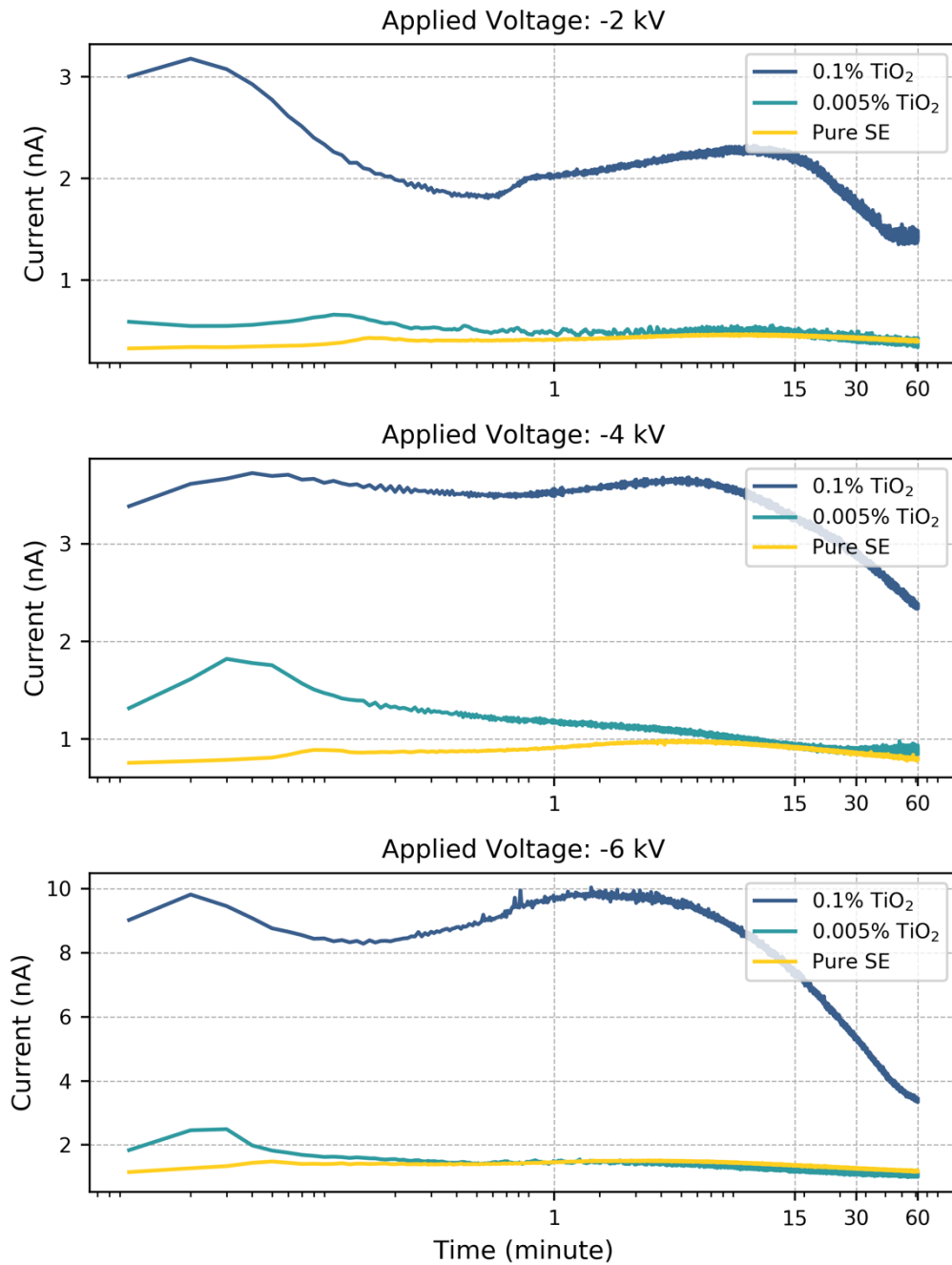


Figure 8-2. Current through the SE-based nanofluids with 0.1% b/w and 0.005% b/w concentrations of TiO<sub>2</sub> particles (negative DC voltage). Each individual current line is an average of three individual tests. The current through the pure SE is shown as a reference.

The final current in all three types of dielectric liquids under the negative DC stress was obtained following the procedure described for the positive energisation, and the results are listed in Table 8-3.

Table 8-3 Final current for the SE-based nanofluids (negative energisation)

Liquid	Final Current (nA)		
	-2 kV	-4 kV	-6 kV
Pure Synthetic Ester	0.399±0.001	0.791±0.001	1.182±0.002
SE-based Nanofluid (0.005% b/w TiO <sub>2</sub> particles)	0.376±0.004	0.874±0.009	1.044±0.008
SE-based Nanofluid (0.1% b/w TiO <sub>2</sub> particles)	1.417±0.038	2.364±0.004	3.399±0.008

It can be seen from Table 8-3 that the final currents in the nanofluids with 0.1% b/w concentration of TiO<sub>2</sub> nanoparticles are approximately three times higher than the final currents in both pure SE and the SE-based nanofluid with 0.005% b/w concentration of TiO<sub>2</sub> nanoparticles under the same DC voltage.

The final currents in the nanofluids with 0.1% b/w concentration of TiO<sub>2</sub> stressed negatively are ~ 50% higher than the final currents in the same nanofluid under positive energisation under the same voltage level. However, the final currents in the nanofluid with 0.005% b/w concentration of TiO<sub>2</sub> nanoparticles under positive DC energisation are similar to the final currents in the same nanofluids under negative energisation.

In the case of the negative energisation, the current waveforms also demonstrate two current peaks, which are like the case of the positive energisation. The ToF obtained using the first

current peak were used to calculate the mobility of charge carriers in the nanofluids, and the results with the relative uncertainties are presented in Table 8-4.

Table 8-4 Mobility of charge carriers in the tested liquids under negative DC voltage

Liquid	Mobility ( $\times 10^{-9} \text{ m}^2/(\text{V}\cdot\text{s})$ )		
	-2 kV	-4 kV	-6 kV
Pure Synthetic Ester	0.69 $\pm$ 0.17	0.54 $\pm$ 0.13	0.62 $\pm$ 0.14
SE-based Nanofluid (0.005% b/w TiO <sub>2</sub> particles)	1.21 $\pm$ 1.01	1.10 $\pm$ 0.61	1.07 $\pm$ 0.45
SE-based Nanofluid (0.1% b/w TiO <sub>2</sub> particles)	2.07 $\pm$ 1.09	1.96 $\pm$ 0.29	1.30 $\pm$ 0.19

It shows that the mobility of charge carriers in the SE-based nanofluids under negative energisation is the highest with the largest concentration of the TiO<sub>2</sub> 0.1% b/w and the smallest with the pure SE fluid. This tendency is same with the tendency demonstrated by the mobilities obtained under positive energisation.

The results presented in Table 8-2 and Table 8-4, also demonstrate that the mobility of charge carriers in the pure SE under positive energisation is higher than that under negative energisation (at the same voltage level). However, in the SE-based nanofluids, the mobility of charge carriers under positive energisation is similar to that under negative energisation (at the same voltage level).

It was also found that the uncertainties in the mobility for both SE-based nanofluids with 0.005% b/w and 0.1% b/w concentrations of TiO<sub>2</sub> nanoparticles decreases with an increase in the applied voltage, which is like the tendency observed under positive energisation.

## **8.2.2 Electric Current and Mobility of Charge Carriers in Natural-ester-based Nanofluids**

Figure 8-3 and Figure 8-4 show the current plots of the NE-based nanofluids under positive and negative voltages, respectively. The current plots of the NE from Section 5.3.2 are also included in Figure 8-3 and Figure 8-4 for reference.

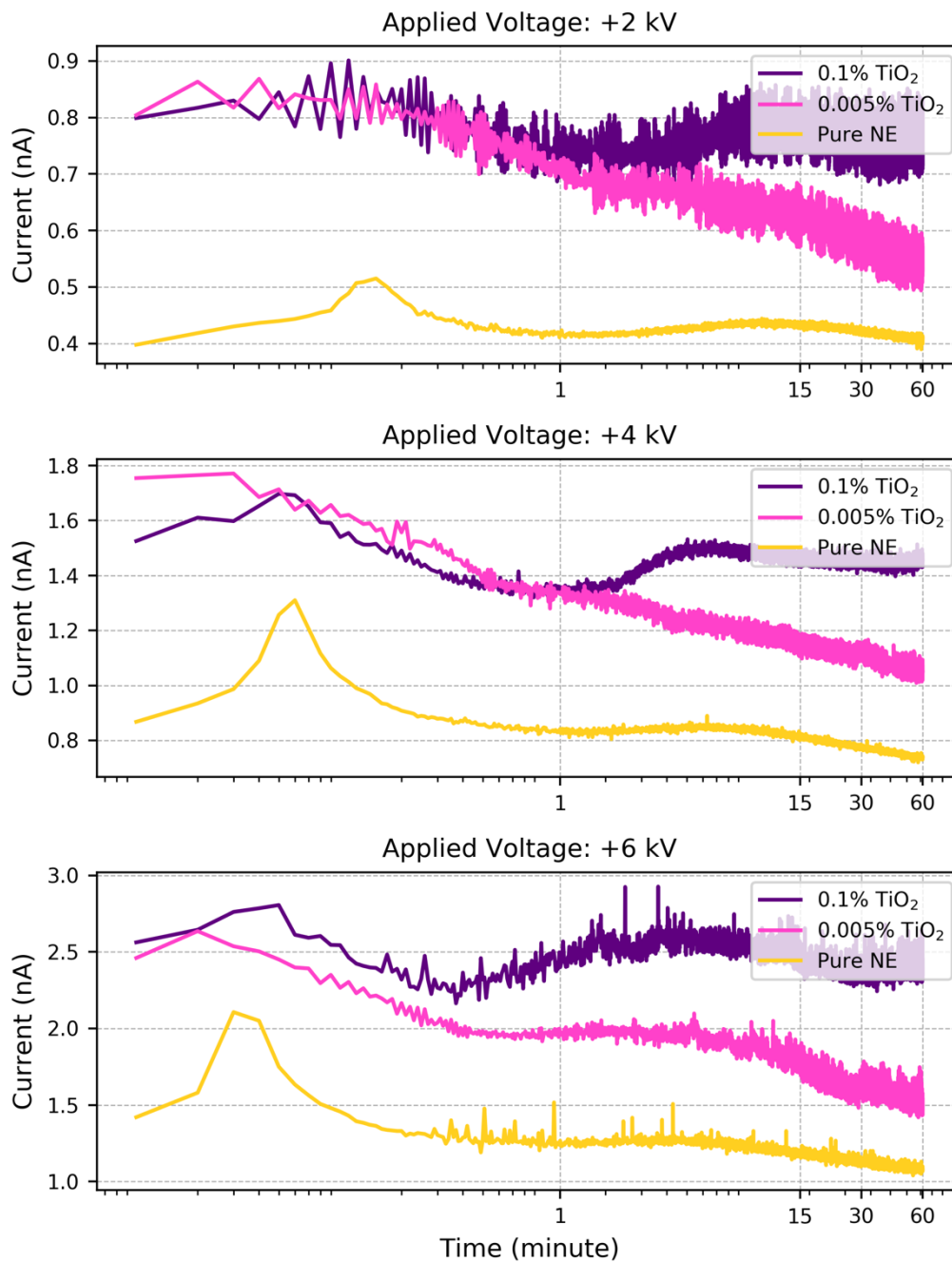


Figure 8-3 Current through the NE-based nanofluids with 0.1% b/w and 0.005% b/w concentrations of TiO<sub>2</sub> particles (positive DC voltage). Each individual current line is an average of three individual tests. The current through the pure NE is shown as a reference.

Figure 8-3 presents the current plots obtained for the NE-based nanofluids with the following concentrations of TiO<sub>2</sub> particles: 0.005% b/w and 0.1% b/w. Each individual current plot in Figure 8-3 represents an averaged result based on three individual tests. Using current waveform shown in Figure 8-3, the final currents in three types of liquids were obtained, and the results with the relative uncertainties are given in Table 8-5:

Table 8-5 Final current for the NE-based nanofluids (positive energisation)

Liquid	Final Current (nA)		
	+2 kV	+4 kV	+6 kV
Pure Natural Ester	0.405±0.001	0.738±0.002	1.083±0.005
NE-based Nanofluid (0.005% b/w TiO <sub>2</sub> particles)	0.545±0.005	1.053±0.005	1.504±0.009
NE-based Nanofluid (0.1% b/w TiO <sub>2</sub> particles)	0.766±0.006	1.460±0.007	2.405±0.012

The results presented in Table 8-5 show that the final currents in both NE-based nanofluids with 0.005% and 0.1% b/w concentration of TiO<sub>2</sub> nanoparticles are higher than the final currents of the pure NE under the same voltage level. The final currents in the NE-based nanofluid with 0.005% b/w concentration of TiO<sub>2</sub> nanoparticles are ~ (1.3 – 1.4) times higher than the final currents in the pure NE, while the final currents in the NE-based nanofluids with 0.1% b/w concentration of TiO<sub>2</sub> nanoparticles are ~ (1.9 – 2.2) times higher than the final currents in the pure NE.

The mobility of charge carriers in the tested liquids was following the same procedure described in the previous section, the obtained mobility values with their relative uncertainties are shown in Table 8-6.

Table 8-6 Mobility of charge carriers in the tested liquids under positive DC voltage

Liquid	Mobility ( $\times 10^{-9} \text{ m}^2/(\text{V}\cdot\text{s})$ )		
	+2 kV	+4 kV	+6 kV
Pure Natural Ester	1.07±0.12	1.26±0.25	1.20±0.32
NE-based Nanofluid (0.005% b/w TiO <sub>2</sub> particles)	1.80±2.81	2.80±2.33	3.36±5.78
NE-based Nanofluid (0.1% b/w TiO <sub>2</sub> particles)	1.48±0.40	1.68±1.45	0.99±0.26

The mobility of charge carriers in the tested liquids is given in Table 8-6. However, due to the large uncertainties in the results, there is no statistically significant difference among the obtained mobility values. For example, the uncertainties in the mobility for the NE-based nanofluid with 0.005% b/w concentration of TiO<sub>2</sub> nanoparticles are greater than or close to the values of the relative mobility.

The reason for much higher uncertainties in the mobility of charge carriers in the two types of nanofluids is not well pronounced current peaks in the current graphs. Thus, it could be problematic to identify the first current peak in the NE-based nanofluids, as shown in Figure 8-3. In this case, it is difficult to quantify the effect of the nanoparticles on the mobility of charge carriers in the NE-based nanofluids.

The results obtained under the negative DC stress are presented in Figure 8-4.

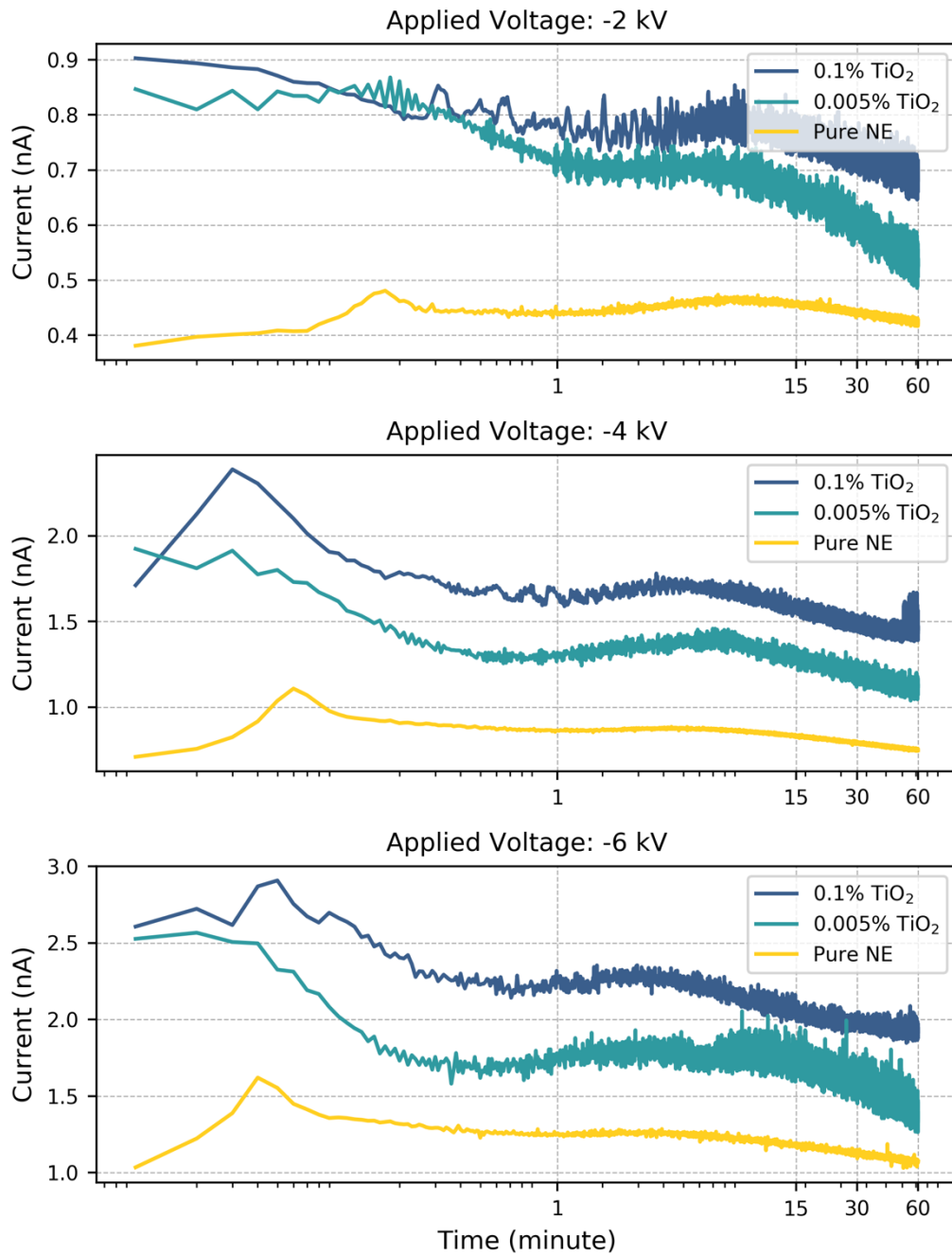


Figure 8-4 Current through the NE-based nanofluids with 0.1% b/w and 0.005% b/w concentrations of TiO<sub>2</sub> particles (negative DC voltage). Each individual current line is an average of three individual tests. The current through the pure NE is shown as a reference.

The final current in the three types of liquids under the negative DC voltage is calculated using the same procedure as in the case of positive polarity, the final current values with their relative uncertainties are listed in Table 8-7.

Table 8-7 Final current for the NE-based nanofluids (negative energisation)

Liquid	Final Current (nA)		
	-2 kV	-4 kV	-6 kV
Pure Natural Ester	0.424±0.001	0.751±0.002	1.073±0.004
NE-based Nanofluid (0.005% b/w TiO <sub>2</sub> particles)	0.529±0.004	1.112±0.009	1.456±0.009
NE-based Nanofluid (0.1% b/w TiO <sub>2</sub> particles)	0.682±0.004	1.443±0.010	1.925±0.010

According to the results shown in Table 8-7, the final currents in the nanofluids with 0.005% b/w concentration of TiO<sub>2</sub> nanoparticles are ~ (1.2 – 1.4) times higher than the final currents in the pure NE, while the final currents in the nanofluid with 0.1% b/w concentration of TiO<sub>2</sub> nanoparticles are ~ (1.7 – 1.9) times higher than the final currents in the pure NE. Both of these two findings are similar to the results under the positive energisation.

The mobility of charge carriers in the tested liquids was obtained based on the current plots shown in Figure 8-4, the mobility values with their uncertainties are shown in Table 8-8.

Table 8-8 Mobility of charge carriers in the tested liquids under negative DC voltage

Liquid	Mobility ( $\times 10^{-9} \text{ m}^2/(\text{V}\cdot\text{s})$ )		
	-2 kV	-4 kV	-6 kV
Pure Natural Ester	0.97 $\pm$ 0.16	1.14 $\pm$ 0.21	1.05 $\pm$ 0.24
NE-based Nanofluid (0.005% b/w TiO <sub>2</sub> particles)	2.80 $\pm$ 4.92	1.80 $\pm$ 1.12	1.12 $\pm$ 0.57
NE-based Nanofluid (0.1% b/w TiO <sub>2</sub> particles)	1.14 $\pm$ 0.74	2.10 $\pm$ 0.18	2.40 $\pm$ 2.95

The mobilities of charge carriers in the nanofluids obtained under negative energisation also have large uncertainties in the case of negative energisation. For example, for the nanofluids with 0.005% b/w concentration of TiO<sub>2</sub> nanoparticles, the mobility obtained under -2 kV is smaller than its relative uncertainty, and the uncertainty in the mobility values obtained under -4 kV and -6 kV is more than half of the mobility values. Thus, further studies on the mobility in the NE-based are required.

### 8.2.3 Electric Current in Mineral-oil-based Nanofluids

In Chapter 5 and 6, the mobility of charge carriers in the esters and the mineral oils was presented and discussed, it was also shown that the space charge density in the ester liquids is approximately one order of magnitude higher than that in the mineral oils. In Chapter 7, it was concluded that the nanoparticles are polarised in the mineral oils however they become negatively charged (acquired a net negative charge) in the ester liquids stressed with the external electric field.

In this section, the current plots for the MO-based nanofluids under positive and negative voltages are presented and analysed. The current plots for the MO-based nanofluids are shown in Figure 8-5 and Figure 8-6, respectively. These current waveforms in the MO-based

nanofluids were obtained using the single-polarity method, which is discussed in Section 5.3.3. The current plots obtained in the pure MO are shown as reference.

It was found that the conduction current through the nanofluid with 0.1% b/w concentration of TiO<sub>2</sub> nanoparticles is significantly higher than the conduction current through the nanofluid with 0.005% b/w concentration of TiO<sub>2</sub> nanoparticles at the same voltage level. To provide the detailed current waveforms for these two nanofluids, the current plots for the nanofluid with 0.1% b/w and 0.005% b/w concentrations of TiO<sub>2</sub> nanoparticles are presented in different graphs.

For the nanofluids with 0.005% b/w concentration of TiO<sub>2</sub> nanoparticles, the current plots obtained under the positive energisation are shown in Figure 8-5. The current in the nanofluids with 0.1% b/w concentration of TiO<sub>2</sub> nanoparticles under positive energisation is shown in Figure 8-6. Each individual current line in Figure 8-5 and Figure 8-6 represent an averaged result from three individual tests.

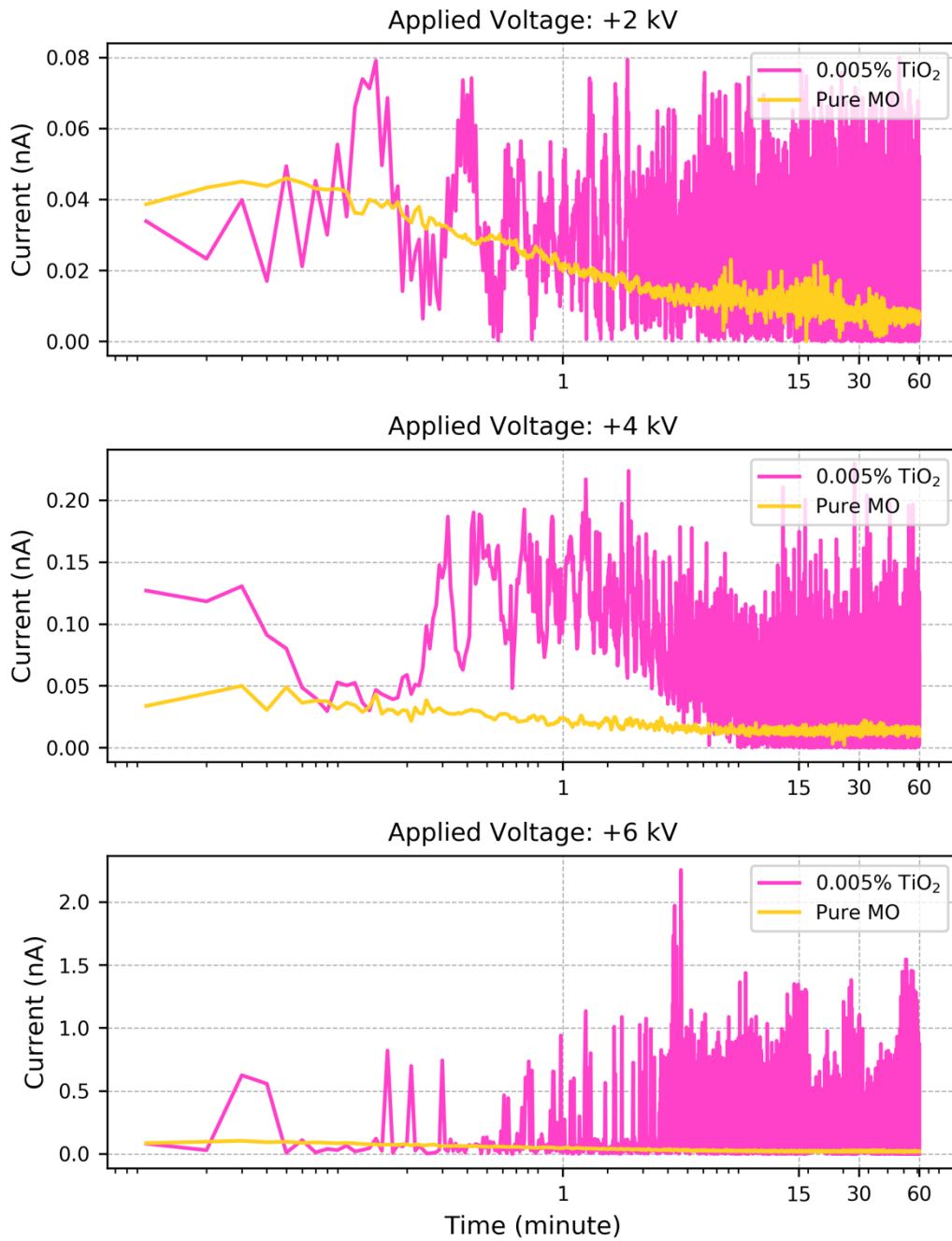


Figure 8-5 Current through the MO-based nanofluids with 0.005% b/w concentrations of TiO<sub>2</sub> particles (positive DC voltage). Each individual current line is an average of three individual tests. The current through the pure MO is shown as a reference.

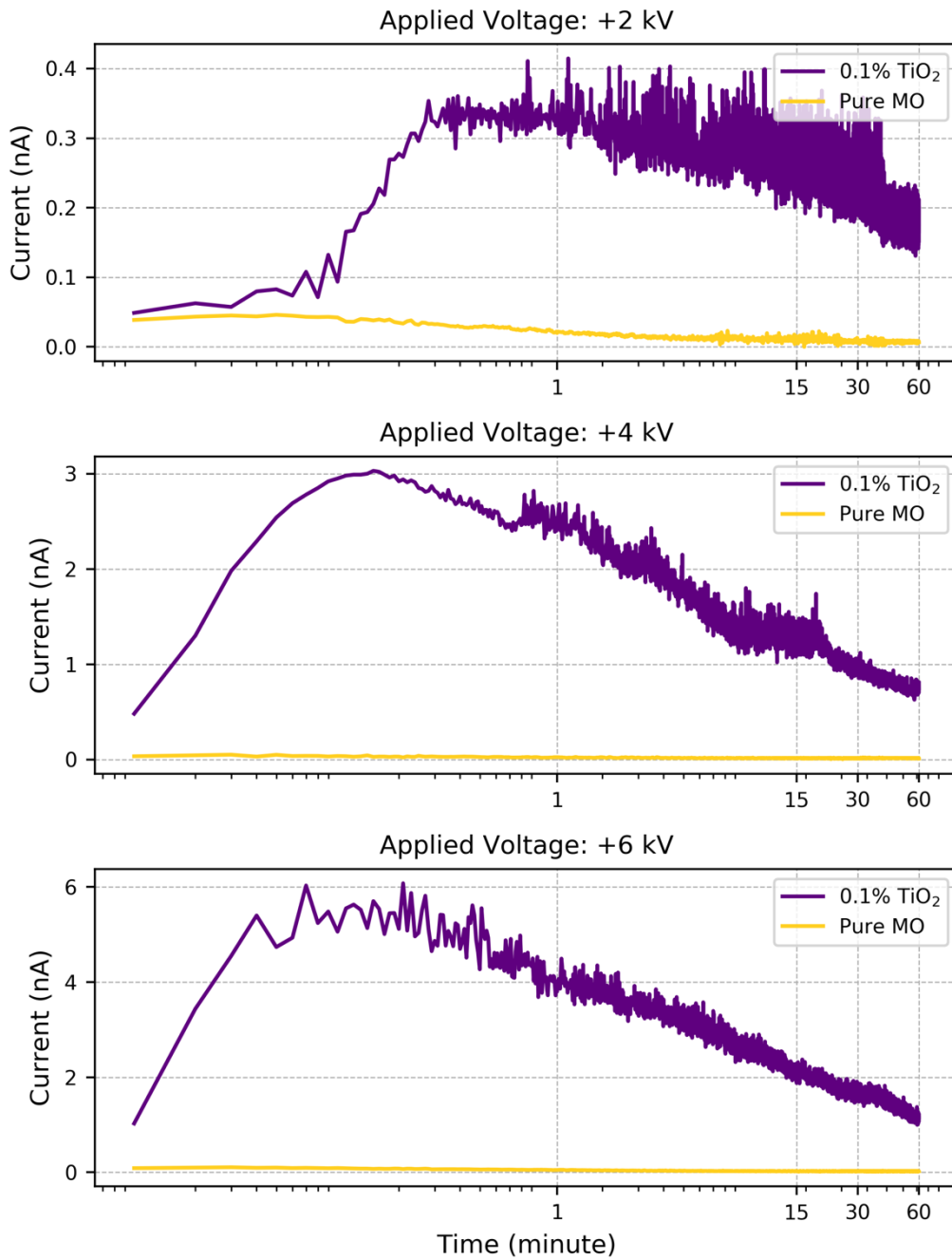


Figure 8-6 Current through the MO-based nanofluids with 0.1% b/w concentrations of TiO<sub>2</sub> particles (positive DC voltage). Each individual current line is an average of three individual tests. The current through the pure MO is shown as a reference.

The final current in all three types of liquids under the positive DC voltage were obtained using individual current waveforms, the final currents with their relative uncertainties are listed in Table 8-9:

Table 8-9 Final current for the MO-based nanofluids (positive energisation)

Liquid	Final Current (nA)		
	+2 kV	+4 kV	+6 kV
Pure Mineral Oil	0.007±0.000	0.014±0.000	0.022±0.000
MO-based Nanofluid (0.005% b/w TiO <sub>2</sub> particles)	0.026±0.003	0.040±0.006	0.087±0.032
MO-based Nanofluid (0.1% b/w TiO <sub>2</sub> particles)	0.178±0.004	0.638±0.061	1.118±0.088

Using the current waveforms shown in Figure 8-5, it can be concluded that the current through the nanofluid with 0.005% b/w concentrations of TiO<sub>2</sub> nanoparticles is ~ (2.9 – 4.0) times higher than that through the pure MO.

The variation of the current through the nanofluid with 0.005% b/w concentration of TiO<sub>2</sub> nanoparticles is significantly higher than the variation in the current through the pure MO, which is reflected by the relevant uncertainties in the final currents listed in Table 8-9. It should be emphasised here that the higher variations in the current in the nanofluids with 0.005% b/w concentration of TiO<sub>2</sub> nanoparticles results in a difficult identification of the first peak. Thus, the mobility of the charge carriers in the nanofluids with the 0.005% b/w concentration of TiO<sub>2</sub> nanoparticles requires further investigation.

Compared with the pure MO, the nanofluids with 0.1% b/w concentrations of TiO<sub>2</sub> nanoparticles show ~ (25.4 – 50.8) times higher final currents compared with that through the pure MO. As shown in Figure 8-6, one clearly resolved current peak occurs in each individual current waveform. This current peak typically occurs within ~ 5 s after the voltage switch-on. Then, the current keeps decreasing until the end of the test. Combination this finding with the observations shown in Section 7.4.1 and 7.4.2, leads to that this current peak is formed due to the motion of the TiO<sub>2</sub> particles in the nanofluids. Thus, the ‘ToF’ obtained from this current peak cannot be used for the calculation of the mobility.

Figure 8-7 and Figure 8-8 show the current through the nanofluids obtained under negative energisation.

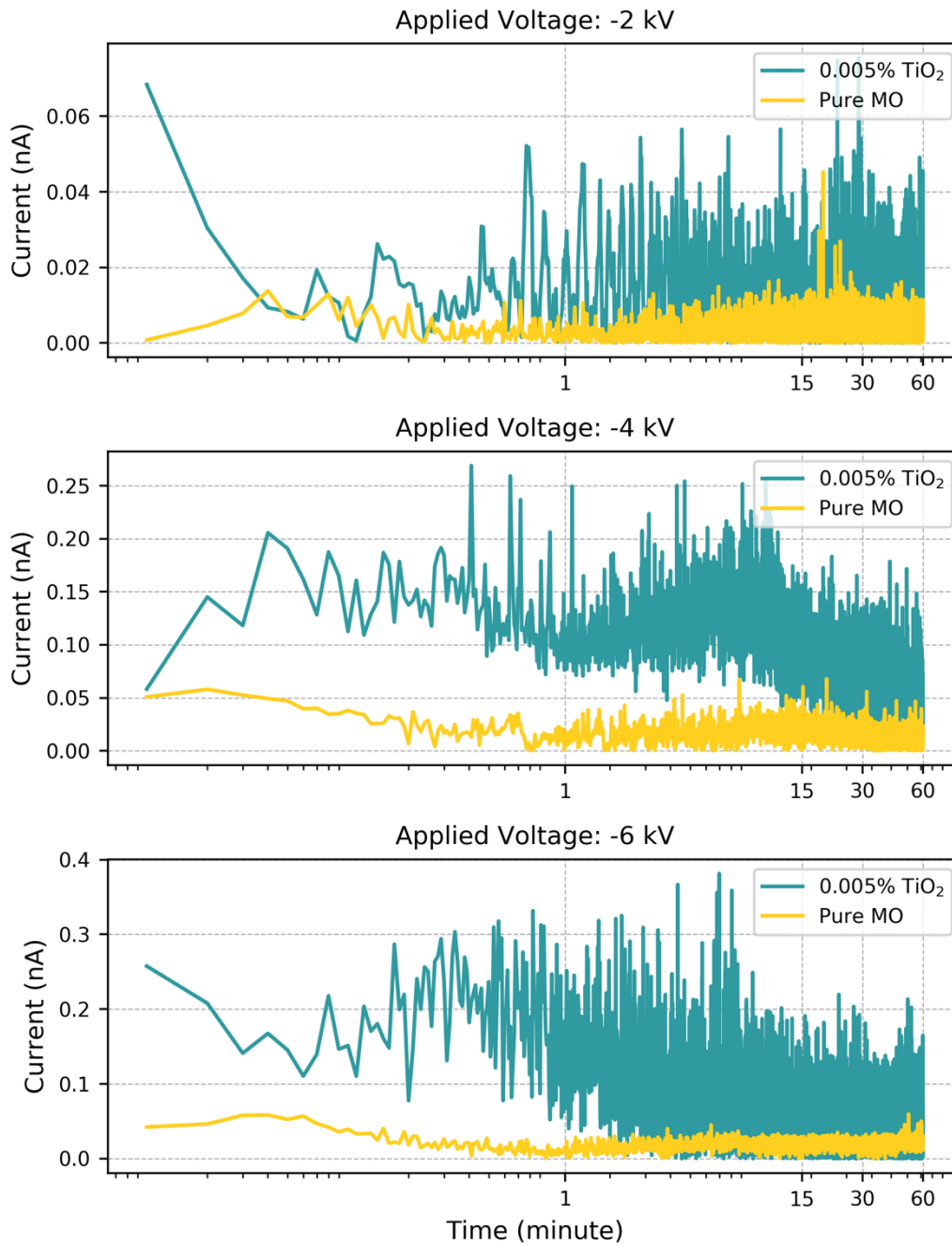


Figure 8-7 Current through the MO-based nanofluids with 0.005% b/w concentrations of TiO<sub>2</sub> particles (negative DC voltage). Each individual current line is an average of three individual tests. The current through the pure MO is shown as a reference.

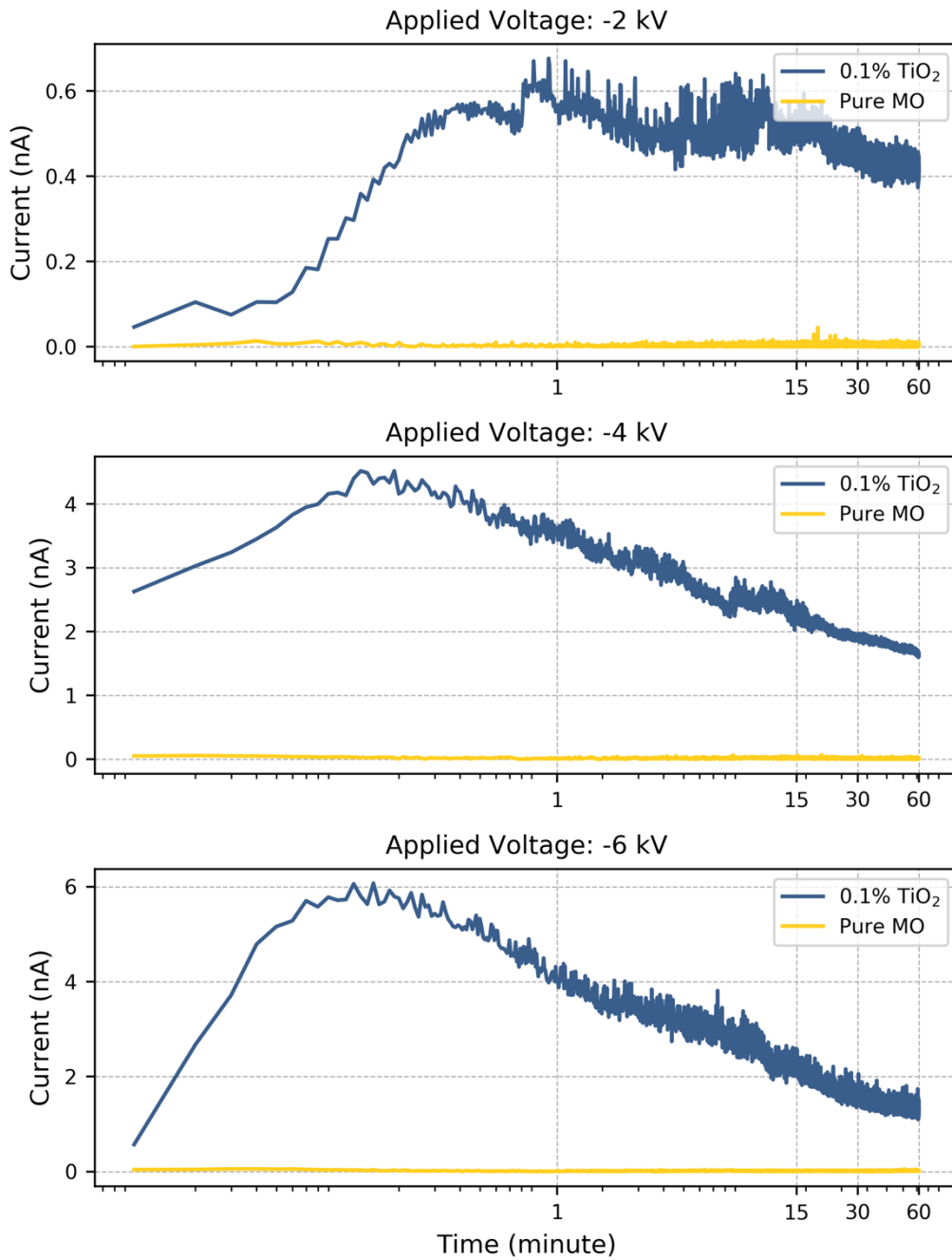


Figure 8-8 Current through the MO-based nanofluids with 0.1% b/w concentrations of TiO<sub>2</sub> particles (negative DC voltage). Each individual current line is an average of three individual tests. The current through the pure MO is shown as a reference.

The Final current in all three types of liquids obtained under the negative energisation with their relative uncertainties are listed in Table 8-10:

Table 8-10 Final current for the MO-based nanofluids (negative energisation)

Liquid	Final Current (nA)		
	-2 kV	-4 kV	-6 kV
Pure Mineral Oil	0.007±0.001	0.015±0.001	0.023±0.001
MO-based Nanofluid (0.005% b/w TiO <sub>2</sub> particles)	0.023±0.001	0.049±0.005	0.063±0.009
MO-based Nanofluid (0.1% b/w TiO <sub>2</sub> particles)	0.415±0.031	1.642±0.053	1.292±0.049

The current passing through the nanofluids with 0.005% b/w concentration of TiO<sub>2</sub> nanoparticles under negative energisation is ~ (2.7-3.3) times higher than the current passing through the pure MO. As shown in Table 8-10, the variation of the currents through the nanofluids with 0.005% b/w concentration of TiO<sub>2</sub> nanoparticles are also higher than that through the pure MO. Therefore, an accurate identification of the first current peak requires further, higher resolution measurements.

The current as a function of time for the nanofluids with 0.1% b/w concentration of TiO<sub>2</sub> nanoparticles, is shown in Figure 8-8. These current waveforms have demonstrated the tendencies similar to the tendencies found in the current under the positive energisation: the first current peak is observed in each individual test typically within ~ 5 s after application of the voltage. The current after this peak decreasing until the end of each individual measurement, which can be attributed to the motion of the TiO<sub>2</sub> particles in the nanofluids. Moreover, the motion of the TiO<sub>2</sub> particles also causes significantly higher currents compared

with the currents through the MO: the currents through the nanofluids with 0.1% b/w concentrations of TiO<sub>2</sub> nanoparticles are  $\sim$  (56.2 – 109.5) times higher than the currents through the pure MO.

Apart from the nanofluids with TiO<sub>2</sub> particles, this study also included investigation of nanofluids prepared with the BN particles. From Section 8.3.1 to 8.3.3, the current through the SE-, NE-, MO-based nanofluids with BN particles are presented and discussed, respectively.

### **8.3 Experimental Results: Nanofluids with BN Particles**

In this section, the conduction current through the SE-, NE- and MO-based nanofluids with BN particles have been obtained and discussed. The conduction current as a function of time was obtained under different voltage levels using the single-polarity method. Based on these current plots, the mobility of charge carriers in these nanofluids was calculated and analysed. The current plots and mobilities for the pure dielectric liquids first presented in Section 5.3.1 to 5.3.3 are used in this chapter as reference data.

#### **8.3.1 Electric Current and Mobility of Charge Carriers in Synthetic-ester-based Nanofluids**

The current through the synthetic-ester-based nanofluids obtained under positive and negative voltages are shown in Figure 8-9 and Figure 8-10, respectively. The current through the pure Synthetic Ester (SE, MIDEL 7131) obtained by the single-polarity method, is also presented in Figure 8-9 and Figure 8-10 for reference.

Figure 8-9 presents the current waveforms obtained for the SE-based nanofluids with the following concentrations of BN particles: 0.005% b/w and 0.1% b/w. Each current line in Figure 8-9 represents an averaged result from three independent tests.

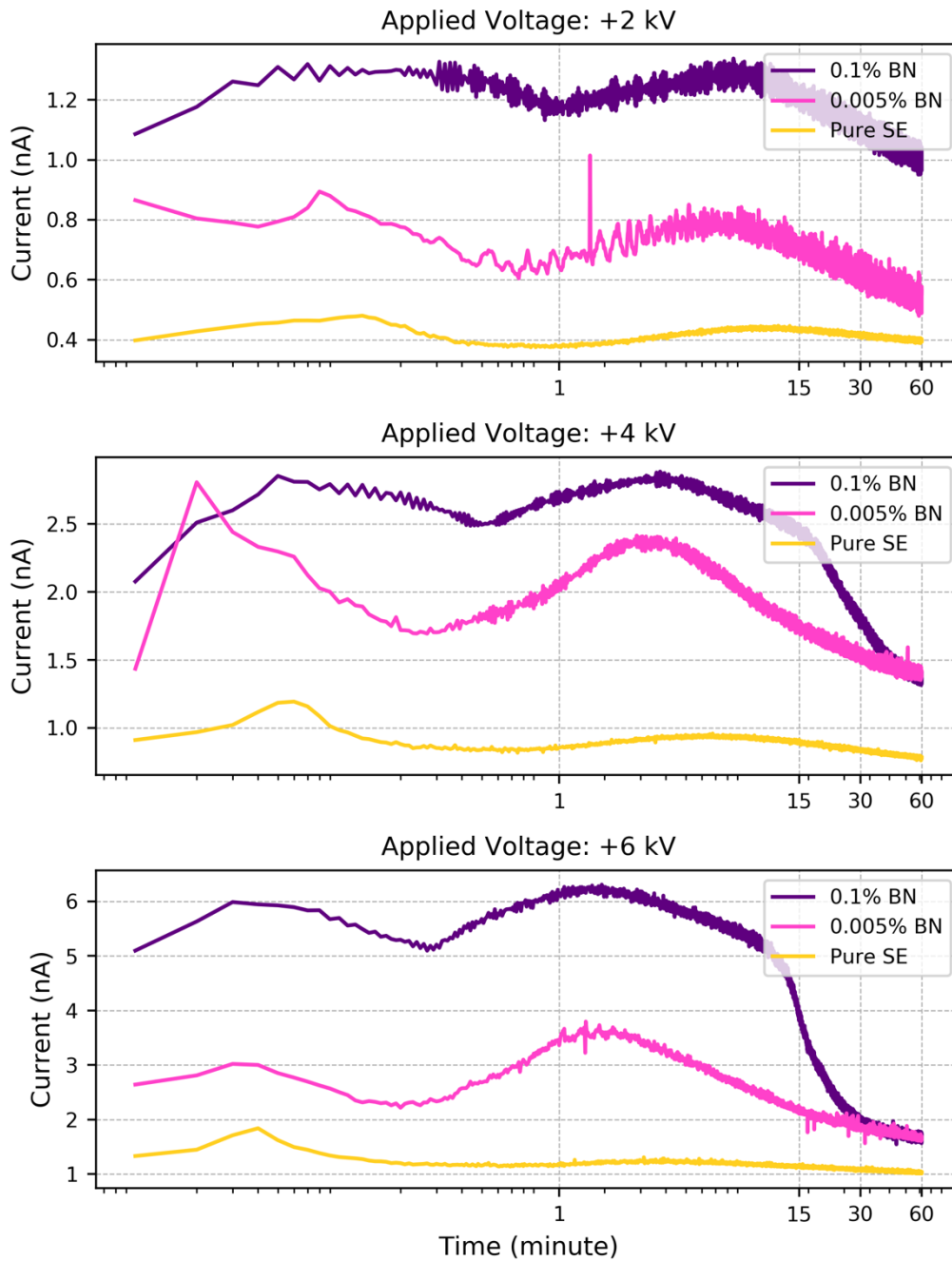


Figure 8-9 Current through the SE-based nanofluids with 0.1% b/w and 0.005% b/w concentrations of BN particles (positive DC voltage). Each individual current line is an average of three individual tests. The current through the pure SE is shown as a reference.

Using the results presented in Figure 8-9, the final current for all three types of liquids under the positive DC voltage was calculated, the final currents and their relative uncertainties are listed in Table 8-11:

Table 8-11 Final current for the SE-based nanofluids (positive energisation)

Liquid	Final Current (nA)		
	+2 kV	+4 kV	+6 kV
Pure Synthetic Ester	0.397±0.002	0.780±0.001	1.033±0.004
SE-based Nanofluid (0.005% b/w BN particles)	0.533±0.005	1.405±0.012	1.660±0.007
SE-based Nanofluid (0.1% b/w BN particles)	1.003±0.005	1.369±0.019	1.711±0.003

The final currents listed in Table 8-11 show that BN particles cause an increase in the currents in both nanofluids with 0.005% and 0.1% b/w concentrations of BN nanoparticles compared with the current in the pure SE: the final currents in the nanofluid with 0.005% b/w concentration of BN nanoparticles is ~ (1.4 – 1.8) times greater than the final currents in the pure SE, while the final current in the nanofluids with the 0.1% b/w concentrations of BN nanoparticles is ~ (1.7 – 2.3) times greater than the final current in the pure SE.

It can be found from both Table 8-11 and Figure 8-9 that the final currents in the nanofluids with 0.005% and 0.1% b/w concentration of BN nanoparticles are closed to each other under +4 kV and +6 kV, energisation. On the other hand, the final current in the nanofluid with 0.1% b/w concentration of BN nanoparticles is approximately twice higher than the final currents through the nanofluid with 0.005% b/w concentration of BN nanoparticles under +2 kV. Besides, the ratio between the final currents in the nanofluid with 0.1% b/w concentration of

BN nanoparticles and in the pure SE decreases when the voltage level increases: ~ 2.5 for +2 kV, ~ 1.8 for +4 kV and ~ 1.7 for +6 kV. This tendency is like the tendency observed in the nanofluids prepared with TiO<sub>2</sub> particles. Further analysis of these effects will be presented in the discussion section in this chapter.

Based on the current plots shown in Figure 8-9, the mobility of charge carriers in the nanofluids was calculated, the mobility values and their relative uncertainties are presented in Table 8-12:

Table 8-12 Mobility of charge carriers in the tested liquids under positive DC voltage

Liquid	Mobility ( $\times 10^{-9} \text{ m}^2/(\text{V}\cdot\text{s})$ )		
	+2 kV	+4 kV	+6 kV
Pure Synthetic Ester	0.95±0.17	0.88±0.20	0.78±0.12
SE-based Nanofluid (0.005% b/w BN particles)	2.35±4.05	0.98±1.08	0.84±0.29
SE-based Nanofluid (0.1% b/w BN particles)	2.20±2.34	0.93±0.25	0.98±0.14

The mobility of charge carriers in the tested liquids is given in Table 8-12. The uncertainties in the mobility results show an obvious decreasing trend under the higher voltage levels. Thus, there is no statistically significant difference between the mobility values obtained for three liquids under 2 kV and 4 kV. However, in the case of 6 kV, the mobility of charge carriers decreases with a decrease in concentration of nanoparticles: the largest mobility was obtained for the nanofluids with 0.1% b/w concentration of BN nanoparticles and the smallest mobility was obtained for the pure liquids. This tendency agrees with the tendency found in the case of nanofluids prepared with TiO<sub>2</sub> particles. (As can be seen in Table 8-3 in Section 8.2.1).

The results obtained under the negative DC stress are also presented in Figure 8-10.

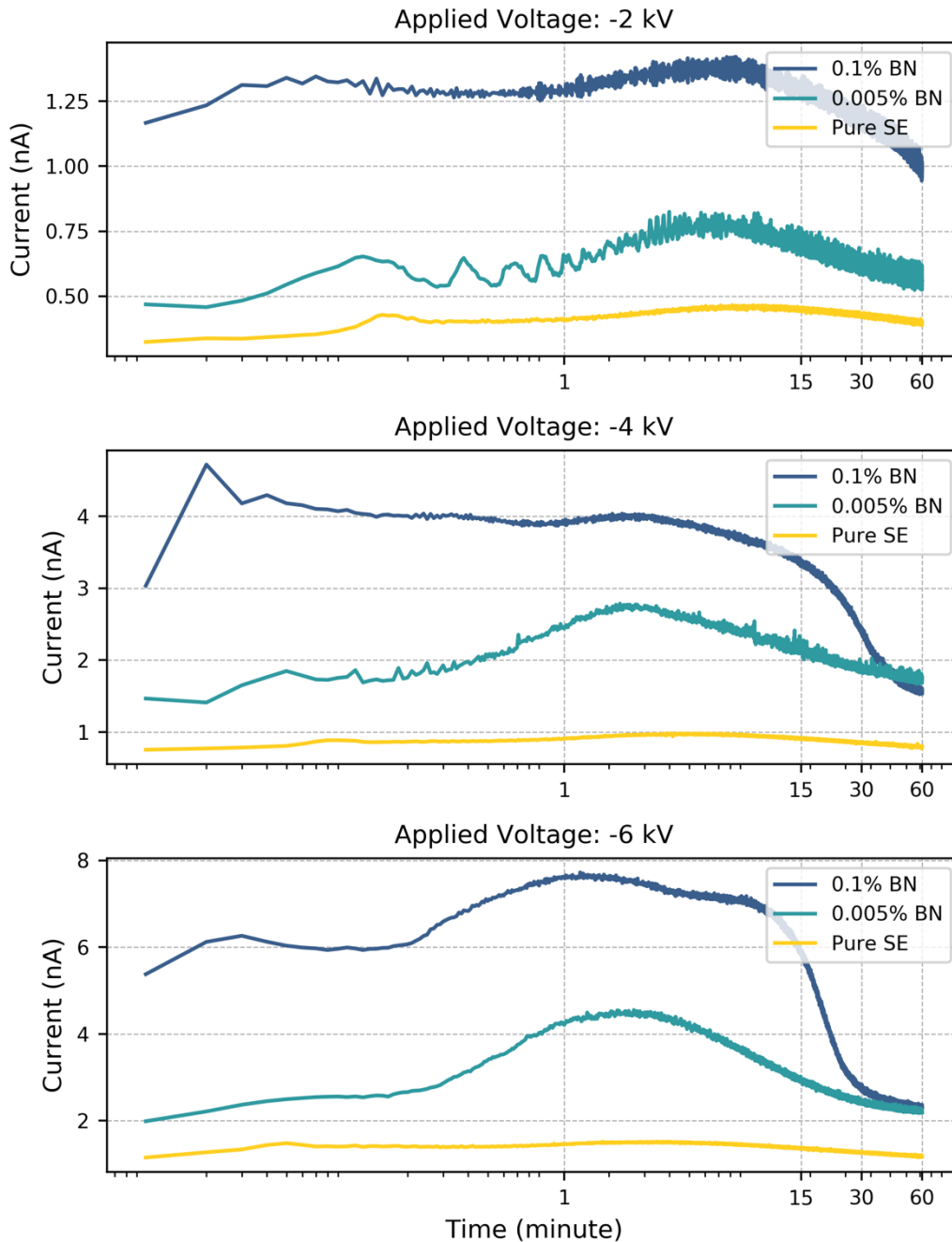


Figure 8-10 Current through the SE-based nanofluids with 0.1% b/w and 0.005% b/w concentrations of BN particles (negative DC voltage). Each individual current line is an average of three individual tests. The current through the pure SE is shown as a reference.

Based on the currents presented in Figure 8-10, the final current through the tested liquids under the negative DC voltage was calculated, and the final current values with their relative uncertainties are listed in Table 8-13:

Table 8-13 Final current for the SE-based nanofluids (negative energisation)

Liquid	Final Current (nA)		
	-2 kV	-4 kV	-6 kV
Pure Synthetic Ester	0.399±0.001	0.791±0.001	1.182±0.002
SE-based Nanofluid (0.005% b/w BN particles)	0.568±0.004	1.726±0.020	2.227±0.005
SE-based Nanofluid (0.1% b/w BN <sub>2</sub> particles)	0.991±0.006	1.578±0.026	2.308±0.007

The final currents presented in Table 8-13 show that BN particles cause an increase in the final currents in both nanofluids with 0.005% and 0.1% b/w concentration of BN nanoparticles compared with the current through the pure SE. The final currents through the nanofluid with 0.005% b/w concentration of BN nanoparticles is ~ (1.4 – 2.2) times greater than the final current in the pure SE, while the final currents through the nanofluids with 0.1% b/w concentration of BN nanoparticles is ~ (2.0 – 2.5) times greater than the final currents in the pure SE.

It can be found from both from both Table 8-13 and Figure 8-10 that the final current in the nanofluid with 0.1% b/w concentration of BN nanoparticles is approximately twice higher than the current through the nanofluid with 0.005% b/w concentration of BN nanoparticles under -2 kV. However, the final currents in the nanofluids with the 0.005% and 0.1% b/w

concentrations of BN nanoparticles are similar to each other under -4 kV and -6 kV. This finding is like the tendencies obtained under the positive polarity (as shown in Table 8-11).

Based on the current plots in Figure 8-10, the mobility of charge carriers in the nanofluids were calculated, the mobilities and their relative uncertainties are presented in Table 8-14:

Table 8-14 Mobility of charge carriers in the tested liquids under negative DC voltage

Liquid	Mobility ( $\times 10^{-9} \text{ m}^2/(\text{V}\cdot\text{s})$ )		
	-2 kV	-4 kV	-6 kV
Pure Synthetic Ester	0.69±0.17	0.54±0.13	0.62±0.14
SE-based Nanofluid (0.005% b/w BN particles)	0.95±0.26	0.93±0.25	0.98±0.14
SE-based Nanofluid (0.1% b/w BN particles)	1.85±1.14	1.35±0.92	0.98±0.14

It was found that like the results obtained under positive energisation, the uncertainties of the mobility values decrease with an increase in the applied voltage.

Based on the results presented in Table 8-14, it can be concluded that the mobility of charge carriers in both two types of SE-based nanofluids is higher than that in the pure SE, which agrees with the tendency obtained in the case of positive energisation.

### **8.3.2 Electric Current and Mobility of Charge Carriers in Natural-ester-based Nanofluids**

Figure 8-11 and Figure 8-12 show the current through the NE-based nanofluids (NE – Natural Ester, MIDEL eN1204) under positive and negative energisation, respectively. Figure 8-11 presents the current in the NE-based nanofluids with the following concentrations of BN particles: 0.005% b/w and 0.1% b/w. Each individual current plot in Figure 8-11 is an averaged result from three individual tests.

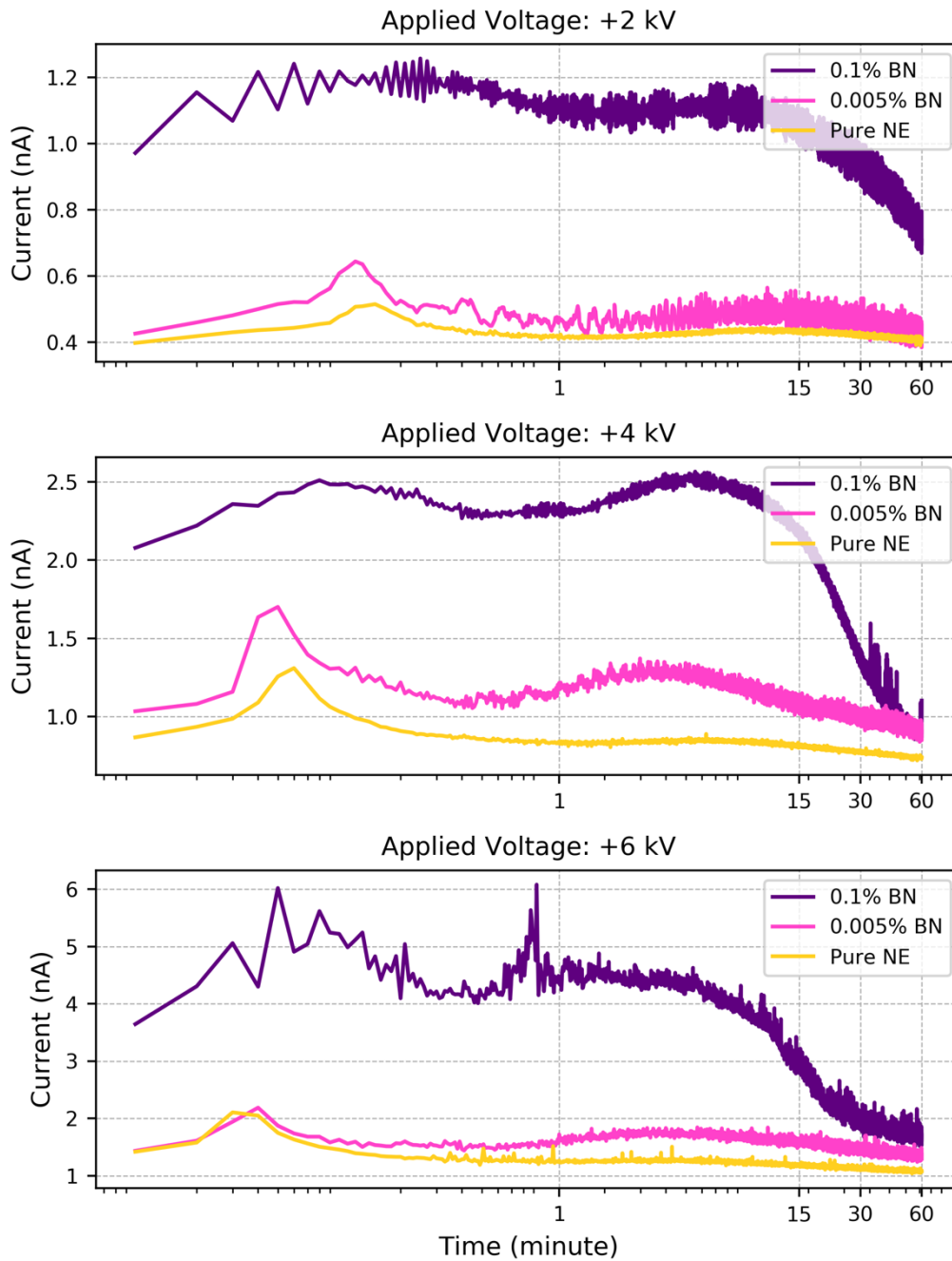


Figure 8-11 Current through the NE-based nanofluids with 0.1% b/w and 0.005% b/w concentrations of BN particles (positive DC voltage). Each individual current line is an average of three individual tests. The current through the pure NE is shown as a reference.

Based on the obtained current waveforms, the final current in all three types of liquids under the positive DC voltage was obtained, the final current values with their relative uncertainties are listed in Table 8-5:

Table 8-15 Final current for the NE-based nanofluids (positive energisation)

Liquid	Final Current (nA)		
	+2 kV	+4 kV	+6 kV
Pure Natural Ester	0.405±0.001	0.738±0.002	1.083±0.005
NE-based Nanofluid (0.005% b/w BN particles)	0.425±0.004	0.908±0.005	1.334±0.015
NE-based Nanofluid (0.1% b/w BN particles)	0.736±0.005	0.929±0.014	1.659±0.020

The results in Table 8-15, demonstrate that the nanoparticles in the fluids affect the final current: the final current in the nanofluids with 0.005% b/w concentrations of BN nanoparticles is ~ (1.0 – 1.2) times higher than the final current in the pure NE, while the final current in the nanofluids with 0.1% b/w concentrations of BN nanoparticles is ~ (1.3 – 1.8) times greater than the final current in the pure NE.

Like the SE-based nanofluids prepared with the BN particles (as seen in Table 8-13), the final current through the NE-based nanofluid with 0.1% b/w concentrations of BN nanoparticles show the decreasing tendency with an increase in the applied voltage.

Based on the obtained currents, the mobility of charge carriers in the tested liquids was calculated. The mobility values and their relative uncertainties are shown in Table 8-16.

Table 8-16 Mobility of charge carriers in the tested liquids under positive DC voltage

Liquid	Mobility ( $\times 10^{-9} \text{ m}^2/(\text{V}\cdot\text{s})$ )		
	+2 kV	+4 kV	+6 kV
Pure Natural Ester	1.07±0.12	1.26±0.25	1.20±0.32
NE-based Nanofluid (0.005% b/w BN particles)	1.29±0.11	1.40±0.59	1.12±0.09
NE-based Nanofluid (0.1% b/w BN particles)	1.44±1.77	0.93±0.27	0.80±0.29

The obtained mobility does not show a clear functional dependency on the applied voltage. For example, for the nanofluids with 0.005% b/w concentration of BN nanoparticles, the mobility of the charges carriers is higher than that in the pure NE under +2 kV but lower than that in the pure NE under +6 kV. For the nanofluids with 0.1% b/w concentration of BN nanoparticles, the mobility of charge is lower than that in the pure NE under +4 kV and +6 kV, however, the wide uncertainty in the mobility results (+2 kV stress) does not allow for identifications of statistically significant tendencies.

It is expected that the results obtained under the negative energisation will provide more detailed information on the functional dependency of the mobility of charge carriers.

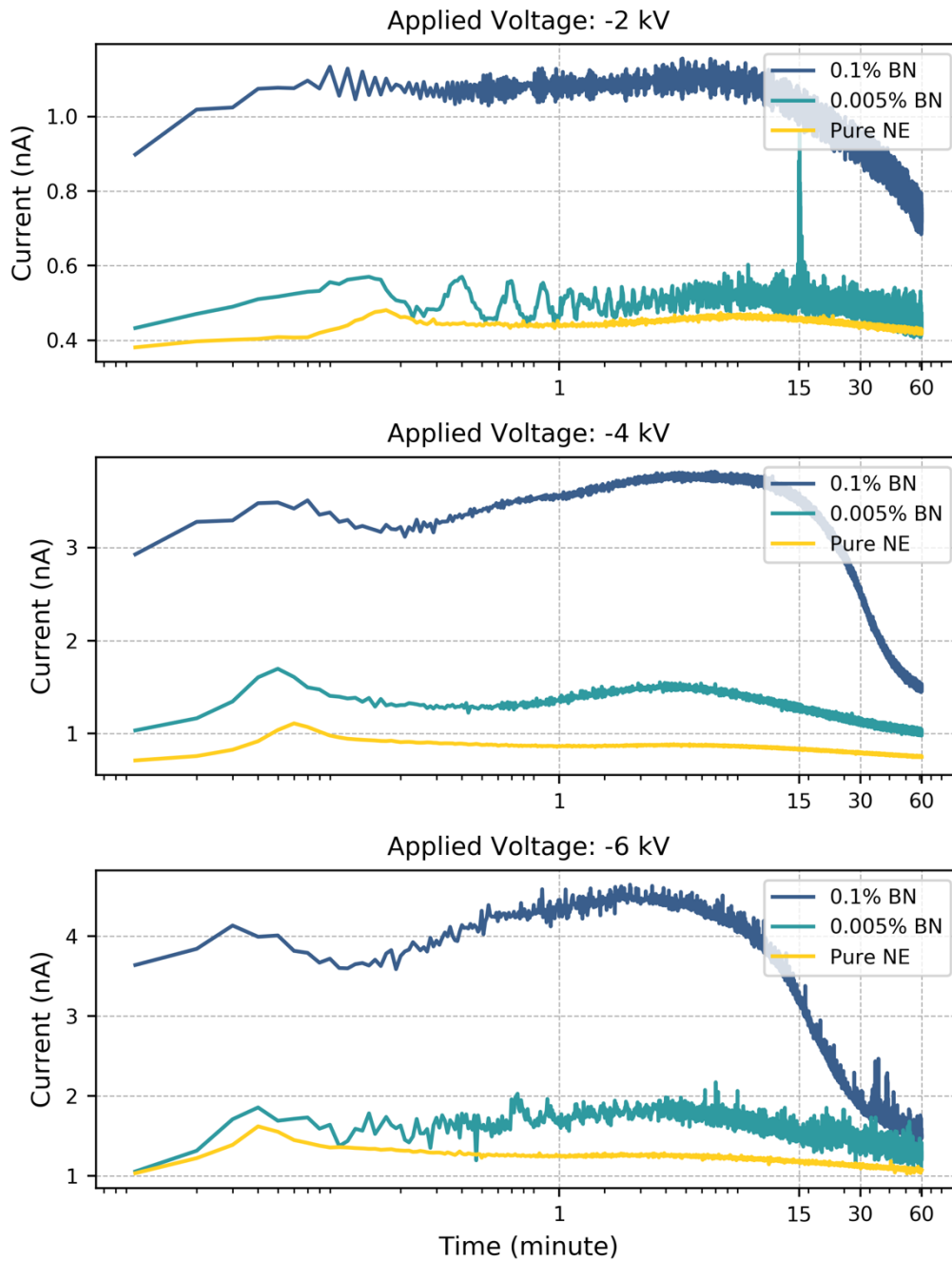


Figure 8-12 Current through the NE-based nanofluids with 0.1% b/w and 0.005% b/w concentrations of BN particles (negative DC voltage). Each individual current line is an average of three individual tests. The current through the pure NE is shown as a reference.

The final current in all three types of liquids under the negative DC voltage were obtained, the final currents with their relative uncertainties are listed in Table 8-17.

Table 8-17 Final current for the NE-based nanofluids (negative energisation)

Liquid	Final Current (nA)		
	-2 kV	-4 kV	-6 kV
Pure Natural Ester	0.436±0.001	0.751±0.001	1.073±0.004
NE-based Nanofluid (0.005% b/w BN particles)	0.450±0.005	1.015±0.007	1.363±0.015
NE-based Nanofluid (0.1% b/w BN particles)	0.739±0.004	1.063±0.008	1.499±0.008

From Table 8-17, it can be seen that both NE-based nanofluids with 0.005% and 0.1% b/w concentrations of BN nanoparticles demonstrate higher final currents compared with the pure NE under the same voltage level. The final current in the nanofluids with 0.005% b/w concentration of BN nanoparticles is up to ~ 1.4 times greater the final current in the pure NE, while the final current in the nanofluids with 0.1% b/w concentrations of BN nanoparticles is ~ (1.4 – 1.7) times greater than the final currents in the pure NE.

It was also found that final current through the nanofluid with 0.1% b/w concentration of BN nanoparticles decreases when the applied voltage increases: ~ 1.69 for -2 kV, ~ 1.42 for -4 kV and ~ 1.40 for -6 kV, which confirms the similar tendency found in the results under positive polarity.

Table 8-18 Mobility of charge carriers in the tested liquids under negative DC voltage

Liquid	Mobility ( $\times 10^{-9} \text{ m}^2/(\text{V}\cdot\text{s})$ )		
	-2 kV	-4 kV	-6 kV
Pure Natural Ester	0.97±0.16	1.14±0.21	1.05±0.24
NE-based Nanofluid (0.005% b/w BN particles)	1.48±0.51	1.40±0.59	1.20±0.38
NE-based Nanofluid (0.1% b/w BN particles)	1.40±0.59	1.20±0.44	1.20±0.74

As shown in Table 8-18, the mobility of charge carriers in all tested liquids under the negative DC voltages is higher than the mobility in the pure NE under the same voltage level.

### 8.3.3 Electric Current in Mineral-oil-based Nanofluids

The current through the Shell Diala B MO-based nanofluids under positive and negative voltages was obtained and shown in Figure 8-13 and Figure 8-14, respectively. The current through the pure MO, obtained in Section 5.3.3 previously, are included in Figure 8-13 and Figure 8-14 for reference.

Figure 8-13 presents the current through the MO-based nanofluids with the following concentrations of BN particles: 0.005% b/w and 0.1% b/w. Each individual current plot in Figure 8-13 represents an averaged result from three individual tests.

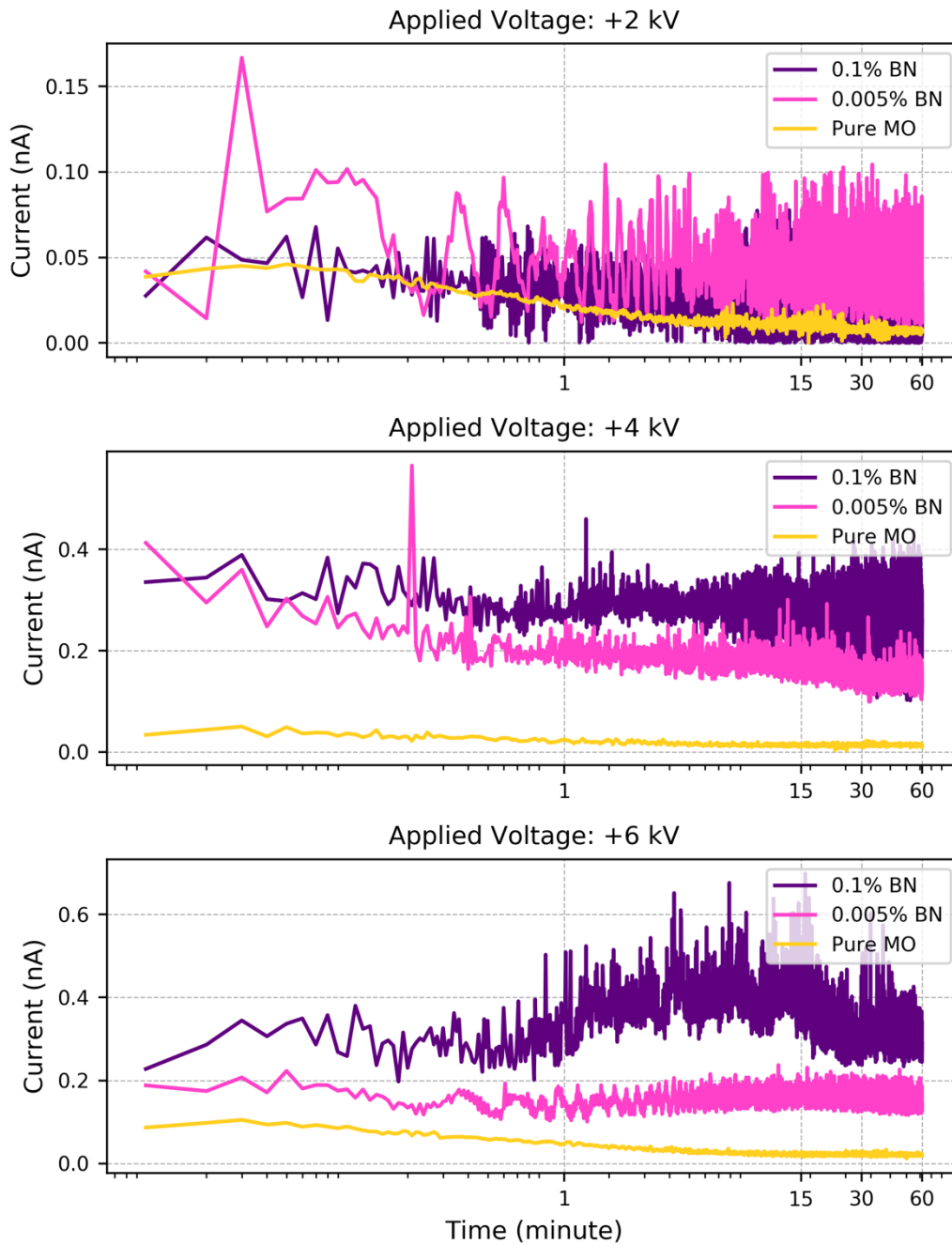


Figure 8-13 Current through the MO-based nanofluids with 0.1% b/w and 0.005% b/w concentrations of BN particles (positive DC voltage). Each individual current line is an average of three individual tests. The current through the pure MO is shown as a reference.

Using the current as a function of time shown in Figure 8-13, the final current in the tested liquids is calculated, of which the results with the uncertainties are listed in Table 8-19.

Table 8-19 Final current for the MO-based nanofluids (positive energisation)

Liquid	Final Current (nA)		
	+2 kV	+4 kV	+6 kV
Pure Mineral Oil	0.007±0.000	0.014±0.000	0.022±0.000
MO-based Nanofluid (0.005% b/w BN particles)	0.040±0.003	0.142±0.010	0.153±0.003
MO-based Nanofluid (0.1% b/w BN particles)	0.034±0.002	0.263±0.007	0.286±0.009

It was found that the addition of the BN particles significantly increased the current through the nanofluids as compared with the current through the pure MO. For example, the final current through the nanofluid with the 0.005% b/w concentration of BN nanoparticles is ~ (5.7 – 7.0) times greater than the final currents through the pure MO, while the final currents through the nanofluid with 0.1% b/w concentrations of BN nanoparticles is ~ (4.9 – 18.8) times greater than the final current through the pure MO.

In Section 8.2.3, an obvious current peak is observed in the current plots obtained for the MO-based nanofluids with the 0.1% b/w concentration of TiO<sub>2</sub> nanoparticles. However, there is no similar current peak in the current through the MO-based nanofluids with the 0.1% b/w concentration of BN nanoparticles.

To calculate the mobility, the first current peak is required to obtain the ToF, (as shown in Figure 8-13). However, as the peaks are not clearly pronounced in the present current graphs,

it is not possible to identify ToF and to obtain mobility. Therefore, further studies using electrometer with a larger sampling rate (higher resolution in time) are required for identification of time of flight of the charge carriers in these nanofluids.

Figure 8-14 shows the current through the nanofluids obtained under negative energisation.

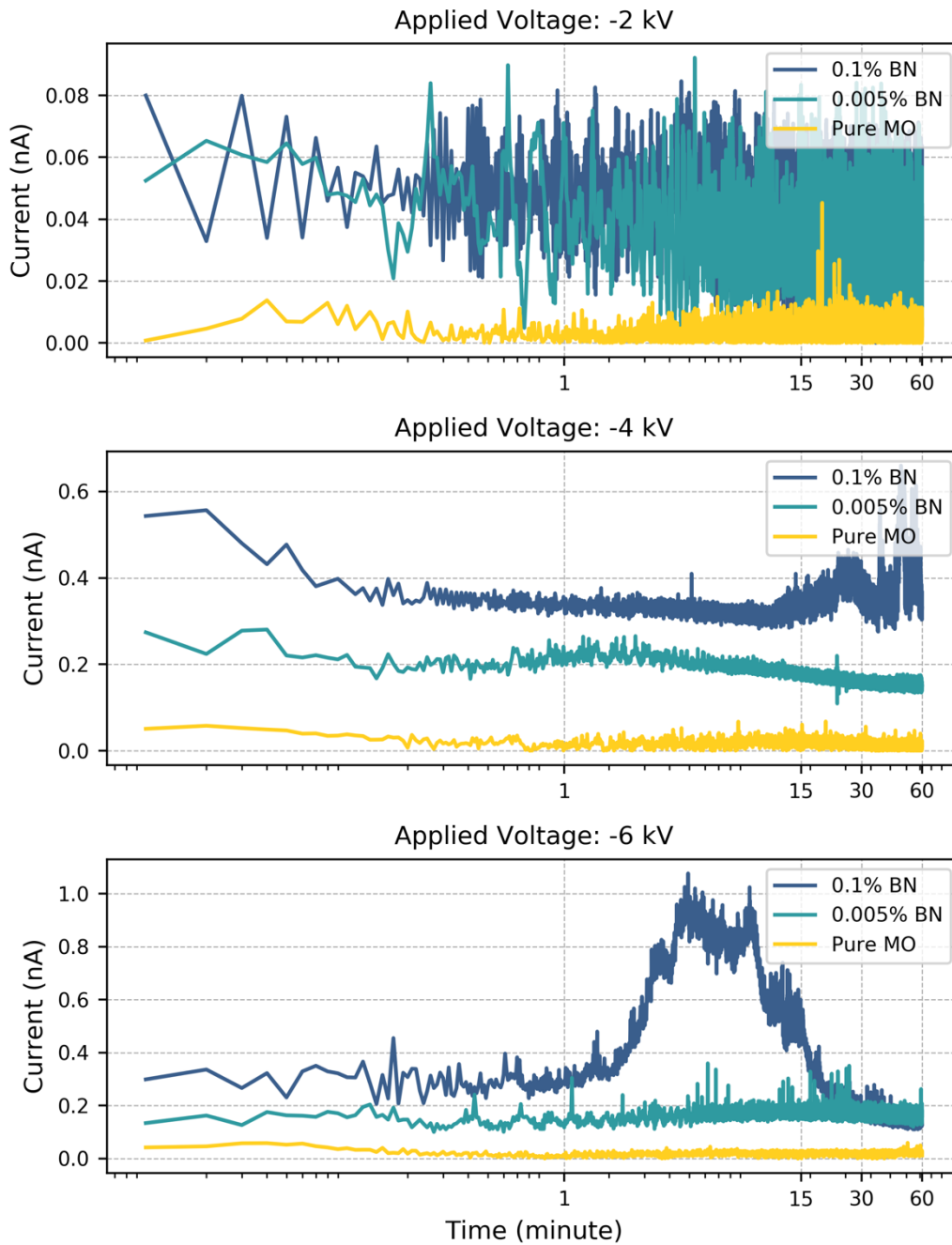


Figure 8-14 Current through the MO-based nanofluids with 0.1% b/w and 0.005% b/w concentrations of BN particles (negative DC voltage). Each individual current line is an average of three individual tests. The current through the pure MO is shown as a reference.

Using the currents shown in Figure 8-14, the final current in all tested liquids and its relative uncertainty was obtained, Table 8-20.

Table 8-20 Final current for the MO-based nanofluids (negative energisation)

Liquid	Final Current (nA)		
	-2 kV	-4 kV	-6 kV
Pure Mineral Oil	0.007±0.001	0.015±0.001	0.023±0.001
MO-based Nanofluid (0.005% b/w BN particles)	0.027±0.003	0.150±0.007	0.161±0.004
MO-based Nanofluid (0.1% b/w BN particles)	0.035±0.003	0.262±0.006	0.140±0.003

As shown in Figure 8-14, the current through the nanofluids increases when concentration of BN particles increases: the final current through the MO-based nanofluid with 0.005% b/w concentration of BN nanoparticles is ~ (3.9 – 7.0) times higher than the current through the pure MO, and the final current through the MO-based nanofluid with the 0.1% b/w concentrations of BN nanoparticles is ~ (5.0 – 17.5) times greater than the current through the pure MO.

As in the case of the positive energisation (as seen in Figure 8-13), the current peak indicating the ToF is not well resolved under the negative polarity (as seen in Figure 8-14). Thus, to obtain the mobility of charge carriers in the nanofluids in this case, further investigation is required.

However, as can be seen from Figure 8-14, there are several unusual current peaks that occurred in the current waveforms obtained in the nanofluids with the 0.1% b/w concentration

of BN nanoparticles under -4 kV and -6 kV. Further discussion on this phenomenon will be presented in the discussion part of this chapter.

## **8.4 Discussion and Summary**

The electric current through the Synthetic Ester, Natural Ester, and Mineral Oil based the nanofluids was obtained in the present chapter.

Using the methodology presented in Section 2.3.1, the ToF values have been obtained for the ester-based and MO-based nanofluids. The mobility of charge carriers in the ester-based nanofluids was calculated and presented.

The ‘final current’, which is the averaged current at the end of each one-hour test, was obtained for all the nanofluids and the pure dielectric liquids. The values of the final current are used to deliver the quantitative analysis of the current plots obtained in this study. And particularly, the final current values were used for investigations of the effect of nanoparticles on the conduction current.

First of all, using the current plots presented for all nanofluids, it can be concluded that the addition of TiO<sub>2</sub> and BN particles increases the conduction current through the nanofluids compared with the current through the relative pure liquid. The nanofluids with 0.1% b/w concentration of TiO<sub>2</sub>/BN nanoparticles have a higher electric current than the nanofluids with 0.005% b/w concentration of TiO<sub>2</sub>/BN nanoparticles. This can be attributed to the motion of the particles under the action of the external electric field.

For example, as it can be seen from Figure 8-1 the current through the nanofluids with 0.1% b/w concentration of TiO<sub>2</sub> nanoparticles under +4 kV and +6 kV reach its quasi-steady state by the end of one-hour DC test. At the same time, the direct observation images (Figure 7-1 (g) and (k)) show that the nanofluids in the test cell become transparent by the end of one-hour period: the electrode can be clearly seen in the two images.

On the other hand, according to the current plots shown in Figure 8-1, the currents through the nanofluids with 0.1% b/w concentration of TiO<sub>2</sub> nanoparticles under +2 kV decreases to

the end of test. At the same time, the direct observation images (Figure 7-1 (c)) in indicates that for the nanofluids with 0.1% b/w concentration of TiO<sub>2</sub> nanoparticles under +2 kV, there are residual particles between two electrodes which can be observed after 30 minutes of application of DC voltage.

Similar correlation between the observation images and measured current can also be found for other nanofluids, including the NE-based nanofluids with 0.1% b/w concentration of BN nanoparticles, the MO-based nanofluids with 0.1% b/w concentration of TiO<sub>2</sub> nanoparticles. It demonstrates an increase in the electric current through the nanofluids due to the motion of nanoparticle in these nanofluids.

This mechanism can be used to explain the drop of the ratio between the final currents of the 0.1% concentrated nanofluids and the relative dielectric liquids, for example, the ratio between the final currents in the SE-based nanofluid with 0.1% b/w concentration of BN nanoparticles and in the pure SE decreases when the voltage level increases: ~ 2.5 for +2 kV, ~ 1.8 for +4 kV and ~ 1.7 for +6 kV (as seen in Section 8.3.1). For the nanofluids being tested with the lower DC voltage, like 2 kV, there are more nanoparticles dispersed in the nanofluids than the nanofluids being tested with the higher DC voltage, like 6 kV. Higher concentration of nanoparticles in the nanofluids leads to a higher current through the nanofluid, therefore the ratio of the final currents in the nanofluids and in the pure liquids stressed with lower voltage levels will be higher than in the case of higher voltage stress.

Another aspect reflected by the current signal of the nanofluids can also be potentially linked with the motion of the particles: it can be found that the end current of the nanofluids typically has a higher uncertainty than that of the dielectric liquids. The reason for this higher uncertainty can be proposed that the particles are proved to be charged in the nanofluids, and hence the precipitation of these charged particles could also influence the measured current signal through the electrode, resulting the higher uncertainty than the dielectric liquids.

Apart from the analysis on the electric current, the investigation on the mobility of charge carriers in the nanofluids was conducted in this chapter. The mobility of charge carriers in the ester-based nanofluids were obtained. However, the mobility values for the MO-based were not resolved in this study and further investigation is required to obtain the mobility values in

these nanofluids. It was shown that the mobility values for all the nanofluids are higher than the mobility values obtained for pure dielectric liquids.

According to the relaxation time model [83][84][85], and the electron trapping model [73][74], a potential explanation of observed functional dependencies of the mobility of charge carriers in nanofluids can be proposed as follows:

For nanofluids stressed with an external electric field, the charge carriers start to move due to the Coulomb force. During this process, the charge carriers with various mobilities in the liquids, were possible to be trapped by the dispersed nanoparticles. This trapping process can be described by the Maxwell-Wagner relaxation process. However, not all charge carriers become trapped, the charge carriers with higher mobility continue to move in the fluid leading to the formation of the first current peak. Thus, the first current peak in the current through the nanofluid is formed by fast-moving charge carriers, resulting in higher mobility values obtained by the ToF method.

In conclusion, the results presented in this chapter show that the electric conduction process in the dielectric liquids is affected by the interaction between the dispersed nanoparticles and the host liquids. It is suggested that this increase in the spread in the mobility values is due to the presence of nanoparticles in the liquid and their effect on the dynamic of the charge carriers in the nanofluids. This result agrees with the analysis of the dynamic behaviour of the particles provided in the previous chapter. Analysis of the conduction mechanisms in nanofluids can be used as a baseline for future investigations to make contributions to the development of nanofluids.

## Chapter 9 CONCLUSIONS AND FURTHER WORK

---

### 9.1 Main conclusions

#### 9.1.1 Liquids in Uniform Electric Field

The mobility of charge carriers was obtained in 3 pure dielectric liquids stressed with the uniform electric field: synthetic ester, natural ester, and mineral oil.

The results showed that the mobility of charge carriers in all three liquids have the same magnitude when stressed with the same electric field strength. The mobility results obtained in the higher field (400 kV/m to 1200 kV/m) was approximately one order of magnitude higher than the mobility obtained in the low electric fields (40 kV/m to 80 kV/m), which can be explained by the electrohydrodynamic effect due to the external field.

Based on the obtained mobilities of charge carriers and nominal values of electrical conductivities of the dielectric liquids, it was found that the space charge density in the mineral oil was approximately one order of magnitude lower than the space charge density in the synthetic and natural esters.

The reverse-polarity method was used to study the electric current in the low field range (40 kV/m to 80 kV/m). It was found that the mobility of charge carriers in the synthetic ester is  $\sim 1.18 \times 10^{-10} \text{ m}^2/(\text{V}\cdot\text{s})$ ; the mobility of charge carriers in the natural ester is  $\sim 1.26 \times 10^{-10} \text{ m}^2/(\text{V}\cdot\text{s})$ ; the mobility of charge carriers in the mineral oil ranges from  $\sim 2.92 \times 10^{-10} \text{ m}^2/(\text{V}\cdot\text{s})$  to  $\sim 7.43 \times 10^{-10} \text{ m}^2/(\text{V}\cdot\text{s})$ , and shows a statistically significant increase with an increase in the applied voltage.

The single-polarity method was used to measure the conduction current in the higher fields from 400 kV/m to 1200 kV/m. In this field range, it was found that the mobility of charge

carriers in the synthetic ester is  $\sim 0.41 \times 10^{-9} \text{ m}^2/(\text{V}\cdot\text{s})$  for the positive polarity and  $\sim 0.29 \times 10^{-9} \text{ m}^2/(\text{V}\cdot\text{s})$  for the negative polarity; the mobility of charge carriers in the natural ester is  $\sim 0.79 \times 10^{-9} \text{ m}^2/(\text{V}\cdot\text{s})$  for the positive polarity and  $\sim 0.71 \times 10^{-9} \text{ m}^2/(\text{V}\cdot\text{s})$  for the negative polarity; the mobility of charge carriers in the mineral oil is  $\sim 1.76 \times 10^{-9} \text{ m}^2/(\text{V}\cdot\text{s})$  for the positive polarity and to  $\sim 2.25 \times 10^{-9} \text{ m}^2/(\text{V}\cdot\text{s})$  for the negative polarity.

### **9.1.2 Dielectric Liquids in Non-uniform Electric Field**

A highly divergent electric field was employed to obtain the mobility of charge carriers in the dielectric liquids in the case of the space charge limited current. The space charge limited current method was used to measure the conduction current through the dielectric liquids stressed the voltage ranging from 1 kV to 40 kV (in the needle-plane topology with a gap distance of 10 mm and the needle tip radius of  $\sim 20 \mu\text{m}$ ). The obtained results confirmed the positive correlation between the mobility and the electric field strength, as in the case of the mobility obtained under the uniform electric field. It was also confirmed that the space charge density in the esters was about one order of magnitude higher than that in the mineral oil.

In the case of the space charge limited method, it was found that the mobility of charge carriers in the synthetic ester is  $\sim 5.0 \times 10^{-9} \text{ m}^2/(\text{V}\cdot\text{s})$ ; the mobility of charge carriers in the natural esters is  $\sim 6.0 \times 10^{-9} \text{ m}^2/(\text{V}\cdot\text{s})$ ; the mobility of charge carriers in the mineral oils is  $\sim 4.6 \times 10^{-9} \text{ m}^2/(\text{V}\cdot\text{s})$ .

The field distribution along the central line between the needle tip and the centre of the plane electrode was calculated using the Poisson equation which considers the space charge in the dielectric liquids, The electric field strength at the needle tip was obtained for all pure liquids used in this study:  $\sim 4.33 \cdot 10^9 \text{ kV/m}$  for the synthetic ester,  $\sim 3.67 \cdot 10^9 \text{ kV/m}$  for the natural ester, and  $\sim 1.63 \cdot 10^9 \text{ kV/m}$  for the mineral oil.

The literature data on the mobility published by other researchers and the experimental methods used to obtain this mobility were also reviewed in this study.

### **9.1.3 Nanofluids in Uniform Electric Field**

Two types of particles, TiO<sub>2</sub> and BN particles, were used to develop nanofluids using three dielectric liquids: synthetic ester, natural ester and mineral oil.

It was found that both TiO<sub>2</sub> and BN particles become negatively charged (obtained a net negative charge) in the ester-based nanofluids stressed with the external electric field. On the other hand, it was shown that TiO<sub>2</sub> and BN particles were only polarised in the mineral-oil-based nanofluids stressed with the external electric field. The experimental results showed that the mobility of the charge carriers in the ester-based nanofluids is higher than the mobility in the pure dielectric liquids under the same field strength.

For the synthetic-ester-based nanofluids and the natural-ester-based nanofluids, the micro-scale and the normal observation methods demonstrated that the TiO<sub>2</sub> and BN particles were attracted to the electrode with a higher potential and repulsed from the electrode with a lower potential. However, for the mineral-oil-based nanofluids, both the micro-scale and the normal observation methods showed that the TiO<sub>2</sub> and BN particles were attracted to both electrodes in the test cell. In addition, particle chains consisting of BN and TiO<sub>2</sub> particles were found in the mineral-oil-based nanofluids. The micro-scale images demonstrated that these particle chains are aligned with the direction of the electric field. In the nanofluids with BN particles, particle chains formed perpendicular to the electrode surface were found; in the nanofluids with TiO<sub>2</sub> particles, the particle bridges between the two electrodes were formed.

The modelling part of the thesis included the developed mathematical model of the polarisation and charging of particles in the dielectric liquids. It was found that the surface charge on the TiO<sub>2</sub> and BN particles suspended in the ester liquids is higher than that in the mineral oil under the same external field strength. This could result in the net negative charge on TiO<sub>2</sub> and BN particles in the esters, while it was established that these particles were only polarised in the mineral oils stressed with the external electric field.

## **9.2 Summary of Contributions**

The major contributions of this thesis are listed as follows:

- In this thesis, a comprehensive study of the mobility of charge carriers in the dielectric liquids (synthetic ester, natural ester, and mineral oil) was conducted, and the obtained results were analysed and presented. The mobility of charge carriers was obtained under the electric field ranging from 40 kV/m to 80 kV/m, from  $4 \cdot 10^2$  kV/m to  $1.2 \cdot 10^3$  kV/m, and from  $\sim 1.6 \cdot 10^9$  kV/m to  $\sim 4 \cdot 10^9$  kV/m.
- A mathematical model developed in this research provides the analytical expression for the surface charge distribution on the single particle in dielectric (poorly conductive) liquids under external electric fields. The Coulomb forces acting between two particles immersed in dielectric liquid were calculated based on this model.
- The electrohydrodynamic behaviour of TiO<sub>2</sub> and BN particles suspended in different hosting liquids (synthetic ester, natural ester, and mineral oil) were reported for the first time. The charging and polarisation of the particles suspended in the dielectric liquid stressed with the external electric field was described analytically for the first time.

### 9.3 Future work

This thesis provides a comprehensive investigation of the mobility of charge carriers and charging processes in dielectric liquids. It is important to continue this work, and this section outlines the potential direction of future research initiated in this research project:

- As discussed in Chapter 3, the forces between two spheres were calculated according to the dipole-dipole interaction based on the image method. The pre-condition of utilizing the image method is the particles/objects should be conductive. This condition was extrapolated into the domain of non-conductive/dielectric particles suspended in the liquid by putting  $R \rightarrow 1$ , where  $R$  is the ratio of the dielectric constants from the dispersed particle and hosting liquids. Although this extrapolation enabled the force calculation for TiO<sub>2</sub> particles, with  $R \rightarrow 0.92$ , the results for BN particles still require further confirmation through another force calculation method.
- In this work, only the force acting between two particles was obtained. However, this analysis could be extended into multiple particles using other analytical and computational methods, like the Monte Carlo simulations.

- The second stage in the Fowler-Nordheim plot can provide the energy barrier for the electron excitation in the dielectric liquids. However, this analysis requires numerical value(s) for the energy barrier, which are unknown currently. Once this information will be available, the source for the charge carriers can be established.
- More details on the particles, including their dimensions, surface geometry, surfactant information, will benefit both the mathematical modelling work and the analysis of the experimental results. For example, the DLS measurement involves a group of parameters to calculate the dimensions of the dispersed particles, which can potentially cause errors in the calculated dimensions. In this case, the scanning electron microscope or transmission electron microscope can be used to obtain the particle dimension and the surface geometry directly and accurately, enabling more effective analysis.
- The information on the molecules' structures is also required to reveal the surface charge distribution on the particles. The actual dimensions of the molecules in the dielectric liquids are essential for understanding their distributions on the particle's surface. Moreover, this molecule structure information can also help to understand the excitation state of the molecules under an external electric field, assisting the investigations on the sources of the charge carriers and the reason causing the second current peak in the ester liquids.

## REFERENCES

- [1] 'MIDEL 7131 - premium performance since the 1970s', <https://www.midel.com/midel-range/midel-7131/>, accessed July 2020
- [2] 'MIDEL eN 1204', <https://www.midel.com/midel-range/midel-en1204/>, accessed July 2020
- [3] 'Envirotemp 360 fluid', <https://www.cargill.com/bioindustrial/dielectric-fluids/envirotemp>, accessed July 2020
- [4] 'FR3® NATURAL ESTER DIELECTRIC FLUID: LEADING THE WAY', <https://www.cargill.com/bioindustrial/dielectric-fluids/fr3-fluid>, accessed July 2020
- [5] 'BIOTEMP® Biodegradable Dielectric Insulating Fluid', [https://library.e.abb.com/public/30607acbfe454ae0c1257b130057e21a/1LUS471050-LTE\\_BIO.pdf?x-sign=nfiiApXgg98L82FKfyJbN1Z/AJMq4SuEc1q5xPOx2tdPnh0/6cbqM+0AKSCgDw+2](https://library.e.abb.com/public/30607acbfe454ae0c1257b130057e21a/1LUS471050-LTE_BIO.pdf?x-sign=nfiiApXgg98L82FKfyJbN1Z/AJMq4SuEc1q5xPOx2tdPnh0/6cbqM+0AKSCgDw+2), accessed July 2020
- [6] Lee, S., Choi, S.U.-S., Li, S., Eastman, J.A.: 'Measuring Thermal Conductivity of Fluids Containing Oxide Nanoparticles', *J. Heat Transfer*, 1999, **121**, (2), pp. 280–289.
- [7] Segal, V., Hjortsberg, A., Rabinovich, A., Nattrass, D., Raj, K.: 'AC (60 Hz) and impulse breakdown strength of a colloidal fluid based on transformer oil and magnetite nanoparticles', *Conf. Rec. 1998 IEEE Int. Symp. Electr. Insul. (Cat. No.98CH36239)*, 1998, **2**, pp. 619–622.
- [8] Timofeeva, E. V., Moravek, M.R., Singh, D.: 'Improving the heat transfer efficiency of synthetic oil with silica nanoparticles', *J. Colloid Interface Sci.*, 2011, **364**, (1), pp. 71–79.
- [9] Cavallini, A., Karthik, R., Negri, F.: 'The effect of magnetite, graphene oxide and silicone oxide nanoparticles on dielectric withstand characteristics of mineral oil', *IEEE Trans. Dielectr. Electr. Insul.*, 2015, **22**, (5), pp. 2592–2600.
- [10] Du, B.X., Li, X.L., Li, J.: 'Thermal conductivity and dielectric characteristics of transformer oil filled with bn and Fe<sub>3</sub>O<sub>4</sub> nanoparticles', *IEEE Trans. Dielectr. Electr. Insul.*, 2015, **22**, (5), pp. 2530–2536.
- [11] Du, B.X., Li, X.L.: 'High thermal conductivity transformer oil filled with BN nanoparticles', *IEEE Electr. Insul. Mag.*, 2014, **June 30**, (2), pp. 1–4.
- [12] Katiyar, A., Dhar, P., Nandi, T., Das, S.K.: 'Effects of nanostructure permittivity and dimensions on the increased dielectric strength of nano insulating oils', *Colloids Surfaces A Physicochem. Eng. Asp.*, 2016, **509**, pp. 235–243.
- [13] Liu, D., Zhou, Y., Yang, Y., Zhang, L., Jin, F.: 'Characterization of high performance AlN nanoparticle-based transformer oil nanofluids', *IEEE Trans. Dielectr. Electr.*

- Insul.*, 2016, **23**, (5), pp. 2757–2767.
- [14] Qiu, X.Q., Chalmers, I.D., Coventry, P.: ‘Study of alternative insulating gases to SF<sub>6</sub>’, *J. Phys. D. Appl. Phys.*, 1999, **32**, (22), pp. 2918–2922.
- [15] Ravishankara, A.R., Solomon, S., Turnipseed, A.A., Warren, R.F.: ‘Atmospheric Lifetimes of Long-Lived Halogenated Species’, *Science (80-. )*, 1993, **259**, (5092), pp. 194–199.
- [16] Borsi, H., Dumke, K., Gockenbach, E.: ‘Relation between faults and generated gases in transformer liquids’, *IEEE Int. Conf. Conduct. Break. Dielectr. Liq. ICDL*, 1999.
- [17] Tortai, J.H., Bonifaci, N., Denat, A.: ‘Insulating properties of some liquids after an electrical arc’, *IEEE Trans. Dielectr. Electr. Insul.*, 2002, **9**, (1), pp. 3–9.
- [18] CIGRE Working Group A2.35: ‘Experiences in service with new insulating liquids (436)’, (CIGRE publication, 2010)
- [19] Contreras, J.E., Rodríguez-Díaz, J., Rodríguez, E.A.: ‘Environmentally friendly fluids for high-voltage applications’, in ‘Handbook of Ecomaterials’ (2019), pp. 3081–3106
- [20] Nelson, J.K.: ‘Insulating Liquids: their Uses, Manufacture and Properties’, (Inst of Engineering & Technology, 1980)
- [21] Jing, Y.: ‘Breakdown properties of mineral oil and ester based TiO<sub>2</sub> and BN nanofluids’,. PhD thesis, University of Strathclyde, 2016
- [22] ASTM Committee D27: ‘Standard Specification for Mineral Insulating Oil Used in Electrical Apparatus 1’, (2016)
- [23] International Electrotechnical Commission: ‘IEC 60296:2012’, (2012)
- [24] CIRGÉ Working Group D1.30: ‘Chapter 2. Types and Behavior of Insulation Fluid’, in ‘Oxidation Stability of Insulating Fluids’ (2013), pp. 12–16
- [25] Rouse, T.O.: ‘Mineral insulating oil in transformers’, *IEEE Electr. Insul. Mag.*, 1998, **14**, (3), pp. 6–13.
- [26] Market Research Future: ‘Global Transformer Oil Market - Trends & Forecast, 2016-2022’, (2018)
- [27] Sheppard, H.: ‘A Century of Progress in Electrical Insulation 1886-1986’, *IEEE Electr. Insul. Mag.*, 1986, **2**, (5), pp. 20–30.
- [28] Krawiec, S.: ‘Production of Corrosive Sulphur Free Transformer Fluids’, in ‘Conference Record of the 2008 IEEE International Symposium on Electrical Insulation’ (IEEE, 2008), pp. 174–177
- [29] Fofana, I.: ‘50 Years in the Development of Insulating Liquids’, *IEEE Electr. Insul. Mag.*, 2013, **29**, (5), pp. 13–25.
- [30] Rafiq, M., Lv, Y.Z., Zhou, Y., *et al.*: ‘Use of vegetable oils as transformer oils-A review’, *Renew. Sustain. Energy Rev.*, 2015, **52**, pp. 308–324.

- 
- [31] Fernández, I., Ortiz, A., Delgado, F., Renedo, C., Pérez, S.: ‘Comparative evaluation of alternative fluids for power transformers’, *Electr. Power Syst. Res.*, 2013, **98**, pp. 58–69.
- [32] Bandara, K., Ekanayake, C., Saha, T.K.: ‘Compare the performance of natural ester with synthetic ester as transformer insulating oil’, in ‘2015 IEEE 11th International Conference on the Properties and Applications of Dielectric Materials (ICPADM)’ (IEEE, 2015), pp. 975–978
- [33] Spear, S.K., Griffin, S.T., Granger, K.S., Huddleston, J.G., Rogers, R.D.: ‘Renewable plant-based soybean oil methyl esters as alternatives to organic solvents’, *Green Chem.*, 2007, **9**, (9), p. 1008.
- [34] Fernández, I., Ortiz, A., Delgado, F., Renedo, C., Pérez, S.: ‘Comparative evaluation of alternative fluids for power transformers’, *Electr. Power Syst. Res.*, 2013, **98**, pp. 58–69.
- [35] CIGRE Working Group A2-35: ‘Experiences in Service with New Insulating Liquids’, (2010)
- [36] Rycroft, M.: ‘Vegetable oil as insulating fluid for transformers’, *Ee.Co.Za*, 2014, (April), pp. 37–40.
- [37] Gosse, J.P.: ‘Electric Conduction in Dielectric Liquids - The Liquid State and Its Electrical Properties’, in Kunhardt, E.E., Christophorou, L.G., Luessen, L.H. (Eds.): (Springer US, 1988), pp. 503–517
- [38] Lewis, J.: ‘Basic electrical processes in dielectric liquids’, *IEEE Trans. Dielectr. Electr. Insul.*, 1994, **1**, (4), pp. 630–643.
- [39] Tobazéon, R.: ‘Electrical Phenomena of Dielectric Materials’, in ‘Handbook of Electrostatic Processes’ (Marcel Dekker, Inc., 1995), pp. 51–82
- [40] Nicholls, J., Dimitrijević, S., Tanner, P., Han, J.: ‘Description and Verification of the Fundamental Current Mechanisms in Silicon Carbide Schottky Barrier Diodes’, *Sci. Rep.*, 2019, **9**, (1), p. 3754.
- [41] Bronger, W., Kranz, H.G., Möller, K.: ‘Electrolytical phenomena in liquid hydrocarbons of thermally highstressed rectifier transformers’, *J. Electrostat.*, **12**, pp. 573–579.
- [42] Debye, P.: ‘Reaction Rates in Ionic Solutions’, *Trans. Electrochem. Soc.*, 1942, **82**, (1), pp. 265–272.
- [43] Eigen, M., De Maeyer, L.: ‘Self-dissociation and protonic charge transport in water and ice’, *Proc. R. Soc. London. Ser. A. Math. Phys. Sci.*, 1958, **247**, (1251), pp. 505–533.
- [44] Bjerrum, N.: ‘A new form for the electrolytic dissociation theory’, in ‘Proceedings of the Seventh International Congress of Applied Chemistry’ (1909)
- [45] Onsager, L.: ‘Deviations from Ohm’s law in weak electrolytes’, *J. Chem. Phys.*, 1934, **2**, (9), pp. 599–615.

- 
- [46] Timoshkin, I.V., Given, M.J., Fouracre, R.A., MacGregor, S.J., Lehr, J.M.: ‘Charge injection energy barriers and charge mobilities in insulating liquids’, in ‘2009 IEEE Conference on Electrical Insulation and Dielectric Phenomena’ (IEEE, 2009), pp. 613–616
- [47] Latham, R.: ‘The origin of prebreakdown electron emission from vacuum-insulated high voltage electrodes’, *Vacuum*, 1982, **32**, (3), pp. 137–140.
- [48] Mesiats, G.A., Proskurovskii, D.I.: ‘Review of Vacuum Breakdown and Discharge Studies’, in ‘Pulsed Electric Discharges in Vacuum’ (Springer-Verlag Berlin Heidelberg, 1989), pp. 5–40
- [49] Butcher, M., Neuber, A., Kromphoiz, H., Dickens, J.: ‘Pre-breakdown current behavior in DC volume breakdown in transformer oil’, in ‘Digest of Technical Papers. PPC-2003. 14th IEEE International Pulsed Power Conference (IEEE Cat. No.03CH37472)’ (IEEE, 2004), pp. 289–292
- [50] Helmholtz, H.: ‘Studien über elektrische Grenzschichten’, *Ann. der Phys. und Chemie*, 1879, **243**, (7), pp. 337–382.
- [51] Gouy, M.: ‘Sur la constitution de la charge électrique à la surface d’un électrolyte’, *J. Phys. Théorique Appliquée*, 1910, **9**, (1), pp. 457–468.
- [52] Stern, O.: ‘Zur theorie der elektrolytischen doppelschicht’, *Zeitschrift für Elektrochemie Angew. Phys. Chemie*, 1924, **30**, (21–22), pp. 508–516.
- [53] Raza, W., Ali, F., Raza, N., *et al.*: ‘Recent advancements in supercapacitor technology’, *Nano Energy*, 2018, **52**, pp. 441–473.
- [54] Srinivasan, S.: ‘Electrode/Electrolyte Interfaces: Structure and Kinetics of Charge Transfer’, in ‘Fuel Cells From Fundamentals to Applications’ (Springer, Boston, MA, 2006), pp. 27–92
- [55] Cosgrove, T.: ‘Charge in Colloidal Systems’, in ‘Colloid Science: Principles, Methods and Applications’ (Blackwell Publishing, 2005), pp. 14–35
- [56] Hunter, R.J.: ‘Electrified Interfaces: the Electrical Double Layer’, in ‘Foundations of Colloid Science’ (Oxford University Press, 2001, 2nd edn.), pp. 305–369
- [57] Kepler, R.G.: ‘Charge carrier production and mobility in anthracene crystals’, *Phys. Rev.*, 1960, **119**, (4), pp. 1226–1229.
- [58] Schmidt, W.F., Allen, A.O.: ‘Mobility of Free Electrons in Dielectric Liquids’, *J. Chem. Phys.*, 1969, **50**, (11), pp. 5037–5037.
- [59] Röhr, J.A., Moia, D., Haque, S.A., Kirchartz, T., Nelson, J.: ‘Exploring the validity and limitations of the Mott–Gurney law for charge-carrier mobility determination of semiconducting thin-films’, *J. Phys. Condens. Matter*, 2018, **30**, (10), p. 105901.
- [60] R.S.Sigmond: ‘Simple approximate treatment of unipolar space-charge-dominated coronas: The Warburg law and the saturation current’, *J. Appl. Phys.*, 1982, **53**, (2), pp. 891–898.

- 
- [61] Halpern, B., Gomer, R.: 'Field emission in liquids', *J. Chem. Phys.*, 1969, **51**, (3), pp. 1031–1047.
- [62] Coelho, R., Debeau, J.: 'Properties of the tip-plane configuration', *J. Phys. D. Appl. Phys.*, 1971, **4**, (9), pp. 1266–1280.
- [63] Denat, A., Gosse, J.P., Gosse, B.: 'Electrical Conduction of Purified Cyclohexane in a Divergent Electric', *IEEE Trans. Electr. Insul.*, 1988, **23**, (4), pp. 545–554.
- [64] Atten, P., Seyed-Yagoobi, J.: 'Electrohydrodynamically induced dielectric liquid flow through pure conduction in point/plane geometry', *IEEE Trans. Dielectr. Electr. Insul.*, 2003, **10**, (1), pp. 27–36.
- [65] Landau, L.D., Lifshitz, E.M.: 'Electrostatics of Dielectrics', in 'Electrodynamics of Continuous Media ( Volume 8 of A Course of Theoretical Physics )' (PERGAMON PRESS LTD., 1960, 1st edn.), pp. 36–83
- [66] Atten, P., Seyed-Yagoobi, J.: 'Electrohydrodynamically induced dielectric liquid flow through pure conduction in point/plane geometry', *IEEE Trans. Dielectr. Electr. Insul.*, 2003, **10**, (1), pp. 27–36.
- [67] Kattan, R., Denat, A., Lesaint, O.: 'Generation, growth, and collapse of vapor bubbles in hydrocarbon liquids under a high divergent electric field', *J. Appl. Phys.*, 1989, **66**, (9), pp. 4062–4066.
- [68] Choi, S.U.S., Eastman, J.A.: 'Enhancing thermal conductivity of fluids with nanoparticles', in '1995 International mechanical engineering congress and exhibition' (1995)
- [69] Viswanathan, P.K., Chandrasekar, S.: 'Influence of carbon quantum dots modified silica nanoparticles on insulation properties of mineral oil', *Proc. 2019 Int. Conf. High Volt. Eng. Technol. ICHVET 2019*, 2019, pp. 1–5.
- [70] Maharana, M., Bordeori, M.M., Nayak, S.K., Sahoo, N.: 'Nanofluid-based transformer oil: effect of ageing on thermal, electrical and physicochemical properties', *IET Sci. Meas. Technol.*, 2018, **12**, (7), pp. 878–885.
- [71] Sartoratto, P.P.C., Neto, A.V.S., Lima, E.C.D., Rodrigues de Sá, A.L.C., Morais, P.C.: 'Preparation and electrical properties of oil-based magnetic fluids', *J. Appl. Phys.*, 2005, **97**, (10), p. 10Q917.
- [72] Sima, W., Shi, J., Yang, Q., Huang, S., Cao, X.: 'Effects of conductivity and permittivity of nanoparticle on transformer oil insulation performance: experiment and theory', *IEEE Trans. Dielectr. Electr. Insul.*, 2015, **22**, (1), pp. 380–390.
- [73] Du, Y., Lv, Y., Li, C., *et al.*: 'Effect of electron shallow trap on breakdown performance of transformer oil-based nanofluids', *J. Appl. Phys.*, 2011, **110**, (10), pp. 6–10.
- [74] Du, Y., Lv, Y., Li, C., *et al.*: 'Effect of semiconductive nanoparticles on insulating performances of transformer oil', *IEEE Trans. Dielectr. Electr. Insul.*, 2012, **19**, (3), pp. 770–776.

- 
- [75] Meena, R.R., Chaki, S.H., Khimani, A.J., Deshpande, M.P.: 'Investigation of ultrasonic parameters and measurement of thermal conductivity of CuO-transformer oil nanofluids', *Mater. Res. Express*, 2019, **6**, (8), p. 0850f3.
- [76] Hosokawa, M., Nogi, K., Naito, M., Yokoyama, T.: 'Nanoparticle Technology Handbook', (Elsevier, 2008)
- [77] Lee, J.-C., Kim, W.-Y.: 'Experimental Study on the Dielectric Breakdown Voltage of the Insulating Oil Mixed with Magnetic Nanoparticles', *Phys. Procedia*, 2012, **32**, pp. 327–334.
- [78] Atiya, E.G., Mansour, D.-E.A., Khattab, R.M., Azmy, A.M.: 'Dispersion behavior and breakdown strength of transformer oil filled with TiO<sub>2</sub> nanoparticles', *IEEE Trans. Dielectr. Electr. Insul.*, 2015, **22**, (5), pp. 2463–2472.
- [79] Keblinski, P., Phillpot, S.R., Choi, S.U.S., Eastman, J.A.: 'Mechanisms of heat flow in suspensions of nano-sized particles (nanofluids)', *Int. J. Heat Mass Transf.*, 2002, **45**, (4), pp. 855–863.
- [80] Eastman, J.A., Phillpot, S.R., Choi, S.U.S., Keblinski, P.: 'Thermal transport in nanofluids', *Annu. Rev. Mater. Res.*, 2004, **34**, (1), pp. 219–246.
- [81] Wang, X., Xu, X., Choi, S.U.S.: 'Thermal conductivity of nanoparticle-fluid mixture', *J. Thermophys. heat Transf.*, 1999, **13**, (4), pp. 474–480.
- [82] Lee, D., Kim, J.-W., Kim, B.G.: 'A New Parameter to Control Heat Transport in Nanofluids: Surface Charge State of the Particle in Suspension', *J. Phys. Chem. B*, 2006, **110**, (9), pp. 4323–4328.
- [83] O'Sullivan, F.M.: 'A model for the initiation and propagation of electrical streamers in transformer oil and transformer oil based nanofluids', 2007
- [84] O'Sullivan, F., Hwang, J.G., Zahn, M., *et al.*: 'A Model for the Initiation and Propagation of Positive Streamers in Transformer Oil', in 'Conference Record of the 2008 IEEE International Symposium on Electrical Insulation' (IEEE, 2008), pp. 210–214
- [85] Hwang, J.G., O'Sullivan, F., Zahn, M., Hjortstam, O., Pettersson, L.A.A., Liu, R.: 'Modeling of streamer propagation in transformer oil-based nanofluids', *Annu. Rep. - Conf. Electr. Insul. Dielectr. Phenomena, CEIDP*, 2008, pp. 361–366.
- [86] Chiesa, M., Das, S.K.: 'Experimental investigation of the dielectric and cooling performance of colloidal suspensions in insulating media', *Colloids Surfaces A Physicochem. Eng. Asp.*, 2009, **335**, (1–3), pp. 88–97.
- [87] Sima, W., Shi, J., Yang, Q., Huang, S., Cao, X.: 'Effects of conductivity and permittivity of nanoparticle on transformer oil insulation performance: Experiment and theory', *IEEE Trans. Dielectr. Electr. Insul.*, 2015, **22**, (1), pp. 380–390.
- [88] Kao, K.C.: '8 - Electrical Aging, Discharge, and Breakdown Phenomena', in 'Dielectric Phenomena in Solids' (Academic Press, 2004), pp. 515–572
- [89] Takahashi, H., Watanabe, R., Miyauchi, Y., Mizutani, G.: 'Discovery of deep and

- shallow trap states from step structures of rutile TiO<sub>2</sub> vicinal surfaces by second harmonic and sum frequency generation spectroscopy', *J. Chem. Phys.*, 2011, **134**, (15), p. 154704.
- [90] Aljure, M., Becerra, M., Jonsson, B.L.G.: 'Simulation of the electrical conduction of cyclohexane with TiO<sub>2</sub> nanoparticles', in '2014 IEEE 18th International Conference on Dielectric Liquids (ICDL)' (IEEE, 2014), pp. 1–4
- [91] Becerra, M., Aljure, M., Masoud Pourrahimi, A., Roman, F.: 'High field conduction in mineral oil based ZnO nanofluids prior to negative streamer inception', *J. Phys. Commun.*, 2021, **5**, (4), p. 045006.
- [92] Du, B.X., Li, X.L., Li, J.: 'Thermal conductivity and dielectric characteristics of transformer oil filled with BN and Fe<sub>3</sub>O<sub>4</sub> nanoparticles', *IEEE Trans. Dielectr. Electr. Insul.*, 2015, **22**, (5), pp. 2530–2536.
- [93] Wagner, K.W.: 'Erklärung der dielektrischen Nachwirkungsvorgänge auf Grund Maxwellscher Vorstellungen', *Arch. für Elektrotechnik*, 1914, **2**, (9), pp. 371–387.
- [94] Hippel, A. Von: 'Dielectrics and waves', *L. Willey Sons, New York*, 1966, **1**, pp. 1–294.
- [95] J., B.P.: 'An electrical model for coalescers that employ pulsed DC fields', *Chem. Eng. Res. Des.*, 1995, **73**, pp. 559–566.
- [96] Jones, T.B.: 'Electromechanics of Particles', (Cambridge University Press, 2005)
- [97] Jackson, J.D.: 'Classical Electrodynamics, 3rd ed.', (1999)
- [98] Yu, K.W., Wan, J.T.K.: 'Interparticle force in polydisperse electrorheological fluids', *Comp. Phys. Comm.*, 2000, **129**, pp. 177–184.
- [99] Sjoblom, J.: 'Electrocoalescence for Oil–Water Separation: Fundamental Aspects', in 'Emulsions and Emulsion Stability' (CRC Press, 2005), pp. 549–592
- [100] Lu, Y., Matsuda, Y., Sagara, K., Hao, L., Otomitsu, T., Yoshida, H.: 'Fabrication and Thermoelectric Properties of Magneli Phases by Adding Ti into TiO<sub>2</sub>', *Adv. Mater. Res.*, 2011, **415–417**, pp. 1291–1296.
- [101] AMERICAN ELEMENTS ®: 'BORON NITRIDE POWDER', <https://www.americanelements.com/boron-nitride-powder-10043-11-5>, accessed July 2020
- [102] Wypych, A., Bobowska, I., Tracz, M., *et al.*: 'Dielectric Properties and Characterisation of Titanium Dioxide Obtained by Different Chemistry Methods', *J. Nanomater.*, 2014, **2014**, pp. 1–9.
- [103] Madelung, O., Rössler, U., Schulz, M. (Eds.): 'Boron nitride (BN) dielectric constants', in 'Group IV Elements, IV-IV and III-V Compounds. Part a - Lattice Properties' (Springer Berlin Heidelberg, 2001), pp. 1–5
- [104] Timoshkin, I. V., Fouracre, R.A., Given, M.J., MacGregor, S.J., Mason, P., Clephan, R.: 'Dielectric properties of Diala D, MIDEL 7131 and THESO insulating liquids',

- Annu. Rep. - Conf. Electr. Insul. Dielectr. Phenomena, CEIDP*, 2008, pp. 622–625.
- [105] ‘Shell Diala Oil B High performance insulating oil’, (Technical Data Sheet, Royal Dutch Shell PLC, 2006), pp. 1–2
- [106] M&I MATERIALS: ‘MIDEL 7131 Safety Data Sheet’, (2018)
- [107] M&I MATERIALS: ‘MIDEL eN 1204 MIDEL ® SAFETY INSIDE’, (2018)
- [108] Rakhshan, N., Pakizeh, M.: ‘Removal of triazines from water using a novel OA modified SiO<sub>2</sub> /PA/PSf nanocomposite membrane’, *Sep. Purif. Technol.*, 2015, **147**, pp. 245–256.
- [109] Lewand, L.R.: ‘Laboratory Testing of Natural Ester Dielectric Liquids’, *Neta World*, 2004.
- [110] Kisch, R.J.: ‘Using Refractive Index to Monitor Oil Quality in High Voltage Transformers’, The University of British Columbia, 2008
- [111] Malvern Panalytical: ‘Selecting an appropriate particle absorption for laser diffraction particle size calculations’, (2014)
- [112] Yamada, Y., Uyama, H., Watanabe, S., Nozoye, H.: ‘Deposition at low substrate temperatures of high-quality TiO<sub>2</sub> films by radical beam-assisted evaporation’, *Appl. Opt.*, 1999, **38**, (31), p. 6638.
- [113] DeVore, J.R.: ‘Refractive Indices of Rutile and Sphalerite’, *J. Opt. Soc. Am.*, 1951, **41**, (6), p. 416.
- [114] Takahashi, T., Itoh, H., Kuroda, M.: ‘Structure and properties of CVD-BN thick film prepared on carbon steel substrate’, *J. Cryst. Growth*, 1981, **53**, (2), pp. 418–422.
- [115] Deng, J.X., Zhang, X.K., Yao, Q., Wang, X.Y., Chen, G.H., He, D.Y.: ‘Optical properties of hexagonal boron nitride thin films deposited by radio frequency bias magnetron sputtering’, *Chinese Phys. B*, 2009, **18**, (9), pp. 4013–4018.
- [116] Pouch, J.J., Alterovitz, S.A., Miyoshi, K., Warner, J.O.: ‘Boron Nitride: Composition, Optical Properties, and Mechanical Behavior’, *MRS Proc.*, 1987, **93**, p. 323.
- [117] Mahidhar, G.D.P., Somasundaram Karthikeyan, A., Sarathi, R., Taylor, N., Edin, H.: ‘Dielectric properties of mixed mineral and synthetic ester oil’, *IET Sci. Meas. Technol.*, 2020, **14**, (9), pp. 704–714.
- [118] Aljure, M., Becerra, M., Karlsson, M.E.: ‘On the injection and generation of charge carriers in mineral oil under high electric fields’, *J. Phys. Commun.*, 2019, **3**, (3), p. 035019.
- [119] Ouellette, R.J., Rawn, J.D., Ouellette, R.J., Rawn, J.D.: ‘Carboxylic Acid Derivatives’, *Org. Chem.*, 2014, pp. 699–745.
- [120] Wang, Y., Wang, F., Li, J., Liang, S., Zhou, J.: ‘Electronic Properties of Typical Molecules and the Discharge Mechanism of Vegetable and Mineral Insulating Oils’, *Energies*, 2018, **11**, (3), p. 523.

- 
- [121] Butcher, M., Neuber, A.A., Cevallos, M.D., Dickens, J.C., Krompholz, H.: ‘Conduction and breakdown mechanisms in transformer oil’, *IEEE Trans. Plasma Sci.*, 2006, **34**, (2 III), pp. 467–475.
- [122] Li, Y., Dong, M., Zhang, C., *et al.*: ‘Investigation on charge-carrier transport characteristics of transformer oil-based nanofluids’, *IEEE Trans. Dielectr. Electr. Insul.*, 2018, **25**, (6), pp. 2443–2451.
- [123] Jing, Y., Timoshkin, I. V., Wilson, M.P., *et al.*: ‘Dielectric properties of natural ester, synthetic ester midel 7131 and mineral oil diala D’, *IEEE Trans. Dielectr. Electr. Insul.*, 2014, **21**, (2), pp. 644–652.
- [124] Atten, P., Malraison, B., Zahn, M.: ‘Electrohydrodynamic plumes in point-plane geometry’, *IEEE Trans. Dielectr. Electr. Insul.*, 1997, **4**, (6), pp. 710–718.
- [125] Chen, G., Given, M., Timoshkin, I., Wilson, M.P., MacGregor, S.: ‘Measurements of mobility in aged mineral oil in the presence of nanoparticles’, in ‘2017 IEEE 19th International Conference on Dielectric Liquids, ICDL 2017’ (2017), pp. 1–4
- [126] Yang, L., Gubanski, S., Serdyuk, Y. V., Schiessling, J.: ‘Dielectric properties of transformer oils for HVDC applications’, *IEEE Trans. Dielectr. Electr. Insul.*, 2012, **19**, (6), pp. 1926–1933.
- [127] Zadeh, M.S.: ‘Measurement of ion mobility in dielectric liquids, Master Thesis’, Chalmers University of Technology, 2011
- [128] Lv, Y., Du, Q., Wang, L., *et al.*: ‘Effect of TiO<sub>2</sub> nanoparticles on the ion mobilities in transformer oil-based nanofluid’, *AIP Adv.*, 2017, **7**, (10), p. 105022.
- [129] Nichols, K.G., Vernon, E. V.: ‘Space-Charge-Limited Currents in Semiconductors and Insulators. Majority Carrier Transistors.’, in ‘Transistor Physics. Modern Electrical Studies.’ (Springer, Dordrecht, 1966), pp. 283–311
- [130] Mahmud, S., Chen, G., Golosnoy, I.O., Wilson, G., Jarman, P.: ‘Bridging in contaminated transformer oil under DC and AC electric field’, *J. Phys. Conf. Ser.*, 2013, **472**, (1), p. 012007.

## APPENDIX I MATHEMATICAL DERIVATION

This section presents the mathematical work on modelling of single particle in Dielectric liquids, which follows the conditions listed in Section 3.1.1. The electric potential across the particle-liquids interface should be continues:

$$\varphi_1 = \varphi_2 \qquad \qquad \qquad \text{at } r = R \qquad \qquad \text{I-1}$$

The rate of change of the surface charge density at the interface must be equal to the difference of the radial current from either side of the interface:

$$J_1 - J_2 = \frac{d\sigma_{surface}}{dt} \qquad \qquad \qquad \text{at } r = R \qquad \qquad \text{I-2}$$

where,  $J_1 = \sigma_1 E_{r1}$ , and  $J_2 = \sigma_2 E_{r2}$  is the radial current from the particle and the liquid respectively,  $\sigma_{surface}$  is the charge density at the interface and can be presented as:

$$\sigma_{surface}(t) = \varepsilon_1 E_{r1} - \varepsilon_2 E_{r2} \qquad \qquad \qquad \text{at } r = R \qquad \qquad \text{I-3}$$

This relationship between the rate of change of the surface charge density and the radial current can be summarised as the charge continuity condition. This condition is time dependent and can be written for three time domains at  $t = 0$ ,  $0 < t < \infty$  and  $t \rightarrow \infty$ :

$$\sigma_{surface}(t) = \varepsilon_1 E_{r1} - \varepsilon_2 E_{r2} = 0 \qquad \qquad \qquad \begin{array}{l} \text{for } t = 0 \\ r = R \end{array} \qquad \qquad \text{I-4}$$

$$J_1 - J_2 = \frac{d\sigma_{surface}}{dt} \quad \begin{array}{l} \text{for} \\ 0 < t < \infty \\ r = R \end{array} \quad \text{I-5}$$

$$J_1 - J_2 = \sigma_1 E_{r1} - \sigma_2 E_{r2} = 0 \quad \begin{array}{l} \text{for } t \rightarrow \infty \\ r = R \end{array} \quad \text{I-6}$$

The relationship between  $A(t)$  and  $B(t)$  can be established by combining Equations I-1 with I-5, which yields:

$$A(t)R^3 + Ef(t)R^3 = B(t) \quad \text{at } r = R \quad \text{I-7}$$

Substituting this relationship into Equation I-6, gives:

$$A(t) + \frac{\varepsilon_1 + 2\varepsilon_2}{\sigma_1 + 2\sigma_2} \frac{\partial A(t)}{\partial t} \Big|_{r=R} + 3E \frac{\sigma_2 f(t) + \varepsilon_2 \delta(t)}{\sigma_1 + 2\sigma_2} = 0 \quad \text{I-8}$$

As Equation I-8 is a nonhomogeneous differential equation its solution requires the associated homogeneous differential equation:

$$\frac{\partial A(t)}{\partial t} \Big|_{r=R} + \frac{1}{\tau} A(t) = 0 \quad \text{I-9}$$

where,  $\tau = \frac{\varepsilon_1 + 2\varepsilon_2}{\sigma_1 + 2\sigma_2}$ , and Equation I-9 yields:

$$A(t) = C \exp\left(-\frac{t}{\tau}\right) \quad \text{I-10}$$

where  $C$  is an arbitrary constant for a general solution,  $A(t)$ . By exchanging the constant  $C$  with an unknown function  $u(t)$ , Equation I-10 turns into:

$$A(t) = u(t) \exp\left(-\frac{t}{\tau}\right) \quad \text{I-11}$$

Substituting Equation I-11 into Equation I-8, and solving the expression for  $u(t)$ :

$$\begin{aligned} \left. \frac{\partial u(t)}{\partial t} \right|_{r=R} &= -3E \frac{\sigma_2 f(t) + \varepsilon_2 \delta(t)}{\varepsilon_1 + 2\varepsilon_2} \exp\left(\frac{t}{\tau}\right) \\ du(t) &= -3E \frac{\sigma_2 f(t) + \varepsilon_2 \delta(t)}{\varepsilon_1 + 2\varepsilon_2} \exp\left(\frac{t}{\tau}\right) dt \\ \int du(t) &= -3E \frac{\sigma_2}{\varepsilon_1 + 2\varepsilon_2} \int f(t) \exp\left(\frac{t}{\tau}\right) dt \\ &\quad - 3E \frac{\varepsilon_2}{\varepsilon_1 + 2\varepsilon_2} \int \delta(t) \exp\left(\frac{t}{\tau}\right) dt \end{aligned} \quad \text{I-12}$$

Since Equation I-12 origins from Equation I-5, which is only available for  $0 < t < \infty$ . Therefore, the  $\int \delta(t) \exp\left(\frac{t}{\tau}\right) dt$  equals to zero, and  $f(t) = 1$ , then Equation I-12 turns into:

$$\begin{aligned} u(t) &= -3E \frac{\sigma_2}{\varepsilon_1 + 2\varepsilon_2} \int \exp\left(\frac{t}{\tau}\right) dt \\ &= -3E \frac{\sigma_2}{\sigma_1 + 2\sigma_2} \left[ \exp\left(\frac{t}{\tau}\right) + C \right] \end{aligned} \quad \text{I-13}$$

And:

$$A(t) = -3E \frac{\sigma_2}{\sigma_1 + 2\sigma_2} - 3CE \frac{\sigma_2}{\sigma_1 + 2\sigma_2} \exp\left(-\frac{t}{\tau}\right) \quad \text{I-14}$$

By introducing another boundary condition into Equation I-14, the arbitrary constant  $C$  in Equation I-14 can then be solved and the final expressions for both  $A(t)$  and  $B(t)$  are provided below:

$$A(t) = -3E \left[ \frac{\varepsilon_2}{\varepsilon_1 + 2\varepsilon_2} \exp\left(-\frac{t}{\tau}\right) + \frac{\sigma_2}{\sigma_1 + 2\sigma_2} \left(1 - \exp\left(-\frac{t}{\tau}\right)\right) \right] \quad \text{I-15}$$

$$B(t) = ER^3 \left[ \frac{\varepsilon_1 - \varepsilon_2}{\varepsilon_1 + 2\varepsilon_2} \exp\left(-\frac{t}{\tau}\right) + \frac{\sigma_1 - \sigma_2}{\sigma_1 + 2\sigma_2} \left(1 - \exp\left(-\frac{t}{\tau}\right)\right) \right] \quad \text{I-16}$$

where,

$$\tau = \frac{\varepsilon_1 + 2\varepsilon_2}{\sigma_1 + 2\sigma_2} \quad \text{I-17}$$

is the Wagner-Maxwell relaxation time, according to Equation I-15 and I-16 above, the radial electric field can be presented as:

$$\vec{E}_{r1} = 3E \left[ \frac{\varepsilon_2}{\varepsilon_1 + 2\varepsilon_2} \exp\left(-\frac{t}{\tau}\right) + \frac{\sigma_2}{\sigma_1 + 2\sigma_2} \left(1 - \exp\left(-\frac{t}{\tau}\right)\right) \right] \cos\theta \check{r} \quad \text{I-18}$$

$$\vec{E}_{r2} = Ef(t)\cos\theta + 2E \frac{R^3}{r^3} \left[ \frac{\varepsilon_1 - \varepsilon_2}{\varepsilon_1 + 2\varepsilon_2} \exp\left(-\frac{t}{\tau}\right) + \frac{\sigma_1 - \sigma_2}{\sigma_1 + 2\sigma_2} \left(1 - \exp\left(-\frac{t}{\tau}\right)\right) \right] \cos\theta \check{r} \quad \text{I-19}$$

## APPENDIX II PARAMETERS FOR QUICKFIELD MODELLING

By introducing the QuickField software, the electric field distribution in the two self-designed test cells can be simulated, of which the simulations are presented in Figure 4-7 and 4-9, respectively. The simulations show that the electric field distribution in the two test cells is quasi-uniform. This section presents the simulation parameters, including both the dimensional information and the electrical information.

The simulations are conducted based on the ‘electrostatic analysis mode’ in the QuickField. The modelling of the two test cells is based on two-dimensional condition. The dimensional information of the modelling is shown in Figure II-1.

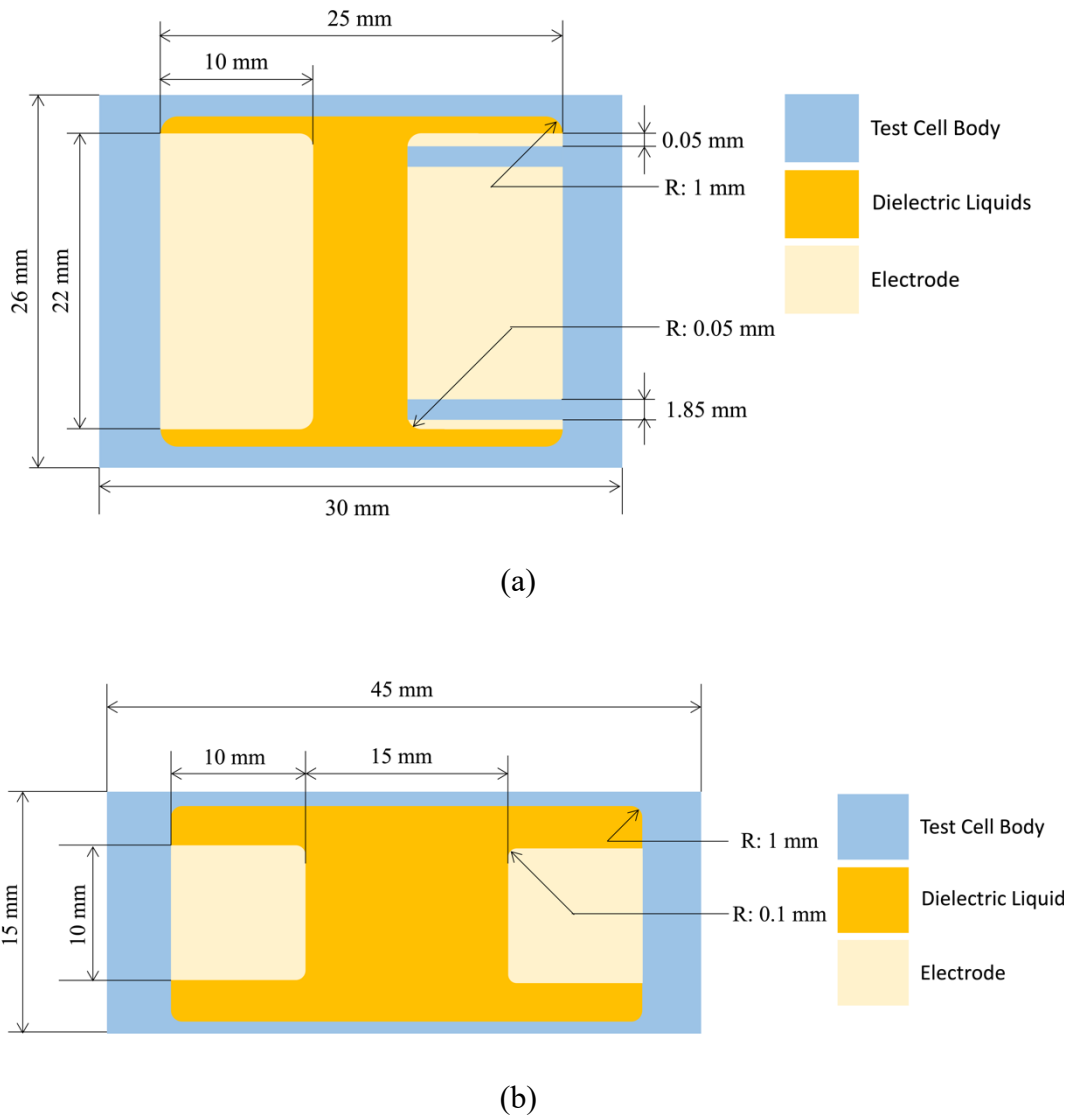


Figure II-1 (a) Schematic illustration of the Guard Ring Test Cell. (b) Schematic illustration of the Transparent Test Cell with Parallel Disk Electrodes.

Correspondingly, the parameters for the modelling work are listed in Table II-1 below. Any other parameters not listed in Table II-1 are selected as the default values in the QuickField.

Table II-1 Parameters for QuickField Modelling

<b>Materials</b>	<b>Test Cell Body</b>	<b>Electrode</b>	<b>Dielectric Liquids</b>
<b>Problem</b>	Electrostatic		
<b>Area Label Property</b>			
<b>Relative Permittivity X</b>	3.8	10000	3.2
<b>Relative Permittivity Y</b>	3.8	10000	3.2
<b>Electric Charge Density</b>			
<b>Coordinates</b>	Cartesian	Cartesian	Cartesian
<b>Edge Label Property</b>			
<b>Voltage</b>	0 kV	4 kV	0 kV
<b>Noddle Label Property</b>			
<b>Voltage</b>	0 kV	4 kV	0 kV

## APPENDIX III DATA ANALYSIS METHODS

The data acquired in the experimental tests should be processed before further analytical analysis. This processing includes filtering raw data and statistical analysis of the obtained results. The filtering method used in the present work, its implementation in Python 3.7 and the error analysis methodology are discussed in this section.

### **Errors and Uncertainty**

The term ‘error’ describes the difference between the true and measured values [1]. Most of measured values obtained in this research include both systematic and random errors, which leads to the uncertainty in the final results. Section 4.4.1 presents an overview of the methodology used to obtain the uncertainties used in this study.

Measurement errors occur due to multiple factors, including instrument accuracy, environmental changes, the measuring process itself. The experimental errors are divided into two main categories: the random and systematic errors. The random errors are related to the unknown and unpredictable elements in the measurements and can be reduced by increasing the number of measurements. The systematic errors are related to the instrument(s) accuracy and the measurement methodology and cannot be reduced simply by increasing the number of tests.

To describe the errors quantitatively, two types of evaluation of uncertainties, Type A and Type B evaluation, can be introduced.

Type A uncertainty evaluation can be conducted using the statistical method(s) for treating the obtained experimental data [2]. An example of such evaluation includes obtaining the mean and its standard deviation or a number of independent, repeated measurements. However, it should be noted that the standard deviation can be obtained only when the number of observations is sufficiently high. To obtain a more reliable evaluation of the experimental results, the t-distribution (also known as the Student Distribution) can be used. This

distribution allows for evaluation of the uncertainty in measurements using smaller sample sizes.

As outlined in [3], Type B evaluation of uncertainty can be conducted by taken into account of the information related to the measurement procedures including any previously obtained results, knowledge on the behaviour of the materials and instruments involved in the measurements, manufacture’s data sheets/specifications, relevant reference data etc, [3]. In this research, the uncertainty caused by the instrument is evaluated as the Type B uncertainty. The relevant information is provided in Table III-1.

Table III-1 Uncertainty of Instruments

<b>Item</b>	<b>Uncertainty</b>	<b>Data Source</b>
Voltage Source (AU-60)	$\pm 1\%$	User Manual [4]
Voltage Source (Keithley-617)	$\pm 50$ mV	User Manual [5]
Digital Caliper	$\pm 0.01$ mm	User Manual
Digital Electrometer (Keithley-6514)	$\pm 0.001$ nA	User Manual [6]
Clock (LabVIEW)	$\pm 1$ millisecond	User Manual [7]

Generally, obtaining uncertainty in practical measurements involves more than one input, and each individual uncertainty can be evaluated via either Type A or Type B methods. Then, the uncertainty propagation formula can be used to obtain the final uncertainty from each individual input.

Assuming  $Y$  value is obtained as  $Y = f(X_1, X_2, \dots, X_n)$ , with individually measured inputs:  $X_1, X_2, \dots, X_n$ . If inputs  $x_i$ , and  $x_j$  are not related to each other, the uncertainty of  $Y$  can then be obtained as the combined uncertainty of each input:

$$u_c(y) = \sqrt{\sum_{i=1}^N \left(\frac{\partial f}{\partial x_i}\right)^2 u^2(x_i)} \quad \text{III-1}$$

where,  $u_c$  denotes the combined uncertainty of value  $Y$ ,  $u(x_i)$  denotes the uncertainty of each individual input  $x_i$ . Since the measured experimental data are acquired via different methods and instruments, the details of the uncertainty calculations may differ from each other. However, the main principles of these uncertainty calculations are based on the principles introduced above.

## Data Filtering

The parameters which were measured / obtained experimentally in this work include electric current, voltage, and time. Among them, the electric current values, including the current measurements acquired via the electrometer, are used to determine the electric conductivity of the tested fluids and the time of flight. However, as the current through insulating liquids is low (pA to nA), there are variations in the measured current values.

Since the accuracy in measurement of the ToF is based on the identification of the current peak position in time, the variations in the raw current data can result in significant error in the obtained ToF values and generate further errors. Thus, signal processing, filtering and denoising of raw current-time characteristics should be conducted to identify current peaks which are used to measure the ToF values.

In this research, the Savitzky-Golay (SG) filter was used in the current data analysis. The SG filter is based on averaging a group of input data sets and converting them into the data output. The averaging coefficients are calculated using the least-squares fit with a high order

polynomial in the moving window [8]. The details of the SG filter are introduced in the following paragraphs.

First, a brief review of the Moving Average filter is provided, as this filter is the most commonly used filter and lays the foundation for the SG filter. It can be mathematically expressed as:

$$y_i = \frac{1}{n_L + n_R + 1} \sum_{j=-n_L}^{n_R} x_{i+j} \quad \text{III-2}$$

where,  $x$  is the input signal,  $y$  is the filtered output. The integer  $n_L$ , and  $n_R$  represent the number of data points on either side of the  $i_{th}$  data, respectively. Once  $n_L = n_R$ , the moving average filter is called the symmetric moving average filter. Compared with the other moving average filter(s), the symmetric filter can remove the shift between the original and filtered data, which is especially beneficial in the time domain data.

The Signal-to-Noise Ratio (SNR) of moving average filter can be improved by increasing the averaging window length, namely  $n_L + n_R + 1$ . However, the length of the averaging window must be limited as otherwise, the data will be excessively filtered, resulting in losing or distorting some information.

To overcome these limitations (time delay and data lost), the SG filter was introduced by Abraham Savitzky and Marcel Golay in 1964, this filter has an advantage of preserving information on peaks in the filtered data [9].

The basic idea of the SG filter is the high order polynomial approximation based on the least-squares fitting. Assuming that there is a set of equally spaced data  $f_i$ , and a moving window with window length  $2n + 1$ , a polynomial with higher order,  $m$ , for the approximation of the data within the window:  $f_{i-n}, f_{i-n+1}, \dots, f_0, \dots, f_{i+n-1}, f_{i+n}$ , can be written as:

$$p(i) = \sum_{k=0}^m a_k t^k \quad \text{III-3}$$

where,  $a_k$  are unknown coefficients. Before moving to the next step, one thing must be pointed out: the precondition for solving Equation III-3 is that the number of the unknown coefficients  $a_k$  must be no more than the number of the unsolved equations:  $m \leq 2n + 1$ , i.e., the order degree of the approximation polynomial must be no more (typically less) than the length of the filtering window.

To obtain the values of  $a_k$ , the least squares method is used:

$$\varepsilon = \sum_{i=-n}^n (p(i) - f_i)^2 \quad \text{III-4}$$

where,  $\varepsilon$  is the mean-squared approximation error of data  $f_i$  within the moving window. The least-squares method requires  $\varepsilon$  to be minimised:

$$\frac{\partial \varepsilon}{\partial a_k} = 0 \quad \text{for } k \in [0, m] \quad \text{III-5}$$

$a_k$  can hence be resolved with Equation III-5, which gives the values of  $p(i)$ .  $p_0$  is located in the centre of the data set  $p_i$ , its value equals to first coefficient  $a_0$ , and corresponds to the filtered output value of the original  $f_0$ .

After this procedure, only the centre value is kept as the filtered result. The moving window is then moved by one value to make a new approximation. Once the window goes through the whole data set,  $f_i$ , the filtering procedure is completed. However, the procedure above provides only a generic algorithm of the SG filter. In practice, it was pointed out by Savitzky

and Golay that there are specific sets of the filter coefficients used for fitting within a moving window.

To get a general solution for Equation III-5, Equations III-3 and III-4 are introduced, yielding:

$$\frac{\partial \sum_{i=-n}^n (\sum_{k=0}^m a_k i^k - f_i)^2}{\partial a_r} = 0 \quad \text{for } r \in [0, m] \quad \text{III-6}$$

Solving Equation III-6 yields:

$$\sum_{k=0}^m \left( \sum_{i=-n}^n i^{k+r} \right) a_k = \sum_{i=-n}^n f_i i^r \quad \text{for } r \in [0, m] \quad \text{III-7}$$

It can be helpful to convert Equation III-7 into a matrix form, which requires defined matrix  $\mathbf{A}$ , as presented below [10]:

$$\mathbf{A} = \begin{bmatrix} (-n)^0 & (-n)^1 & \dots & (-n)^{m-1} & (-n)^m \\ (1-n)^0 & (1-n)^1 & \dots & (1-n)^{m-1} & (1-n)^m \\ \vdots & \vdots & \vdots & \vdots & \vdots \\ (n-1)^0 & (n-1)^1 & \dots & (n-1)^{m-1} & (n-1)^m \\ (n)^0 & (n)^1 & \dots & (n)^{m-1} & (n)^m \end{bmatrix} \quad \text{III-8}$$

Then Equation III-7 can be expressed as:

$$\mathbf{A}^T \mathbf{A} \mathbf{a} = \mathbf{A}^T \mathbf{F} \quad \text{III-9}$$

where,  $\mathbf{a} = [\mathbf{a}_0, \mathbf{a}_1, \dots, \mathbf{a}_{m-1}, \mathbf{a}_m]^T$ , and  $\mathbf{F} = [f_{-n}, f_{1-n}, \dots, f_0, \dots, f_{n-1}, f_n]^T$ . Following these results, the relationship between the polynomial coefficients and the observed data can be expressed as:

$$\mathbf{a} = (\mathbf{A}^T \mathbf{A})^{-1} \mathbf{A}^T \mathbf{F} \quad \text{III-10}$$

Matrix  $\mathbf{A}$  only depends on  $n$  and  $m$ , i.e., the moving window length and polynomial order, which are fixed once the filtering starts. It hence can be concluded that there is a fixed linear relationship between the observed data and the polynomial coefficients from the beginning to the end of the observed data. Thus, each filtered result from each single moving window can be calculated with a set of the fixed coefficients and the observed data within the window.

Recalling that the first value,  $a_0$  is the value of the filtered result of the centre of the observed data in the moving window, the coefficients are the first row of the matrix  $(\mathbf{A}^T \mathbf{A})^{-1} \mathbf{A}^T$ . Therefore, the SG filter turns into a weighted moving average filter in terms of the practical calculations, the specific weights are decided by the window length and the approximation polynomial order.

In this research, the current values acquired via the electrometer represent a discrete-time signal. The time sequence of the signal amplitude (i.e., the current value) is required to obtain the ToF for calculations of the mobility. Compared with the moving average filter, the SG filter's ability to maintain the shape and heights of the signal peak during the data smoothing can significantly reduce the bias without delays. Particularly, as the smoothing degree of the SG filter can be modified not only by the window length but also by the polynomial order, the various types of signal peaks in the observed data can then be preserved or smoothed,

The SG filter was implemented in Python 3.7 (`scipy.signal.savgol_filter` in SciPy Python library [11]) to implement the practical data filtering process.

## References

- 
- [1] Dunn, P.F.: 'Chapter 7 Uncertainty Analysis', in 'Measurement and Data Analysis for Engineering and Science' (CRC Press, 2014), pp. 229–283

- [2] National Institute of Standards and Technology: ‘Evaluating uncertainty components: Type A’, <https://physics.nist.gov/cuu/Uncertainty/typea.html>, accessed June 2021
- [3] National Institute of Standards and Technology: ‘Evaluating uncertainty components: Type B’, <https://physics.nist.gov/cuu/Uncertainty/typeb.html>, accessed June 2021
- [4] Matsusada Precision Inc.: ‘Low profile / High power Rack-mount type HV power supply’, (2019)
- [5] Keithley Instruments Inc.: ‘Model 617 Programmable Electrometer Instruction Manual Contains Operating and Servicing Information’, (1984)
- [6] Keithley Instruments Inc.: ‘Model 6514 System Electrometer Instruction Manual’, (2004, Fourth)
- [7] National Instruments: ‘Accuracy of Software-Timed Applications in LabVIEW’, <https://knowledge.ni.com/KnowledgeArticleDetails?id=kA00Z000000P9QiSAK&l=en-US>, accessed June 2021
- [8] Press, W.H., Teukolsky, S.A., Vetterling, W.T., Flannery, B.P.: ‘14.8 Savitzky-Golay Smoothing Filters’, in ‘Numerical Recipes in Fortran 77: The Art of Scientific Computing’ (1987), pp. 644–649
- [9] Savitzky, A., Golay, M.J.E.: ‘Smoothing and Differentiation of Data’, *Anal. Chem.*, 1964, **36**, (8), pp. 1627–1639.
- [10] Schafer, R.: ‘What Is a Savitzky-Golay Filter?’, *IEEE Signal Process. Mag.*, 2011, **28**, (4), pp. 111–117.
- [11] The SciPy communit: ‘`scipy.signal.savgol_filter`’, [https://docs.scipy.org/doc/scipy/reference/generated/scipy.signal.savgol\\_filter.html](https://docs.scipy.org/doc/scipy/reference/generated/scipy.signal.savgol_filter.html), accessed June 2021

## APPENDIX IV PUBLISHED WORK

### Published Journal Paper:

- (1) Xue, Q., Timoshkin, I., Wilson, M., Given, M., and MacGregor, S., 2020. 'Mobility of Charge Carriers in Mineral Oil and Ester liquids'. *IET High Voltage*. 10.1049/hve2.12098.

### Published Conference Paper:

- (1) Xue, Q., Timoshkin, I., Wilson, M., Given, M., and MacGregor, S., 2019. 'Mobility of Charge Carriers in Dielectric Liquids.' ICDL 2019 Proceedings. Roma, Italy, 23<sup>rd</sup> -27<sup>th</sup> June, 2019, pp.1-4.
- (2) Xue, Q., Timoshkin, I., Given, M., Wilson, M., Wang, T., and MacGregor, S., 2018. 'Dynamic Behaviour of Sub- $\mu\text{m}$  Particles in Dielectric Liquids under DC Stress'. EAPPC & BEAMS 2018 Proceedings, Changsha, China, 2018, 16<sup>th</sup> -20<sup>th</sup> Sep, pp.223-226.

### Conference Presentation:

- (1) 'Analysis of Charge Carrier Mobility in Insulating Liquids', Oral Presentation, 13<sup>th</sup> UHVnet conference, Glasgow, UK. 15<sup>th</sup> – 16<sup>th</sup> Jan, 2020
- (2) 'Dynamic behaviour of particles in dielectric liquids under DC stress', Oral Presentation, 7<sup>th</sup> EAPPC conference, Changsha, China. 16<sup>th</sup> – 20<sup>th</sup> Sep, 2018
- (3) 'A study of the force distribution between two water droplets under a step current electric field', Poster Presentation, 10<sup>th</sup> UHVnet conference, Glasgow, UK. 15<sup>th</sup> – 16<sup>th</sup> Jan, 2017